

Imperial College of Science, Technology and Medicine  
Department of Materials

# **Atomistic Simulation of Fission Products in Zirconia Polymorphs**

Alexandros Kenich

Submitted in part fulfilment of the requirements for the degree of  
Doctor of Philosophy and the Diploma of Imperial College

September 2019



## DECLARATION

I declare that the work presented in this thesis is my own, and that all efforts from others are referenced.

The copyright of this thesis rests with the author and is made available under a Creative Commons Attribution Non-Commercial No Derivatives licence. Researchers are free to copy, distribute or transmit the thesis on the condition that they attribute it, that they do not use it for commercial purposes and that they do not alter, transform or build upon it. For any reuse or redistribution, researchers must make clear to others the licence terms of this work.

---

## Abstract

Zirconium alloys are used as a cladding material in most nuclear reactors worldwide due to properties uniquely suited to the operating environment of a reactor. In this thesis, density functional theory (DFT) simulations were conducted to investigate the behaviour of fission product dopants in the inner cladding oxide, and to examine the role this layer plays in limiting corrosion in the context of pellet-cladding interaction (PCI).

Simulations in undoped monoclinic, tetragonal and cubic  $\text{ZrO}_2$  yielded structure properties in addition to intrinsic defect energies, volumes and defect equilibria. Fully-charged Schottky defects  $\{2\text{V}_\text{O}^{\bullet\bullet}:\text{V}_\text{Zr}'''\}^\times$  had the smallest formation energies in each phase, followed by O Frenkels and then Zr Frenkels. Defective cubic  $\text{ZrO}_2$  simulations are sensitive to finite-size effects, and would often break symmetry or collapse into the tetragonal phase when defect clusters were introduced. Free energy calculations predicted a transition from monoclinic to tetragonal as temperature was increased, but not from tetragonal to cubic.

Iodine defects adopt oxidation states of +1 ( $\text{I}_\text{O}^{\bullet\bullet\bullet}$ ,  $\text{I}_\text{i}^\bullet$  and  $\text{I}_\text{Zr}'''$ ) or -1 ( $\text{I}_\text{O}^\bullet$ ) in  $\text{ZrO}_2$ , with fewer defects in the 0 oxidation state ( $\text{I}_\text{O}^{\bullet\bullet}$ ). At high oxygen partial pressures ( $p_{\text{O}_2}$ ), iodine defects in tetragonal  $\text{ZrO}_2$  fall significantly. Iodine defects in monoclinic  $\text{ZrO}_2$  changed by small amounts as  $p_{\text{O}_2}$  was increased. This demonstrated competition between iodine and oxygen in  $\text{ZrO}_2$ , and that it is dependent on both  $p_{\text{O}_2}$  and phase. High  $p_{\text{O}_2}$  in the tetragonal phase provides the greatest barrier to iodine ingress.

During reactor power ramps, the quantity of fission products implanted in the oxide layer will increase. Decay rates of Te and I isotopes were found to be commensurate with time to failure in irradiation tests. Defect equilibria and volumes of Te, I, Xe and Cs were obtained in tetragonal  $\text{ZrO}_2$  to investigate the effect of nuclear transmutation while dopant atoms are present. Defect evolution on the O site is predicted to be  $\text{Te}_\text{O}^{\bullet\bullet} \rightarrow \text{I}_\text{O}^\bullet \rightarrow \text{Xe}_\text{O}^{\bullet\bullet} \rightarrow \text{Cs}_\text{O}^{\bullet\bullet}$ . On the Zr site, Brouwer diagrams predict  $\text{Te}_\text{Zr}''' \rightarrow \text{I}_\text{Zr}''' \rightarrow \text{Xe}_\text{Zr}'''' \rightarrow \text{Cs}_\text{Zr}'''$ . These defects have large defect volumes and will generate stresses which may promote crack formation.



## Acknowledgements

Firstly I would like to thank my supervisors Robin Grimes and Mark Wenman for giving me this opportunity and opening the door to pursue nuclear engineering at such a high level. I would also like to thank the EPSRC for funding my studentship through the ICO CDT, the Imperial College HPC team for their quick responses whenever something went wrong, Philipp Frankel and his research group at the University of Manchester for the fruitful discussions and insightful conferences over the years, the Department of Materials administration staff for all their help with my admin woes and the Centre for Nuclear Engineering for being my second home for half a decade.

In no particular order, I want to give a shout-out to the great people who have left a strong impression on me and influenced my growth both as a scientist and as a person: Wael Al Jishi, Aman Pujara, Conor Galvin, Paul Fossati, Claudia Gasparrini, Navaratnarajah Kuganathan, Emma Warriss, Mamdouh Farid, Selman Mawad, Ingrid Kenich, Dhan-Sham Rana, Said El Chamaa, Filippo Vecchiato, Jana Smutna, Vlad Podgurschi, Matt Jackson, Lloyd Jones, Marco Loaiza, Mateusz Balasz, Diana Wan, Coyes Subhan, Nipun Wickramasundara, Hussam Zaghal, Safa Abu-Saba, Ramy Daoud, Vartan Shadarevian, Usaama Latif, Amro Sehly, Patrick Burr, Mohammed El Shbib, William White, Mark Mawdsley, Richard Pearson, Sophie Morrison, Alan Charles, Jonathan Tate, Andy Wilson, John Brokx, Victoria Moustaki, Stefanos Moustaki, Rita Konstantinidi, Alexandru Paunoiu, Maria Etegan, Jasmin Vu, Antonia Mateescu, Gion Margadant, Elena-Maria Budurean, Irina Dumitrescu, Julian Sutherland, Diana Cucu, Pepa Matein, Laura Dumitru, Diana Mincu, Mihaela Rosca, Niklas Hambüchen, Daniela Baloiu, Ioana Marinica, Dorina Dobre, Jack Shortiss and Anca Semenescu.

Finally, I give my everlasting gratitude and love to my parents, my wife Cristina Budurean and my daughter Livia-May.

*In memory of Emma Warriss*

# Contents

<b>Abstract</b>	<b>i</b>
<b>Acknowledgements</b>	<b>iii</b>
<b>1 Introduction</b>	<b>1</b>
1.1 Nuclear Power . . . . .	1
1.1.1 Fission . . . . .	2
1.1.2 Reactor design . . . . .	4
1.1.3 Fuel pellets and cladding . . . . .	8
1.1.4 Effects of radiation on materials . . . . .	10
1.1.5 Fission products, their distribution and decay chains . . . . .	13
1.1.6 Formation of plutonium and minor actinides . . . . .	16
<b>2 Literature Review</b>	<b>19</b>
2.1 PCI . . . . .	19
2.1.1 Fuel pellet relocation . . . . .	20
2.1.2 Pellet-clad gap and bonding . . . . .	22
2.1.3 Reactor power ramps . . . . .	23
2.1.4 PCI Failures . . . . .	24
2.1.5 Fission products and SCC . . . . .	29
2.1.6 Iodine availability . . . . .	33
2.2 Oxidation of zirconium . . . . .	37
2.2.1 Oxide growth mechanism . . . . .	38

2.2.2	Oxygen solubility of zirconium . . . . .	39
2.2.3	Outer oxide vs inner oxide . . . . .	39
2.2.4	Sources of oxygen . . . . .	42
2.3	Atomistic scale computer simulation . . . . .	44
2.3.1	Classical approach - molecular dynamics . . . . .	45
2.3.2	Quantum mechanical approach - DFT . . . . .	46
2.3.3	Band gap . . . . .	47
<b>3</b>	<b>Crystallography and Point Defects</b>	<b>51</b>
3.1	ZrO <sub>2</sub> phases . . . . .	51
3.1.1	Monoclinic . . . . .	53
3.1.2	Tetragonal . . . . .	55
3.1.3	Cubic . . . . .	58
3.1.4	Other phases . . . . .	58
3.2	Dopant stabilisation . . . . .	61
3.3	Kröger-Vink notation . . . . .	63
<b>4</b>	<b>Computational Methodology</b>	<b>65</b>
4.1	Density functional theory . . . . .	65
4.1.1	The Schrödinger equation . . . . .	66
4.1.2	Kohn-Sham Method . . . . .	67
4.1.3	Pseudopotentials . . . . .	69
4.2	Periodic boundaries . . . . .	73
4.2.1	Bloch's theorem . . . . .	73
4.2.2	Plane-waves . . . . .	75
4.3	Computational details . . . . .	75
4.3.1	Cell dimensions and initialisation . . . . .	75
4.3.2	Geometry optimisation . . . . .	77
4.3.3	Convergence criteria for geometry optimisation . . . . .	77
4.3.4	Charged cell correction . . . . .	79

4.3.5	Helmholtz free energy . . . . .	79
4.3.6	Incorporation energies . . . . .	80
4.3.7	Stiffness matrix generation . . . . .	82
4.3.8	Defect relaxation volumes . . . . .	82
4.4	Defect energies and equilibria . . . . .	84
4.4.1	Defect formation energies . . . . .	84
4.4.2	Defect equilibria . . . . .	84
4.4.3	Effect of space charge . . . . .	88
4.5	Convergence testing . . . . .	89
4.5.1	Plane-wave cut-off energy . . . . .	89
4.5.2	$\mathbf{k}$ -point convergence . . . . .	91
4.5.3	Exchange-correlation functionals . . . . .	93
4.5.4	On-the-fly pseudopotentials . . . . .	94
4.5.5	Chemical potential of oxygen . . . . .	95
4.5.6	Chemical potential of iodine . . . . .	97
4.5.7	+U study . . . . .	98
<b>5</b>	<b>Structure properties and intrinsic defects</b>	<b>104</b>
5.1	Introduction . . . . .	104
5.1.1	Previous work . . . . .	104
5.2	Methodology . . . . .	105
5.2.1	Simulation parameters . . . . .	105
5.2.2	Helmholtz free energy . . . . .	106
5.2.3	Brouwer diagrams . . . . .	106
5.3	Non-defective ZrO <sub>2</sub> . . . . .	107
5.3.1	Unit cells . . . . .	107
5.3.2	Elastic stiffness constants . . . . .	108
5.3.3	Electronic density of states . . . . .	109
5.3.4	Helmholtz energies . . . . .	112

5.4	Defective ZrO <sub>2</sub>	113
5.4.1	Formation energies	113
5.4.2	Frenkel and Schottky defects	117
5.4.3	Defect Volumes	124
5.4.4	Defect equilibria	126
5.5	Conclusions	129
<b>6</b>	<b>Iodine defect energies and equilibria in ZrO<sub>2</sub></b>	<b>131</b>
6.1	Introduction	131
6.2	Methodology	134
6.2.1	Simulation parameters	134
6.2.2	Defect Equilibrium Response to Oxygen Partial Pressure	134
6.3	Results	135
6.3.1	Incorporation energies	135
6.3.2	Dopant interstitial defects	138
6.3.3	Brouwer Diagrams	141
6.4	Conclusions	146
<b>7</b>	<b>Radioparagenesis of fission products in tetragonal ZrO<sub>2</sub></b>	<b>148</b>
7.1	Introduction	148
7.2	Methodology	151
7.2.1	Defect volumes and stress states	151
7.2.2	Brouwer diagrams	152
7.3	Results	153
7.3.1	Brouwer diagrams	153
7.3.2	Stress magnitudes and defect volumes	158
7.4	Conclusions	161

<b>8 Summary and further work</b>	<b>163</b>
8.1 Structure properties and intrinsic defects in ZrO <sub>2</sub>	163
8.2 Iodine doping and oxygen competition	165
8.3 Decay chain elements in ZrO <sub>2</sub>	166
8.4 Further work	167
8.4.1 Temperature effects in intrinsic defect simulations	167
8.4.2 Fission product empirical potential	168
8.4.3 Zr/ZrO/ZrO <sub>2</sub> interface study	168
8.4.4 Defect volumes	170
8.4.5 Experimental work	170
<b>References</b>	<b>172</b>
<b>Appendix</b>	<b>200</b>
<b>A ParaSweep</b>	<b>201</b>
<b>B CASTEP Scripts and Other Files</b>	<b>202</b>
<b>C Defect volumes without charge correction</b>	<b>203</b>
<b>D Steady state calculation of iodine inventory</b>	<b>206</b>



# List of abbreviations

<b>DFT</b>	Density Functional Theory
<b>PCI</b>	Pellet Cladding Interaction
<b>LWR</b>	Light Water Reactor
<b>PWR</b>	Pressurised Water Reactor
<b>BWR</b>	Boiling Water Reactor
<b>GCR</b>	Gas Cooled Reactor
<b>FNR</b>	Fast Neutron Reactor
<b>IDR</b>	Integrated Dry Route
<b>SCC</b>	Stress Corrosion Cracking
<b>NDT</b>	Non Destructive Testing
<b>GGA</b>	Generalised Gradient Approximation
<b>MD</b>	Molecular Dynamics
<b>PBE</b>	Perdew-Burke-Ernzerhof
<b>LDA</b>	Local Density Approximation
<b>VBM</b>	Valence Band Maximum
<b>CBM</b>	Conduction Band Minimum
<b>DOS</b>	Density Of States
<b>PP</b>	Pseudopotential
<b>RPV</b>	Reactor Pressure Vessel
<b>NTV</b>	Neutral Tri-Vacancy
<b>YSZ</b>	Yttria-Stabilised Zirconia

<b>PSZ</b>	Partially-Stabilised Zirconia
<b>VASP</b>	Vienna Ab Initio Simulation Package
<b>LHR</b>	Linear Heat Rating
<b>SEM</b>	Scanning Electron Microscope
<b>TEM</b>	Transmission Electron Microscope
<b>LCAO</b>	Linear Combination of Atomic Orbitals

# List of Tables

1.1	Type and number of different reactors operational worldwide at the end of 2017. Change from 2016 shown in parentheses. . . . .	7
1.2	Independent fission product yields and half-lives for the major iodine isotopes and precursors in a thermal neutron reactor. Yields taken from the Joint Evaluated Fission and Fusion File (JEFF 3.3). All isotopes undergo single $\beta$ - decay. Metastable states are included. . . . .	16
3.1	ZrO <sub>2</sub> phases and their details. . . . .	52
3.2	Ionic radii of Zr <sup>4+</sup> , Y <sup>3+</sup> and Ce <sup>4+</sup> in various coordination environments. . . . .	63
3.3	Examples of Kröger-Vink notation for several defects in ZrO <sub>2</sub> . . . . .	64
4.1	Composition of the supercells in terms of the number of individual unit cells stacked in each direction. . . . .	76
5.1	Calculated unit cell parameters for the different crystal structures of ZrO <sub>2</sub> . Experimental data for pure monoclinic, yttria-stabilised tetragonal and magnesia-stabilised cubic phases at 295 K are shown in parentheses. Energy difference between structures is shown with respect to the cubic phase. . . . .	107
5.2	Elastic stiffness constants for different phases of ZrO <sub>2</sub> from DFT calculations. . .	108
5.3	Experimentally determined band gaps alongside values calculated from DFT simulations for each crystal structure of zirconia. . . . .	111
5.4	Wyckoff positions of interstitial sites used for each crystal structure. . . . .	118
5.5	Formation energies in eV of Frenkel and Schottky defects calculated from point defects in ZrO <sub>2</sub> . . . . .	119
5.6	Formation energies of bound defects in ZrO <sub>2</sub> . . . . .	123
5.7	Individual point defect volumes in the three ZrO <sub>2</sub> structures. . . . .	124
5.8	Defect volumes of Frenkel and Schottky defects in the three ZrO <sub>2</sub> structures calculated from individual point defects. . . . .	125

6.1	Incorporation energies of iodine at different interstitial sites of ZrO <sub>2</sub> . . . . .	136
6.2	Incorporation energies of iodine in oxygen sites of the monoclinic, tetragonal, and cubic ZrO <sub>2</sub> phases. . . . .	137
6.3	Incorporation energies of iodine in zirconium sites of ZrO <sub>2</sub> . . . . .	138
7.1	Calculated defect volumes and stress tensor magnitudes of the dominant defect types in tetragonal ZrO <sub>2</sub> . Stress tensors are calculated for defective supercells. .	160
C.1	Individual point defect volumes in the three ZrO <sub>2</sub> structures. . . . .	204
C.2	Defect volumes of Frenkel and Schottky defects in the three ZrO <sub>2</sub> structures calculated from individual point defects. . . . .	204
C.3	Calculated defect volumes and stress tensor magnitudes of the dominant defect types in tetragonal ZrO <sub>2</sub> . Stress tensors are calculated for defective supercells. .	205

# List of Figures

1.1	Energy from thermal fission of U <sup>235</sup> as a function of mass ratios of daughter nuclei. Total energy release includes contributions from gamma rays and subsequent radioactive decays. . . . .	3
1.2	Plot of binding energy per nucleon against mass number. Arrows indicate the reaction shown in equation 1.2. . . . .	5
1.3	Schematic illustration of a PWR power plant. . . . .	6
1.4	Schematic view of a PWR fuel assembly and a PWR fuel pin. . . . .	8
1.5	UO <sub>2</sub> LWR fuel pellet showing dishes and chamfers. . . . .	10
1.6	Schematic cross-section of a single PWR fuel pin with an expanded view of the pellet-gap-cladding system. . . . .	11
1.7	Plot of neutron number against proton number for nuclei with half-lives greater than 10 <sup>-8</sup> s. . . . .	13
1.8	Plot of the percentage yield of nuclei with a given mass following a fission event. Range of masses corresponding to isotopes of iodine shown in purple and isotopes of yttrium shown in green, based on Equation 1.2. . . . .	15
2.1	Illustration of fuel swelling and clad deformation due to PCI. <b>a)</b> Fresh fuel before irradiation. <b>b)</b> Thermal expansion and swelling of fuel pellets and closing of fuel-pellet gap during operation. <b>c)</b> Fuel contact with cladding and subsequent ‘bamboozing’ of the cladding. . . . .	20
2.2	Concept of pellet-cladding gap model showing stages of fuel pellet fragment relocation with onset of soft and hard PCI. . . . .	21
2.3	Reactor startup procedure for a typical US PWR. Dashed line indicates % withdrawal of control rods. . . . .	23
2.4	Cracking of PWR fuel pellets and cladding. <b>a)</b> Transversal macrography of a fuel rod irradiated for two annual PWR operating cycles. <b>b)</b> Axial macrography of a fuel rod irradiated for two annual PWR operating cycles. <b>c)</b> SCC cladding failure. . . . .	25

2.5 Optical micrographs of incipient cracks in BWR cladding liners at a burnup of 30 MWd/kg U following <b>a</b> ) a ramp test with a peak LHR of 57 kW/m and <b>b</b> ) subsequent irradiation for 422 hours with a peak LHR of 47 kW/m. Black arrow indicates oxidised crack. . . . .	27
2.6 TRANS-RAMP I PCI failure progression for BWR fuel rods at a burnup of 30 MWd/kg U. . . . .	28
2.7 I-SCC susceptibility of stress relieved Zircaloy fuel cladding at 573 K as a function of burnup and cladding yield strengths at 553 K. Numbers next to data points indicate number of rings from the sample used in yield data. . . . .	29
2.8 Power ramping test data for the different phases of the Chalk River Nuclear Lab experiment. . . . .	31
2.9 Schematic of a proposed I-SCC process for cladding crack penetration. . . . .	33
2.10 Neutron absorption and fission spectra of $I^{131}$ and $U^{235}$ , respectively. . . . .	34
2.11 <b>a</b> ) TRIM distributions for iodine implantation in $ZrO_2$ at 50 keV, 800 keV and 6.5 MeV. <b>b</b> ) Rutherford backscattering spectrometry profile of 50 keV iodine implanted in $ZrO_2$ samples. . . . .	36
2.12 Diagrammatic representation of the cyclical oxidation behaviour of $ZrO_2$ . . . . .	38
2.13 Phase diagram of the Zr-O binary system. . . . .	40
2.14 Scanning transmission electron microscope (STEM) image of the outer oxide layer formed in an autoclave under simulated PWR water conditions showing the prevalence of different $ZrO_2$ phases. . . . .	41
2.15 High resolution scanning electron microscope (SEM) image of the bonding layer between a PWR $UO_2$ fuel pellet and Zr cladding in a fuel pin at an approximate burnup of 60 GWd/tU. . . . .	42
2.16 Elemental composition of the bonded $UO_2/ZrO_2$ layer from a PWR $UO_2$ fuel pellet with a burnup of 61 GWd/tU. . . . .	43
2.17 Partial U-O temperature binary phase diagram between O/U ratios of 1.2 and 2.25. . . . .	44
2.18 Illustration of the band gap in diamond as a function of interatomic spacing. . . . .	48
3.1 Temperature-pressure phase diagram of $ZrO_2$ . . . . .	51
3.2 A monoclinic $ZrO_2$ unit cell indicating the two different oxygen bond coordinations. Small spheres represent oxygen ions while large spheres represent zirconium ions. . . . .	53
3.3 Zirconium centre unit cell in monoclinic $ZrO_2$ showing nearest oxygen atoms and their respective bond co-ordinations. Zirconium atoms are shown in green and oxygen atoms in red. . . . .	54

3.4	Monoclinic-tetragonal phase transition in ZrO <sub>2</sub> as a function of temperature only.	55
3.5	<b>A)</b> Tetragonal ZrO <sub>2</sub> viewed along the [110] direction. <b>B)</b> Cubic ZrO <sub>2</sub> viewed along the [100] direction. Zirconium atoms are shown in green and oxygen atoms in red. . . . .	56
3.6	Pressure-temperature phase diagram for zirconia. Dash-dotted lines represent more recent data. Diamonds mark transition points during an increase in temperature or pressure, while open circles represent a decrease in pressure or temperature. Solid circles represent transition points for a fresh, single crystal sample.	57
3.7	Unit cell of cubic ZrO <sub>2</sub> . Zirconium atoms are shown in green and oxygen atoms shown in red. . . . .	58
3.8	Density plot of the nearest neighbour Zr-O bond distances in ZrO <sub>2</sub> for each crystal structure. Specific volumes from DFT calculations are 11.99 Å <sup>3</sup> ion <sup>-1</sup> , 11.51 Å <sup>3</sup> ion <sup>-1</sup> , and 11.13 Å <sup>3</sup> ion <sup>-1</sup> for monoclinic, tetragonal, and cubic phases respectively. . . . .	59
3.9	Illustrations of the orthorhombic OI (Pbca) crystal structure of ZrO <sub>2</sub> showing <b>a)</b> the unit cell viewed along the <i>a</i> direction and <b>b)</b> the zirconium ion centre with 7 coordinated oxygen ions. Zirconium and oxygen ions are coloured green and red respectively. . . . .	60
3.10	Illustration of <b>a)</b> OII cotunnite (Pnma) unit cell and <b>b)</b> zirconium ion with nearest neighbour oxygens with coordination number indicated. Zirconium and oxygen ions are shaded dark and light respectively. . . . .	61
4.1	Sketch of an all-electron potential V <sub>AE</sub> and a pseudopotential V <sub>PS</sub> with their corresponding wave functions. r <sub>cut</sub> indicates the radius beyond which both the potentials and their wave functions are the same. . . . .	70
4.2	Plots of the valence <i>s</i> and <i>p</i> orbital potentials for oxygen with two projectors per angular momentum. Dashed lines indicate the all-electron potentials while solid lines indicate the corresponding pseudopotential. Dotted vertical line marks the radius beyond which the potentials match. . . . .	71
4.3	Plots of the valence <i>s</i> , <i>p</i> and <i>d</i> orbital potentials for zirconium with two projectors per angular momentum. Dashed lines indicate the all-electron potentials while solid lines indicate the corresponding pseudopotential. Dotted vertical line marks the radius beyond which the potentials match. . . . .	72
4.4	Two dimensional illustration of periodic boundary around a primitive cell. . . . .	74
4.5	Flowchart for Brouwer diagram construction based on program provided in Appendix B. Red and green ovals represent unsuccessful and successful termination sequences, respectively. Blue borders highlight the Fermi energy calculation while green borders highlight the dopant chemical potential calculation. Red borders highlight the iteration procedure for different oxygen pressures. . . . .	87
4.6	Tetragonal phase Brouwer diagrams of intrinsic point defects at a temperature of 1500 K <b>a)</b> without a space charge and <b>b)</b> with a space charge of 10 <sup>-1</sup> e <sup>-1</sup> /fu.	90

4.7	Log of the energy difference with respect to a highly converged calculation against plane-wave cut-off energy. The red arrow indicates the cut-off energy beyond which the error is below 0.01 eV. . . . .	91
4.8	Log of the energy difference with respect to a highly converged calculation against $\mathbf{k}$ -point spacing. The red arrow indicates the $\mathbf{k}$ -point spacing which yields an error below 0.01 eV for all structures. . . . .	92
4.9	Calculated energy of a unit cell of monoclinic, tetragonal and cubic $\text{ZrO}_2$ when using different exchange-correlation functionals. . . . .	94
4.10	Energy deviation in meV of supercells with candidate OTF pseudopotential pairs. Energy deviations are shown with respect to the pseudopotential pair that resulted in the lowest total energy calculated. . . . .	96
4.11	Energy minimisation of two iodine atoms from an initial separation of 3.0 Å. . .	97
4.12	Calculated band gaps for different +U values in monoclinic, tetragonal and cubic $\text{ZrO}_2$ . . . . .	100
4.13	Individual lattice parameters as a function of +U term in monoclinic $\text{ZrO}_2$ . . .	101
4.14	Individual lattice parameters as a function of +U term in tetragonal $\text{ZrO}_2$ . . .	102
4.15	Lattice parameter as a function of +U term in cubic $\text{ZrO}_2$ . . . . .	103
5.1	Electronic density of states for the different crystal structures of $\text{ZrO}_2$ showing the band gap predicted by DFT. . . . .	110
5.2	Helmholtz free energy as a function of temperature for the monoclinic, tetragonal, and cubic crystal structures of $\text{ZrO}_2$ . . . . .	112
5.3	Monoclinic phase formation energies of intrinsic vacancy defects as a function of Fermi level. Gradient indicates defect charge. Oxygen coordination number shown in legend. . . . .	114
5.4	Tetragonal phase formation energies of intrinsic vacancy defects as a function of Fermi level. Gradient indicates defect charge. . . . .	116
5.5	Cubic phase formation energies of intrinsic vacancy defects as a function of Fermi level. Gradient indicates defect charge. . . . .	117
5.6	Zirconium centre cell showing nearest oxygen atoms in tetragonal $\text{ZrO}_2$ . Schottky trios indicated by oxygen enumeration with Zr, O and a second oxygen in either the 1 <sup>st</sup> , 2 <sup>nd</sup> or 3 <sup>rd</sup> nearest neighbour with respect to the initial oxygen. Zirconium atoms are shown in green and oxygen atoms in red. . . . .	122
5.7	Zirconium centre cell showing nearest oxygen atoms in cubic $\text{ZrO}_2$ . Schottky trios indicated by oxygen enumeration with Zr, O and a second oxygen in either the 1 <sup>st</sup> , 2 <sup>nd</sup> or 3 <sup>rd</sup> nearest neighbour with respect to the initial oxygen. Zirconium atoms are shown in green and oxygen atoms in red. . . . .	123
5.8	Monoclinic phase Brouwer diagram of intrinsic defects at 650 K. . . . .	126

5.9	Tetragonal phase Brouwer diagrams of intrinsic defects at 1500 K. . . . .	128
5.10	Cubic phase Brouwer diagrams of intrinsic defects at 2000 K. . . . .	129
6.1	Iodine interstitial formation energies in monoclinic ZrO <sub>2</sub> as a function of Fermi level. Gradient indicates defect charge. . . . .	139
6.2	Iodine interstitial formation energies in tetragonal ZrO <sub>2</sub> as a function of Fermi level. Gradient indicates defect charge. . . . .	141
6.3	Iodine interstitial formation energies in cubic ZrO <sub>2</sub> as a function of Fermi level. Gradient indicates defect charge. . . . .	142
6.4	Monoclinic phase Brouwer diagrams of point defects at iodine concentrations of a) 10 <sup>-5</sup> and b) 10 <sup>-3</sup> , at a temperature of 650 K. . . . .	143
6.5	Tetragonal phase Brouwer diagrams of point defects at iodine concentrations of a) 10 <sup>-5</sup> and b) 10 <sup>-3</sup> , at a temperature of 1500 K. . . . .	145
7.1	Plot of the percentage yield of nuclei with a given mass following a fission event. Range of masses corresponding to isotopes of Te, I, Xe and Cs are highlighted. .	149
7.2	Diagram of the production of Te <sup>135</sup> decay chain elements with decay modes and half-lives shown. . . . .	150
7.3	Brouwer diagrams for tetragonal phase ZrO <sub>2</sub> point defects at tellurium concentrations of a) 10 <sup>-5</sup> and b) 10 <sup>-3</sup> , at a temperature of 1500 K. . . . .	154
7.4	Brouwer diagrams for tetragonal phase ZrO <sub>2</sub> point defects at xenon concentrations of a) 10 <sup>-5</sup> and b) 10 <sup>-3</sup> , at a temperature of 1500 K. . . . .	157
7.5	Tetragonal phase Brouwer diagrams of point defects at caesium concentrations of a) 10 <sup>-5</sup> and b) 10 <sup>-3</sup> , at a temperature of 1500 K. . . . .	159
8.1	STEM image of a Zr-1.0%Nb sample oxidised in simulated PWR water at 360 °C for 120 days. . . . .	169



# Chapter 1

## Introduction

### 1.1 Nuclear Power

In the summer of 1956, the world's first commercial nuclear power plant was connected to the grid in the north of England. This marked a significant departure from previous forms of commercial energy production, which relied on relatively low energy density sources such as the combustion of coal, oil and gas. Before this, the closest anyone had come to utilising nuclear energy commercially was through geothermal power, where the thermal energy input is partly due to radiogenic heat from unstable isotopes in the Earth's mantle [1].

Combustion is a chemical process whereby energy differences between reactants and products are exploited via electron exchange. Nuclear energy exploits the energy difference between nuclei. Both rely on the conversion of mass into energy, however, the amount of energy that can be extracted from the nucleus is several orders of magnitude greater.

Consider methane, with an enthalpy of combustion of -887.2 kJ/mol [2]. This is the equivalent

of 9.14 eV per particle. By comparison, the total energy release from fission of one uranium-235 nucleus is at least  $1.65 \times 10^8$  eV, as shown in Figure 1.1.

Combustion-based power as a technology has matured over hundreds of years, with modern optimisations only looking to offer fractional percent gains in efficiency. By comparison, nuclear power technology is far from mature, with large improvements yet to be realised. One such feature is load-following, an enormously useful feature for a power plant which is currently underutilised in nuclear reactors. Load-following, as currently practiced in some French and German nuclear power plants, is defined as operation where power output follows a variable load programme on a daily basis with several power changes (i.e. to follow the change in electricity demand over a 24 hour period). These power variations can be as large as 50% of a reactor's rated power [3]. The biggest obstacle to load-following in nuclear reactors is the issue of pellet-cladding interaction (PCI), which is the basis of the work in this thesis.

### 1.1.1 Fission

Commercial nuclear power plants extract energy through the process of fission, where a large nucleus is split into smaller nuclei. While it is also possible to extract energy from certain small nuclei by the process of fusing them into larger ones, no fusion reactor currently exists which achieves a net positive energy output. At a fundamental level, both fission and fusion rely upon mass-energy equivalence. The relationship between mass and energy is shown using Einstein's equation:

$$E = mc^2 \quad (1.1)$$

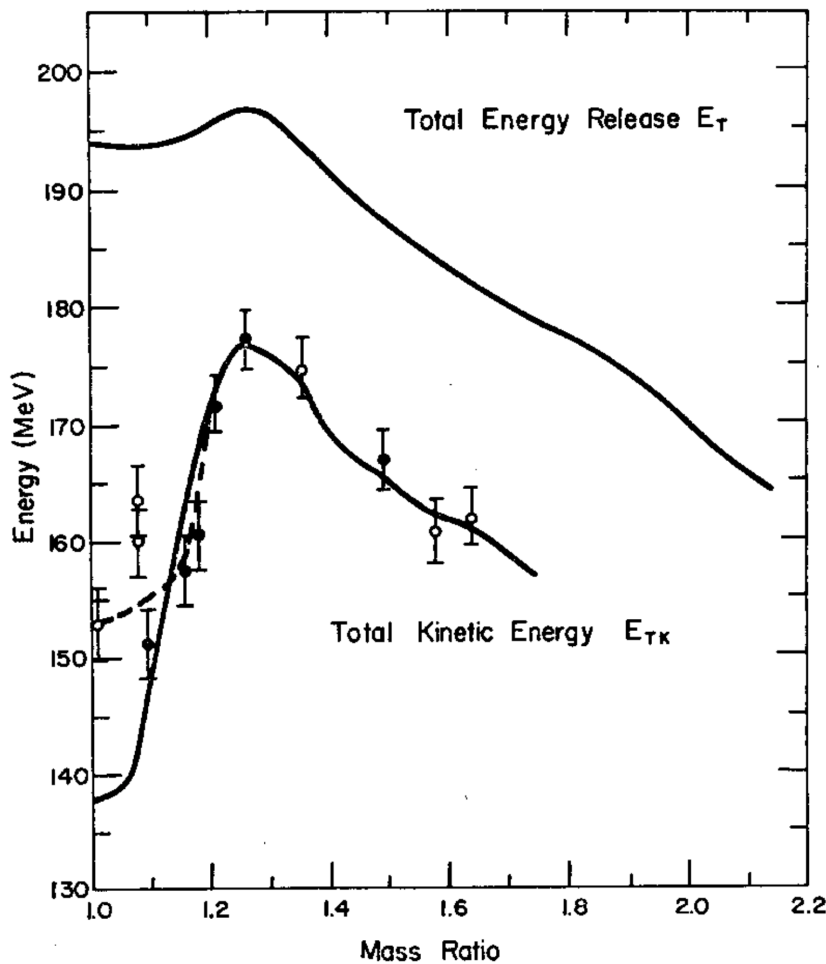
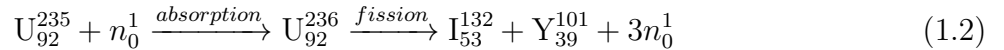


Figure 1.1: Energy from thermal fission of  $\text{U}^{235}$  as a function of mass ratios of daughter nuclei. Total energy release includes contributions from gamma rays and subsequent radioactive decays. Taken from [4].

where  $E$  is the energy of the system,  $m$  is the mass and  $c$  is the speed of light in a vacuum.

Using this equation we can analyse a typical fission reaction:



While the number of protons and neutrons are conserved throughout the reaction, a mass difference calculation will show that there is actually less mass in the products than the reactants by approximately  $0.188$  amu ( $3.127 \times 10^{-28}$  kg). This missing mass, known as the *mass defect*, is converted to energy ( $\sim 175$  MeV). In this way, the total mass-energy of the system is conserved.

Some of this energy is carried away as kinetic energy of the fission products (in Equation 1.2, I and Y) and also the kinetic energy of the neutrons. The neutrons at this stage have energies  $\sim 1$  MeV and are known as *fast* neutrons.

This change in mass arises due to the phenomenon of *binding energy*. In order for two or more nucleons to be thermodynamically stable when bound together, the total free energy of the bound configuration must be less than the sum of constituent nucleon free energies. Much as with energy stored in a chemical bond, the binding energy represents the energy required to separate the nucleus into individual protons and neutrons.

Larger nuclei will generally have a greater total binding energy value compared to smaller nuclei, but the mass defect per nucleon will not necessarily be the same in a larger nucleus. It is therefore useful to normalise the binding energy by the mass number. Different isotopes have different binding energies, and any nuclear reaction that increases the binding energy per nucleon will be exothermic, whether by fission or fusion. Figure 1.2 shows a plot of binding energy per nucleon against mass number with the relevant isotopes from Equation 1.2.

### 1.1.2 Reactor design

Commercial nuclear reactors are large boilers in a Rankine cycle, designed to maximise heat transfer to a working fluid. All nuclear plants use steam turbines on the generation side, though the reactor coolant may be another fluid in a separate loop, such as carbon dioxide in gas-cooled reactors (GCRs), or even in a separate water loop such as in pressurised water reactors (PWRs).

The most prevalent reactor type is the PWR, followed by the boiling water reactor (BWR). A schematic of a PWR power plant is shown in Figure 1.3. This design incorporates a primary

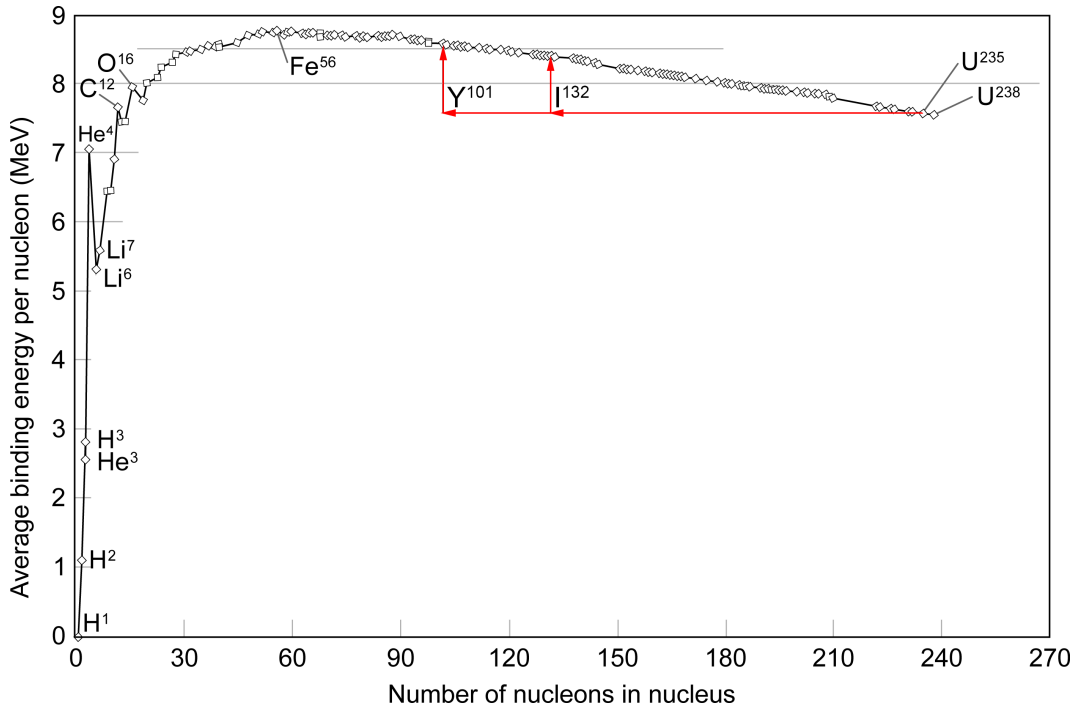


Figure 1.2: Plot of binding energy per nucleon against mass number. Arrows indicate the reaction shown in equation 1.2. Adapted from [5].

coolant loop and heat exchanger to a secondary loop at a lower pressure. Steam is generated on the low pressure side of the heat exchanger which then drives a steam turbine. There are several other reactor types (e.g. fast-neutron reactors and heavy water reactors) used around the world (enumerated in Table 1.1). The work in this thesis is focused on zirconium-based claddings which are used worldwide in all commercial reactors except GCRs and sodium-cooled fast reactors. In total, zirconium fuel cladding is used in over 95% of all nuclear reactor fuel pins, and so performance improvements in these cladding materials have an effect across the entire industry.

The fission of uranium takes place inside a steel reactor pressure vessel (RPV) in PWRs and BWRs, which holds the fuel pins, control rods and other reactor internals. The working fluid in a nuclear reactor is typically under high pressure, with PWR RPV operating pressures between 150 and 160 bar, while BWRs operate at lower pressures of around 70 bar [6–8]. The pressure

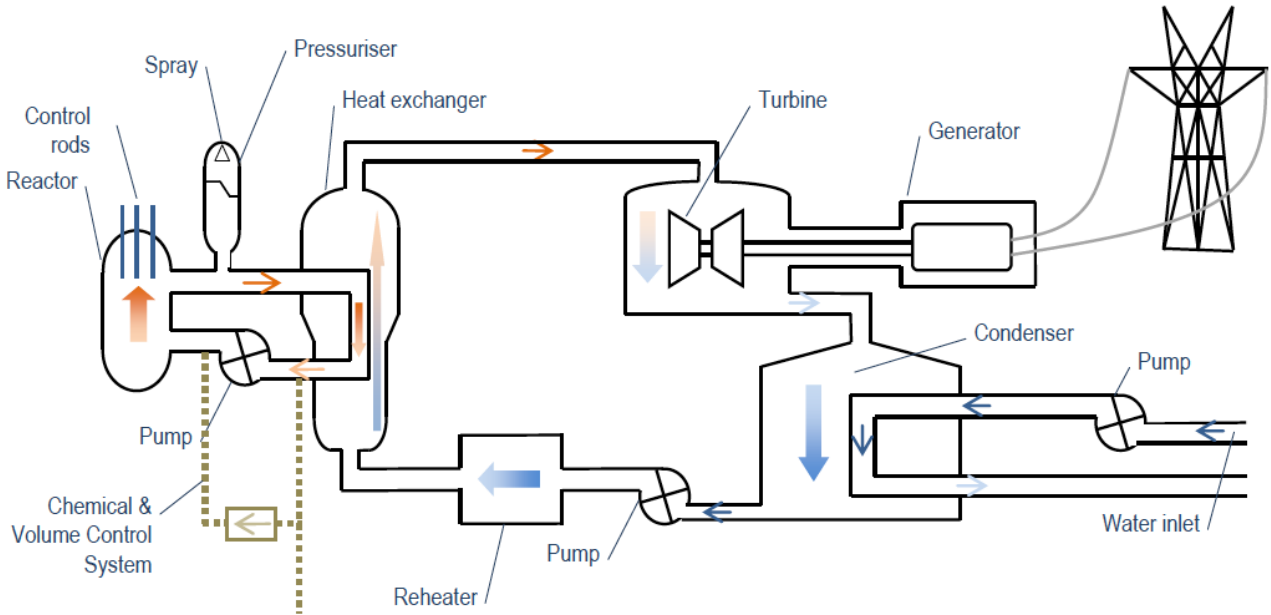


Figure 1.3: Schematic illustration of a PWR power plant. Taken from [3].

of the coolant acts on the fuel cladding, generating radial and hoop stresses which influence crack formation.

The operating temperature of the coolant in a typical PWR is approximately 600 K. This is a low temperature relative to the melting points of Zr metal (2128 K) and  $\text{ZrO}_2$  (2988 K). This temperature together with the high pressure is chosen in order to keep the coolant in the liquid phase for safety reasons, though this limits the thermodynamic efficiency of the plant. The highest temperature in a reactor will occur in the nuclear fuel, with PWR fuel pellets reaching centreline temperatures of up to 1673 K [9].

For both PWRs and BWRs, the coolant is typically light water (as opposed to heavy water,  $\text{D}_2\text{O}$ ). Water is used because it has many useful engineering properties. It has a high heat capacity (compared to the gaseous coolant in gas cooled reactors), has low activation in a free neutron environment and also serves as a good radiation shield. Furthermore, it is plentiful, cheap and easily purified.

Table 1.1: Type and number of different reactors operational worldwide at the end of 2017. Change from 2016 shown in parentheses. Taken from [10].

	Africa	Asia	East Europe & Russia	North America	South America	West & Central Europe	Total
BWR		28		36		11 (-2)	75 (-2)
FNR		1	2				3
GCR						14	14
LWGR			15				15
PHWR		25		19	3	2	49
PWR	2	86 (+3)	33	65	2	104	292 (+3)
<b>Total</b>	<b>2</b>	<b>140 (+3)</b>	<b>50</b>	<b>120</b>	<b>5</b>	<b>131 (-2)</b>	<b>448 (+1)</b>

In addition to its function as a coolant, water also acts as a neutron moderator, slowing down high-energy fast neutrons from fission events and nuclear decay processes. Moderation of neutrons is an important step in the nuclear reactor because slow thermal neutrons (i.e. neutrons at thermal equilibrium with the coolant) are significantly more likely to cause uranium nuclei to undergo fission than fast neutrons. Fast neutrons will typically escape from the fuel pin after they are generated, dispense most of their energy in the coolant via scattering with H and O nuclei, and then some will re-enter the fuel, where they may cause fission of a U<sup>235</sup> nucleus near the outer edge of the fuel pellet. Neutrons which do not end up fissioning fuel will either be absorbed parasitically by other nuclei (e.g. in the control rods or coolant), escape from the reactor entirely (neutron leakage), or decay into protons (free neutrons have a half-life of 10.61 minutes [11]).

### 1.1.3 Fuel pellets and cladding

Fuel assemblies in nuclear reactors are bundles of fuel pins (see Figure 1.4). In most commercial reactors, fuel pins are comprised of a zirconium-based cladding (tubes), which are filled with cylindrical UO<sub>2</sub> fuel pellets, each of which are approximately 1 cm<sup>3</sup> in volume (see Figure 1.5). Fuel pellets in PWRs and BWRs have dishes on the top and bottom faces of the cylinder as well as chamfered edges. The main function of the dishes is to reduce the axial pellet-pellet stresses caused due to swelling of the pellet when irradiated [12]. Chamfers aid in the loading of fuel pellets into the cladding, as well as reducing the risk of chipping at the edges of the fuel pellet. This is important because chipping of the fuel pellet can lead to debris falling into the pellet-cladding gap where it can act as a stress raiser [13].

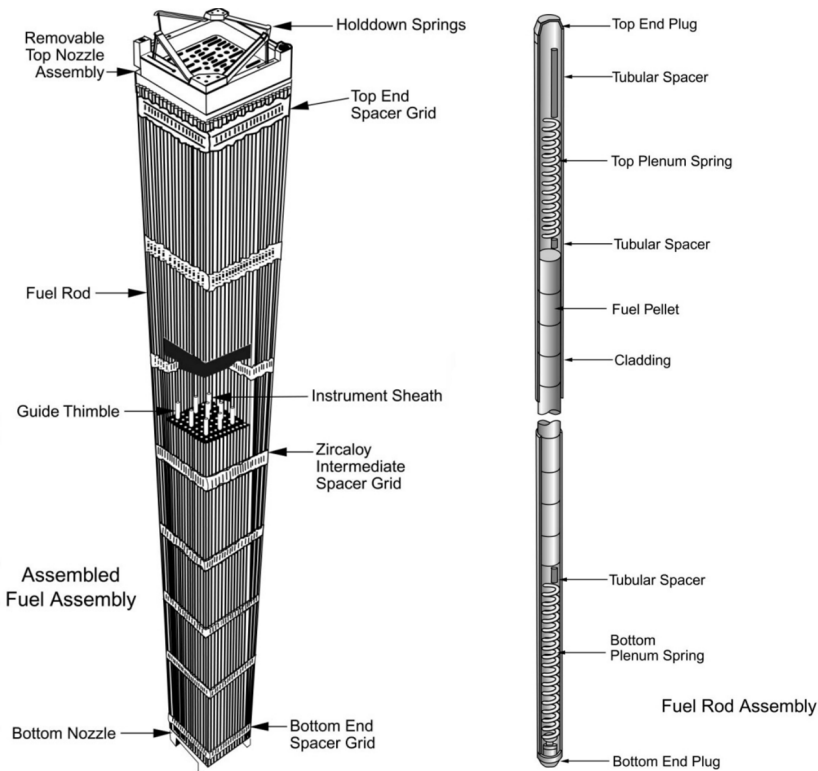


Figure 1.4: Schematic view of a PWR fuel assembly and a PWR fuel pin. Adapted from [14].

Once loaded with fuel pellets, the fuel pins are capped and filled with inert helium gas, pres-

surised to between 2 and 25 atm to improve heat transfer from the fuel pellets to the coolant as well as delaying inward creep deformation of the cladding due to the high coolant pressure [15].

LWR fuel pellets are manufactured in a multi-stage process starting from enriched  $\text{UF}_6$ . The  $\text{UF}_6$  must be converted into  $\text{UO}_2$ , which can be done using either a ‘dry’ or ‘wet’ process, referring to the use of liquid water in the process. The dry process, called the integrated dry route (IDR), is simpler and is described as follows:

- Enriched  $\text{UF}_6$  (a solid at room temperature and pressure) is heated into vapour form using an autoclave.
- $\text{UF}_6$  vapour is mixed with steam and fed into a rotary kiln.
- Hydrogen gas is added to the mixture and the  $\text{UF}_6$  is reduced to solid  $\text{UO}_2$ . The gaseous HF is recovered, leaving pure  $\text{UO}_2$  crystals.

The  $\text{UO}_2$  from this stage is then blended to homogenise the particle sizes and achieve a desired particle surface area. At this stage, additives may be introduced to the  $\text{UO}_2$  (e.g. burnable poisons, lubricants, dopants to improve densification or to control microstructure). This powder is then fed into a pellet pressing die where it is pressed into a cylindrical shape, called a ‘green’ pellet. Green pellets are then sintered in a furnace at temperatures of up to 2000 K in order to consolidate and increase the density of the pellets [16]. These fired pellets are then machined to the appropriate dimensions, including chamfers and dishes, before final inspection and loading into a cladding tube.

In the early stages of a fuel pin’s life, there is a small gap between the fuel pellet and the cladding, known as the pellet-cladding gas gap. This gas gap slowly closes with increasing fuel

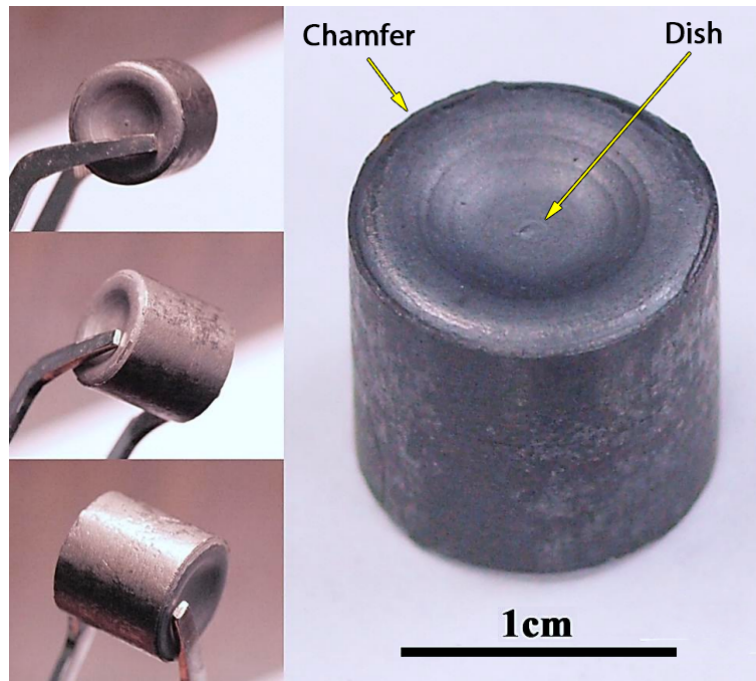


Figure 1.5: UO<sub>2</sub> LWR fuel pellet showing dishes and chamfers. Adapted from [17].

burn-up due to swelling of the fuel pellets and inward creep deformation of the cladding due to the coolant pressure. The pellet-cladding system is shown using a schematic view of the cross section of a PWR fuel pin in Figure 1.6. The cladding internal oxide layer covers the entire internal surface of the cladding and is the first barrier to corrosive species.

#### 1.1.4 Effects of radiation on materials

While ionising radiation is always present in the environment as background radiation, the intensity of radiation in a nuclear reactor is so great that it causes significant engineering challenges because of how it affects change in reactor materials.

Radiation hardening (also known as radiation embrittlement) is a phenomenon which affects most materials subjected to ionising radiation. It is characterised by a loss of plasticity caused by radiation damage over time, leading to an increased risk of cracks and failure of components.

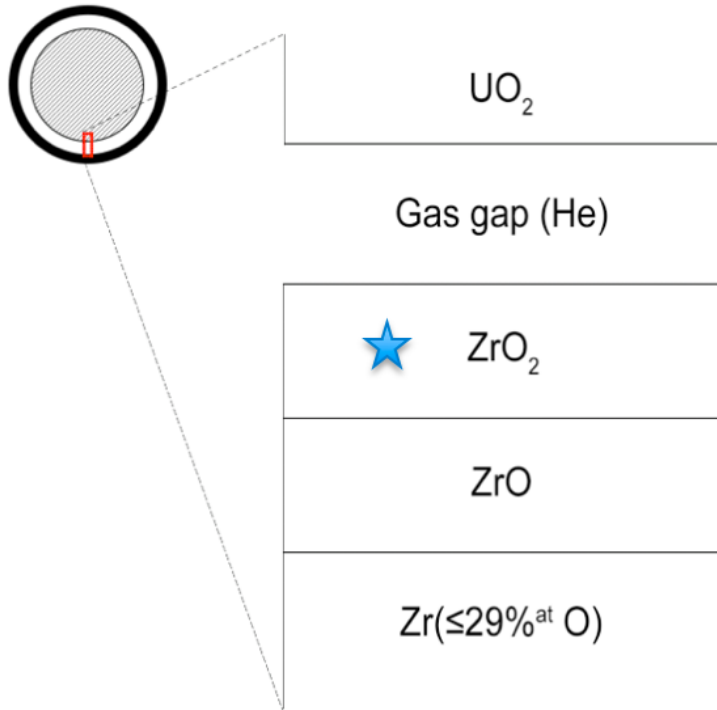


Figure 1.6: Schematic cross-section of a single PWR fuel pin with an expanded view of the pellet-gap-cladding system.

While zirconium is a very useful nuclear material due to its neutron transparency, it is still susceptible to radiation damage [18]. Beyond certain levels of radiation damage, phase changes may also occur.

Amorphisation is another effect of radiation damage, which has been observed in the  $(\text{Zr}, \text{U})\text{O}_2$  bonding layer in fuel pins [19]. This is characterised by an overall loss of long-range order of atoms in a crystal. This typically occurs beyond a certain threshold of radiation damage depending on the material, called the critical amorphisation dose. Amorphisation causes a loss in long range crystallographic structure and a corresponding reduction in structural stability (amorphous materials have a higher Gibbs free energy than their crystalline counterparts), and causes swelling of the material [20]. In the literature, there is evidence of amorphisation in cubic stabilised  $\text{ZrO}_2$  when bombarded with 400 keV  $\text{Cs}^+$  ions up to a fluence of  $1 \times 10^{21}$  ions  $\text{m}^{-2}$  [21]. However, no amorphisation is seen with a 340 keV  $\text{Xe}^{2+}$  fluence of  $2 \times 10^{21}$  ions  $\text{m}^{-2}$ ,

or a 72 MeV I<sup>+</sup> fluence of  $5 \times 10^{19}$  ions m<sup>-2</sup> [22]. Higher energy ions are expected to cause more damage (displacements per atom) in the lattice due to the larger amount of energy being deposited.

One material phenomenon exclusive to nuclear reactor environments is neutron activation. The high free neutron environment leads to neutron capture in various nuclei within the reactor, including those of the fuel assemblies, coolant and RPV. There are many possible (n, x) reactions that may occur in materials experiencing a neutron flux, but of particular concern is transmutation of nuclei following a nuclear capture event. When a stable nucleus captures a neutron and becomes unstable, the nucleus may then emit particles to reduce its free energy, altering its atomic number in the process. This new element will have different chemical properties compared to the parent nucleus by virtue of a different electronic structure. This will change the elemental composition of a material, typically in an unfavourable way with dopants that negatively affect some desired material property. The extremely large number of nuclei relative to neutron flux means that this effect is small, though over time this becomes more significant due to the accumulation of these dopant elements.

In high-radiation environments, it is also possible for some molecules to be split by gamma photons above certain energies through the process of radiolysis. Corrosive fission products such as iodine will be present inside the fuel pin, but may exist in the form of (for example) CsI, which is not highly corrosive. Radiolysis however, decomposes CsI into Cs and I<sub>2</sub> vapour which can diffuse towards the cladding and promote cracking [23].

### 1.1.5 Fission products, their distribution and decay chains

Nuclei which can undergo fission will produce daughter nuclei (fission products) with specific characteristics. At first, these nuclei will almost always be neutron-rich, as compared to their stable isotopes. This is the result of the higher neutron to proton ( $N/Z$ ) ratios of larger nuclei. Figure 1.7 shows how the nuclei of abundant isotopes start with  $N/Z$  ratios of around 1 for small elements (e.g.  $\text{He}_2^4$ ,  $\text{C}_6^{12}$ ,  $\text{O}_8^{16}$ ), whereas larger elements will have isotopes with  $N/Z$  ratios approaching 1.6 (e.g.  $\text{Pb}_{82}^{208}$ ,  $\text{Th}_{90}^{232}$ ,  $\text{U}_{92}^{238}$ ).

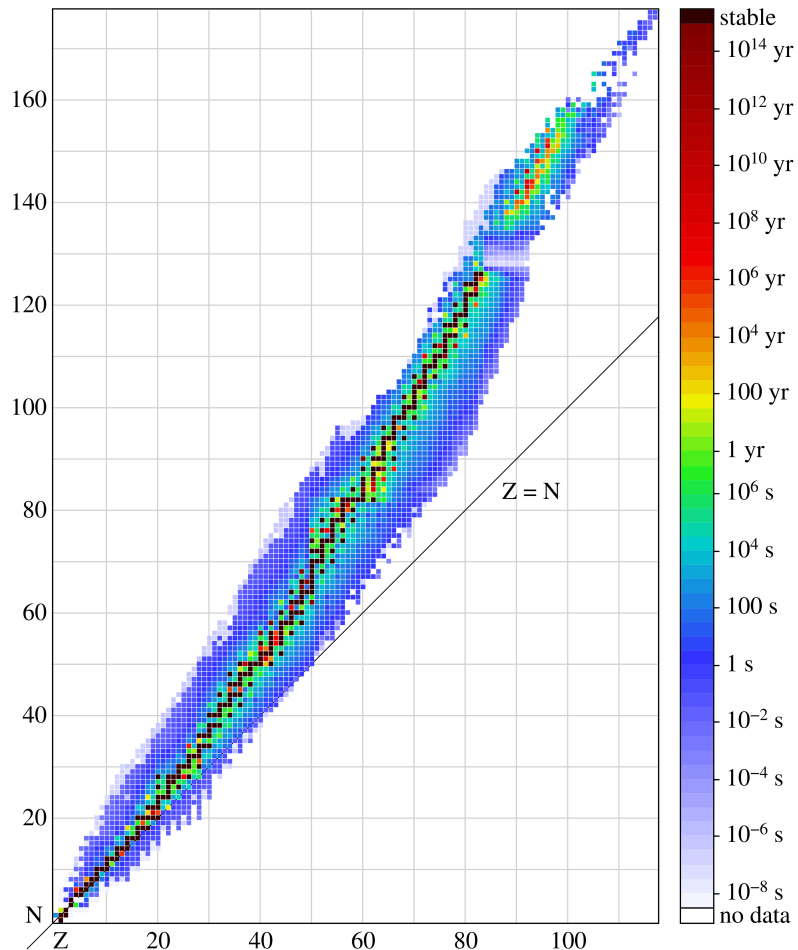


Figure 1.7: Plot of neutron number against proton number for nuclei with half-lives greater than  $10^{-8}$  s. Taken from [24].

Fissionable nuclei are typically very large and when fission occurs, the daughter nuclei will

inherit a high N/Z ratio. These neutron-rich nuclei will generally decay by  $\beta-$  particle emission to reduce their N/Z ratio and increase stability. One decay event is usually not enough to achieve a stable nucleus, so several decays as part of a decay chain are expected. An example is given for Te in Equations 1.3 and 1.4.



Another characteristic feature of fission products is that their masses are bi-modally distributed. Figure 1.8 shows calculated fission yields as a function of mass number, indicating a 40:60 rather than 50:50 mass distribution among daughter nuclei when heavy nuclei are fissioned. This is attributed to smaller nuclei (which have high binding energies per nucleon) separating from the nucleus first at the moment when fission occurs. This results in the majority of fission products centring around atomic masses of 95 and 135, producing a disproportionate number of nuclei such as Sr, Y and Zr on the low side and Te, I and Cs on the high side of the distribution. The distribution of fission products varies slightly depending on which nucleus is fissioned (e.g.  $\text{U}^{233}$ ,  $\text{U}^{235}$ ,  $\text{Pu}^{239}$ ) and the energy of the fissioning neutron. Over time, transmutation of  $\text{U}^{238}$  to  $\text{Pu}^{239}$  and consumption of  $\text{U}^{235}$  means that an increasing proportion of energy output will be due to fission of  $\text{Pu}^{239}$ , but fuel assemblies are typically retired before significant build-up of  $\text{Pu}^{239}$  inventory and so the net yields of fission products will only change slightly over the life of the fuel.

Iodine is an important fission product because it is known to corrode Zr metal. It is part of the  $\text{Te} \rightarrow \text{Cs}$  decay chain, with most isotopes exhibiting half-lives ranging from a few seconds

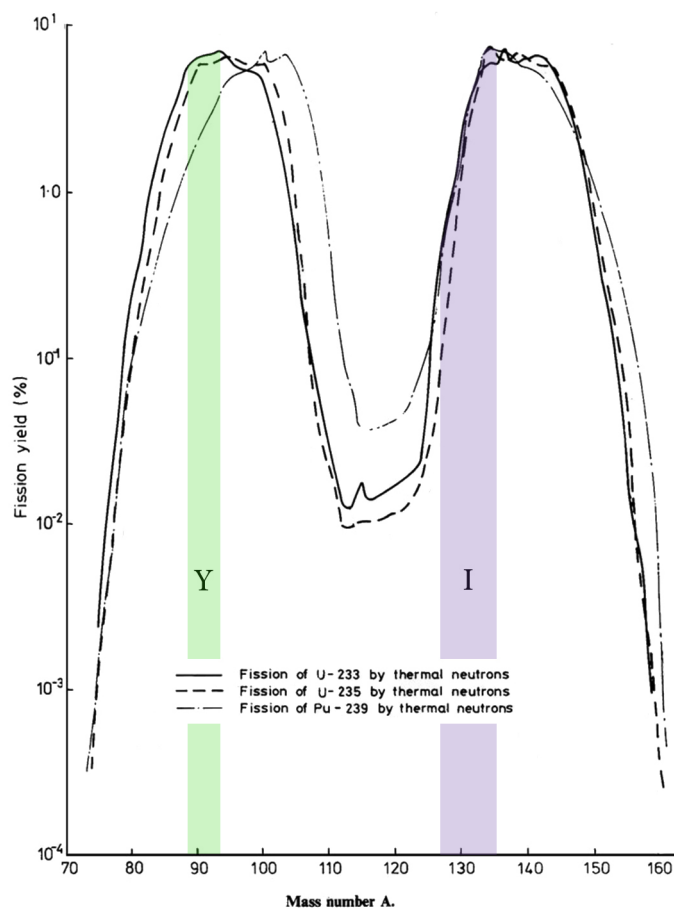


Figure 1.8: Plot of the percentage yield of nuclei with a given mass following a fission event. Range of masses corresponding to isotopes of iodine shown in purple and isotopes of yttrium shown in green, based on Equation 1.2. Adapted from [25].

to several days. Select data on Te and I fission yields are presented in Table 1.2. In total, the independent yield<sup>1</sup> of I isotopes from  $\text{U}^{235}$  fission is 10.4%, while the independent yield of Te isotopes (I precursors) is 17.6%, with  $\text{Te}_{52}^{134}$  having the highest independent yield of all possible fission products (6.3%). These particular elements will also usually be paired with Zr and Y fission products, the latter of which is a common phase stabiliser dopant in  $\text{ZrO}_2$ .

<sup>1</sup>Independent fission yield is defined as the number of specific nuclei produced directly per 100 fission events.

Table 1.2: Independent fission product yields and half-lives for the major iodine isotopes and precursors in a thermal neutron reactor. Yields taken from the Joint Evaluated Fission and Fusion File (JEFF 3.3). All isotopes undergo single  $\beta$ - decay. Metastable states are included.

Isotope	Independent Yield (%)	Half-life
Te <sup>131</sup>	0.126	25.0 m [26]
I <sup>131</sup>	0.00296	8.02 d [27]
Te <sup>132</sup>	1.50	3.18 d [28]
I <sup>132</sup>	0.0284	2.30 h [28]
Te <sup>133</sup>	3.94	12.5 m [29]
I <sup>133</sup>	0.198	20.9 h [30]
Te <sup>134</sup>	6.30	41.8 m [31]
I <sup>134</sup>	0.767	52.5 m [31]
Te <sup>135</sup>	3.48	19.0 s [32]
I <sup>135</sup>	2.46	6.58 h [32]
Te <sup>136</sup>	1.67	17.6 s [33]
I <sup>136</sup>	3.04	83.4 s [33]
Te <sup>137</sup>	0.484	2.49 s [34]
I <sup>137</sup>	2.70	24.5 s [34]
Te <sup>138</sup>	0.113	1.40 s [35]
I <sup>138</sup>	1.24	6.26 s [35]

### 1.1.6 Formation of plutonium and minor actinides

Uranium fuel in LWRs is enriched to contain up to 5% U<sup>235</sup>, which is a fissile isotope. The rest of the uranium is comprised of the more abundant U<sup>238</sup> which is a *fertile* isotope. Fertile isotopes are not<sup>1</sup> fissioned directly, but can be converted into fissile isotopes through nuclear reactions.

---

<sup>1</sup>U<sup>238</sup> has a thermal neutron fission cross section which is 7 orders of magnitude smaller than that of U<sup>235</sup>, so thermal fission of U<sup>238</sup> is insignificant.

In the case of U<sup>238</sup>, the fissile isotope Pu<sup>239</sup> is produced through the following reactions:



UO<sub>2</sub> fuel pellets do not contain any plutonium before irradiation, however, production of Pu<sup>239</sup> and heavier isotopes during reactor operation is so significant that they can account for over 50% of the fissile isotope inventory in a LWR [36]. A fraction of the Pu<sup>239</sup> nuclei will capture additional neutrons, producing heavier isotopes of plutonium which may be fissile (e.g. Pu<sup>241</sup>).

The production of fissile nuclei from fertile nuclei is known as *breeding*.

Plutonium nuclei which are not burned through fission can either be extracted from spent fuel by reprocessing, or will undergo nuclear decay (specifically  $\alpha$  or  $\beta$ - decay) and produce elements such as neptunium, americium and curium which are known as *minor actinides*<sup>1</sup>.

These minor actinides are produced from neutron irradiation of uranium (both U<sup>238</sup> and U<sup>235</sup>) and nuclear decay. The radiotoxicity of spent nuclear fuel is dominated by plutonium and the minor actinides, with global production rates of isotopes like Np<sup>237</sup>, Am<sup>241</sup> and Cm<sup>244</sup> measured in several metric tons per year [37].

In a nuclear fuel pin, the cladding serves as a physical barrier preventing the release of fission products and actinide wastes. The first barrier is the UO<sub>2</sub> matrix itself, however, volatile species can migrate to the pellet-cladding gap. This gap gradually closes during operation and the fuel pellet makes contact with the cladding, leading to mechanical and chemical interactions. This

---

<sup>1</sup>In the nuclear power industry, uranium and plutonium are known as the major actinides.

is discussed in detail in Chapter 2.

# Chapter 2

## Literature Review

### 2.1 PCI

When a fuel pin is first in-pile, there is a gap between the fuel pellet and the cladding (see § 1.1.3). This gap slowly closes over time due to creep-down of the cladding due to coolant pressure, as well as thermal expansion and swelling of the fuel pellet (illustrated in Figure 2.1) due to radiation damage and the accumulation of fission products. At a high enough burnup, the fuel pellet makes contact with the cladding. This phenomenon is PCI and involves both mechanical and chemical interactions which contribute to observed fuel failures [38].

PCI-related failure of nuclear fuel pins has been known since 1963, when the first reported failure occurred in a highly rated fuel pin during reactor start-up [40]. Many studies have since been made regarding the topic [38, 39]. The exact cause of PCI failures has not yet been determined, however it is likely that both the mechanical and chemical effects of contact between the fuel pellet and the cladding are necessary for it to occur. It is also known that

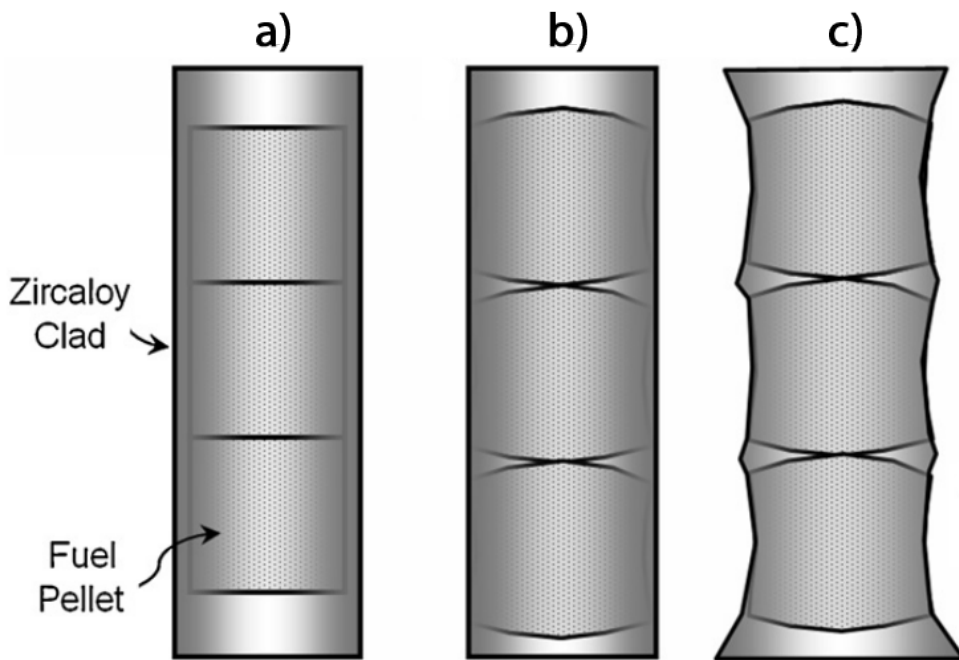


Figure 2.1: Illustration of fuel swelling and clad deformation due to PCI. **a)** Fresh fuel before irradiation. **b)** Thermal expansion and swelling of fuel pellets and closing of fuel-pellet gap during operation. **c)** Fuel contact with cladding and subsequent ‘bambooing’ of the cladding. Adapted from [39].

PCI failures are typically preceded by power transients, such as during reactor startup where several power ramps are performed over many hours [38].

### 2.1.1 Fuel pellet relocation

Irradiated fuel pellets will sometimes crack and break into fragments whilst in the cladding. These fragments are unconstrained and are able to move radially outwards (i.e. towards the pellet-cladding gap). This phenomenon is called ‘relocation’, although this term is also used to refer to movement of the pellet fragments in the axial direction within the cladding [41]. Relocation of fuel fragments means that firm contact between the fuel and cladding can occur earlier in the fuel pin’s life (i.e. before fuel swelling closes the fuel-cladding gap).

The conceptual model of fuel pellet relocation is shown in Figure 2.2 as a plot of the ‘effec-

tive' gap (based on cladding temperature and fuel centreline temperature) against rod power.

Initially, the fuel pellet has no fragmentation and a wide fuel-cladding gap (region I). The gap decreases slowly due to thermal expansion as rod power is increased until point A where the fuel pellet cracks and fragments. The fuel pellet fragments move radially outward and the gap decreases significantly (region II). Point B marks the onset of 'soft' PCI, meaning that the fuel pellet fragments make some contact with the cladding, but are not yet fully constrained (e.g. radial or azimuthal motion is still possible). The fragments' lack of mechanical constraints prevent a stress from being imparted to the cladding, thus the mechanical interaction is considered 'soft' (region III). At point C, thermal expansion due to rod power is large enough that some pellet fragments become mechanically constrained, marking the onset of 'hard' PCI (region IV). As discussed in § 1.1.3, chipping of fuel pellets can cause debris to occupy the pellet-cladding gap, thereby reducing the rod power at which onset of hard PCI occurs.

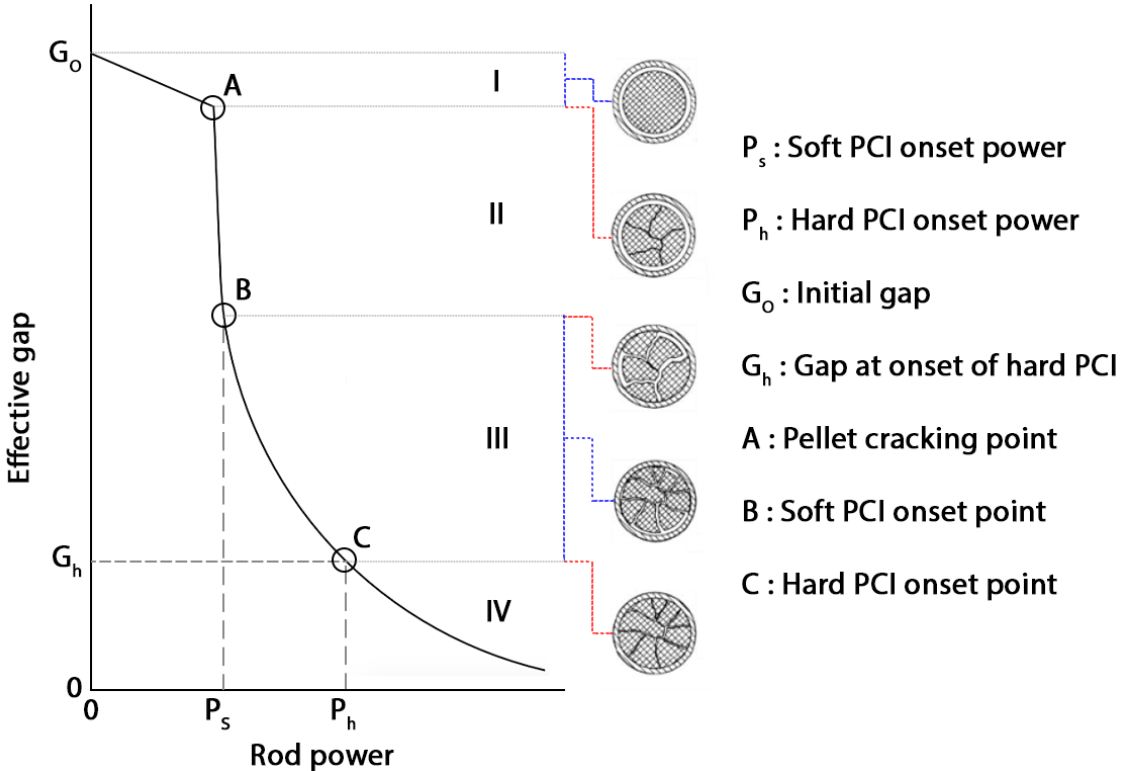


Figure 2.2: Concept of pellet-cladding gap model showing stages of fuel pellet fragment relocation with onset of soft and hard PCI. Adapted from [42] with fuel pin cross-sections from [43].

### 2.1.2 Pellet-clad gap and bonding

The gap between the fuel and the cladding allows fuel pellets to be inserted into the fuel pin easily during manufacture, but this clearance is also designed to accommodate some increase in fuel pellet volume. It is important to consider the thermal expansion of the fuel pellet, as the centreline temperature of a PWR fuel pellet during a power transient can vary between 1500 and 1800 °C, depending on the burnup of the fuel, magnitude of the reactivity insertion and location within the core [44]. In addition, fuel pellets will swell due to radiation damage throughout their operational lifetime. Once the pellet-clad gap has closed entirely, any pellet expansion during a power transient will translate to a force exerted on the cladding, generating hoop stresses which open cracks on the inner cladding surface. This is the mechanical component of PCI.

In LWRs, the pellet-cladding gap closes completely at high burnups of approximately 50 GWd/tU [19, 45, 46]. When the surface of the fuel pellet makes contact with the cladding, there is also a chemical interaction between the UO<sub>2</sub> (and fission products) and the internal surface oxide of the cladding. UO<sub>2</sub> has some solid solubility in ZrO<sub>2</sub>, and a bonded reaction layer, which has a chemical composition (U, Zr)O<sub>2</sub> is observed. Due to the large U atom, cation substitution allows some of this mixed layer to adopt the crystal structure of cubic fluorite, the high temperature phase of ZrO<sub>2</sub>. The uranium nuclei in both this bonding layer and the outer rim of the fuel pellet experience the highest number of fission events (due to proximity to the moderator), and therefore this region contains fission products that contribute to the chemical degradation of the fuel cladding, in particular iodine. This is the chemical component of PCI.

### 2.1.3 Reactor power ramps

It has been established that power ramping of a reactor is associated with PCI failures [47–50].

This presents a problem for reactors when it comes to events such as start-up, load-following and any other power transients experienced by the fuel pins. Figure 2.3 shows how reactor power varies over time during a typical PWR start-up procedure. A combination of low ramping rates and long holds at low power (to remain below ramping limits, to condition<sup>1</sup> fuel [51], and conduct coolant chemistry checks) require the entire procedure to be completed in a period of 90 hours, with several operator switch-overs in between. This is a costly procedure for the utility owner to perform, with millions of US\$ foregone in electricity sales for larger reactors.

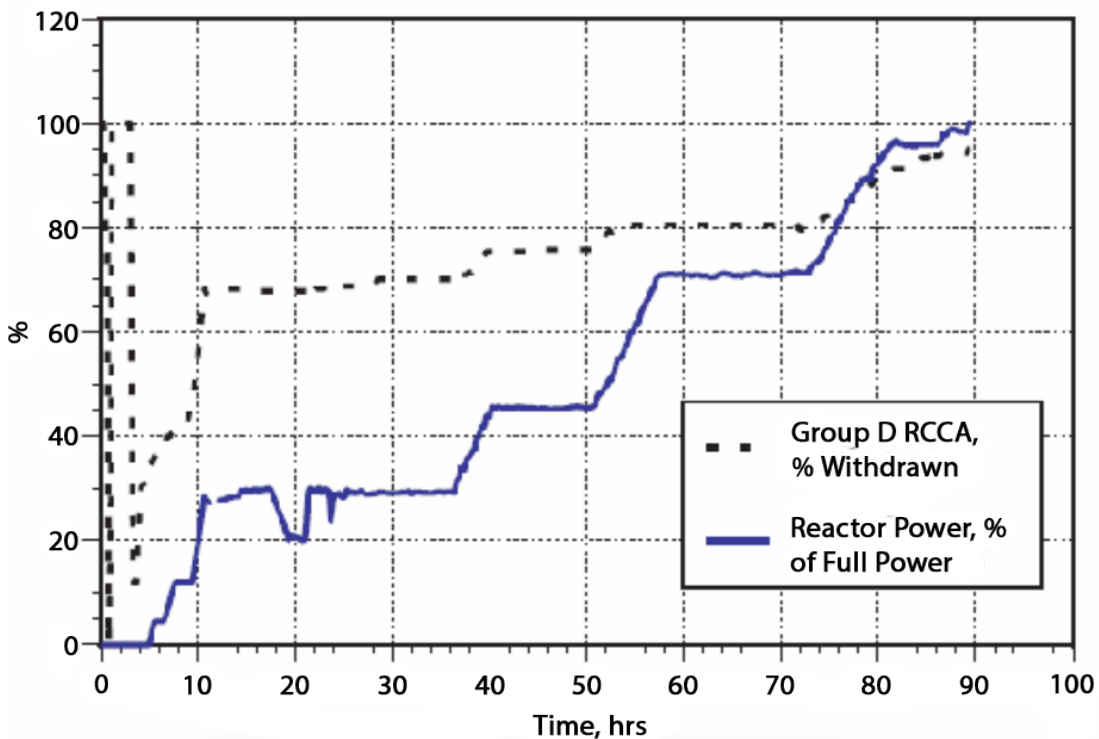


Figure 2.3: Reactor startup procedure for a typical US PWR. Dashed line indicates % withdrawal of control rods. Adapted from [52].

Scheduled reactor shutdowns or extended reduced power operation (ERPO) events occur whenever refuelling or maintenance of the reactor is required (and in some cases there may be a grid

<sup>1</sup>Fuel is considered ‘conditioned’ after it has operated at a specified power level for a certain period of time.

demand to reduce power output). Refuelling is typically performed every 1 to 2 years, while unscheduled maintenance may be required at any time. Emergency shutdowns may also occur and have their own challenges to consider (e.g. xenon poisoning, decay heat removal), though they are rarer. In each case, it is necessary to go through the lengthy power ramping procedure, and since these shutdowns cannot be avoided, being able to ramp up power faster would be a significant improvement. Ramp rates in reactors are restricted to between 3-4% of full power per hour above a certain threshold level to avoid PCI failures [52]. Additionally, fuel conditioning holds (operation at certain power levels for long periods) are performed to further reduce the incidence of PCI failures.

The limits described above present a challenge not just when restarting reactors, but also for the implementation of load-following in reactors. PWRs have thermal feedback loops which provide some level of intrinsic load-following behaviour. For example, an increase in steam demand leads to increased boiling in the steam generators. The subsequent decrease in coolant temperature in the primary circuit leaving the steam generator causes a reactivity increase and therefore a power increase in the reactor. The reactor returns to critical (reactivity = 0) after some fluctuation, and the average temperature of the primary coolant remains unchanged.

#### 2.1.4 PCI Failures

PCI failures are typically associated with cracks which span the thickness of the cladding (so-called *pinhole* defects), and lead to fission product contamination of the primary loop coolant. A fuel cladding breach is detected when a sharp spike in radioactivity is registered by sensors in the primary loop (i.e. a signal that is distinguishable above the previous background). This

means that the time to detection of a failure from the failure-inducing event (e.g. a power ramp) is known, but the time taken for the PCI failure to occur is unknown [38].

Figure 2.4 shows the typical cracking behaviour of fuel pellets and stress-corrosion cracking (SCC) of the Zr cladding from a PWR fuel pin subjected to two annual operating cycles. Fragmentation of the fuel pellet can be seen and the absence of a pellet-cladding gap caused by swelling of the pellet. The axial cross-section in Figure 2.4b shows the gap at the chamfers almost completely closed (axial expansion of the pellet). The pellet dishes are also visible as dark horizontal discs. Note that these samples have been cooled down and so the swelling seen does not include the thermal expansion effect.

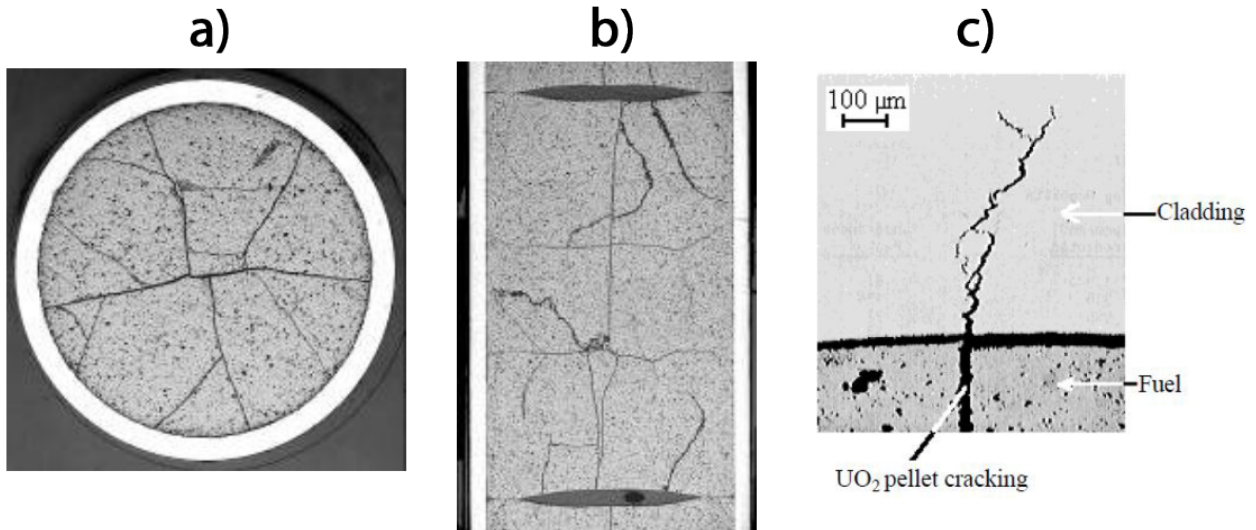


Figure 2.4: Cracking of PWR fuel pellets and cladding. **a)** Transversal macrography of a fuel rod irradiated for two annual PWR operating cycles. **b)** Axial macrography of a fuel rod irradiated for two annual PWR operating cycles. **c)** SCC cladding crack. Adapted from [53].

Figure 2.4c shows an SCC crack which has not progressed through the entire thickness of the cladding and exhibits intergranular morphology. The crack initiation site is also aligned with a radial crack in the fuel pellet. There is much evidence in post-irradiation examinations of fuel pins that I-SCC of the cladding will occur ahead of these radial pellet cracks and at the ends

of the pellet [54–60].

### Cladding Zr liners

Claddings in BWRs are more prone to PCI failures, and therefore differ from claddings in PWRs by including an additional layer of Zr metal up to 0.1 mm thick, called a *liner*, bonded to the inner surface of the cladding [61, 62]. The liner material is softer than the the Zr alloy used in the rest of the cladding for the purpose of suppressing cracks. The introduction of a liner in BWR fuel pins has been successful in reducing the incidence of PCI failures [63, 64], and this has prompted interest in introducing liners to PWR claddings [65]. Zr liners are still susceptible to SCC however, and their function is to alleviate the mechanical component of PCI rather than the chemical component. Figure 2.5a shows incipient cracks in a Zr liner after a ramp test in a BWR. The cracks are up to  $10 \mu\text{m}$  in length, spanning the thickness of the oxide layer and stopping near the metal/oxide interface. Crack arrest in this case was attributed solely to the softness of metal, although this same study showed that the hardness of the metal measured in this region was almost double that of the rest of the liner (due to radiation hardening). It should be noted that the metal near the metal/oxide interface will contain up to 29 at.% oxygen and this has implications for the corrosion process (see § 2.2.2).

Figure 2.5b shows an incipient crack in a BWR cladding liner which has been oxidised in a long (422 hour) irradiation test. This shows that repassivation of the cladding can occur during operation, preventing further attack at a crack site by iodine and other fission products. Additionally, a bonding layer between the pellet and cladding liner several microns thick is observed. In this case, the crack in the liner does not follow a crack in the fuel pellet as

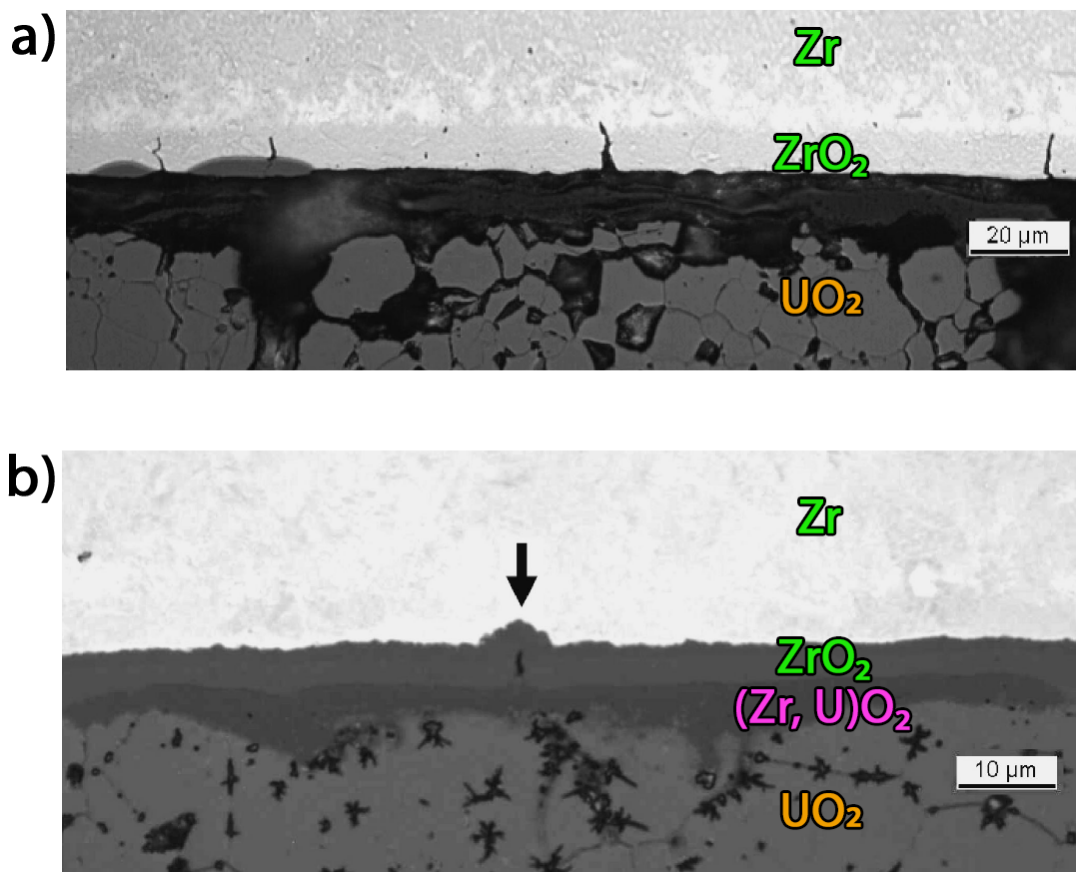


Figure 2.5: Optical micrographs of incipient cracks in BWR cladding liners at a burnup of 30 MWd/kg U following **a)** a ramp test with a peak LHR of 57 kW/m and **b)** subsequent irradiation for 422 hours with a peak LHR of 47 kW/m. Black arrow indicates oxidised crack. Adapted from [61].

expected (see Figure 2.4), but this particular sample did not fail so it is not clear if this type of crack would eventually lead to a PCI failure.

### Failure thresholds

The propensity for a fuel pin to fail due to PCI is a function of both burnup and ramp rate.

Many ramp rate studies have therefore been conducted to establish failure thresholds [66–76].

Figure 2.6 shows one such ramp test on BWR fuel at a burnup of approximately 30 MWd/kg U. The ramps, measured as the change in the linear power rating (also known as linear heat rating or simply linear rating) with units kW/m, lead to cladding failures after a certain duration

when above a threshold level. In the case of the BWR fuel in Figure 2.6, this threshold linear rating is around 41 kW/m. As linear rating increases from this level, the time to failure falls significantly, leading to failure within several minutes. A time delay between cladding failure and subsequent detection of fission products in the coolant is also shown (in this case, up to ten times as long as the failure time). This time delay and its implications are discussed in more detail in Chapter 7. Of the fuel claddings which did not fail near the failure boundary, SCC damage was present on the internal surface.

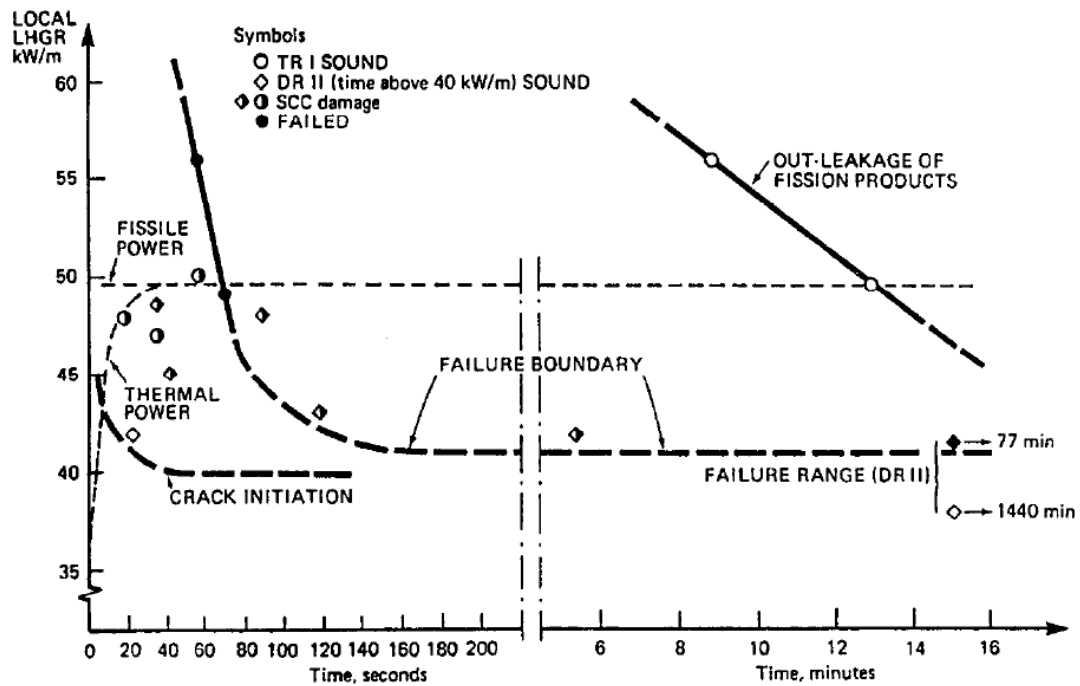


Figure 2.6: TRANS-RAMP I PCI failure progression for BWR fuel rods at a burnup of 30 MWd/kg U. Taken from [77]

SCC damage has also been observed to occur with a threshold effect based on fuel burnup [78]. Figure 2.7 shows the results of I-SCC tests on irradiated Zircaloy cladding C-rings. A failure threshold exists at a burnup of approximately 24 MWh/kg U (i.e. 1 MWd/kg U). All samples were loaded and held for 25 hours, and the failure fraction was plotted against burnup. Yield strengths of samples from the same irradiated claddings are also provided and clearly show a radiation hardening effect, increasing yield strength of the samples from 470 MPa at a burnup

of 1 MWd/kg U, to 730 MPa at approximately 20 MWd/kg U. This is accompanied by a large decrease in both ductility and ability to resist crack propagation. C-ring samples have failure rates approaching 100% at these higher burnups [38].

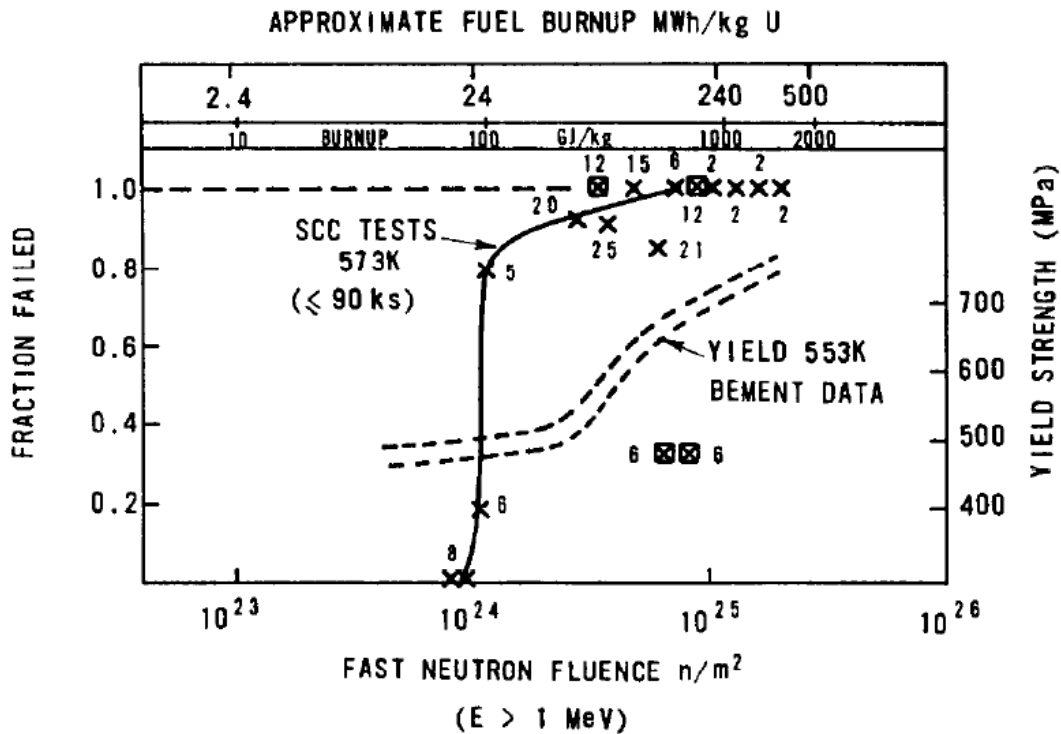


Figure 2.7: I-SCC susceptibility of stress relieved Zircaloy fuel cladding at 573 K as a function of burnup and cladding yield strengths at 553 K. Numbers next to data points indicate number of rings from the sample used in yield data. Figure from [38] with yield strength data from [79].

### 2.1.5 Fission products and SCC

Although PCI failures were found to occur during power ramping, it was not yet known whether these failures were due to fission product induced SCC or tensile failure of the cladding due to radiation embrittlement.

In 1971, a series of tests were carried out at Chalk River Nuclear Laboratories to determine if fission products were necessary for PCI failures to occur [48]. The experiments involved taking highly irradiated zirconium fuel pins (fluence of  $8 \times 10^{24} n/m^2$  with 1 MeV neutrons) and then

inserting fresh, unirradiated  $\text{UO}_2$  fuel pellets into them. These fuel pins were then inserted back into a reactor and subjected to large power ramps with peak linear power ratings of up to 77 kW/m, as shown in Figure 2.8. These ramps (phase I and II) would typically cause failures in fuel pins with similar irradiation histories (see Figures 2.6 and 2.7). In the initial ramp tests however, all the fuel pins survived the ramps intact. Six fuel pins were then irradiated in the reactor at low power to a burnup in excess of 50 MWh/kg U (i.e 2.1 MWd/kg U) in order to build up fission products in the fuel (phase III).

In a subsequent ramp test (phase IV), two of the high burnup fuel pins failed in the reactor. This finding provided the strongest evidence to date that fission products are necessary for PCI failure of zirconium-based claddings. The fission product most likely to cause cracking, based on known SCC susceptibility of Zr metal, is iodine.

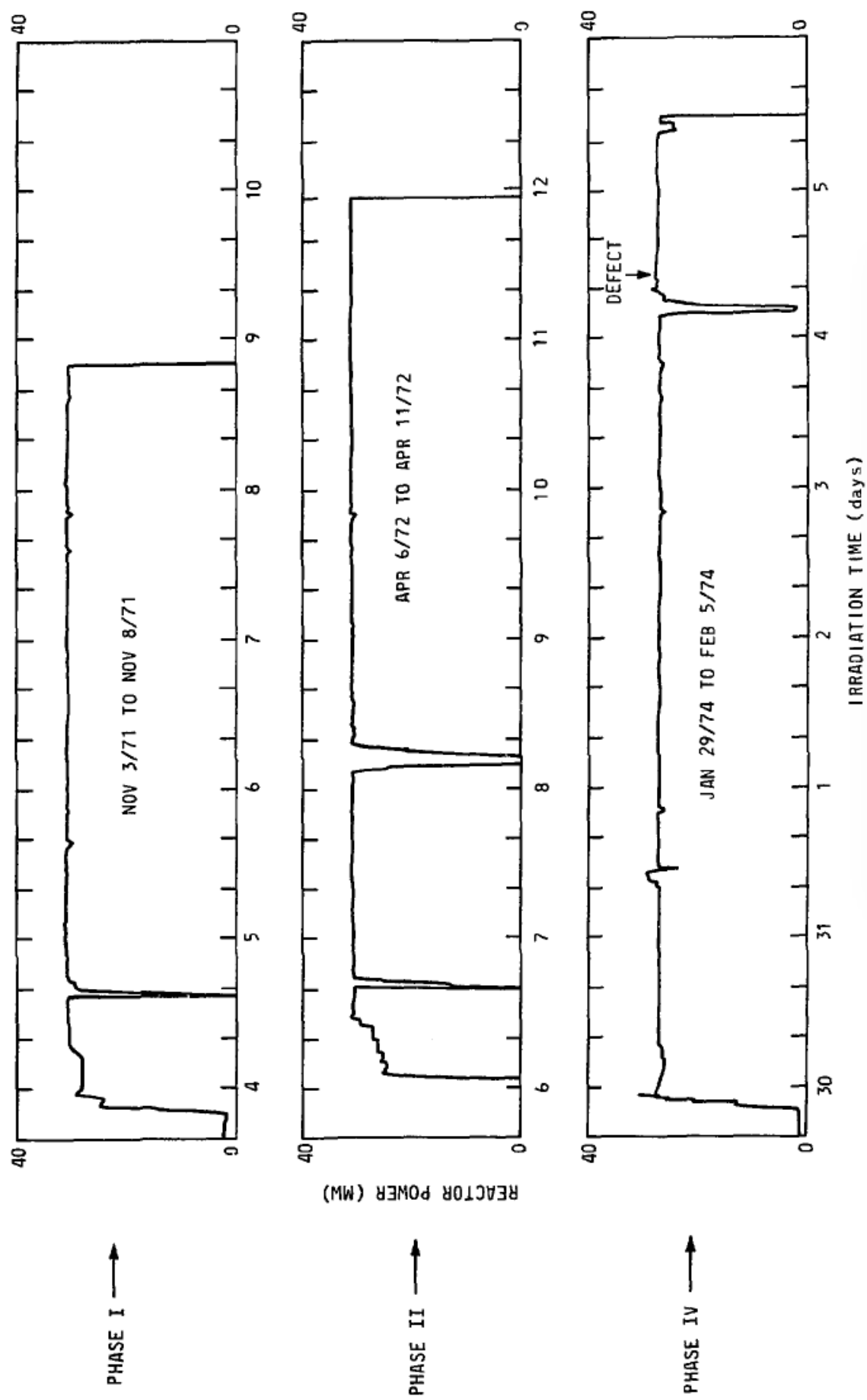


Figure 2.8: Power ramping test data for the different phases of the Chalk River Nuclear Lab experiment. Taken from [48].

As discussed earlier, iodine is one of the most prevalent fission products and it is known to corrode zirconium metal [80–85]. The exact mechanism by which this occurs in fuel pins is not yet known, though a combination of radiolysis,  $I_2$  diffusion and chemical attack (I-SCC) are considered to be most likely.

The most commonly proposed mechanism is illustrated in Figure 2.9. In the first step, iodine and caesium are produced through fission of the fuel and diffuse towards the outer surface of the fuel pellet (though not necessarily together [86]). A thin film of CsI is deposited on the outer surface of the fuel pellet and subsequently decomposes via radiolysis, liberating iodine in vapour form. The iodine vapour then diffuses towards a crack site in the cladding and reacts with Zr to produce  $ZrI_4$ . The  $ZrI_4$  then breaks away from the metal due to the high surface energies, causing pitting and progressing the crack tip further into the metal. This model however, fails to consider the effect of the oxide on the internal layer of the cladding (as a barrier layer to ingress of corrosive species), and it does not take into account the presence of oxygen in the pellet-cladding gap and in the metal matrix (in solution) near the metal-oxide interface. Both these factors are important as the oxide provides a protective effect (otherwise I-SCC failures would be far more prevalent, regardless of ramp rate limitations and conditioning holds) and where the oxide has been ruptured, repassivation and competition between iodine and oxygen will occur. The effect of this internal oxide layer is one of the gaps in knowledge that is addressed in this thesis.

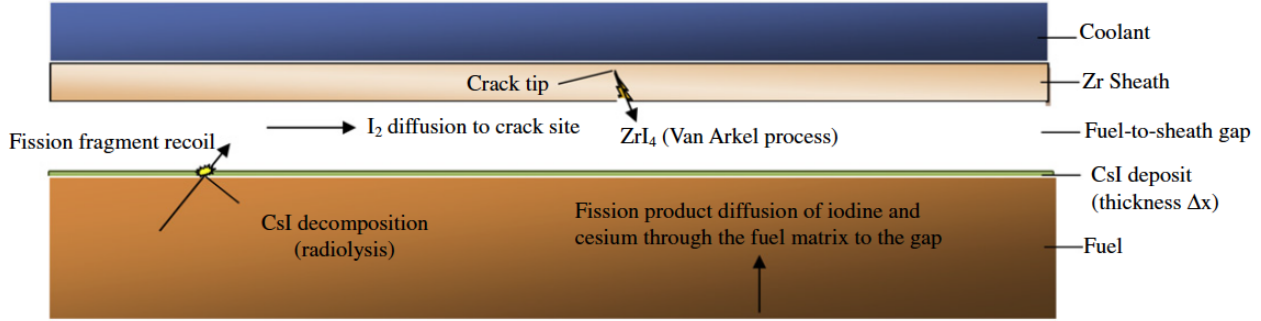


Figure 2.9: Schematic of a proposed I-SCC process for cladding crack penetration. Taken from [84].

### 2.1.6 Iodine availability

The amount of iodine available in the fuel pin is dependent on many different factors (e.g. temperature, pressure, power history, axial location in fuel pin, diffusion rate through fuel), making it difficult to measure. Additionally, iodine nuclei (and fission products in general) will implant in either the fuel pellet or the cladding due to their large kinetic energies following a fission event. To get an idea of the quantity of iodine in a reactor, a calculation was performed to obtain a lower-bound for the mass of radioactive iodine present in a 1000 MWe reactor core at steady-state operation (see Appendix D), yielding a value of 203.84 grams. The distribution of iodine, however, is not known. It is necessary to consider things such as decay of precursors, radiolysis and fission product implantation, described in more detail below.

#### Iodine precursors

Lewis *et al.* [87] showed that the iodine inventory will increase sharply during both startup and shutdown, and attributed the iodine spike during shutdown solely to cracking of the fuel pellet (and subsequent release of trapped iodine). However, this ignores the contribution of iodine

precursors (tellurium isotopes) to the iodine inventory. For example,  $I^{131}$  concentration is shown to increase following shutdown. Production of  $I^{131}$  is dominated by  $\beta$ - decay of  $Te^{131}$  (half-life 25 minutes, see Figure 1.2). Immediately following shutdown from steady state operation, the rate of  $I^{131}$  production from  $Te^{131}$  decay remains the same (because there is still  $Te^{131}$  in the fuel), but ‘burning’ of  $I^{131}$  by neutron capture falls to zero. The thermal neutron absorption cross-section of  $I^{131}$ , shown in Figure 2.10, is significant, being of comparable magnitude to the thermal fission cross-section of  $U^{235}$ . With the absorption reduced to zero,  $I^{131}$  can only be removed by nuclear decay. Decay of  $I^{131}$  (half-life 8.023 days) is much slower than  $Te^{131}$ , and therefore the quantity of  $I^{131}$  will spike immediately after shutdown. All isotopes of tellurium in the mass range 131 to 138 have high fission yields (often higher than iodine) and short half lives, contributing significantly to the iodine inventory in the fuel. This effect has largely been overlooked in the literature.

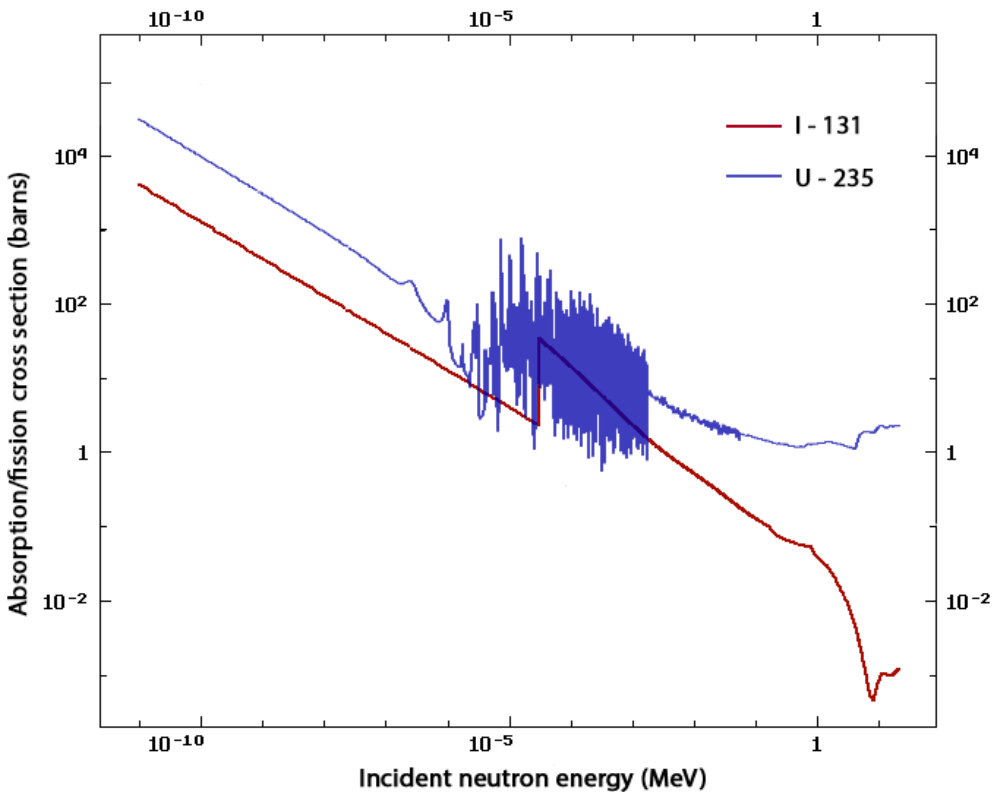


Figure 2.10: Neutron absorption and fission spectra of  $I^{131}$  and  $U^{235}$ , respectively.

## Radiolysis

Thermodynamic calculations performed by Konashi *et al.* [23] estimate the equilibrium partial pressure of iodine in the fuel-cladding gap to be as low as  $10^{-17}$  atm when there is no radiolysis of CsI, and up to  $10^{-8}$  atm with the effect of CsI radiolysis included. For comparison, mandrel tests of irradiated Zr claddings at 350 °C show that susceptibility to I-SCC is reduced when the iodine partial pressure is below 60 Pa (approximately  $6 \times 10^{-4}$  atm) [85]. While these calculated values of the iodine pressure are too low to induce corrosion in Zr, they demonstrate that radiation will increase the partial pressure of iodine by several orders of magnitude. Increasing reactor power (e.g. during a ramp) will increase radiation flux and therefore dissociation of CsI, however, no figures are yet available which demonstrate a clear link between this contribution to the iodine pressure and PCI failures.

## Implantation

Fission products immediately following a fission event have kinetic energies of up to 90 MeV. These are large, highly ionising particles which transfer their energy to the surrounding atoms within several microns of where they are produced, due to the large electronic and nuclear stopping power of crystalline solids such as UO<sub>2</sub> and ZrO<sub>2</sub>. Computer simulations are often used to predict the distribution of ions in a material subjected to some ion fluence. Figure 2.11a shows TRIM calculations of the amount of iodine that is implanted in ZrO<sub>2</sub> at different incident ion energy levels. Iodine at 6.5 MeV is predicted to penetrate ZrO<sub>2</sub> up to a thickness of 1.6 μm (the internal oxide thickness is typically between 5 and 10 μm). Less energetic ions will have distribution peaks nearer to the oxide surface. There is good agreement between

TRIM predictions and experimental data (Figure 2.11b) for the distribution of 50 keV iodine ions implanted in  $\text{ZrO}_2$ , with the distribution peak at 12 nm from the surface.

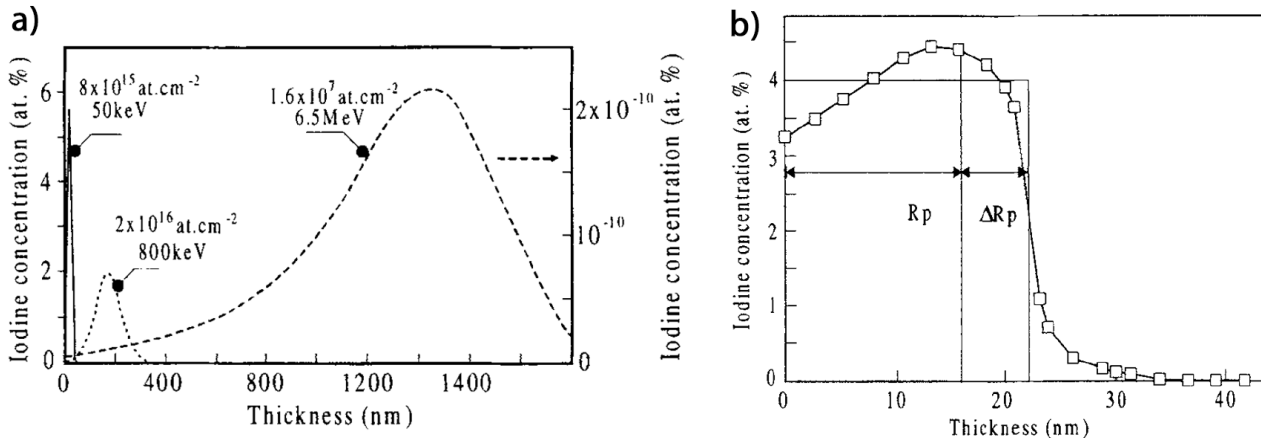


Figure 2.11: **a)** TRIM distributions for iodine implantation in  $\text{ZrO}_2$  at 50 keV, 800 keV and 6.5 MeV. **b)** Rutherford backscattering spectrometry profile of 50 keV iodine implanted in  $\text{ZrO}_2$  samples. Taken from [88].

Implantation of fission products has also been studied experimentally in yttria-stabilised zirconia (YSZ) due to interest in inert matrix fuels and wasteforms for actinide wastes. At dopant concentrations between 0.4 and 1 at.%, caesium was found to preferentially occupy cation sites (i.e. Cs substitutional defect formation), whereas iodine seemed to occupy random sites in the lattice [89]. It was not clear, however, if iodine was occupying interstitial sites or forming defect clusters (or even compounds with Zr). These studies provided limited insight for pure  $\text{ZrO}_2$  because stabilisation of the cubic phase with yttrium will significantly increase the concentration of oxygen vacancy defects, and these defects in addition to the presence of yttrium ions will influence the types of iodine and caesium defects which form in  $\text{ZrO}_2$ .

Further to the mechanisms described above, it is important to consider the role of oxygen in the I-SCC process. Fuel pins do not regularly fail during normal operation, despite iodine being produced continuously from fission of the fuel. As previously mentioned, this is because the

inner surface of the cladding is not pure Zr metal, but rather a protective oxide which provides an effective barrier against corrosive species such as iodine.

## 2.2 Oxidation of zirconium

The oxidation of zirconium to produce  $\text{ZrO}_2$  occurs during manufacture of the fuel cladding when the Zr metal is exposed to oxygen in air.  $\text{ZrO}_2$  is a ceramic with material properties that make it desirable in many industrial applications, including solid-oxide fuel cells [90], refractory linings [91], and nuclear waste storage [92]. However, in the context of nuclear fuel cladding, the most important function of  $\text{ZrO}_2$  is the barrier it provides against the ingress of corrosive species.

$\text{ZrO}_2$  grown thermally on Zr metal exists mainly in either the monoclinic or tetragonal phase [93, 94]. We can expect the internal  $\text{ZrO}_2$  layer of the cladding to be mostly monoclinic in early life, with the stress-stabilised tetragonal phase appearing near the oxide/metal interface due to cohesive strains resulting from the lattice mismatch. With increasing burnup, it is expected that more tetragonal and possibly even the cubic phase of  $\text{ZrO}_2$  forms due to anion vacancy formation and residual stresses in the lattice from radiation damage [22]. Amorphisation due to radiation damage has also been observed in the cubic phase from  $\text{Cs}^+$  implantation [21]. In this thesis however, while defect energies for the cubic phase are reported (see Figures 5.5, 5.6, 6.3), the focus is on monoclinic and tetragonal  $\text{ZrO}_2$  phases, partly due to difficulties predicting the behaviour of the pure high-temperature cubic phase using energies calculated from a static energy technique.

### 2.2.1 Oxide growth mechanism

An oxide layer will form on the surface of zirconium metal even at very low oxygen partial pressures [95]. The oxidation process is mainly driven by the ingress of oxygen ions. Initially, the oxide is highly protective, growing slowly into the metal until it reaches a thickness of approximately  $2\text{-}3 \mu\text{m}$  [96,97], after which the oxide growth mechanism enters a ‘post-transition’ stage where the oxidation kinetics follow a cubic-rate law [98]. At low temperatures relative to the melting point or high pressures, and after reaching a critical thickness (called the transition point), parts of the initial oxide will fail and the oxidation rate will increase again. This process is illustrated in Figure 2.12.

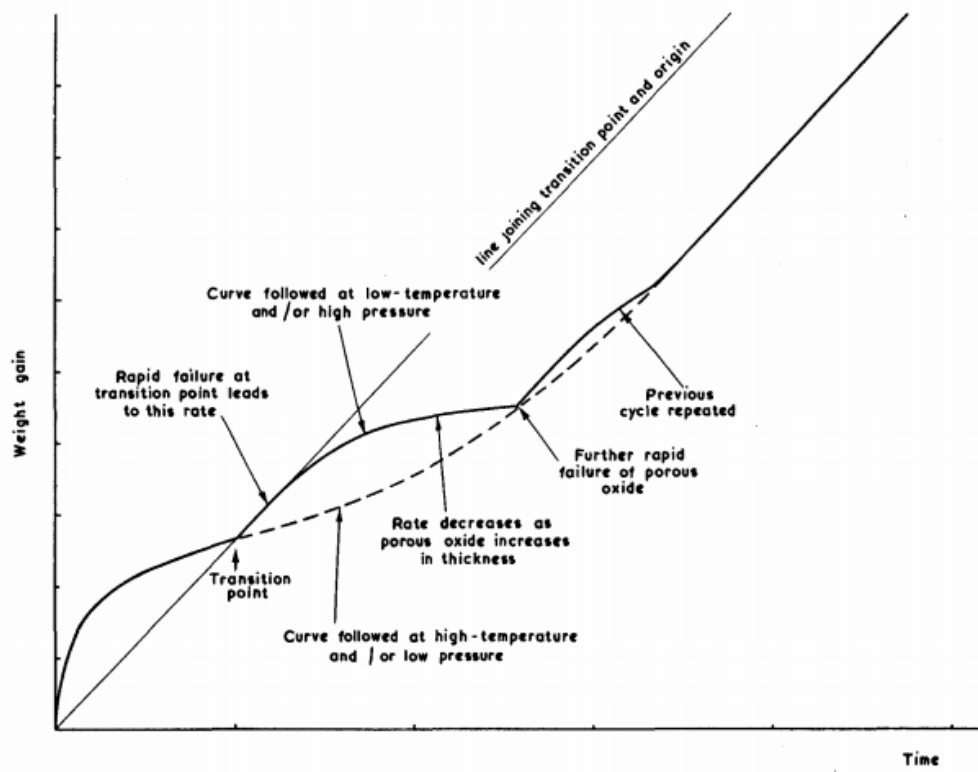


Figure 2.12: Diagrammatic representation of the cyclical oxidation behaviour of  $\text{ZrO}_2$ . Taken from [99].

### 2.2.2 Oxygen solubility of zirconium

Considering the Zr-O binary phase diagram in Figure 2.13, oxygen is soluble in zirconium up to 29 at.% when below 400 °C, commensurate with the operating temperature of a typical PWR (330 °C at the outer surface of the cladding). Solubility increases slightly up to 35 at.% as temperature is increased to the liquidus line at 2065 °C. This is important to note because, in the literature, studies often assume that there is pure Zr metal immediately beneath the  $\text{ZrO}_2$  layer [100]. This assumption leads to an underestimation of the extent to which repassivation occurs when the oxide layer is breached, and disregards the effect of the thin  $\text{ZrO}$  interface that can precede the metal. The amount of oxygen required to grow more oxide near the interface will therefore be at least 37% lower than expected when using this assumption.

The presence of oxygen in the Zr metal will also have an effect on thermodynamic calculations of extrinsic defect formation. Atoms such as Te and I will have to compete with O atoms (and potentially, self-interstitial Zr atoms) for interstitial sites in the metal. This decreases the diffusivity through the Zr matrix because of the lower availability of empty sites to facilitate diffusion. An energy input is required to remove O or Zr atoms occupying these sites, making diffusion paths involving these sites less preferable.

### 2.2.3 Outer oxide vs inner oxide

As mentioned previously, the cladding of an LWR fuel pin develops an oxide on both the inner and outer surfaces due to exposure to oxygen in air during manufacture. Both the outer and inner oxide layers provide protection against corrosion, though the corrosive environment is different.

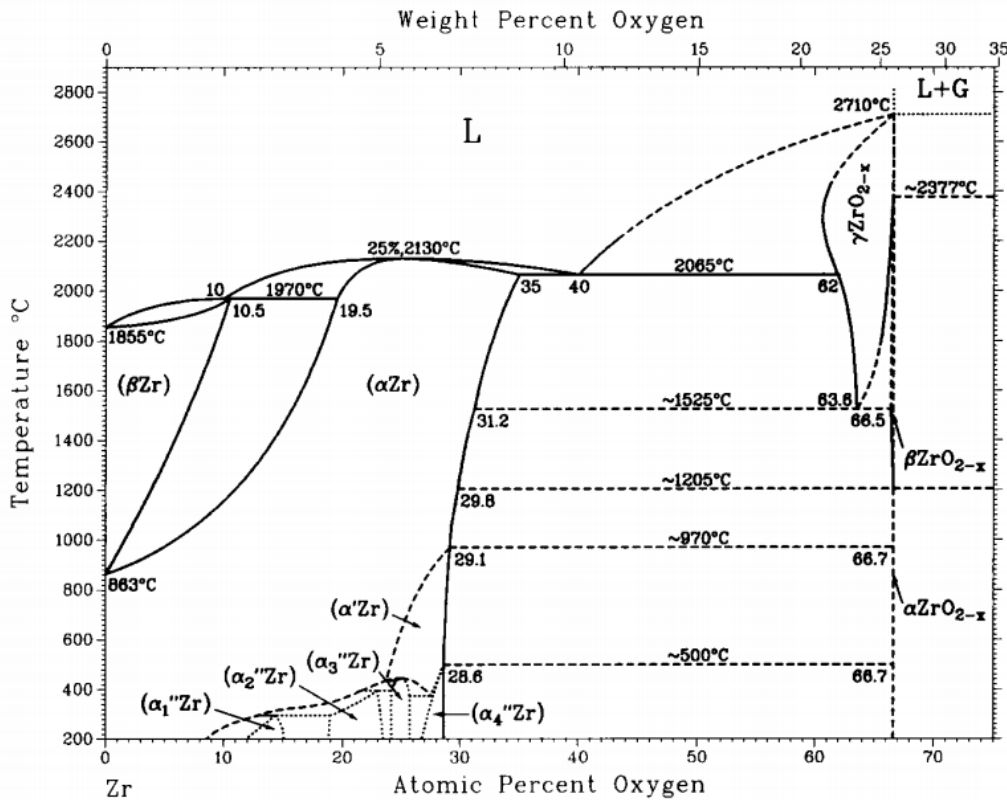


Figure 2.13: Phase diagram of the Zr-O binary system. Taken from [101].

The outer oxide layer is in contact with the coolant, which is mostly light water with some additional dissolved species such as boron and hydrogen to control reactivity and pH. Figure 2.14 shows a section of the cladding with the outer oxide visible. This layer is mostly monoclinic  $\text{ZrO}_2$  with small (nano) grains of tetragonal  $\text{ZrO}_2$  distributed randomly throughout. These grains of tetragonal  $\text{ZrO}_2$  are autostabilised during growth of the oxide because of the large volume expansion associated with oxidation (Zr has a Pilling-Bedworth ratio of 1.57). Of course, transmission electron microscope (TEM) foils under examination are always stress-relieved, whereas the oxide in reactor conditions will be under 1-2 GPa of residual stress due to the growth of the oxide (see § 3.1.2).

The internal oxide layer is much more challenging to examine due to the need to prepare samples in hot cells. This layer is typically very brittle due to radiation damage and implantation of

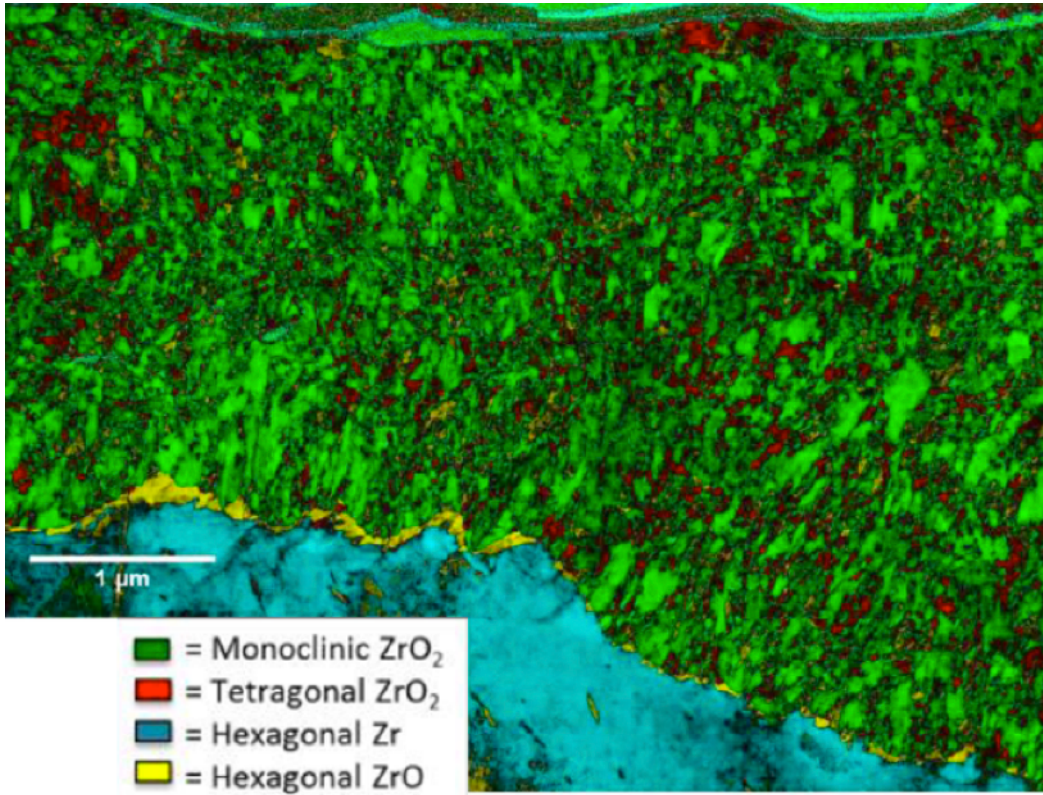


Figure 2.14: Scanning transmission electron microscope (STEM) image of the outer oxide layer formed in an autoclave under simulated PWR water conditions showing the prevalence of different  $\text{ZrO}_2$  phases. Taken from [102].

fission products. At a high enough burnup or LHR, the  $\text{ZrO}_2$  layer makes contact with the  $\text{UO}_2$  fuel, with which it will bond. Figure 2.15 shows a section of the cladding with the inner oxide layer bonded to the pellet. The crystal structure of the  $\text{ZrO}_2$  in this layer is debated. One study reported no monoclinic phase in high burnup fuel pins, with cubic phase  $\text{ZrO}_2$  throughout most of the layer and an amorphous phase nearer the pellet side [19], while other studies report mostly tetragonal phase in this layer [103, 104].

Figure 2.16 shows the composition of the inner oxide of a high burnup fuel pin. The fission product (Ba, Mo, Nd) content is highest at the beginning of the  $\text{ZrO}_2$  layer and decreases almost linearly with distance towards the Zr metal. This is due to fission product implantation rather than diffusion in the oxide as these elements have low volatility and low cation diffusion rates in  $\text{UO}_2$  where they are produced [106, 107], although diffusion rates can be increased due

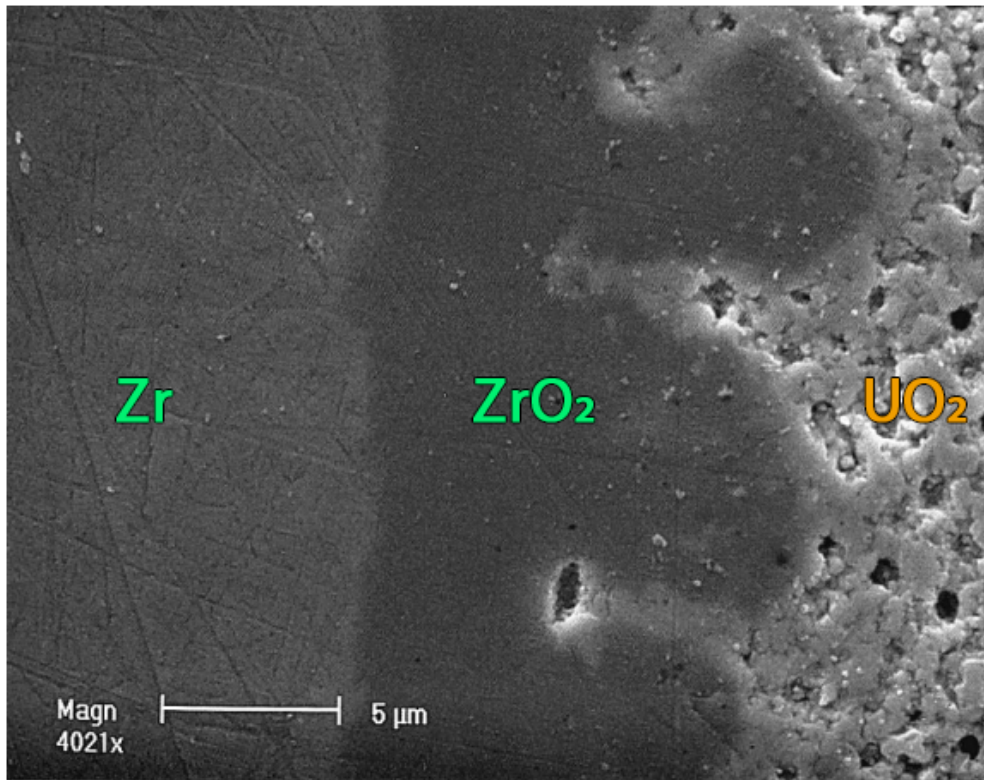


Figure 2.15: High resolution SEM image of the bonding layer between a PWR UO<sub>2</sub> fuel pellet and Zr cladding in a fuel pin at an approximate burnup of 60 GWd/tU. Adapted from [105].

to irradiation.

#### 2.2.4 Sources of oxygen

The internal oxide layer is present before fuel claddings are pressurised with helium gas and sealed. This is from the normal oxidation of Zr in air, where the oxygen pressure is 0.21 atm. After capping of the fuel rods, the only significant source of oxygen is from the UO<sub>2</sub> fuel pellets.

Uranium oxides have a wide range of non-stoichiometric compositions, with U/O ratios ranging from 1.67 to 2.24 in solid UO<sub>2±x</sub>, as shown in Figure 2.17. The oxide form U<sub>3</sub>O<sub>8-y</sub> also exists and is more kinetically and thermodynamically stable than UO<sub>2</sub>, but has lower density, making it less suitable for use as a fuel form. The different stoichiometries have different equilibrium

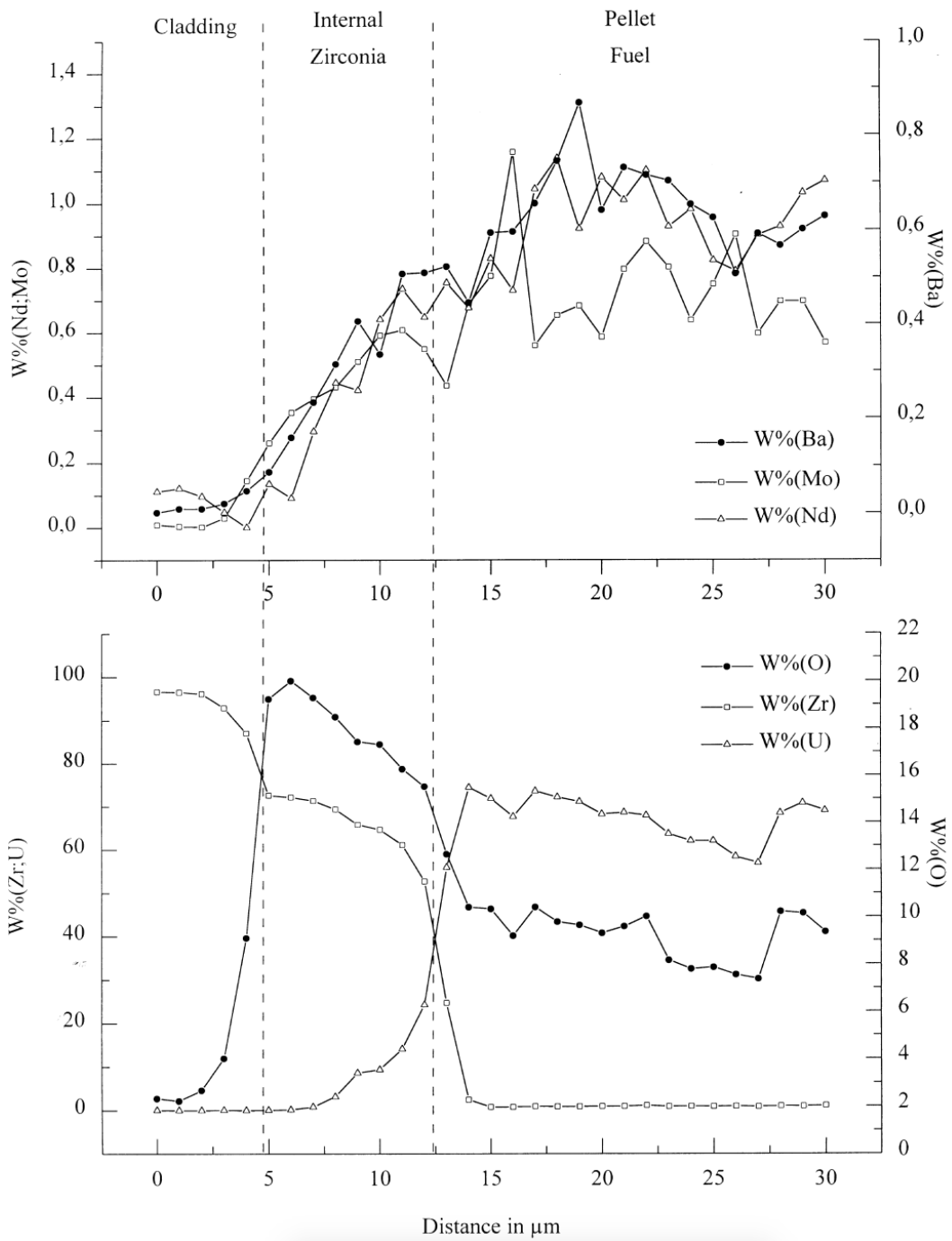


Figure 2.16: Elemental composition of the bonded  $\text{UO}_2/\text{ZrO}_2$  layer from a PWR  $\text{UO}_2$  fuel pellet with a burnup of 61 GWd/tU. Taken from [105].

$\text{O}_2$  pressures at constant temperature, allowing some level of internal cladding environment control depending on whether more or less oxygen is desired.

Oxygen and oxygen precursors may also be produced from fission of  $\text{U}^{235}$ , but this contribution is insignificant compared to changing the stoichiometry of the fuel pellet: that is, liberation of

oxygen from  $\text{UO}_{2\pm x}$  due to fission (which is a function of fuel stoichiometry) is a more significant contributor to the oxygen pressure than direct production via fission.

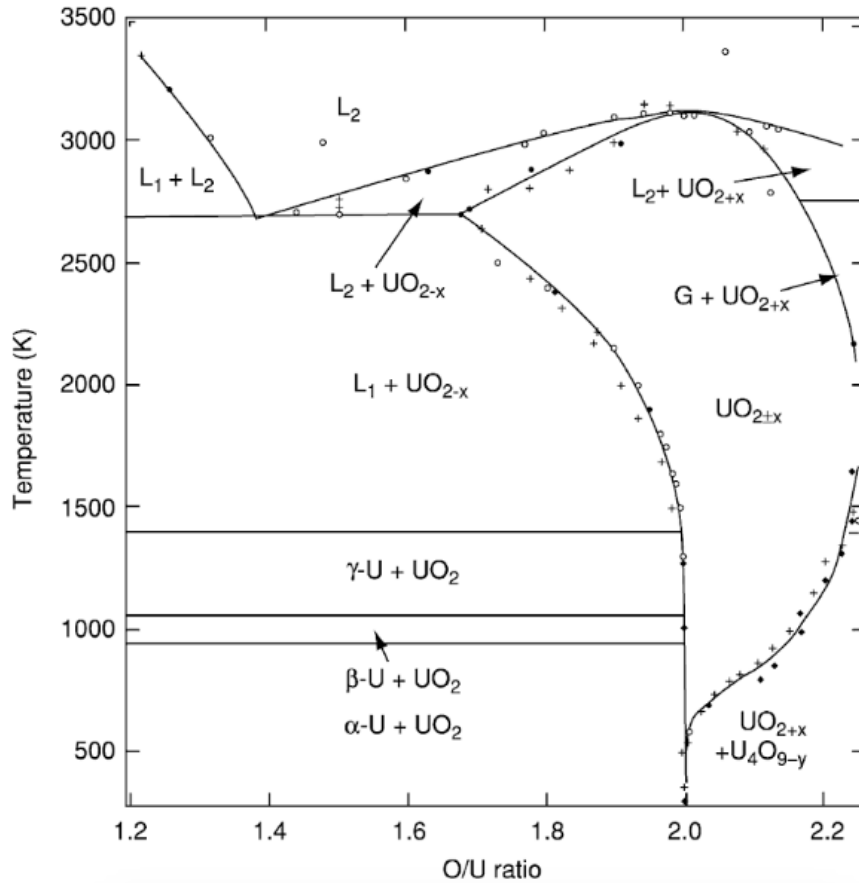


Figure 2.17: Partial U-O temperature binary phase diagram between O/U ratios of 1.2 and 2.25. Figure taken from [108], with phase boundaries from [109–111].

## 2.3 Atomistic scale computer simulation

Conducting experiments on active nuclear materials is a difficult undertaking. Handling irradiated materials is an expensive process, and materials such as uranium are highly controlled (though they are relatively benign before irradiation compared to many typical chemical laboratory materials and solvents). Furthermore, experiments which require samples to be irradiated must be left to cool-down (due to material activation) for up to a year before they can be anal-

ysed in a specialised lab [112]. Thus, any errors in the experimental procedure or problems with samples are not revealed until months later when material analysis is performed. This makes it difficult to study many material phenomena, especially if they are time-dependent. In-situ reactor experiments are also problematic, requiring sensor equipment to be made tolerant to the high radiation environments as well as being acceptable to and consistent with the reactor operation safety case. The risks and costs mean that experimental work is mostly restricted to the largest labs and researchers with enough funding to undertake such work. For these reasons, computer simulation methods are a preferable alternative for nuclear research and can also serve to guide experimental work.

### 2.3.1 Classical approach - molecular dynamics

Molecular dynamics (MD) uses classical mechanics as the basis for calculations [113]. These types of simulations typically use pair potentials (though many-bodied potentials are also used). These are mathematical functions which effectively describe the energy of interaction between two particles. Pair potentials are created by fitting functions to several parameters from empirical data, such as equilibrium bond lengths, thermal properties or even values from quantum mechanical calculations. The simple form of pair potentials allows MD simulations to scale up to billions of atoms, corresponding to a length scale of approximately  $0.1 \mu\text{m}$ .

In the literature, many molecular dynamics studies of  $\text{ZrO}_2$  exist [114–121]. However, these studies typically focus on dopant-stabilised zirconias (i.e. cubic ones as empirical potentials do not capture monoclinic or tetragonal phases and their transitions accurately). The large system sizes possible in molecular dynamics simulations are often necessary for examining properties

such as ion diffusion, thermal conductivity or melting points [122]. Studying fission products in ZrO<sub>2</sub> however, requires potentials which can accurately model interactions of atoms such as Zr, O, and I in the solid phase. A good potential for such a system has not yet been published and so a quantum mechanical study of the ZrO<sub>2</sub> system is the focus of this thesis. The work herein may then be used in the future development of such potentials.

### 2.3.2 Quantum mechanical approach - DFT

Another method for modelling materials at the atomic scale is to use a quantum mechanical approach. In this thesis, the framework of density functional theory (DFT) is used throughout for quantum mechanical calculations (see § 4.1). These techniques use a more fundamental approach than molecular dynamics, and are sometimes referred to as *ab initio* methods (although several empirical approximations are often used in DFT). The CASTEP 8.0 software package was used for all DFT calculations [123].

System sizes are far more constrained when using quantum mechanical methods. The solution algorithms require CPU time proportional to  $N^4$ , where  $N$  is the number of basis functions (functions used to describe electron orbitals). This steep scaling leads to large computational costs even for simple molecules with a few atoms before applying DFT methods [124, 125]. There are several ways to significantly reduce the computational complexity without sacrificing too much accuracy (e.g. the pseudopotential method, periodic boundaries, cell constraints and symmetry). This allows system sizes on the order of hundreds of atoms to be studied, corresponding to a length scale of approximately 1 nm. While this length scale is much smaller than what can be achieved using MD, the use of a more fundamental parameter (electron

density) in calculations provides a stronger scientific basis when material properties are derived from DFT models. Additionally, DFT allows electronic properties such as electron orbital occupancy and band gaps to be studied.

In the literature, DFT studies of ZrO<sub>2</sub> are predominantly focused on the dopant-stabilised cubic phase because of its use in fuel cells and medical applications [126, 127], with few studies on the undoped system [128, 129]. Pure oxide studies also tend to focus on only one of the three common phase, typically the monoclinic [130–132] and tetragonal phases [133–135]. Two notable studies have looked at all three phases. The first focused on the electronic structure and optical properties of ZrO<sub>2</sub> [136], while the second examined the structural properties and band structure of ZrO<sub>2</sub> [137]. Both studies utilised the local density approximation (LDA) for the exchange-correlation functional. In this thesis, a generalised gradient approximation (GGA) is used for the exchange-correlation functional (see § 4.1.2). Although GGAs are considered an improvement upon the LDA, it is always useful to compare results with data from older studies.

Lattice dielectric properties in the three phases have been calculated using DFT [138], and these have been used in this thesis to predict energies and defect equilibria. Various data from these studies have been used either for comparison or to aid in new calculations which have then been published.

### 2.3.3 Band gap

Conductors and insulators are two common ways to describe materials. While this binary characterisation may work as an approximation for many materials, in reality there is more of a continuum between these two states (e.g. semiconductors), and at the heart of this lies the

band gap.

Electron energy levels in a crystalline lattice are quantised, restricting the range of possible electron energies to discrete quantities. More specifically, electrons can only occupy unique quantum states, defined by parameters such as quantum spin and angular momentum. In a crystal, where there are large numbers of electrons and many possible configurations of them, we refer to energy *bands* which are comprised of many quantised energies. There are sometimes gaps between energy bands in crystals (illustrated in Figure 2.18) corresponding to energy levels that cannot be occupied, meaning that if electrons were to be added at the lowest energy levels one by one, there would occasionally be relatively large jumps in energy as an electron is forced to enter a higher energy band.

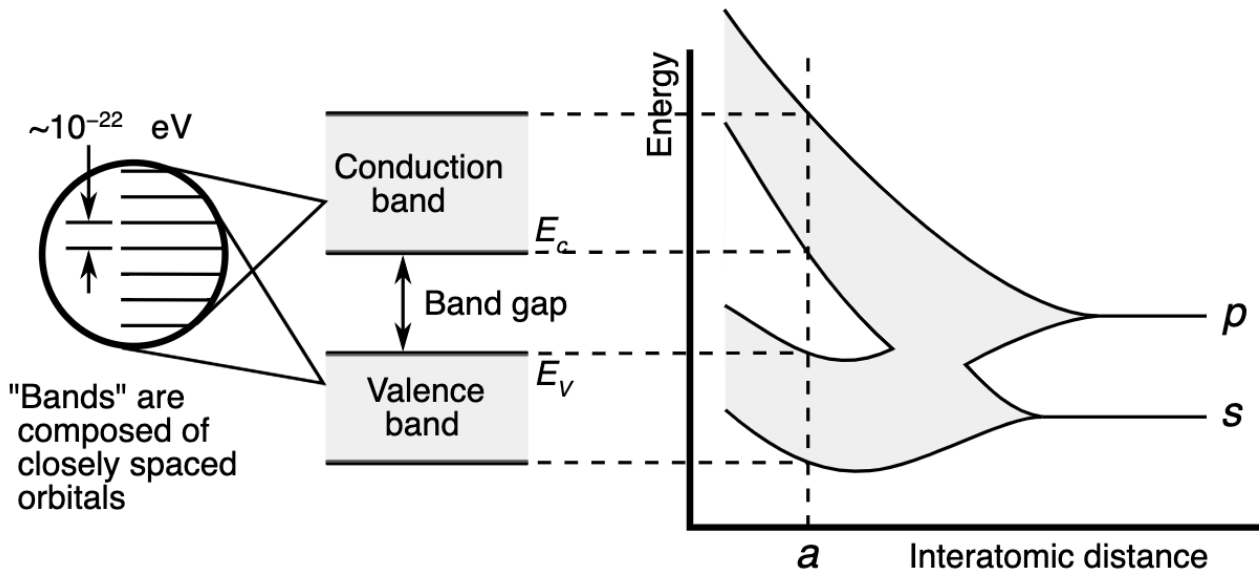


Figure 2.18: Illustration of the band gap in diamond as a function of interatomic spacing. Taken from [139].

Two energy bands, the *valence band* and *conduction band*, help determine a material's metallic or non-metallic character. The valence band contains energy levels occupied by the valence electrons (at absolute zero), while the conduction band contains energy levels which are high

enough that electrons may freely move throughout the crystal. In metals, the valence and conduction bands have some amount of overlap, meaning that once the valence band is full, the highest occupied electron energy states are within the conduction band and so the material acts as a conductor. Materials like  $\text{ZrO}_2$ , however, have large energy gaps between the valence and conduction bands, known as the band gap. These materials are called *band insulators* (as opposed to *Mott insulators* where there is no conventional band gap, but electron-electron interactions impede electron promotion to higher energies), because the band gap is an energy barrier preventing the valence electrons from moving freely around the crystal.

In addition to the valence and conduction bands, a value for the electron chemical potential or Fermi level of the material is needed to determine how the energy bands are filled. If the Fermi level is exactly halfway between the valence band maximum (VBM) and the conduction band minimum (CBM), then the additional energy input required to promote an electron to the conduction band is half the value of the band gap. The Fermi level is strongly dependent on extrinsic defects and temperature. Extrinsic defects (or dopants) can be introduced to materials such as semiconductors in order to change the concentration of electronic defects (electrons and holes), while an increase in temperature will result in an increase in the Fermi level because of the larger quantity of thermal energy available.

It should be noted that band gaps reported in DFT studies using LDA/GGA methods are significantly lower than those obtained experimentally. This is a known problem in DFT, and an exchange-correlation functional which reproduces correct band gap energies in semiconductors and insulators (without overfitting to experimental data) is not yet known. The GW method, which uses a self-energy energy term in place of an exchange-correlation functional, allows more

accurate<sup>1</sup> estimates of the band gap than with DFT, but at a significantly higher computational expense. The band gap from DFT calculations may also be increased by appending an additional potential term, known as a +U parameter, to valence electron orbitals (see § 4.5.7), or by using hybrid potentials which can incorporate the exact exchange energy.

---

<sup>1</sup>The GW approximation still has inaccuracies when modelling strongly correlated systems, but works well with *s-p* systems.

# Chapter 3

## Crystallography and Point Defects

### 3.1 $\text{ZrO}_2$ phases

$\text{ZrO}_2$  exhibits three commonly reported polytypes in its binary phase diagram at ambient pressure. The temperature-pressure phase diagram of  $\text{ZrO}_2$  as currently understood is shown in Figure 3.1, with phase details in Table 3.1. Each will now be described and contrasted.

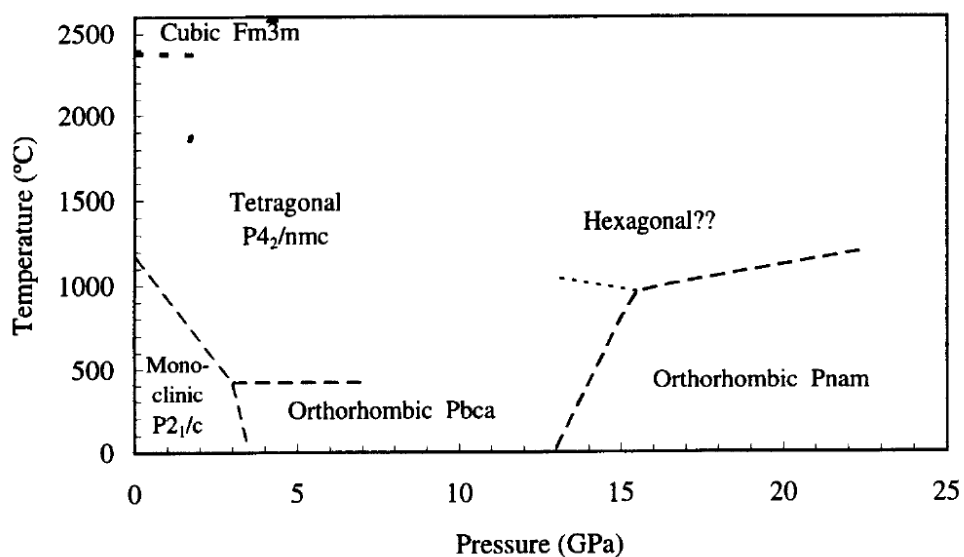


Figure 3.1: Temperature-pressure phase diagram of  $\text{ZrO}_2$ . Taken from [140].

Table 3.1:  $\text{ZrO}_2$  phases and their details. Adapted from [140].

Phase	Stability range (K, GPa)	Cell parameters ( $\text{\AA}$ )			$\beta$	Atom	Atom positions			Space group
		$a$	$b$	$c$			$x$	$y$	$z$	
Cubic [141]	2377-2710 K	5.117	5.117	5.117	90	Zr	0	0	0	$Fm\bar{3}m$
Tetragonal [142]	1205-2377 K	5.074	5.074	5.188	90	Zr	0	0	0	$Fm\bar{3}m$
Monoclinic [93]	0-1205 K	5.1507	5.2028	5.3156	99.194	Zr	0.2754	0.0395	0.2083	$P2_1/c$
						O1	0.0700	0.3317	0.3477	
						O2	0.4416	0.7569	0.4792	
Ortho I [143]	3.5-15 GPa	5.0431	5.2615	5.0910	90	Zr	0.2686	0.0332	0.2558	$Pbca$
						O1	0.0822	0.3713	0.1310	
						O2	0.5442	0.2447	0.0052	
Ortho II [144] (cotunnite)	>15 GPa	5.593	6.484	3.333	90	Zr	0.256	0.110	0.25	$Pnma$
						O1	0.356	0.422	0.25	
						O2	0.022	0.331	0.75	
Ortho (PSZ) [145]	0-500 K	5.068	5.260	5.077	90	Zr	0.267	0.030	0.250	$Pbc2_1$
						O1	0.068	0.361	0.106	
						O2	0.537	0.229	0	

### 3.1.1 Monoclinic

Below 1205 K at atmospheric pressure,  $\text{ZrO}_2$  adopts a monoclinic Baddeleyite ( $\text{P}2_1/c$ ) crystal structure. This is the ground state structure of  $\text{ZrO}_2$ . In this phase, Zr ions have a sevenfold O coordination, down from eight in the higher temperature phases due to a single ‘broken bond’. A unit cell of monoclinic  $\text{ZrO}_2$  is illustrated in Figure 3.2. The dashed line (approximately 3.7 Å in length) shows the Zr-O bond which is broken when transitioning to monoclinic from the tetragonal phase. Zr-O bond lengths range from 2.05 to 2.31 Å.

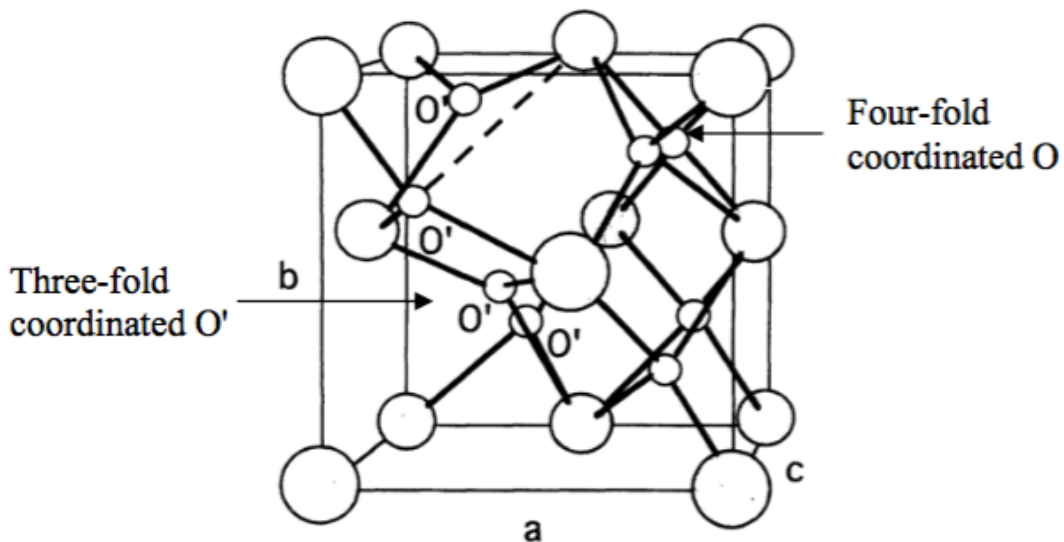


Figure 3.2: A monoclinic  $\text{ZrO}_2$  unit cell indicating the two different oxygen bond coordinations. Small spheres represent oxygen ions while large spheres represent zirconium ions. Taken from [146].

Monoclinic phase  $\text{ZrO}_2$  also has two distinct oxygen ions in its primitive cell. To maintain the stoichiometry of 1:2 Zr to O, half of the oxygen ions exhibit threefold coordination with zirconium (in a planar configuration), while the other half have a fourfold coordination (tetrahedral configuration) with zirconium. Figure 3.3 shows the positions of these oxygen ions around a zirconium ion centre. The distortion from the oxygen rock salt sub-lattice can be seen, specifically in the case of the three coordinated oxygen ions. This is due to the zirconium

ion being too small to hold 8 oxygen ions in an octahedral configuration, as in the fluorite crystal structure. As temperature is increased, so too are the interatomic distances. At the tetragonal temperature range, bonding between all 8 nearest neighbour oxygen and zirconium ions becomes energetically favourable and there is a transition to eightfold coordination.

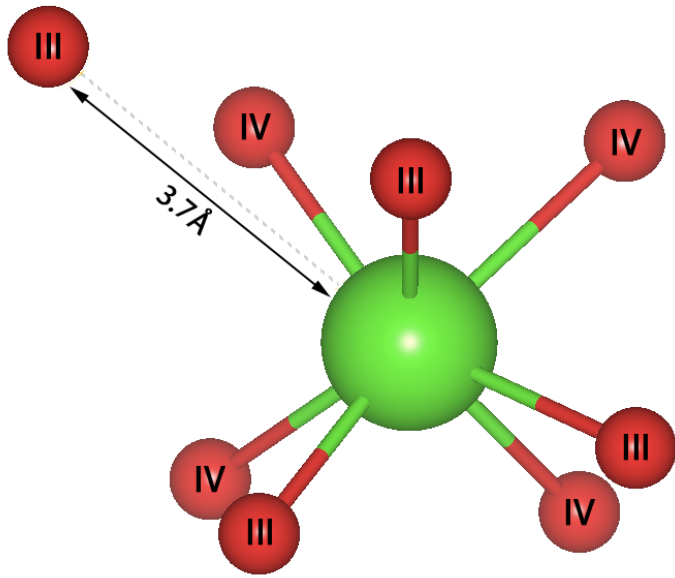


Figure 3.3: Zirconium centre unit cell in monoclinic  $\text{ZrO}_2$  showing nearest oxygen atoms and their respective bond co-ordinations. Zirconium atoms are shown in green and oxygen atoms in red.

The monoclinic-tetragonal phase transition occurs by a diffusionless martensitic transformation with a  $9^\circ$  shear [147]. This is a fast transformation and is accompanied by a large volume change. Tetragonal phase  $\text{ZrO}_2$  (density  $6.10 \text{ g/cm}^3$ ) is around 4.6% more dense than monoclinic  $\text{ZrO}_2$  (density  $5.73 \text{ g/cm}^3$ ) [148], though the volume increase when cooling from tetragonal has been reported to be as high as 9% [149]. This results in a kinetic barrier between the phases, and therefore the phase transition exhibits a hysteresis loop approximately 200 K wide when undergoing thermal cycling, as shown in Figure 3.4.

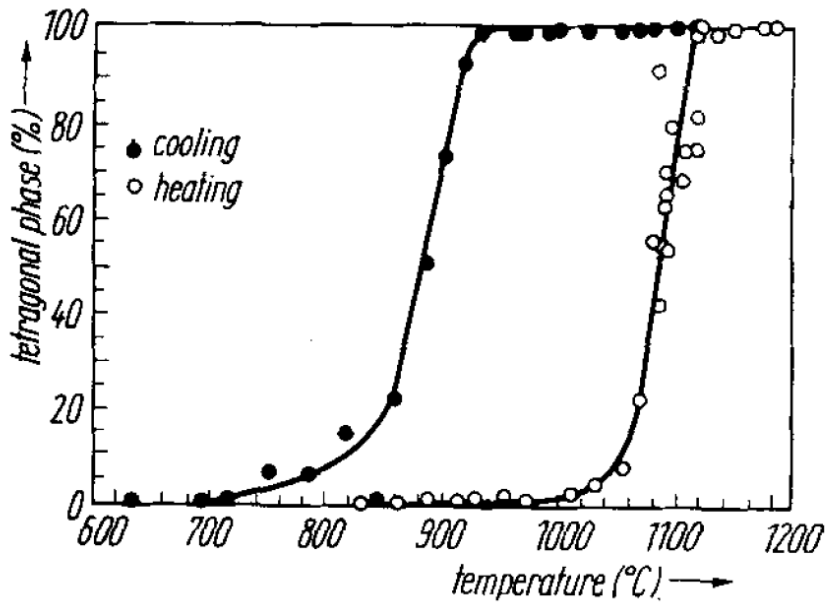


Figure 3.4: Monoclinic-tetragonal phase transition in  $\text{ZrO}_2$  as a function of temperature only. Taken from [150].

### 3.1.2 Tetragonal

The tetragonal phase was first observed in 1929 during studies of polymorphism and phase stabilisation in  $\text{ZrO}_2$  [151]. The tetragonal phase (space group  $\text{P}4_2/\text{nmc}$ ) can be easily derived from the cubic phase by shifting alternating columns of oxygen ions slightly up or down the  $[001]$  direction [94]. This change is so subtle that the two phases are almost identical when viewed in certain orientations. Figure 3.5 shows a view of a tetragonal unit cell down the  $[110]$  direction alongside a  $[100]$  view of a cubic unit cell. Going from the cubic to the tetragonal phase, the oxygen ions can clearly be seen to deviate from their equilibrium sites in the cubic sublattice. This is consistent with the interpretation that the ionic radius of Zr is slightly too small to maintain the cubic fluorite structure, which is therefore only seen at high temperatures (where thermal fluctuations mean the effective ionic radius is larger) or when under high compressive stress (where interatomic spacings are smaller).

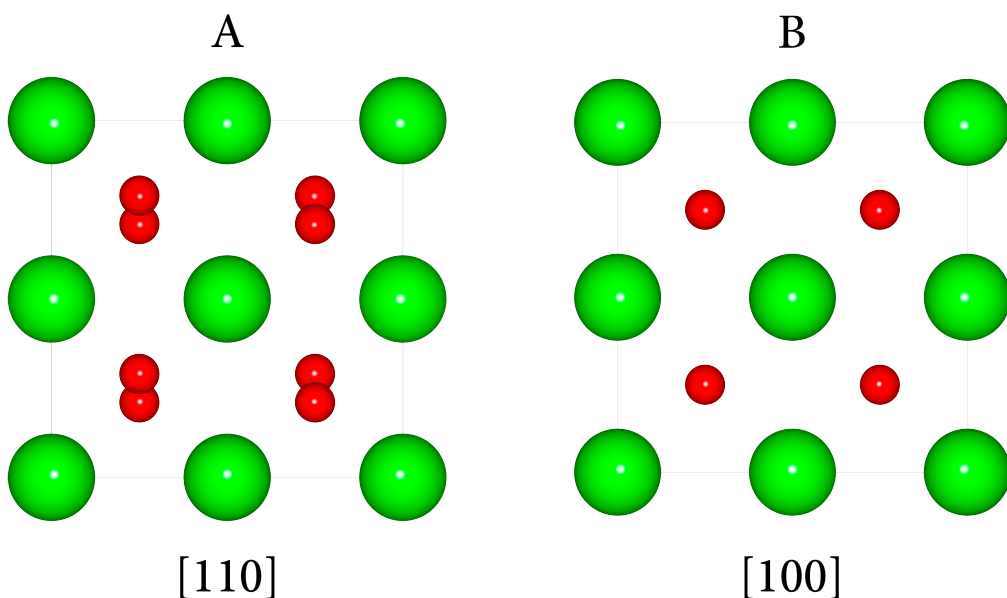


Figure 3.5: **A)** Tetragonal ZrO<sub>2</sub> viewed along the [110] direction. **B)** Cubic ZrO<sub>2</sub> viewed along the [100] direction. Zirconium atoms are shown in green and oxygen atoms in red.

## Tetragonal phase stress stabilisation

The pressure-temperature phase diagram of  $\text{ZrO}_2$  (Figure 3.6)<sup>1</sup> shows how the monoclinic-tetragonal phase transition temperature is strongly dependent on pressure, with an almost linear reduction in transition temperature of  $300 \text{ }^{\circ}\text{C/GPa}$ . The phase diagram also shows the extent of the hysteresis effect in the monoclinic-tetragonal transition.

There is some degree of tetragonal phase autostabilisation during the oxidation process of zirconium. This is possible because of the resulting increase in volume when zirconium is oxidised. Zirconium has a Pilling-Bedworth ratio of 1.57, meaning that the oxide would occupy a volume 57% larger than the metal if unconstrained [153, 154]. In the case of zirconia, the oxide grows into the metal by transport of oxygen through the oxide layer to the metal/oxide interface, generating large compressive stresses of up to 2.5 GPa [96, 155, 156]. This is an important

<sup>1</sup>Tetragonal I in this figure refers to the high temperature tetragonal phase of  $ZrO_2$  with space group  $P4_2/nmc$ . Tetragonal II refers to the high pressure orthorhombic phase with space group  $Pbca$ . However, the authors indexed this phase on the basis of a tetragonal cell.

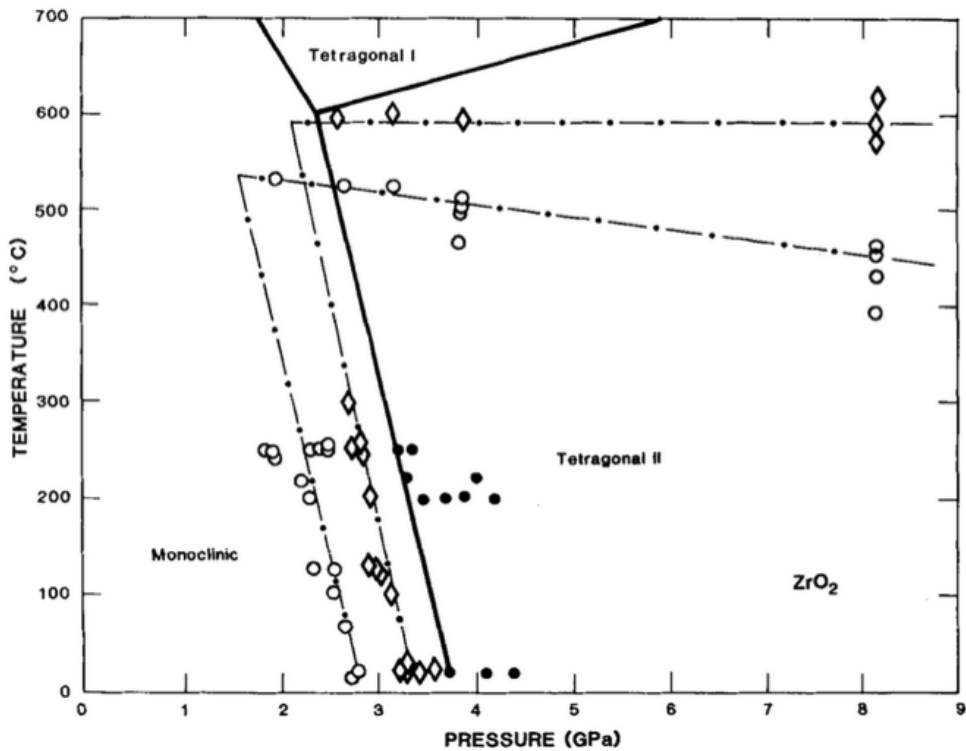


Figure 3.6: Pressure-temperature phase diagram for zirconia. Dash-dotted lines represent more recent data. Diamonds mark transition points during an increase in temperature or pressure, while open circles represent a decrease in pressure or temperature. Solid circles represent transition points for a fresh, single crystal sample. Taken from [152].

contribution to the stabilisation of the tetragonal phase because of the strong dependence on pressure, though this contribution alone may not be sufficient at PWR operating temperatures.

Stabilisation of the tetragonal phase at low temperatures is also dependent on grain size, which can be controlled during the cladding manufacturing process since the oxide inherits the grain size of the zirconium metal grains. Pure  $ZrO_2$  exhibits a strong relationship between grain size and phase stability, where the tetragonal phase is only stable when grown from metal grains below a critical size of approximately 30 nm [157]. This can be explained by increased dislocation interaction in smaller grains due to limited room for dislocation glide, as per the Hall-Petch relationship [158, 159]. Grains of tetragonal  $ZrO_2$  larger than this critical size are therefore likely to have tetragonal-stabilising dopant ions incorporated in the lattice.

### 3.1.3 Cubic

Cubic  $\text{ZrO}_2$  (unit cell shown in Figure 3.7) adopts the cubic fluorite (space group  $\text{Fm}\bar{3}m$ ) crystal structure, consisting of zirconium ions in a face-centred cubic configuration with a rock salt oxygen sub-lattice occupying the tetrahedral sites.

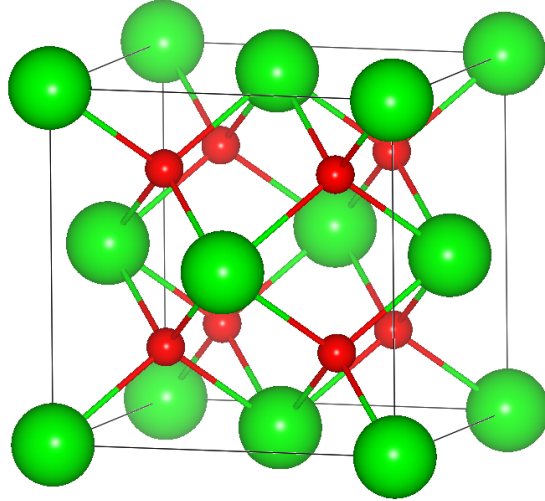


Figure 3.7: Unit cell of cubic  $\text{ZrO}_2$ . Zirconium atoms are shown in green and oxygen atoms shown in red.

The lowest specific volume (i.e. highest density), as calculated from DFT geometry optimisations in this thesis, is exhibited by the cubic phase ( $11.13 \text{ \AA}^3\text{ion}^{-1}$ ) followed by the tetragonal phase ( $11.51 \text{ \AA}^3\text{ion}^{-1}$ ) and then the monoclinic phase ( $11.99 \text{ \AA}^3\text{ion}^{-1}$ ). This is due to it having the largest atomic packing factor, resulting in a mean Zr-O bond distance of  $2.22 \text{ \AA}$ , compared to  $2.26 \text{ \AA}$  in the tetragonal phase and  $2.31 \text{ \AA}$  in the monoclinic phase, as shown in Figure 3.8.

### 3.1.4 Other phases

Two orthorhombic phases have also been observed at high pressures in pure  $\text{ZrO}_2$  [160]. These structures are referred to as OI and OII, the latter of which is isostructural with cotunnite

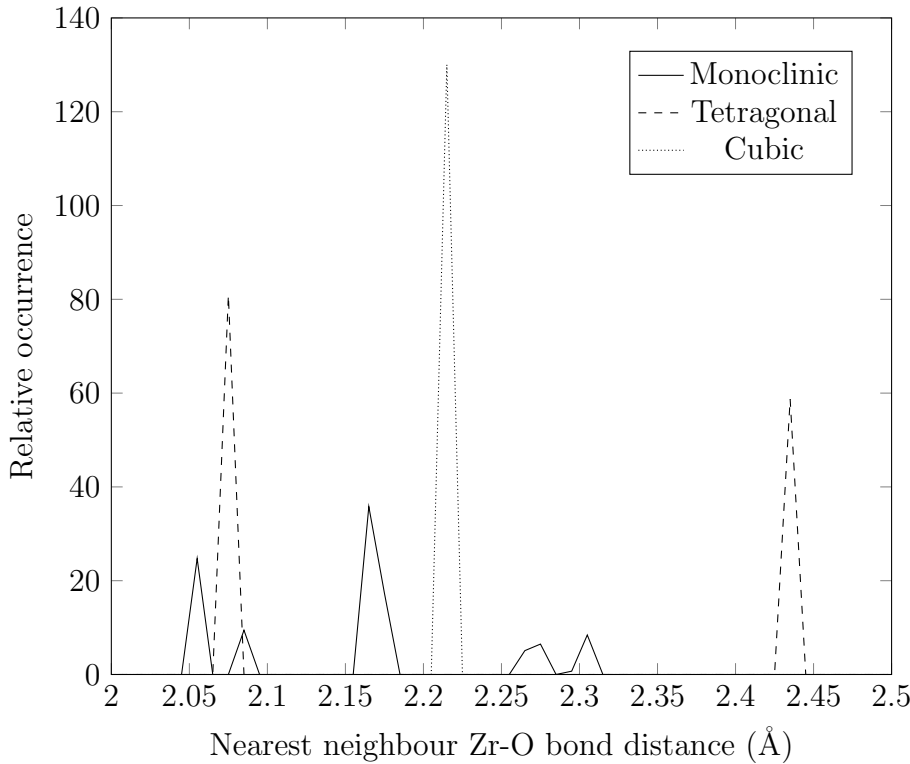


Figure 3.8: Density plot of the nearest neighbour Zr-O bond distances in  $ZrO_2$  for each crystal structure. Specific volumes from DFT calculations are  $11.99 \text{ \AA}^3\text{ion}^{-1}$ ,  $11.51 \text{ \AA}^3\text{ion}^{-1}$ , and  $11.13 \text{ \AA}^3\text{ion}^{-1}$  for monoclinic, tetragonal, and cubic phases respectively.

$(PbCl_2)$ . A third orthorhombic phase ( $bc2_1$ ) has also been reported in partially stabilised zirconia (PSZ), but has not been found in pure zirconia [140].

### Orthorhombic OI

The OI phase, illustrated in Figure 3.9, maintains a 7 oxygen coordinated zirconium ion, as is the case in the monoclinic phase. This phase also exhibits two distinct oxygen atom sites like in the monoclinic phase, but being an orthorhombic phase, it does not exhibit a  $9^\circ$  shear in its unit cell like the monoclinic phase. While this phase is briefly stable at high compressive stresses (3.5 - 15 GPa), it appears to be an intermediate phase before collapse into the more familiar cotunnite structure at pressures greater than 15 GPa. In addition, the OI phase is only

stable at temperatures below approximately 400 °C, transitioning to the tetragonal phase at higher temperatures. While PWRs operate at low enough temperatures for the OI phase to be stable, compressive stresses on the order of several GPa will not be present at any significant scale and thus this phase will not affect the oxide microstructure.

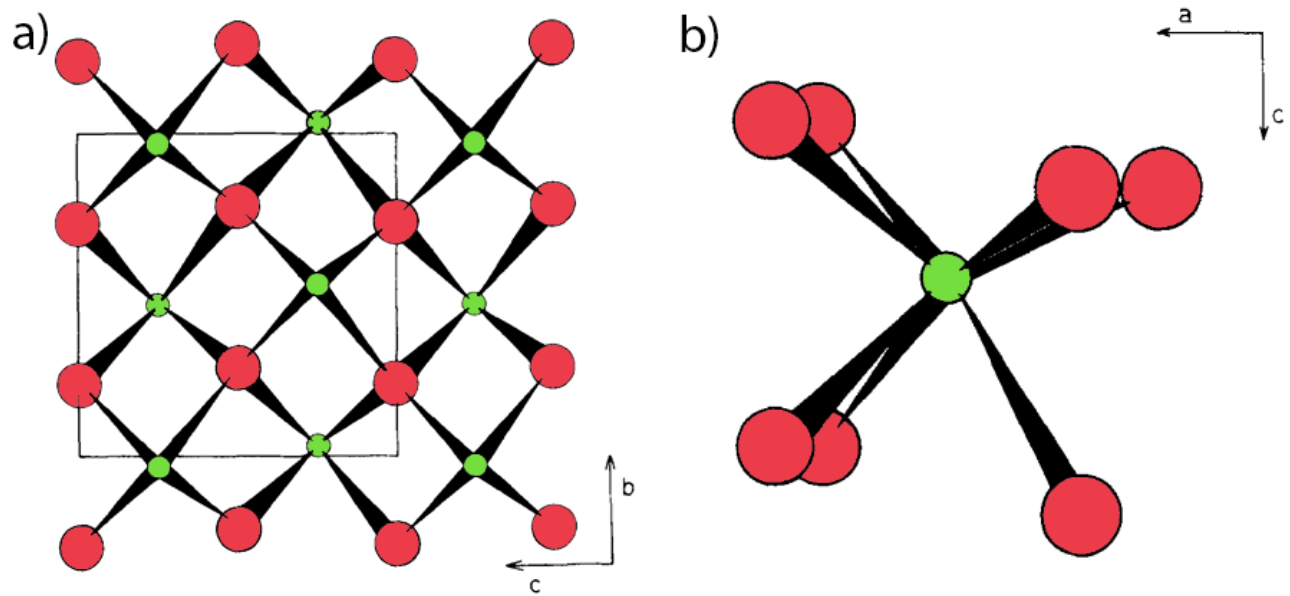


Figure 3.9: Illustrations of the orthorhombic OI ( $\text{Pbca}$ ) crystal structure of  $\text{ZrO}_2$  showing **a**) the unit cell as seen from the  $a$  direction and **b**) the zirconium ion centre with 7 coordinated oxygen ions. Zirconium and oxygen ions are coloured green and red respectively. Adapted from [145].

### Orthorhombic OII (cotunnite)

The OII phase, illustrated in Figure 3.10, maintains a 9 oxygen coordinated zirconium ion. This is due to the high stabilising pressure ( $> 15$  GPa) causing a reduction in the mean interatomic distance, so much so that the zirconium ion, which is typically too small to bond strongly to more than 7 oxygen atoms at standard conditions, can maintain the ninefold oxygen coordination. Such high hydrostatic pressures will not be present in a reactor environment even at the atomic scale, it is therefore not expected to find any OII phase present at any point during

the cladding's operational lifetime.

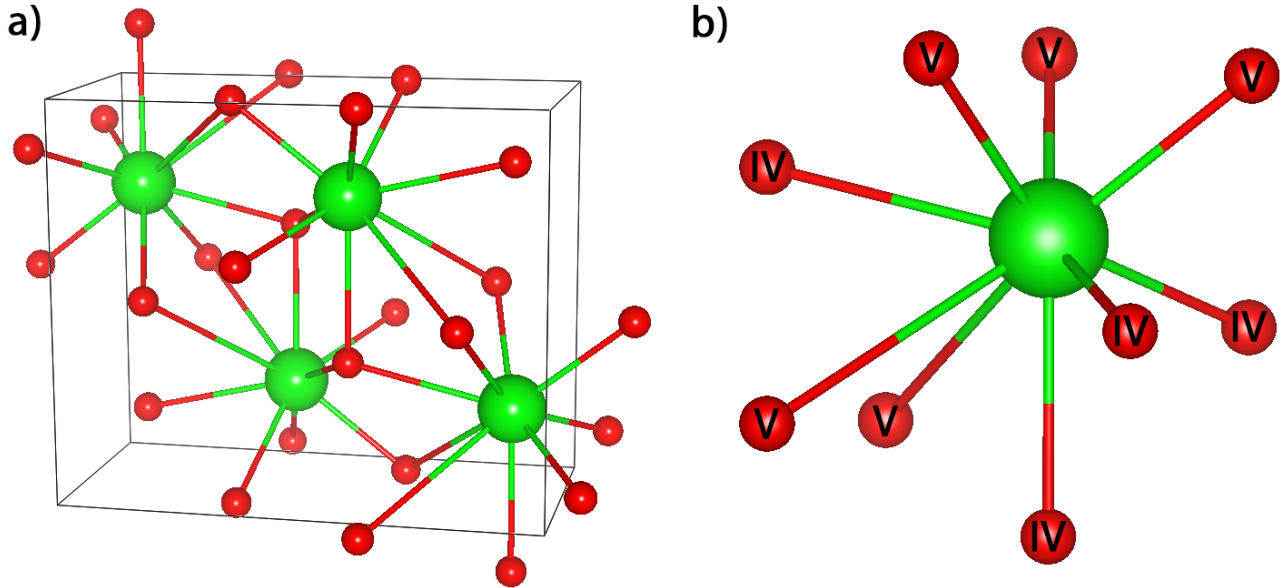


Figure 3.10: Illustration of **a)** OII cotunnite ( $Pnma$ ) unit cell and **b)** zirconium ion with nearest neighbour oxygens with coordination number indicated. Zirconium and oxygen atoms are coloured green and red respectively. Adapted from [161].

## Hexagonal

A hexagonal phase of  $ZrO_2$  has been reported in X-ray diffraction studies at high pressure (20 GPa) and above 1000 °C [162]. This phase retains its structure during isobaric quenching, but transforms back to the monoclinic phase structure once pressure is released. This phase is only observed under extreme conditions, and so is mentioned here for purposes of completeness.

## 3.2 Dopant stabilisation

Particular dopant species will stabilise the tetragonal and cubic phases of  $ZrO_2$  to room temperature. The most technologically significant is yttrium, which at concentrations of 15 mol.%, fully stabilises the cubic phase (which in practical terms means the cubic phase is stable down

at least to room temperature). Zirconia stabilised this way is known as YSZ, and is also sometimes referred to as partially-stabilised zirconia (PSZ). The inclusion of trivalent yttrium promotes the inclusion of charge compensating oxygen vacancy defects (see Equation 3.1 which uses Kröger-Vink notation, explained in the next section). This works in a similar way with several other cation dopants such as trivalent scandium from  $\text{Sc}_2\text{O}_3$ , or divalent magnesium from  $\text{MgO}$  (Equation 3.2), which also act as cubic stabilisers.



As already discussed above, while  $\text{MO}_2$  oxides (e.g.  $\text{CeO}_2$ ,  $\text{UO}_2$ ) often adopt the regular cubic fluorite structure, we only observe cubic stabilisation of  $\text{ZrO}_2$  at elevated temperatures where the effective ionic radii of the zirconium ion increases (possibly due to a stabilising phonon mode contribution [163–166]). Yttrium stabilises the cubic phase, not only due to the presence of oxygen vacancies, but because the yttrium ion is of the appropriate size to maintain its surrounding oxygen ions (which may include a vacant oxygen site) in the VIII coordination at low temperatures. This is supported by the ionic radii values in Table 3.2 which shows that the  $\text{Y}^{3+}$  radii are even larger than the  $\text{Ce}^{4+}$  radii and clearly larger than the corresponding  $\text{Zr}^{4+}$  radii.

Table 3.2: Ionic radii of  $\text{Zr}^{4+}$ ,  $\text{Y}^{3+}$  and  $\text{Ce}^{4+}$  in various coordination environments. Values taken from [167].

Ion	Coordination	Ionic Radius ( $\text{\AA}$ )
$\text{Zr}^{4+}$	IV	0.59
	V	0.66
	VI	0.72
	VII	0.78
	VIII	0.84
$\text{Y}^{3+}$	IX	0.89
	VI	0.90
	VII	0.96
	VIII	1.019
$\text{Ce}^{4+}$	IX	1.075
	VI	0.87
	VIII	0.97
	X	1.07
	XII	1.14

### 3.3 Kröger-Vink notation

Kröger-Vink notation [168] is used throughout this thesis to describe defects. It is widely used in physical chemistry and is a useful shorthand for describing chemical reactions where conservation of mass, charge and lattice sites is required. The notation syntax is of the form  $x_z^y$ , where  $x$  is the substituted atom or missing atom (i.e. a vacancy  $V$ ),  $y$  is the charge of the defect (relative to the lattice species that originally occupied the site) and  $z$  is the site the defect occupies. Positive and negative charges are indicated with dots ( $\bullet$ ) and dashes ( $'$ ) respectively, otherwise a cross ( $\times$ ) is used to denote a neutral defect (i.e. the substitutional ion has the same charge as the ion it is replacing). The site may be either a lattice site (such as Zr or O in  $\text{ZrO}_2$ ) or an interstitial site ( $i$ ). Table 3.3 shows examples of several different types of defects and their respective Kröger-Vink notation.

Table 3.3: Examples of Kröger-Vink notation for several defects in  $\text{ZrO}_2$ .

Defect	Kröger-Vink Notation
Anion vacancy	$V_O^{••}$
Cation vacancy	$V_{\text{Zr}}^{''''}$
Anion interstitial	$O_i''$
Cation interstitial	$Zr_i^{••••}$
Iodine ( $\text{I}^-$ anion) on oxygen site	$I_O^{\bullet}$
Iodine ( $\text{I}^+$ cation) on zirconium site	$I_{\text{Zr}}'''$

# Chapter 4

## Computational Methodology

### 4.1 Density functional theory

Quantum mechanics is currently the most complete modern theory which describes the behaviour of matter at the length scale of atoms. It can be used to predict things such as the energy levels of atoms, the interactions of light with matter, and the thermodynamic stability of systems of atoms. Ideally, the mathematical formalisms of quantum mechanics would be used to predict the properties and behaviour of all possible types of molecules and materials. In reality, this is very difficult to achieve, requiring several approximations and abstractions in order to produce methods which sacrifice some degree of physical accuracy in order to be computationally tractable. Currently, the most successful approach to predict the behaviour of most solids is provided by density functional theory.

### 4.1.1 The Schrödinger equation

The time-independent Schrödinger equation is used to find the total energy of a system:

$$E\Psi(\mathbf{r}) = \hat{H}\Psi(\mathbf{r}) \quad (4.1)$$

where  $E$  is the total energy of the system,  $\Psi$  is the wave function associated with the electrons, and  $\hat{H}$  is the energy Hamiltonian operator.  $\hat{H}$  includes the kinetic energy contributions ( $\hat{T}$ ) and potential energy contributions ( $\hat{V}$ ), shown in atomic units in equations 4.3 and 4.4 respectively:

$$\hat{H} = \hat{T} + \hat{V} \quad (4.2)$$

$$\hat{T} = - \sum_i \frac{1}{2} \nabla_{r_i}^2 - \sum_i \frac{1}{2M_i} \nabla_{R_i}^2 \quad (4.3)$$

$$\hat{V} = \sum_{i,j=i+1} \frac{1}{2|r_i - r_j|} + \sum_{i,j=i+1} \frac{Z_i Z_j}{2|R_i - R_j|} - \sum_{i,j} \frac{Z_i}{2|R_i - r_j|} \quad (4.4)$$

where  $r_i$  is the position of electron  $i$ ,  $R_i$  is the position of nucleus  $i$  and  $M_i$  is the mass of nucleus  $i$ . Thus, the second term on the right of equation 4.3 relates to the kinetic energy of any associated nuclei, and the first term to electrons.

If  $\Psi(\mathbf{r})$  is the wave function, the electron density at position  $\mathbf{r}$  ( $\rho(\mathbf{r})$ ) is given by:

$$\rho(\mathbf{r}) = \Psi(\mathbf{r})^2 \quad (4.5)$$

### 4.1.2 Kohn-Sham Method

DFT was developed by Kohn and Sham in 1964 [169] as an ab initio method for predicting  $\rho(\mathbf{r})$  associated with an ensemble of atoms. The Kohn-Sham Hamiltonian (Equation 4.6) is used in the Schrödinger equation:

$$\hat{H}(\rho(\mathbf{r})) = E_{KE}(\rho(\mathbf{r})) + E_P(\rho(\mathbf{r})) + E_{XC}(\rho(\mathbf{r})) \quad (4.6)$$

where  $E_{KE}$  and  $E_P$  are the kinetic and potential energy functionals (functions of functions),  $E_{XC}$  is the exchange correlation functional, and  $\mathbf{r}$  is the position vector. The main approximation is to consider that the electrons only interact with nuclei and the average field generated by all other electrons, and not other electrons explicitly, thus allowing all the terms to be evaluated using the electron density rather than position. An exchange correlation term is then used to include the non-classical electron-electron interactions, namely electron exchange and correlation. Additionally, the exchange correlation term includes the difference in kinetic energy due to the use of non-interacting electrons. While Kohn and Sham proposed an exchange-correlation functional in the Hamiltonian, a general form of the functional has not yet been found. Several forms have been considered, each with strengths and weaknesses when applied to different systems. One basic form of the functional which is frequently used is the LDA [169]:

$$E_{LDA}(\rho(\mathbf{r})) = \int \rho(\mathbf{r}) e_{uniform}(\rho(\mathbf{r})) dr \quad (4.7)$$

where  $e_{uniform}$  is the normalised exchange-correlation energy of a uniform electron gas (an idealised system). This exchange-correlation functional generates accurate results in materials

such as metals where the electron density is relatively uniform, while systems with more rapidly changing electron densities (e.g. highly ionic materials) require more complex functionals. A natural extension of the LDA is to also take into account the gradient of the electron density, thus allowing a smoother functional fit when electron density is highly variable as a function of position. Such functionals are collectively referred to as GGAs [170–173]. One GGA which has enjoyed widespread use for many different types of systems is the Perdew-Burke-Ernzerhof (PBE) GGA [174]. The accuracy of this functional when modelling solid phase systems is well-established, and its frequent use in DFT studies provides ample reference material for comparing results. After conducting several convergence tests (see § 4.5), the PBE GGA was chosen as the exchange-correlation functional to be used for all calculations in this thesis.

### Born-Oppenheimer approximation

The Born-Oppenheimer approximation is a two-step process for evaluating atomic forces which greatly reduces the computational costs of atomistic simulations. It exploits the large difference in mass between nuclei and electrons in order to separate their interactions. This allows us to decompose the total wave function into a product of an electronic wave function and a nuclear wave function via a separation of variables approach. The first step involves ignoring the kinetic energy contribution of nuclei by assuming they are stationary, thus the nuclear kinetic energy term in Equation 4.3 can be removed. The stationary nuclei assumption also simplifies the nuclear-nuclear Coulombic repulsion term in Equation 4.4 because  $|R_i - R_j|$  becomes a constant throughout the calculation. An electronic Schrödinger equation is then solved where electronic positions are variables and nuclear positions are fixed parameters. This solution contains information of the shape of the electronic orbitals. The next step is to take the

electronic distribution and calculate the resultant forces on the nuclei. The nuclear positions are then modified to minimise these forces, followed by feeding these nuclear positions back into the electronic Schrödinger equation to obtain the new electronic distribution. This process is repeated until the required convergence criterion (such as energy change per iteration and forces on nuclei) are satisfied.

### 4.1.3 Pseudopotentials

The electron-electron interaction component of the potential energy presents a problem when it comes to scaling experimental models. The number of terms in this interaction grows quadratically with the number of electrons in the system, quickly becoming computationally intractable for even small systems. However, it is known that in chemical reactions, the majority of chemical behaviour is determined by relatively few valence electrons, while the more numerous core electrons have a far smaller effect.

Consider the zirconium atom with 40 electrons, of which 4 ( $4d^25s^2$ ) are typically involved in bonding and chemical reactions. By considering only these valence electrons for Coulombic-term calculations, we reduce the system size by 90%, which provides a more than tenfold reduction in computational requirements.

Although the core electrons do not participate in chemical reactions, they still influence the properties of the atom, such as the atomic radius. Instead of modelling the core electrons explicitly, we can approximate their aggregate effect with a potential energy function. This is what we aim to achieve by using the pseudopotential method. An example indicative pseudopotential is shown in figure 4.1.

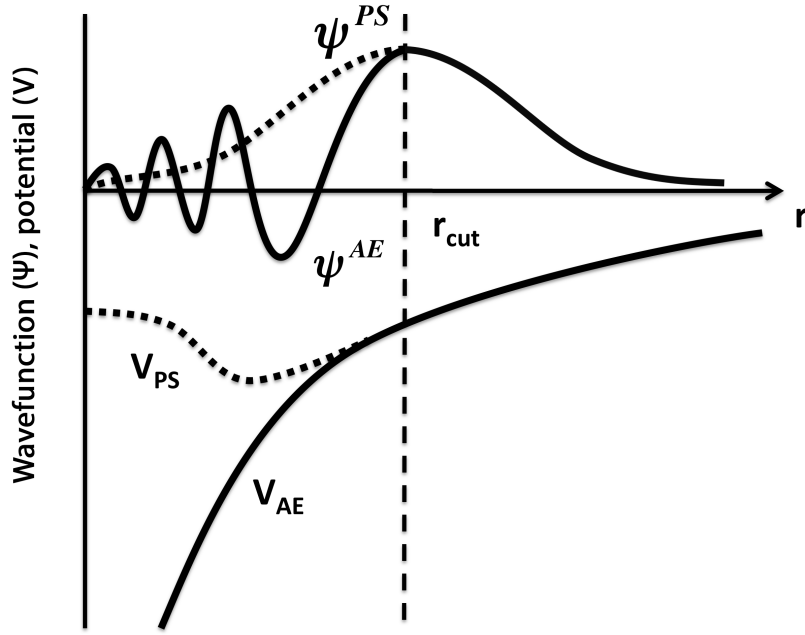


Figure 4.1: Sketch of an all-electron potential  $V_{AE}$  and a pseudopotential  $V_{PS}$  with their corresponding wave functions.  $r_{cut}$  indicates the radius beyond which both the potentials and their wave functions are the same. Adapted from [175].

Figures 4.2 and 4.3 show the actual pseudopotentials used throughout this work for oxygen and zirconium respectively. The potentials are shown broken down by the electronic sub-shells occupied by the valence electrons. The pseudopotentials are shown in order of increasing sub-shell energies, thus the 5s electron orbitals are filled before the 4d orbitals in zirconium. Two lines for the all-electron wavefunction are shown, corresponding to the different electron angular momenta.

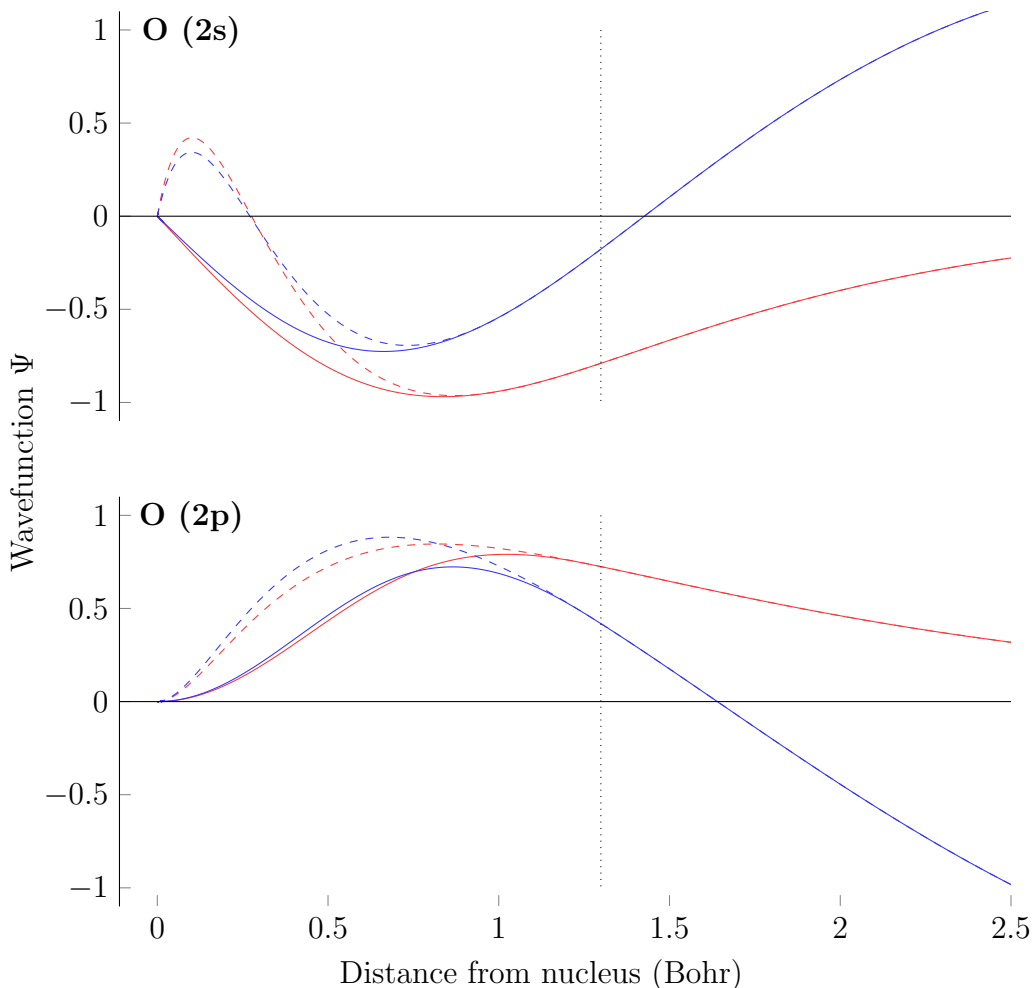


Figure 4.2: Plots of the valence  $s$  and  $p$  orbital potentials for oxygen with two projectors per angular momentum. Dashed lines indicate the all-electron potentials while solid lines indicate the corresponding pseudopotential. Dotted vertical line marks the radius beyond which the potentials match.

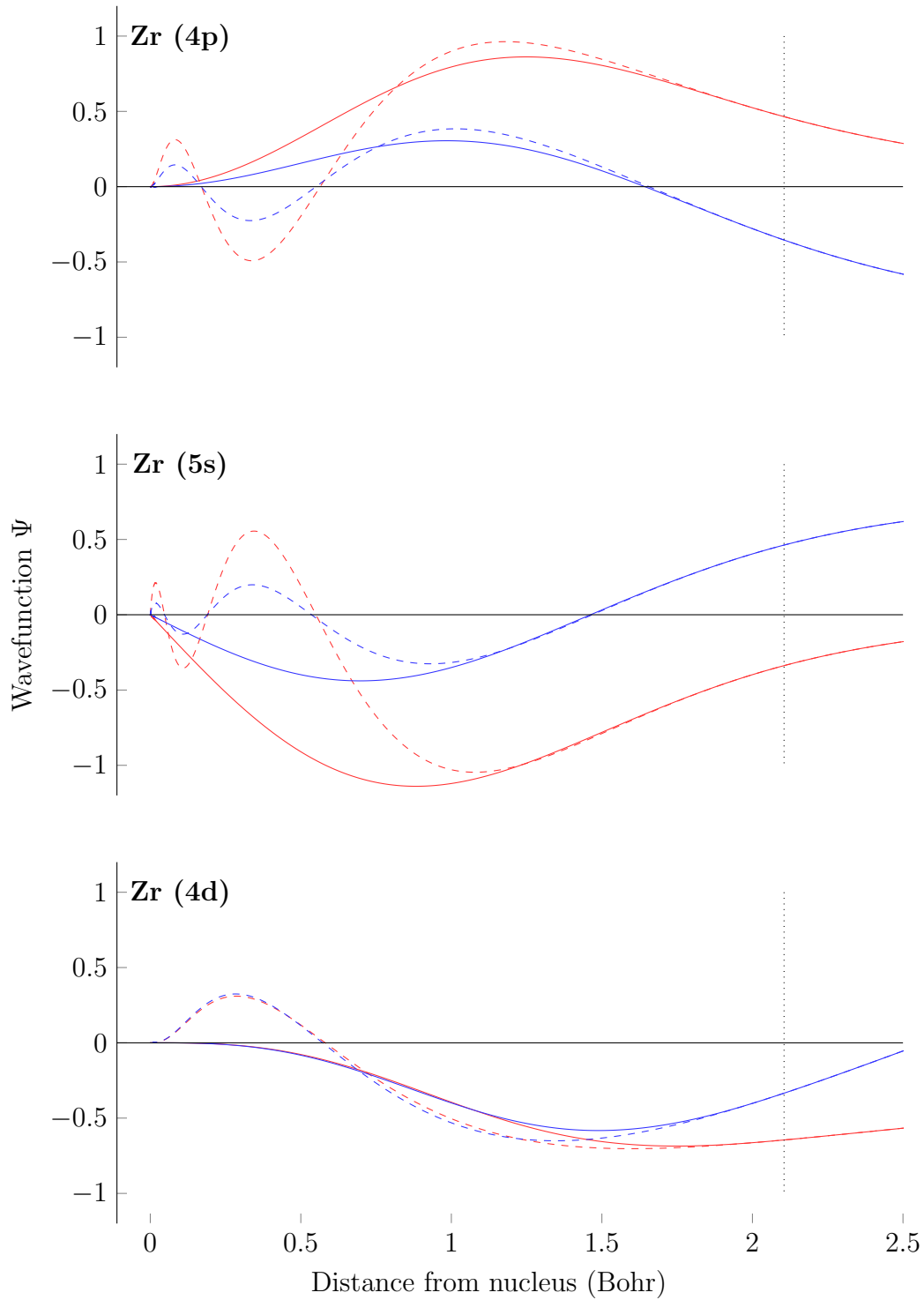


Figure 4.3: Plots of the valence  $s$ ,  $p$  and  $d$  orbital potentials for zirconium with two projectors per angular momentum. Dashed lines indicate the all-electron potentials while solid lines indicate the corresponding pseudopotential. Dotted vertical line marks the radius beyond which the potentials match.

## 4.2 Periodic boundaries

### 4.2.1 Bloch's theorem

The repeating nature of a crystal structure, defined by the lattice vectors plus a basis set of atoms that are repeated, is well-suited for computer models. It allows us to define periodicity in three dimensions for a given unit cell. An example of this periodicity is illustrated in Figure 4.4 in two dimensions. A model based on this periodicity is justified as follows:

- Nuclei are arranged in a periodically repeating pattern, thus their potentials acting on electrons are also periodic.
- If the potential is periodic, it follows that the electron density is also periodic.
- The electron density is equivalent to the square of the wave function magnitude, thus the magnitude of the wave function is also periodic.

Knowing that the magnitude of the wave function is periodic greatly simplifies the calculation process; only one ‘period’ of the function needs to be evaluated. However, the phase of the wave function can take any of an infinite number of values and still satisfy the periodicity condition.

At this point, we consider Bloch's theorem which states that the possible wave functions are all quasi-periodic, and thus the wave function can be expressed as:

$$\psi_k(\mathbf{r}) = e^{i\mathbf{k}\cdot\mathbf{r}} u_k(\mathbf{r}) \quad (4.8)$$

Where  $\psi_k(\mathbf{r})$  is the wave function evaluated at position  $\mathbf{r}$ ,  $e^{i\mathbf{k}\cdot\mathbf{r}}$  is an arbitrary phase factor,

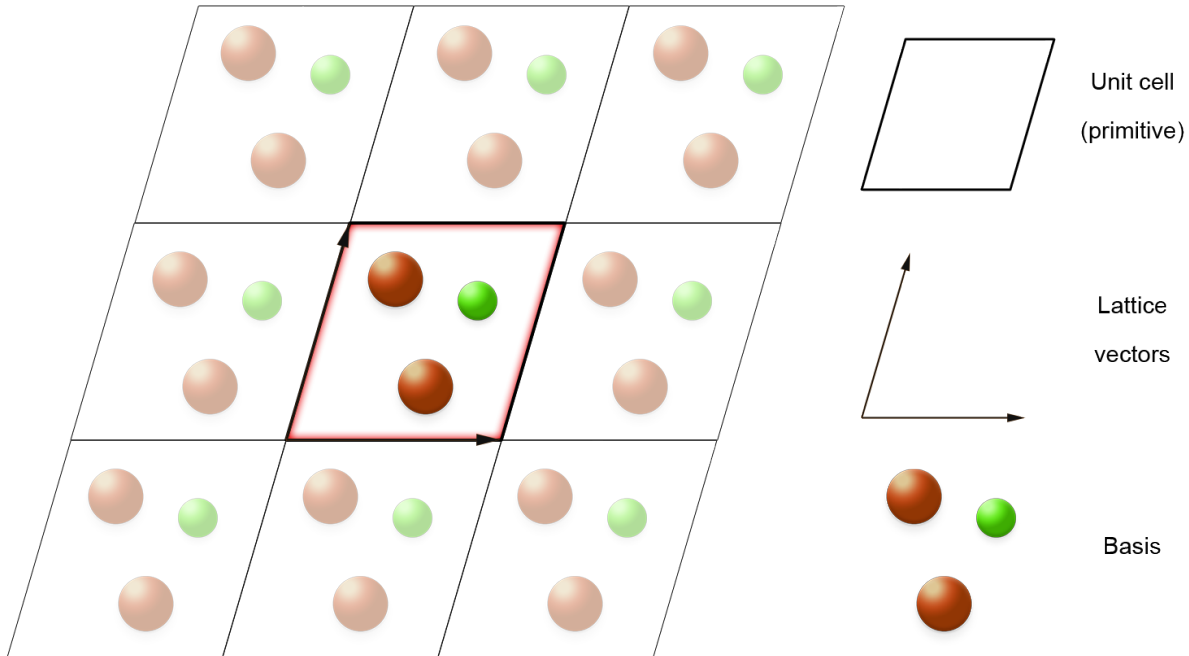


Figure 4.4: Two dimensional illustration of periodic boundary around a primitive cell.

and  $u_k(\mathbf{r})$  is a periodic function with the same periodicity as the wave function. Solutions to this equation exist for any value of  $\mathbf{k}$  and so the general solution can be expressed as an integral over the first Brillouin zone, the primitive lattice cell in reciprocal space. Instead of evaluating the integral over the range of  $\mathbf{k}$  (a computationally costly task as it is done for many wave functions), a sum of values at discrete points, known as  $\mathbf{k}$ -points, is used. This approximation is valid because the wave function varies slowly over  $\mathbf{k}$ , thus allowing the integral to be approximated with several appropriately spaced  $\mathbf{k}$ -points. In general, a finer  $\mathbf{k}$ -point grid results in increased accuracy, but at an increased computational cost [176]. For all DFT calculations in this thesis, a Monkhorst-Pack sampling scheme [177] was used for Brillouin zone integration, with a minimum  $\mathbf{k}$ -point separation of  $0.09 \text{ \AA}^{-1}$ .

### 4.2.2 Plane-waves

The electron density of a system is described in the context of a basis set. A basis set is a collection of functions (known as basis functions) which can be combined to produce some relevant output, typically the mathematical description for the shape of an electron orbital. For example, any sound wave can be generated from a combination of sine functions (basis functions).

The purpose of a basis set in DFT calculations is to describe the varying amplitude of the electron density in space. Any complete basis set (e.g. plane-wave, correlation-consistent, split-valence) may be used to represent the behaviour of electron orbitals, but a plane-wave method was chosen due to its greater suitability for periodic systems (plane-waves are intrinsically periodic). Since the electron densities are represented by a finite sum of plane-waves with different energies, a truncation error will be incurred. Plane-waves of higher energies provide a smaller contribution to the overall density, so only plane-wave up to a chosen cut-off energy value are considered in order to reduce computational requirements. An appropriate plane-wave cut-off energy must therefore be determined through a convergence test.

## 4.3 Computational details

### 4.3.1 Cell dimensions and initialisation

A supercell method is used for the study of various defects. The first step is to create a unit cell of  $\text{ZrO}_2$  in each of the three crystal structures. Each unit cell is then fully relaxed through

a geometry optimisation process (see § 4.3.2). The resulting cell is used to construct supercells through tessellation in three dimensions, before being fully relaxed again. In this way, we generate systems with up to ten times as many atoms as the unit cell (supercell details can be found in Table 4.1). This is necessary because introducing defects into a small unit cell will result in the defect interacting with itself across the periodic boundary. A supercell increases the distance between the defect and its periodic image, using the bulk material as an interaction buffer.

When constructing a supercell, it is important to consider making the supercell equally large in all directions, such that any directional bias in defect-defect interaction is minimised. Larger supercells carry an increased computational cost when running calculations, limiting the sizes we can achieve. For example, a constant-volume defect calculation with 300 atom supercells will take upwards of 500 hours to complete (on the Imperial College HPC using four 32-core nodes), whereas the equivalent 100 atom supercell will take just 72 hours (fully relaxed calculations are even more computationally expensive).

Table 4.1: Composition of the supercells in terms of the number of individual unit cells stacked in each direction.

<b>Crystal Structure</b>	<b>No. unit cells</b>			<b>Supercell size (Å)</b>			<b>No. atoms</b>
	<b>a</b>	<b>b</b>	<b>c</b>	<b>a</b>	<b>b</b>	<b>c</b>	
Monoclinic <i>(P2<sub>1</sub>/c)</i>	2	2	2	10.37	10.47	10.75	96
Tetragonal <i>(P4<sub>2</sub>/nmc)</i>	3	3	2	10.85	10.85	10.56	108
Cubic <i>(Fm̄3m)</i>	2	2	2	10.22	10.22	10.22	96

### 4.3.2 Geometry optimisation

The geometry optimisation task in CASTEP follows a simple steepest-descent algorithm which attempts to satisfy certain convergence criteria, depending on the constraints applied to the system. This is an iterative process which takes an initial system state, modifies ion positions slightly and then calculates the difference in properties between the states to check for convergence.

The variational principle in quantum mechanics tells us that the lowest system energy calculated is always an upper bound for the ground state energy, thus providing a way to check if modifications to the system are actually optimising the geometry. The exception is when the system converges upon a local minimum, which may not be an experimentally observed state. This can be avoided to some extent by having good initial ion placement from which to optimise.

### 4.3.3 Convergence criteria for geometry optimisation

Four convergence criteria are used for the geometry optimisation tasks throughout this work, one of which is only used when performing constant-pressure calculations, such as when a supercell is being fully relaxed. These criteria are evaluated with respect to the previous iteration during the geometry optimisation task:

- *Change in energy per ion:* The largest change in the energy per ion between iterations must be below  $10^{-5}$  eV. Below this value, the total energy improvement towards the ground state for a 100 atom supercell is less than 0.001 eV, and is therefore considered

converged.

- *Maximum force on an ion:* The maximum force requirement on any single ion in an iteration must be below  $10^{-2}$  eV/Å. This is required to make sure that the ion position will not change significantly in the following iteration, possibly bringing another convergence criterion above its threshold.
- *Maximum change in ion position:* This must be below  $5 \times 10^{-4}$  Å between iterations to be considered converged. This criterion specifies the maximum ‘rattle’ of the ion that is tolerated once the minimum energy is reached (i.e. displacements above this value may still be important for achieving a correct atomic configuration).
- *Maximum stress (constant-pressure only):* During unconstrained relaxation, the maximum change in stress between iterations should be below 50 MPa. This is necessary to avoid large deviations which may distort the symmetry of the supercell, resulting in anomalous energy values.

Using these convergence criteria, non-defective supercells of ZrO<sub>2</sub> were relaxed under constant pressure. The resulting structure was used as the starting point to which defects were introduced, and subsequently relaxed again, this time under constant volume conditions to simulate low defect concentrations [178, 179]. Finally, all DFT calculations on doped and defective structures in this thesis employed the Pulay method for density mixing [180] to take into consideration changes in electronic behaviour of the system caused by the defect and to speed up convergence.

#### 4.3.4 Charged cell correction

When calculating the energy of a defect with an overall non-zero charge, this charge introduces a systematic error in the energy value which is a function of the charge magnitude. This is typically the case in high band-gap materials such as ZrO<sub>2</sub> where electron mobility is far lower than in metals or semiconductors, allowing defects such as V<sub>O</sub><sup>••</sup> and V<sub>Zr</sub><sup>'''</sup> to be thermodynamically stable in the lattice.

The source of the error from charged defects is self-interaction across the periodic boundary, made necessary by the finite cell size. A common solution is to append a Makov-Payne correction term when calculating formation energies of defects [181, 182]. This works well in many cases, but does not take into consideration the anisotropy in the material's dielectric properties, as is the case in tetragonal ZrO<sub>2</sub> due to the non-unity lattice  $c/a$  ratio. These effects are better captured when using a screened Madelung correction [183]. This method provides a more complete description of the dielectric properties by utilising a dielectric tensor rather than a single value of the dielectric constant (or relative permittivity). Dielectric tensors for the different phases of ZrO<sub>2</sub> were taken from the literature [138, 184]. The screened Madelung correction is therefore used in preference to a Makov-Payne correction throughout this thesis.

#### 4.3.5 Helmholtz free energy

In order to examine the relationship between temperature and energy for the different ZrO<sub>2</sub> phases, phonon calculations were performed in CASTEP using a method outlined by Burr *et al.* [185, 186]. This entails using the harmonic approximation to determine the shape of the potential well that an atom sits in. The potential well is approximated by a spherically symmetric

harmonic well, centred at an atom's equilibrium position in the lattice. At a temperature of 0 K, an atom will occupy the lowest region of its potential well, known as the ground state (though they will still have energy, known as zero-point energy). As temperature increases, the atom will sometimes occupy higher energy states in the potential well due to increased thermal vibrations, moving from its equilibrium position. The total energy ( $A(T, V)$ ) of this system, known as the Helmholtz free energy, is calculated using the internal energy ( $U(V)$ ), vibrational enthalpy ( $H_v(T, V)$ ), vibrational entropy ( $S_v(T, V)$ ) and configurational entropy ( $S_{conf}$ ):

$$A(T, V) = U(V) + H_v(T, V) - TS_v(T, V) - TS_{conf} \quad (4.9)$$

where  $T$  is temperature and  $V$  is volume. The configurational entropy is calculated using Boltzmann statistics:

$$S_{conf} = k_B \ln(\Omega) \quad (4.10)$$

where  $k_B$  is the Boltzmann constant and  $\Omega$  denotes the number of possible configurations (i.e. valid permutations of energy level occupancy). The vibrational terms in Equation 4.9 are obtained by performing a constant-volume phonon calculation in CASTEP and then integrating over the resulting phonon density of states (DOS). This is done over a range of temperatures for each crystal structure of  $\text{ZrO}_2$ .

### 4.3.6 Incorporation energies

The inner oxide of the fuel cladding will be highly defective due to radiation damage, resulting in a high concentration of pre-existing intrinsic defect sites relative to the concentration of

fission products. We therefore consider the energy of fission product incorporation on to these existing defect sites. The energies to incorporate atoms at interstitial and substitutional sites in  $ZrO_2$  were calculated from the set of defective and perfect supercell DFT energies. For iodine, incorporation energies were established to place atoms into vacancy sites of different charge to generate defects from  $I_O^\times$  to  $I_O^{\bullet\bullet}$ , and  $I_{Zr}^\times$  to  $I_{Zr}^{\bullet\bullet\bullet}$ . I was also incorporated onto the interstitial sites.

The incorporation energy equation for iodine uses  $\frac{1}{2}I_2$  as the reference state of iodine, while Te, Xe and Cs use the DFT energy calculated as a single atom in a large cell:

$$E_{inc}(I_i^\times) = E_{DFT}(I_i^\times) - (E_{DFT}(ZrO_2) + \frac{1}{2}\mu_{I_2}) \quad (4.11)$$

where  $E_{inc}(I_i^\times)$  is the incorporation energy of a neutral iodine interstitial,  $E_{DFT}(I_i^\times)$  is the energy of a neutral iodine interstitial,  $E_{DFT}(ZrO_2)$  is the energy of a non-defective  $ZrO_2$  supercell and  $\mu_{I_2}$  is the chemical potential of an  $I_2$  molecule, taken from a single point DFT calculation of the  $I_2$  dimer. For incorporation of a charged interstitial (e.g.  $I_i^\bullet$ ), the energy required to add or remove an electron is included in the calculation:

$$E_{inc}(I_i^n) = E_{DFT}(I_i^n) - (E_{DFT}(ZrO_2) + \frac{1}{2}\mu_{I_2} + n(E_{VBM} + \mu_e)) \quad (4.12)$$

Similarly, for a substitutional defect:

$$E_{inc}(I_O^n) = E_{DFT}(I_O^n) - (E_{DFT}(V_O^n) + \frac{1}{2}\mu_{I_2}) \quad (4.13)$$

where  $I_O^n$  is an iodine substitutional defect at an oxygen site of charge  $n$  and  $V_O^n$  is the corresponding oxygen vacancy.

### 4.3.7 Stiffness matrix generation

The elastic stiffness matrices for the pure monoclinic, tetragonal and cubic phases of ZrO<sub>2</sub> were calculated using CASTEP's *elastic constants* task. The calculation of elastic constants is a multi-step process involving up to 36 individual DFT calculations. Several scripts have been made available to simplify this process (see Appendix B).

The first step is to generate multiple different .cell files, each with either a small deviation in the lattice parameter or an additional shear on the cell. This requires starting with a unit cell that has already been completely relaxed via the *geometry optimisation* task. In total, 36 .cell files are generated, each corresponding to a single element of the eventual stiffness matrix. The next step is to run a single point DFT calculation on each .cell file with the *calculate stress* parameter enabled to output the resulting stress matrix. The final step is to use Hooke's Law to calculate the elastic stiffness constants using the known stress and strain state.

### 4.3.8 Defect relaxation volumes

Defect relaxation volumes of point defects were calculated using an isobaric method, requiring two calculations to be performed under constant-pressure using the geometry optimisation task in CASTEP. The defect relaxation volume ( $\Delta V$ ) is defined as:

$$\Delta V = V_{def} - V_{perf} \quad (4.14)$$

where  $V_{def}$  is the relaxation volume of the defective supercell and  $V_{perf}$  is the relaxation volume of the non-defective (perfect) supercell. In this thesis, mentions of ‘volume’ will refer to relaxation volumes unless stated otherwise.

After completing an energy calculation, CASTEP provides the volume of the resulting cell, defined as the space enclosed by the repeating unit of atoms within the calculated lattice parameters. By subtracting the volume of a non-defective cell from the volume of a defective cell, we obtain a value for the total defect volume.

It is important to consider that if there is a non-zero charge on the system, this will affect the calculated volume. Two systems with the same type, amount and arrangement of atoms, but different overall charges, will have different energies (due to the number of electrons). Different electronic orbital occupancies will affect the inter-atomic forces and therefore the shape of the cell. In order to compensate for this effect, a ‘corrected’ relaxation volume, as described by Goyal *et al.* [187] is calculated when the defect has a non-zero charge:

$$\Delta V = V_{def}^q - V_{perf}^q \quad (4.15)$$

where  $q$  is the defect charge. This formulation uses the volume of a non-defective supercell with equal charge magnitude as the reference structure. This method has been shown to yield more reasonable defect volumes than when using neutral non-defective supercells as the reference structure. Defect volumes without this correction applied are provided in Appendix C for comparison.

## 4.4 Defect energies and equilibria

### 4.4.1 Defect formation energies

Defect formation energies are calculated using equation 4.16:

$$E_f = E_{def} - (E_{perf} \pm \sum_i n_i \mu_i + q(E_{VBM} + \mu_e)) + E_{corr} \quad (4.16)$$

where  $E_f$  is the formation energy,  $E_{def}$  is the energy of the defective supercell,  $E_{perf}$  is the energy of a non-defective supercell,  $q$  is the defect charge,  $E_{VBM}$  is the valence band maximum,  $\mu_e$  is the Fermi level relative to the VBM and  $E_{corr}$  is a charged-cell correction term (see § 4.3.4). Since  $\mu_e$  is not a fixed value, plots of formation energy against  $\mu_e$  are produced to examine the behaviour of defects across the entire range of the band gap. These are reported in Figures 5.3, 5.4 and 5.5.

### 4.4.2 Defect equilibria

Typically in materials, several types of defects will exist simultaneously. These defects will be present at an equilibrium concentration based on their thermodynamic stability. Predicting the defect equilibria is possible with statistical mechanics and some approximations. For example, it is expected that a crystal lattice will usually be overall charge-neutral (exceptions can be made under certain conditions, see § 4.4.3), otherwise we would see a build-up of charge with a large Coulomb energy penalty which would be thermodynamically unsustainable.

Brouwer diagrams, also known as Kröger-Vink diagrams, were produced using a method out-

lined by Murphy *et al.* [178,188] through which it is possible to determine defect concentrations as a function of oxygen partial pressure. We start from the statement that the chemical potential of  $\text{ZrO}_2$  is equivalent to the sum of chemical potentials  $\mu$  of its constituent species, Zr and O:

$$\mu_{\text{ZrO}_2(s)} = \mu_{\text{Zr}}(p_{\text{O}_2}, T) + \mu_{\text{O}_2}(p_{\text{O}_2}, T) \quad (4.17)$$

where  $T$  denotes temperature and  $p_{\text{O}_2}$  denotes oxygen partial pressure. The chemical potential of  $\text{ZrO}_2$  in the solid state is assumed to have negligible dependence on  $T$  and  $p_{\text{O}_2}$  relative to  $\mu_{\text{Zr}}$  and  $\mu_{\text{O}_2}$ . Energies can be obtained for bulk  $\text{ZrO}_2$  and Zr, but the ground state of oxygen is not correctly reproduced in DFT [189,190]. Instead, we use the approach of Finnis *et al.* [191] to infer the oxygen chemical potential from standard state values. We can use the experimental Gibbs free energy to produce an equation where  $\mu_{\text{O}_2}$  is the only unknown:

$$\Delta G_{f,\text{ZrO}_2}^{\ominus} = \mu_{\text{ZrO}_2(s)} - (\mu_{\text{Zr}(s)} + \mu_{\text{O}_2}^{\ominus}) \quad (4.18)$$

where  $\Delta G_{f,\text{ZrO}_2}^{\ominus}$  is the experimental Gibbs energy at standard temperature and pressure and  $\mu_{\text{O}_2}^{\ominus}$  is the oxygen chemical potential under the same conditions. Only monoclinic  $\text{ZrO}_2$  is stable under standard conditions, with  $\Delta G_{f,\text{ZrO}_2}^{\ominus} = -1042.746 \text{ kJ/mol}$  (10.807 eV) [192]. Values of the Gibbs free energy of formation for the tetragonal (10.697 eV) and cubic (10.595 eV) phases were obtained by adding the energy difference between the phases from DFT calculations. The values of  $\mu_{\text{ZrO}_2(s)}$  and  $\mu_{\text{Zr}(s)}$  are calculated using DFT. Once  $\mu_{\text{O}_2}^{\ominus}$  is calculated, we can generalise the chemical potential of oxygen for any value of  $T$  and  $p_{\text{O}_2}$  by appending an ideal gas relationship

$\Delta\mu(T)$  and a Boltzmann distribution:

$$\mu_{O_2}(p_{O_2}, T) = \mu_{O_2}^\ominus + \Delta\mu(T) + \frac{1}{2}k_B \log\left(\frac{p_{O_2}}{p_{O_2}^\ominus}\right) \quad (4.19)$$

$$\Delta\mu(T) = -\frac{1}{2}(S_{O_2}^\ominus - C_p^\ominus)(T - T^\ominus) + C_p^\ominus T \log\left(\frac{T}{T^\ominus}\right) \quad (4.20)$$

where  $S_{O_2}^\ominus$  is the molecular entropy at standard temperature and pressure ( $T^\ominus = 273.15$  K,  $P^\ominus = 10^5$  Pa), and  $C_p^\ominus$  is the constant pressure heat capacity of oxygen. These quantities have values of  $S_{O_2}^\ominus = 0.0021$  eV/K and  $C_p^\ominus = 0.000302$  eV/K [193].

Using our generalised formula for  $\mu_{O_2}$ , we fix the temperature within the range of thermal phase-stabilisation (e.g. 1500 K for tetragonal ZrO<sub>2</sub>) and calculate  $\mu_{O_2}$  for many different values of  $p_{O_2}$  between  $10^{-35}$  and  $10^0$  atm, corresponding to oxygen deficient and oxygen rich environments, respectively ( $p_{O_2}$  in air is approximately 0.2 atm). While the tetragonal phase will be stress-stabilised in practice, thermal-stabilisation in such models has been shown to qualitatively approximate the effect of stress-stabilisation, while allowing a wider range of dopant behaviours to be predicted [194].

Once a value of  $\mu_{O_2}$  is calculated, defect concentrations can then be calculated using Boltzmann statistics. These concentrations were calculated using the method outlined by Kasamatsu *et al.* [195] whereby the effect of defects competing for the same lattice site is taken into account. The next step is to calculate the concentration of electron and hole defects. This is done by using the charge-neutrality condition to determine the Fermi level (electrochemical potential) in the system:

$$\sum_i q_i c_i - N_c \exp\left(-\frac{E_g - \mu_e}{k_B T}\right) + N_v \exp\left(-\frac{\mu_e}{k_B T}\right) = 0 \quad (4.21)$$

Where  $c_i$  is the concentration of defect  $i$ ,  $q_i$  is its respective charge,  $N_c$  and  $N_v$  are the integrated density of states for the conduction and valence bands,  $E_g$  is the band gap and  $\mu_e$  is the Fermi level. Using this framework, Brouwer diagrams were constructed according to the algorithm outlined in Figure 4.5.

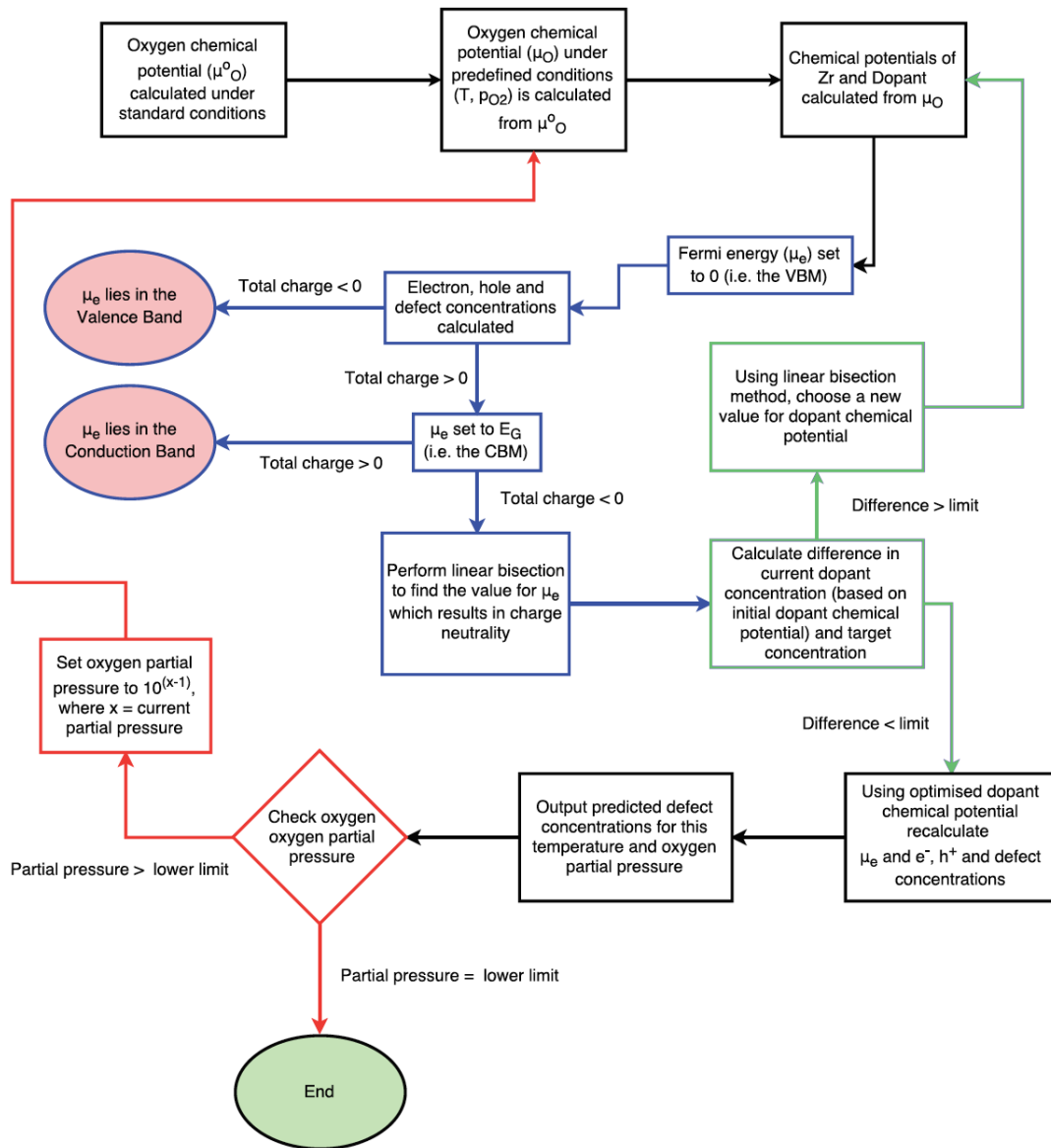


Figure 4.5: Flowchart for Brouwer diagram construction based on program provided in Appendix B. Red and green ovals represent unsuccessful and successful termination sequences, respectively. Blue borders highlight the Fermi energy calculation while green borders highlight the dopant chemical potential calculation. Red borders highlight the iterative procedure for different oxygen pressures. Adapted from [194].

## Temperature and pressure stabilisation

As discussed in Chapter 3, the tetragonal and cubic phases are stabilised at elevated temperatures and pressures. However, DFT calculations of supercells under stress require significantly greater computational resources to yield sufficiently converged energy results, and so all DFT calculations in this thesis are performed on relaxed supercells. To account for this lack of stress stabilisation, Brouwer diagrams are generated at higher temperatures (where the tetragonal and cubic phases are thermally stabilised) rather than at 650 K, which is the expected temperature at the internal surface of the cladding. This approach to compensating for stress stabilisation follows that of similar studies published by other groups [196–198].

### 4.4.3 Effect of space charge

Electrons have a higher rate of diffusion than oxygen vacancies in  $\text{ZrO}_2$ , leading to a build-up of oxygen vacancies near the metal-oxide interface as corrosion progresses [199]. In the case of  $\text{ZrO}_2$ , this effect will be pronounced because the layer is thin. This results in an overall positive charge (since the dominant oxygen vacancy is  $\text{V}_\text{O}^{\bullet\bullet}$ ) referred to as a space charge. This effect can be taken into account when generating Brouwer diagrams by assuming an overall charge in the crystal structure instead of charge-neutrality:

$$\sum_i q_i c_i - N_c \exp\left(-\frac{E_g - \mu_e}{k_B T}\right) + N_v \exp\left(-\frac{\mu_e}{k_B T}\right) = q_s c_s \quad (4.22)$$

where  $q_s$  is the charge of a unit of the artificial space charge defect and  $c_s$  is the concentration.

Figure 4.6 shows an example of the defect equilibria in tetragonal  $\text{ZrO}_2$  with an overall positive

space charge. In order for such a condition to be satisfied, higher concentrations of positively charged oxygen vacancy and hole defects are predicted to be present, while zirconium vacancy defects fall significantly. When extrinsic defects are also present in the lattice in significant concentrations, the space charge condition may influence which defect types are dominant at different oxygen pressures, as different oxidation states may be necessary to satisfy the charge condition.

## 4.5 Convergence testing

### 4.5.1 Plane-wave cut-off energy

In order to determine an appropriate value for the plane-wave cut-off energy, a convergence test was performed to determine the relative error in predicted energy compared to a highly converged value. This convergence test was conducted by running multiple geometry optimisation procedures under fully relaxed conditions on a unit cell of  $\text{ZrO}_2$  for each phase. A small  $\mathbf{k}$ -point spacing of  $0.01 \text{ \AA}^{-1}$  was used for each task (highly converged), while increasing the plane-wave cut-off energy from 300 eV to 750 eV in 50 eV increments. The energy of each run was recorded and compared to the energy of a highly converged value  $E_{conv}$ , taken when a cut-off energy of 900 eV was used. This provides a value for the truncation error at different cut-off energies.

Figure 4.7 shows a log plot of the energy error for each phase of  $\text{ZrO}_2$  as the cut-off energy is increased.

The relative error is shown to be independent of phase, with all lines lying on a single path. This might be expected because the atoms in each phase are the same, and therefore the electrons

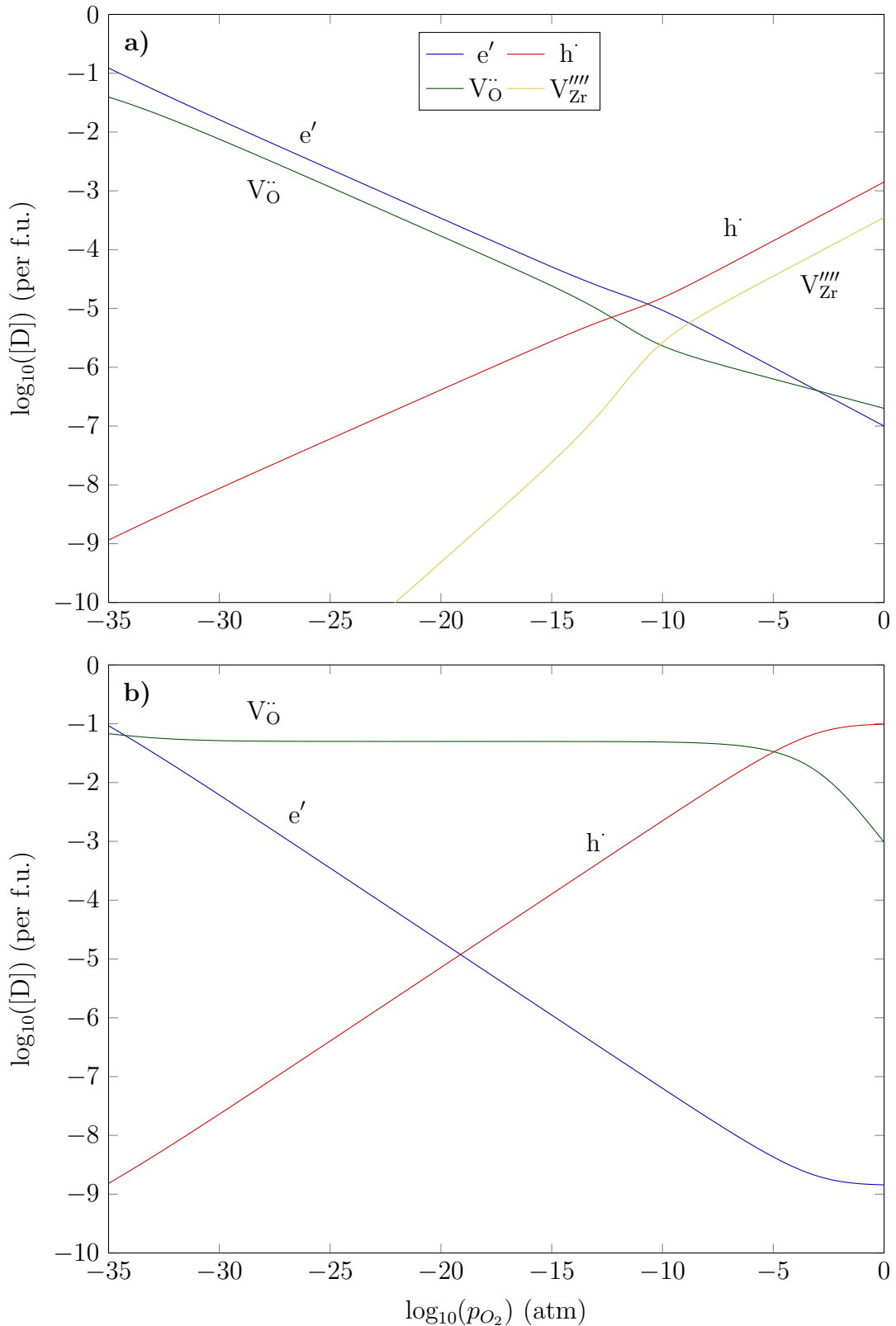


Figure 4.6: Tetragonal phase Brouwer diagrams of intrinsic point defects at a temperature of 1500 K **a)** without a space charge and **b)** with a space charge of  $10^{-1} \text{ e}^{-1}/\text{fu}$ .

involved in the calculations remain unchanged, however, interatomic distances are different in the different phases and thus so are the electron densities, so this equivalence in convergence does not necessarily have to follow. A cut-off energy of 600 eV was found to produce a relative error below 0.01 eV, and was subsequently used for future calculations as it provides a good compromise between computational cost and accuracy.

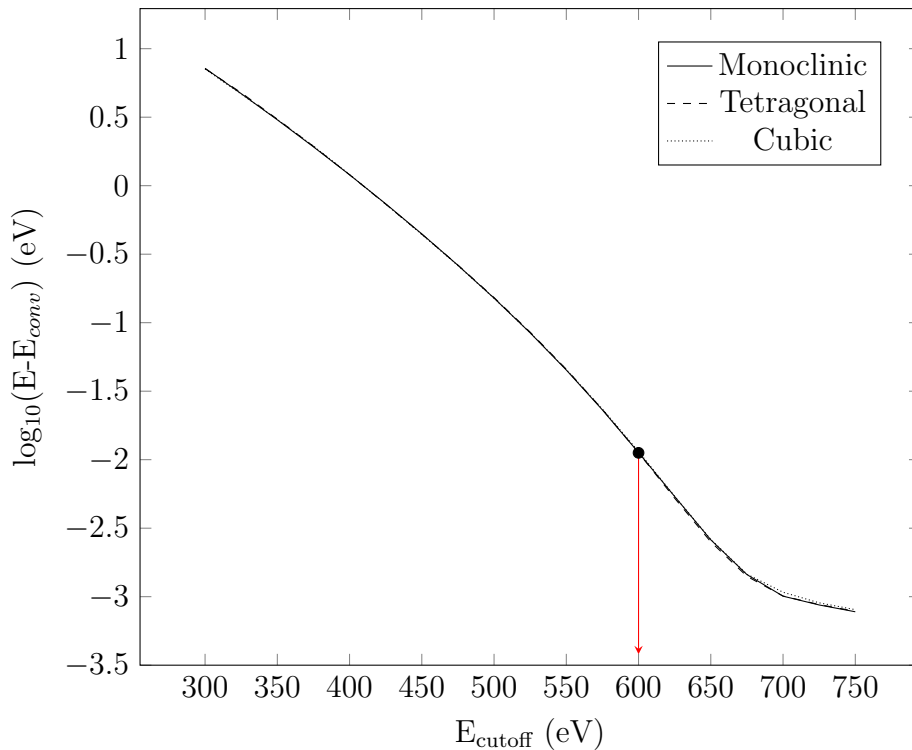


Figure 4.7: Log of the energy difference with respect to a highly converged calculation against plane-wave cut-off energy. The red arrow indicates the cut-off energy beyond which the error is below 0.01 eV.

#### 4.5.2 k-point convergence

Too fine a grid in reciprocal space (i.e. a large number of **k**-points) results in prohibitively computationally expensive simulations, whereas too coarse a grid may have a large truncation error when energies are calculated. To find the optimum spacing of **k**-points, a convergence study was performed across a range of **k**-point spacings, with the output energies compared to

a highly converged calculation, again yielding a value for  $E - E_{conv}$  but this time as a function of  $\mathbf{k}$ -point spacing.

Figure 4.8 shows the relative error for each phase of  $\text{ZrO}_2$  as a function of the  $\mathbf{k}$ -point spacing (given in reciprocal space as  $\text{\AA}^{-1}$ ). The highly converged energy value  $E_{conv}$  was calculated with a  $\mathbf{k}$ -point spacing of  $0.01 \text{\AA}^{-1}$  for error calculations. The plot shows a stepwise change in the error value as the grid spacing is reduced. This is because calculations demand an integer number of  $\mathbf{k}$ -points, and larger spacings do not provide sufficient resolution to effectively fit an integer number of  $\mathbf{k}$ -points into the reciprocal grid, so that the program snaps to the nearest appropriate grid number. An optimum  $\mathbf{k}$ -point spacing was chosen at  $0.09 \text{\AA}^{-1}$ , which was the largest spacing that kept the error below 0.01 eV for all phases, highlighted in the plot by the red arrow.

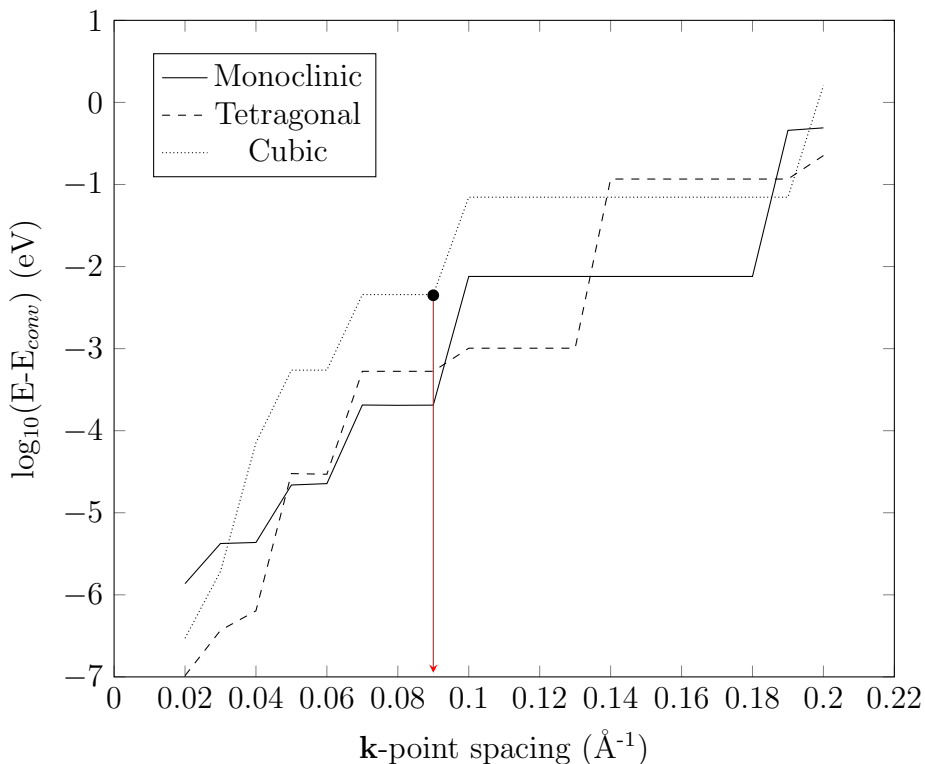


Figure 4.8: Log of the energy difference with respect to a highly converged calculation against  $\mathbf{k}$ -point spacing. The red arrow indicates the  $\mathbf{k}$ -point spacing which yields an error below 0.01 eV for all structures.

### 4.5.3 Exchange-correlation functionals

There are a range of possible exchange-correlation functionals available in CASTEP, spanning both empirical and non-empirical types. Empirical exchange-correlation functionals are typically optimised to capture specific properties or systems particularly well, but perform less well for generalised systems. Non-empirical exchange-correlation functionals, while still not perfect, are preferred for modelling the widest range of properties. In a sense, non-empirical functions benefit from not being ‘over-fit’ to experimental data. They are also more prevalent in the literature, thereby providing a rich corpus of work for comparison studies.

While the PBE-GGA exchange-correlation functional in this work had already been selected, it was helpful to conduct an energy convergence study of the systems across the different functionals available in CASTEP in order to determine how other functionals compared. Only 6 of the 14 functionals available in CASTEP were able to yield a converged energy calculation within a reasonable amount of time, as shown in Figure 4.9. This is because several hybrid functionals partially incorporate the exact exchange using the Hartree-Fock method [200], significantly increasing the computational cost of an energy calculation.

The calculated energies indicate that each functional correctly predicts the order of phase stability in  $\text{ZrO}_2$ , though the magnitude of the energy difference between phases varied. These differences are small, approximately 0.1 eV/fu, but their effects are compounded when defects are introduced into the cell. The total energies were more varied, with several eV differences between functionals, however, lower total energies across different exchange-correlation functionals do not necessarily suggest that a better minima has been found. For example, the PW91 functional resulted in even lower energies than PBE, despite PW91 preceding PBE and both

having been developed by Perdew *et al.* [201, 202]. It is the energy difference between systems calculated with the same exchange-correlation functional which is important.

To better gauge the performance of each functional, further studies across a much larger range of parameters, and even materials, would need to be conducted, however this is beyond the scope of this thesis.

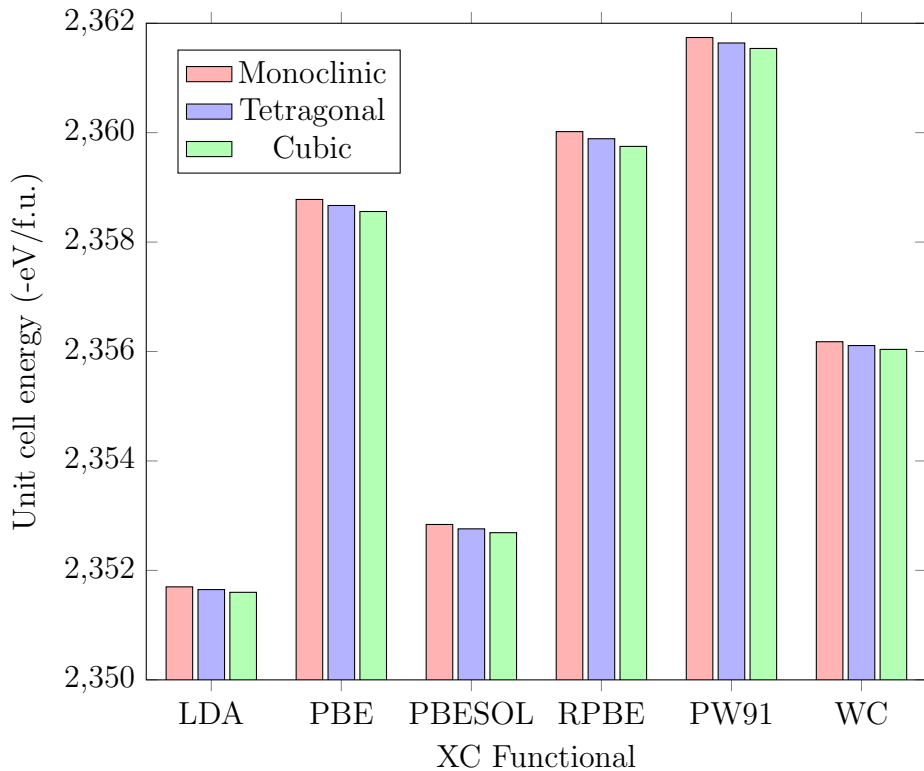


Figure 4.9: Calculated energy of a unit cell of monoclinic, tetragonal and cubic ZrO<sub>2</sub> when using different exchange-correlation functionals.

#### 4.5.4 On-the-fly pseudopotentials

Ultra soft pseudopotentials are generated in CASTEP automatically (known as on-the-fly or OTF pseudopotentials) when none are specified for a particular element. Energies must be calculated and compared with the same set of pseudopotentials in order to keep simulations self-consistent. A single point calculation was performed on a unit cell of ZrO<sub>2</sub> and the resulting

OTF pseudopotentials (one for oxygen and one for zirconium) were saved and used for all subsequent calculations.

It is important to determine the variance in energy values of different pseudopotentials generated OTF in order to avoid systematic error. To assess error, 9 different pairs of OTF pseudopotentials were generated<sup>1</sup> and used to calculate the total energy of a monoclinic ZrO<sub>2</sub> supercell. The difference in energy was then calculated with respect to the pseudopotential pair that resulted in the lowest energy. These deviations in total energy are shown in Figure 4.10. Across all calculations, the largest difference in total energy was 0.0012 eV, while the average difference was 0.0006 eV. Since here the only concern is with choosing other parameters to achieve a precision of 0.01 eV, and the largest deviation calculated is an order of magnitude below that, it is not necessary to take any special measures to correct any systematic error from randomly generated OTF pseudopotentials.

#### 4.5.5 Chemical potential of oxygen

The chemical potential of oxygen is required when performing any defect formation energy calculation where an atom of oxygen is added or removed (see Equation 4.16). Calculating the chemical potential of oxygen requires special consideration of the electronic structure of O<sub>2</sub>. The ground state of the O<sub>2</sub> molecule is known as triplet oxygen ( ${}^3\Sigma_g^-$ ), an allotrope which exhibits a resultant spin magnetic moment (oxygen is paramagnetic). This is in contrast to singlet oxygen ( ${}^1\Delta_g$ ) with a spin magnetic moment of zero.

Two calculations, one for triplet and another for singlet oxygen, were performed using CASTEP.

---

<sup>1</sup>OTF pseudopotential generation in CASTEP uses a random number seed which is generated whenever a calculation is run without specifying a pseudopotential. By default, these are ultra-soft pseudopotentials.

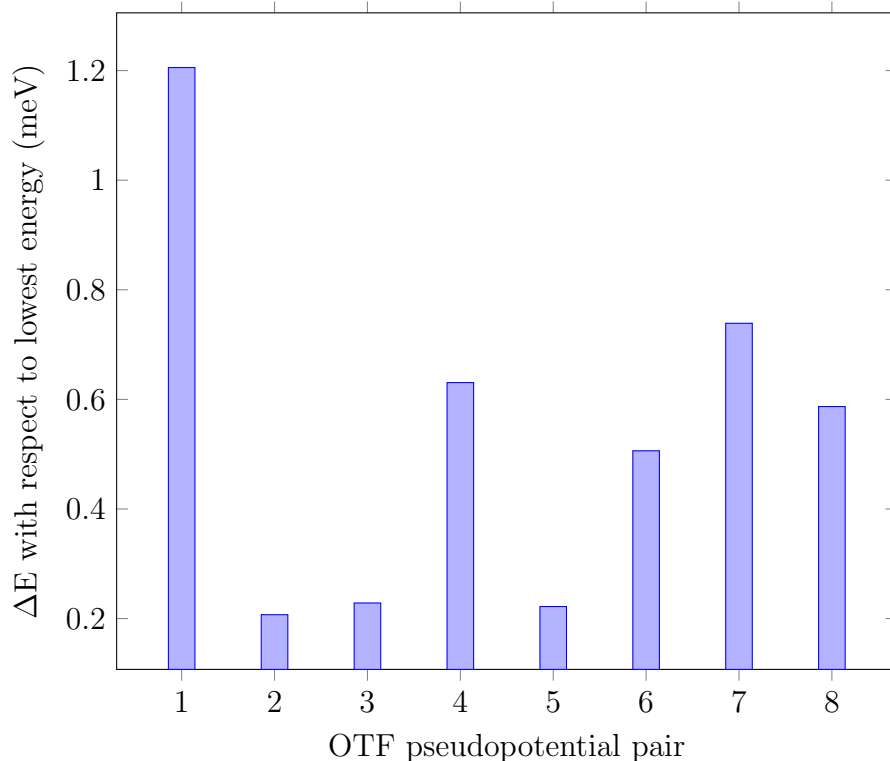


Figure 4.10: Energy deviation in meV of supercells with candidate OTF pseudopotential pairs. Energy deviations are shown with respect to the pseudopotential pair that resulted in the lowest total energy calculated.

Large cells of 15 Å x 15 Å x 15 Å were used to run geometry optimisation tasks on two oxygen atoms initially separated by 1.3 Å. For the triplet oxygen calculation, a net electronic spin of +2 on the  $p$  electrons was enforced, while the singlet oxygen calculation specified a net spin of 0.

The calculated bond lengths of triplet and singlet oxygen were 1.225 Å and 1.227 Å respectively. These bond lengths are within 2% of the experimental value of 1.207 [203], with the triplet state prediction being slightly closer to this value. The calculated energies from DFT for triplet and singlet oxygen were -871.92 eV and -870.70 eV respectively. This gave an energy difference of 1.22 eV between the two forms of diatomic oxygen. While triplet oxygen was correctly predicted as the lower energy allotrope, the energy difference reported in the literature from

microwave spectroscopy measurements is 0.9773 eV [204], an almost 25% difference compared to the DFT value. This large difference is attributed to the exchange-correlation functional and the inability to correctly model electron correlation effects in some cases. In this thesis, the DFT calculated energy of triplet oxygen was used only for formation energy against Fermi level plots, while defect equilibria calculations utilised a different method to calculate this value (see § 4.4.2).

#### 4.5.6 Chemical potential of iodine

To determine the chemical potential of iodine, an energy minimisation of the iodine dimer was performed. Unlike oxygen, iodine dimers do not exhibit a non-zero spin magnetic moment, thus avoiding a source of error in energy calculations with the PBE exchange-correlation functional. Similar to the  $\text{ZrO}_2$  unit cell calculations, the lattice parameter after relaxation (bond length in this case) is compared to experimental data to assess the quality of the simulation parameters.

Figure 4.11 illustrates the energy minimisation of two iodine atoms in a cell of size 15 Å x 15 Å x 15 Å, initially separated by 3.0 Å. The geometry optimisation task finds an energy minima when the iodine atoms are bonded, at a separation of 2.69 Å. This agrees well with the experimental value of 2.6745 Å [205].

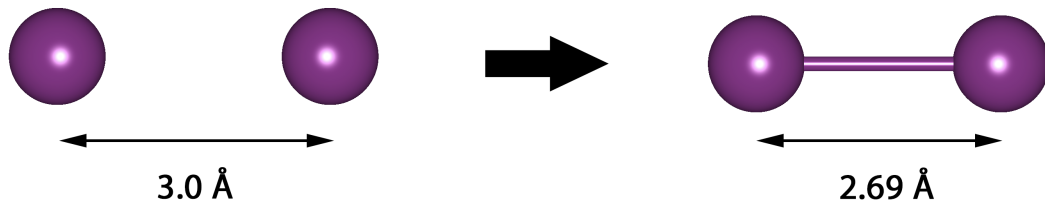


Figure 4.11: Energy minimisation of two iodine atoms from an initial separation of 3.0 Å.

#### 4.5.7 +U study

In some DFT studies, an additional potential energy term (Hubbard U parameter or +U) is sometimes included to better capture the Coulomb interaction of localised electrons. An LDA or GGA functional alone will typically not describe this interaction correctly, especially for localised *d* and *f* electrons<sup>1</sup>. Of particular concern is the calculated value of the band gap from DFT simulations, as this value may deviate by up to 30% from experimental values. Remedyng this shortcoming with an appropriate +U parameter could therefore be valuable in obtaining accurate energies.

In the literature, one GGA+U study of Fe-doped tetragonal ZrO<sub>2</sub> has shown that the inclusion of a +U term on Zr *d* orbital electrons between 0 and 3.3 eV changes the electronic properties (in particular the electronic density of states) of the system significantly, and that the best agreement with experimental data occurs when U = 0 eV [206]. Other GGA+U studies on bulk tetragonal ZrO<sub>2</sub> found that a +U term of 4 eV led to calculated lattice parameters which were in good agreement (within 0.05 Å) with experimental values, but that the calculated band gap was still underestimated by 1.28 eV [207–209]. One LDA+U study in ZrO<sub>2</sub> used a +U parameter of 1 Ry (13.6 eV), and reproduced the correct order of stability of the monoclinic, tetragonal and cubic phase. This shows how the value of the +U parameter can vary significantly depending on the other approximations being used in the DFT calculations, and therefore an appropriate +U value for this thesis would have to be found independently. A +U study of the zirconium atom, with an electronic configuration of [Kr]4*d*<sup>2</sup>5*s*<sup>2</sup>, was performed to determine the response to and therefore the viability of this additional potential term for the *d* electrons.

---

<sup>1</sup>Multiple occupation of *d* and *f* orbitals incurs an energy penalty which is not accurately modelled by the exchange-correlation functional.

Figure 4.12 shows the effect on the calculated band gap when introducing a +U term. While the +U term does increase the band gap, the effect is not significant in bringing the prediction in-line with experimental values. Even with +U terms of 10 eV, the calculated band gap falls short of the experimental band gap by at least 1.5 eV. Moreover, with +U terms greater than 4 eV, we begin to see erratic behaviour in the development of both the band gap, and also in the predicted crystal structure.

For the tetragonal phase, the calculated band gap (4.2 eV) does not agree with that calculated by Puigdollers *et al.* [207] (4.5 eV) when a +U term of 4 eV is used. The PBE GGA exchange-correlation functional and a plane-wave basis set was used in both studies, however, their study utilised the VASP 5.3 DFT software package while CASTEP 8.0 was used in this thesis. Different software packages may use different minimisation methods which could contribute to differing values, but determining the cause of this anomaly would require a separate study of the two codes at a low level which is beyond the scope of this thesis.

## Monoclinic

In monoclinic ZrO<sub>2</sub>, the use of a +U term causes the lattice parameters to change disproportionately to each other, as seen in Figure 4.13. All lattice parameters increased with larger +U terms, however, expansion in the *a* direction proceeded faster than in the *b* direction, resulting in the *a* lattice parameter becoming larger at a +U of 4 eV. +U terms larger than 10.5 eV caused the lattice parameters to snap suddenly onto new values. A investigation of the atomic positions revealed that the monoclinic crystal structure had collapsed into an orthorhombic structure (i.e. the cell experienced a shear strain which resulted in a  $\beta$  of 90°), with

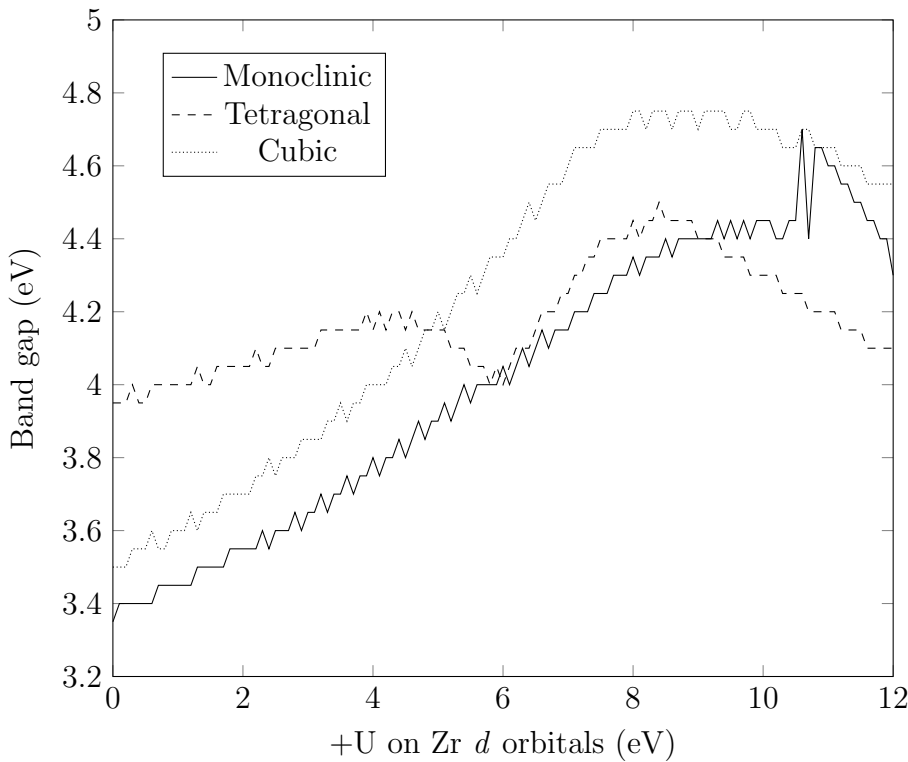


Figure 4.12: Calculated band gaps for different +U values in monoclinic, tetragonal and cubic  $\text{ZrO}_2$ .

the co-ordination number of zirconium ions falling to 6 from 7.

### Tetragonal

In tetragonal  $\text{ZrO}_2$ , increasing the +U term (Figure 4.14) has a strong anisotropic effect on the lattice parameters. Unusually, the  $c$  parameter falls (up to an +U energy of 6 eV) while the  $a$  parameter increases. Typically it would be expected that both parameters would increase, perhaps at different rates, because the +U term increases the total energy (by increasing the Coulombic contribution) in the system. This increase in energy leads to higher stresses and therefore larger interatomic spacings (cells are permitted to relax in these calculations).

Systems will always tend towards the lowest energy configuration. Therefore the reduction of the  $c$  parameter suggests that it is already in a high energy configuration in the  $c$  direction

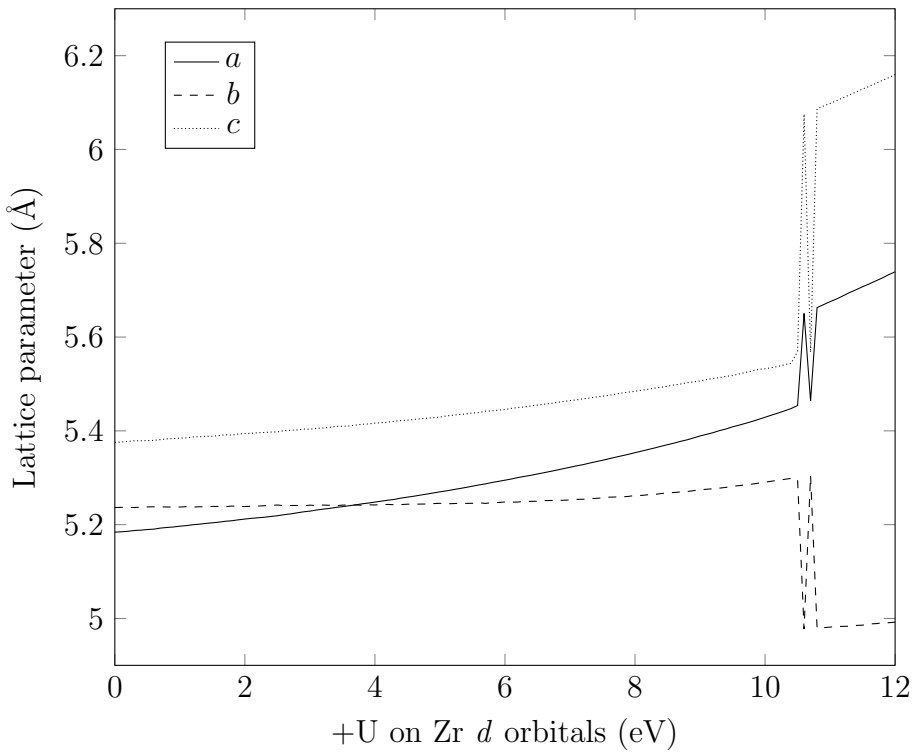


Figure 4.13: Individual lattice parameters as a function of +U term in monoclinic  $\text{ZrO}_2$ .

(overextended) and can reduce its energy by being compressed in that direction (i.e. becoming more cubic). This is consistent with the interpretation that lower temperature phases of  $\text{ZrO}_2$  are distortions of the cubic fluorite phase caused by a small cation radius.

Above a +U parameter of 6 eV however, the  $c$  parameter suddenly begins to increase. Upon further inspection of the resulting cell, it was found that it had transitioned completely to cubic fluorite from tetragonal. This can also be confirmed by observing that the relationship between the parameters becomes  $2a^2 = c^2$  (i.e. the  $c$  parameter is the same length as the unit cell's [110] diagonal, see Figure 3.5).

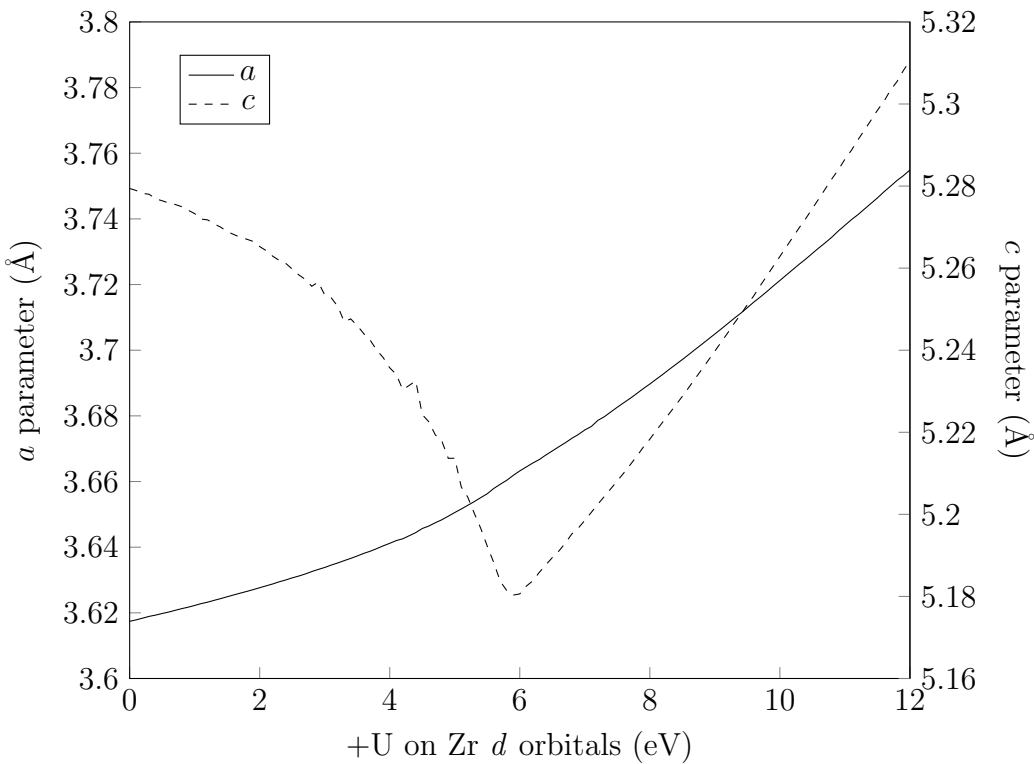


Figure 4.14: Individual lattice parameters as a function of +U term in tetragonal  $\text{ZrO}_2$ .

## Cubic

The effect of a +U term on a lattice parameter of cubic  $\text{ZrO}_2$  is shown in Figure 4.15. Notably, the symmetry of the cell remains intact even up to a +U term of 12 eV, unlike in the monoclinic and tetragonal phases. The lattice parameter also increases superlinearly as the +U term is increased. This is the typical response that is expected when a +U term is introduced.

There was however one instance of unexpected behaviour. Knowing that the tetragonal phase collapses to cubic at +U terms greater than 6 eV, we would expect both to exhibit the same band gap at this +U value. Looking at the band gap results from Figure 4.12, we see that the band gaps of tetragonal and cubic  $\text{ZrO}_2$  continue to be different above 6 eV, despite the crystal structures being the same in this region. One difference between the cells is that the cubic unit cell has 12 atoms while the tetragonal unit cell has 6 atoms. While this suggests a

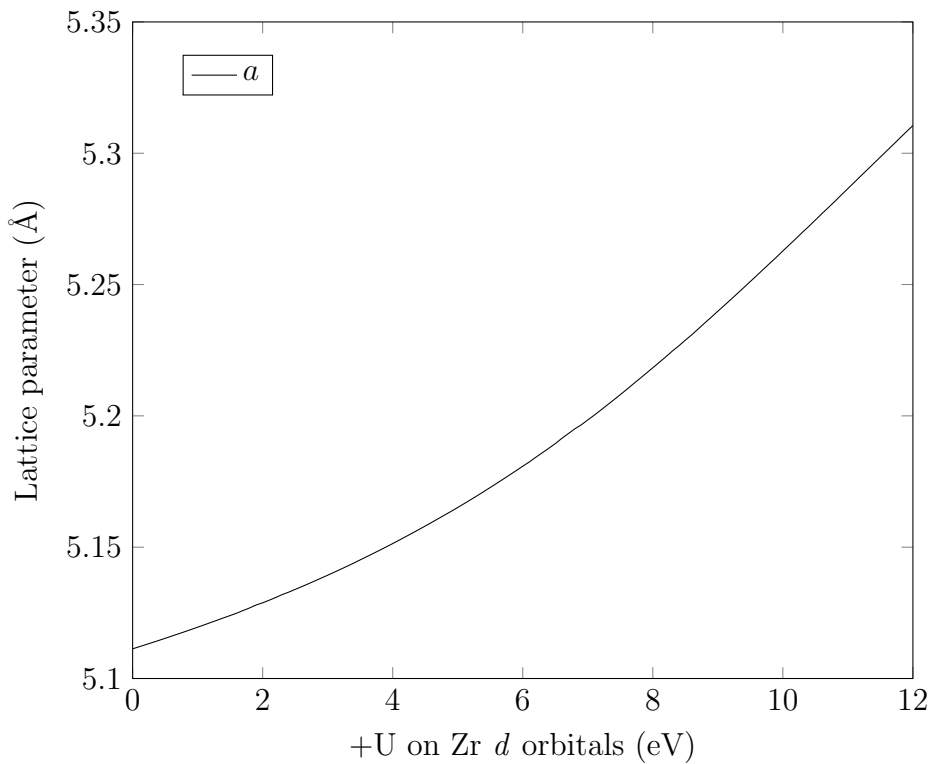


Figure 4.15: Lattice parameter as a function of +U term in cubic  $\text{ZrO}_2$ .

size effect, the band gap difference did not appear when comparing the band gaps of unit cells and supercells in the absence of a +U term.

After considering the impact of a +U term in DFT calculations, the decision was made not to include the term. While it would provide a small improvement in the calculated band gap for the cubic phase, the effect on cell symmetry of the other phases would present a confounding variable, especially when placing defects into the structure. It is therefore more useful to run calculations without a +U term to maintain consistency of results between different phases in this thesis.

# Chapter 5

## Structure properties and intrinsic defects

### 5.1 Introduction

It is important to fully understand the behaviour of intrinsic defects in  $\text{ZrO}_2$  before performing studies with dopant ions. In this chapter, intrinsic defects in monoclinic, tetragonal and cubic  $\text{ZrO}_2$  are compared and contrasted, including values for formation energy, defect volumes and defect equilibria. Elastic stiffness constants, electronic density of states, band gaps and free energies of the non-defective structures are also reported.

#### 5.1.1 Previous work

Previous works studying intrinsic defects in the  $\text{ZrO}_2$  system have utilised quantum mechanical methods to determine defect formation energies in the monoclinic phase [130–132] and defect

equilibria in the tetragonal phase [196]. The cubic phase is mainly studied as a dopant-stabilised system [126, 127], with few undoped defect studies in the literature [128, 129]. Building upon previous quantum mechanical studies, a comprehensive account of intrinsic defect energies, defect volumes, and defect equilibria for all three common crystal structures of ZrO<sub>2</sub> is provided, using state-of-the-art, accessible methods.

## 5.2 Methodology

### 5.2.1 Simulation parameters

As discussed in Chapter 4, DFT calculations were performed using CASTEP 8.0 [123]. Ultra-soft pseudo-potentials were used throughout, employing a 600 eV cut-off energy. The PBE [174] parameterisation of the GGA was used to describe the exchange correlation functional. A Monkhorst-Pack sampling scheme [177] was used for Brillouin zone integration, with a minimum  $k$ -point separation of 0.09 Å<sup>-1</sup>. The Pulay method for density mixing [180] was used to improve convergence of simulations.

The electrical energy convergence criterion was set to  $1 \times 10^{-6}$  eV. The maximum force between atoms was limited to  $1 \times 10^{-2}$  eV Å<sup>-1</sup>. A gradient-descent geometry optimisation task was run on the cell until consecutive iterations differed in energy and atomic displacement by less than  $1 \times 10^{-5}$  eV and  $5 \times 10^{-4}$  Å, respectively.

### 5.2.2 Helmholtz free energy

As discussed in § 4.3.5, a harmonic approximation was used to determine the temperature dependence of the free energies for the non-defective crystal structures of  $\text{ZrO}_2$ . A constant-volume phonon calculation was performed for each structure, from which the vibrational enthalpy  $H_v(T, V)$  and entropy  $S_v(T, V)$  contributions to the Helmholtz free energy were calculated up to a temperature of 2500 K in order to cover the temperature range of the three common  $\text{ZrO}_2$  phases. The complete Helmholtz free energy  $A(T, V)$  was then obtained by including the internal energy  $U(V)$  and configurational entropy  $S_{conf}$  of the system:

$$A(T, V) = U(V) + H_v(T, V) - TS_v(T, V) - TS_{conf} \quad (5.1)$$

The calculated free energy was then plotted against temperature to show the relative stability of each phase at different temperatures and the predicted transition points from one phase to another.

### 5.2.3 Brouwer diagrams

Using the method outlined in § 4.4.2, Brouwer diagrams of the intrinsic defect equilibria for monoclinic, tetragonal and cubic  $\text{ZrO}_2$  were generated. The monoclinic and tetragonal Brouwer diagrams were generated at temperatures of 650 K and 1500 K respectively, corresponding to temperatures at which these phases are thermally stabilised. Defect concentrations are reported in parts/fu (i.e. parts per formula unit  $\text{ZrO}_2$ ). The cubic Brouwer diagram was generated at 2000 K despite being thermally stabilised at temperatures greater than 2400 K. This was

because such high temperatures resulted in very large intrinsic defect concentrations such that defect behaviour could not be meaningfully examined (the system was completely defective). As discussed in § 5.4, issues with modelling cubic  $\text{ZrO}_2$  in DFT mean that calculated energy values may become unreliable, but are presented in this thesis for the purpose of completeness.

## 5.3 Non-defective $\text{ZrO}_2$

### 5.3.1 Unit cells

Having selected and optimised the parameters and functionals, unit cells of  $\text{ZrO}_2$  in each phase were fully relaxed at constant pressure and the resulting structures were compared in detail to experimental data. Table 5.1 shows the calculated lattice parameters and energy differences between the three  $\text{ZrO}_2$  phases.

Table 5.1: Calculated unit cell parameters for the different crystal structures of  $\text{ZrO}_2$ . Experimental data for monoclinic, tetragonal and cubic phases at 295 K are shown in parentheses [93]. Energy difference between structures is shown with respect to the cubic phase.

Phase	a (Å)	b (Å)	c (Å)	$\beta$ (°)	Volume (Å <sup>3</sup> /fu)	$\Delta E$ (eV/fu)
m- $\text{ZrO}_2$	5.18 (5.15)	5.24 (5.21)	5.37 (5.32)	99.63 (99.23)	35.96 (35.22)	-0.215
t- $\text{ZrO}_2$	3.62 (3.61)		5.28 (5.18)	90	34.60 (33.75)	-0.105
c- $\text{ZrO}_2$	5.11 (5.09)			90	33.36 (32.97)	N/A

The first thing to note is that the correct order of  $\text{ZrO}_2$  phases is predicted in the total energy calculations, with monoclinic being the lowest energy phase and cubic being the highest. In addition, the energy difference between phases is small (< 0.1 eV/fu). This is a good indication that the choice of exchange correlation functional can reproduce the energy landscape of the system accurately. This is especially important for when defects are introduced because they

may promote stabilisation of one phase over another, and an inaccurate model will not capture this behaviour. In all cases the predicted cell volumes are consistently within approximately 2% of experimental values.

### 5.3.2 Elastic stiffness constants

Table 5.2 shows the calculated elastic stiffness constants for the monoclinic, tetragonal, and cubic phases of  $\text{ZrO}_2$ . The cubic phase has the greatest elastic stiffness, possibly leading to the short Zr-O bond lengths in the energy-minimised structure (Figure 3.8). It is expected that at high temperatures where the cubic phase is stable, thermal effects (which are not captured in this model) such as larger interatomic spacings will result in a reduction in stiffness.

Table 5.2: Elastic stiffness constants for different phases of  $\text{ZrO}_2$  from DFT calculations.

Elastic stiffness constant	Stiffness (GPa)		
	Monoclinic	Tetragonal	Cubic
$C_{11}$	338.86	334.30	523.38
$C_{12}$	151.80	207.30	92.93
$C_{13}$	89.37	48.93	92.93
$C_{22}$	348.37	334.20	523.39
$C_{23}$	143.04	48.93	92.93
$C_{33}$	262.17	250.50	523.38
$C_{44}$	76.35	9.38	61.98
$C_{55}$	71.65	9.38	61.98
$C_{66}$	114.19	152.60	61.99

The monoclinic and tetragonal phases have similar stiffness along the principal axes, but vary significantly under shearing conditions. The  $C_{44}$  and  $C_{55}$  elastic stiffness constants are considerably smaller in the tetragonal phase. This may be attributed to the directional anisotropy of the tetragonal phase due to the larger  $c$  parameter.

The bulk modulus ( $B$ ) of each phase was calculated from the elastic stiffness constants using the following formulae [210–212]:

$$B_{\text{monoclinic}} = \frac{1}{9}(C_{11} + C_{22} + C_{33} + 2(C_{12} + C_{13} + C_{23})) \quad (5.2)$$

$$B_{\text{tetragonal}} = \frac{1}{9}(2C_{11} + 2C_{12} + 4C_{13} + C_{33}) \quad (5.3)$$

$$B_{\text{cubic}} = \frac{1}{3}(C_{11} + 2C_{12}) \quad (5.4)$$

These yielded bulk modulus values of 190.87 GPa, 169.94 GPa and 236.41 GPa for the monoclinic, tetragonal and cubic phases respectively. These compare with experimental values of 201 GPa for monoclinic at 20 °C [213], 176 GPa for tetragonal at room temperature (pressure stabilised between 1-20 GPa) [214] and 201.09 GPa for 10 % YSZ (cubic) at 300 K [215]. The monoclinic and tetragonal values are in good agreement with experiment. The cubic phase value is difficult to compare as this phase is always studied with a phase stabilising dopant, thus affecting the measured value.

### 5.3.3 Electronic density of states

The electronic density of states for monoclinic, tetragonal and cubic  $ZrO_2$  are generated in a two-step process. First, the non-defective structures are fully relaxed using the geometry optimisation task in CASTEP. This task will also calculate electronic eigenvalues for all k-points and save them to a `.bands` file. Second, the electronic band data is parsed from the `.bands` file using the OptaDOS code [216, 217] and the density of states is output to a text file. Further details on using OptaDOS to view the electronic density of states are given in Appendix B.

The electronic density of states for the three  $\text{ZrO}_2$  phase are given in Figure 5.1. In this figure, the valence and conduction bands can clearly be seen at 2-8 eV and 10-15 eV respectively. Most importantly, the energy values of the VBM and the CBM for each phase can be obtained from this figure. These values are used to calculate the band gap in the different phases, shown in Figure 5.3 alongside experimental values. The VBM value is also used in the calculation of defect formation energies when electrons are added or removed from a system.

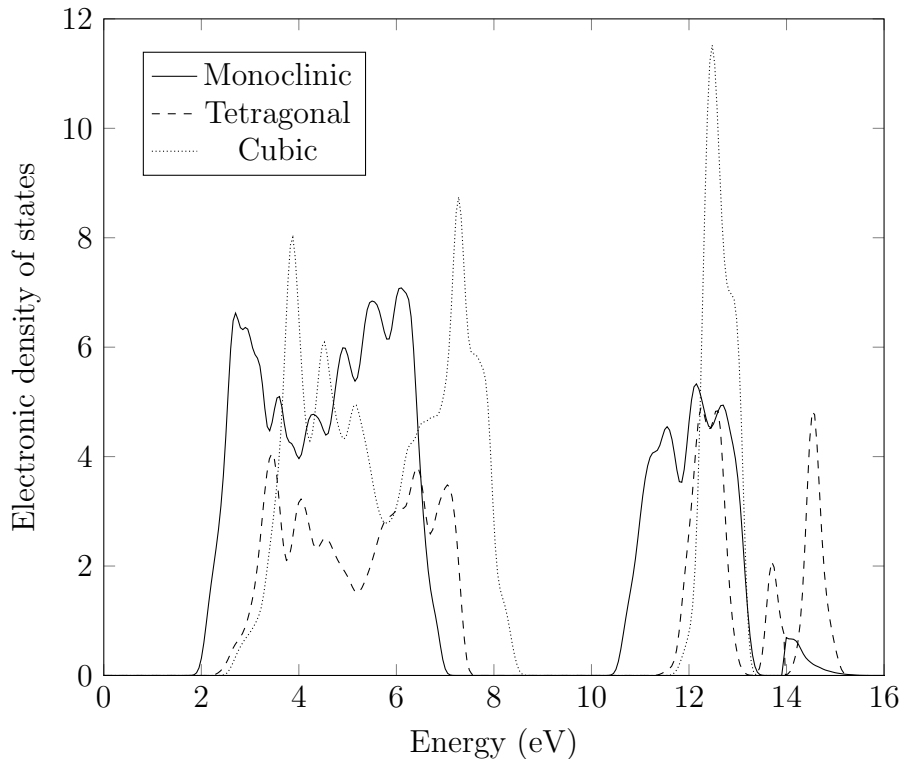


Figure 5.1: Electronic density of states for the different crystal structures of  $\text{ZrO}_2$  showing the band gap predicted by DFT.

The electronic density of states show that the VBM and CBM energies increase from monoclinic to tetragonal to cubic  $\text{ZrO}_2$ . This means that at the same Fermi level, the total electronic energy will be smallest in the monoclinic phase and largest in the cubic phase. This corresponds to the correct order of thermal stability that is seen experimentally.

Other features that can be seen are the band gaps of the different phases between 7 and 12 eV.

These band gaps are significantly underestimated for each phase (see Table 5.3), as is typical when using a GGA exchange-correlation functional.

Table 5.3: Experimentally determined band gaps alongside values calculated from DFT simulations for each crystal structure of zirconia. Experimental values taken from [136].

<b>Crystal Structure</b>	<b>Band gap (eV)</b>	
	<b>Expt.</b>	<b>DFT</b>
Monoclinic	5.83	3.45
Tetragonal	5.78	4.00
Cubic	6.10	3.55

DFT studies of the monoclinic phase have given a band gap of 3.19 eV when using an LDA [218] and 3.20 eV when using a GGA [219]. In the tetragonal phase, two GGA-DFT studies calculated band gaps of 4.21 eV [220] and 3.55 eV [219]. The band gap in the cubic phase has been calculated in a GGA-DFT study as 2.95 eV [219]. An early ab initio study using a LDA also reported band gaps of 8 eV and 7 eV for tetragonal and cubic  $ZrO_2$ , respectively [221]. One study using an ab initio linear combination of atomic orbitals (LCAO) method calculated band gaps of 4.51 eV, 4.11 eV and 3.84 eV for the monoclinic, tetragonal and cubic phases respectively [222].

All of these studies highlight the difficulty in accurately modelling electronic exchange and correlation behaviour in  $ZrO_2$ . The smaller band gaps calculated in this thesis mean that concentrations of electronic defects will be overestimated because their formation energies are proportional to the size of the band gap.

### 5.3.4 Helmholtz energies

The Helmholtz free energy results (Figure 5.2) predicted the correct order of crystal structure stability at low temperature (monoclinic →tetragonal →cubic). A transition from the monoclinic to tetragonal crystal structure is predicted at 390K, but no further transition is seen from tetragonal to cubic. This significantly underestimates the experimental monoclinic →tetragonal transition temperature of 1453 K (1180 °C, see Figure 3.4). The low phase transition temperature may be due to both the kinetic barrier [223, 224], and the inability of the constant volume harmonic model to take into account the effects of thermal expansion.

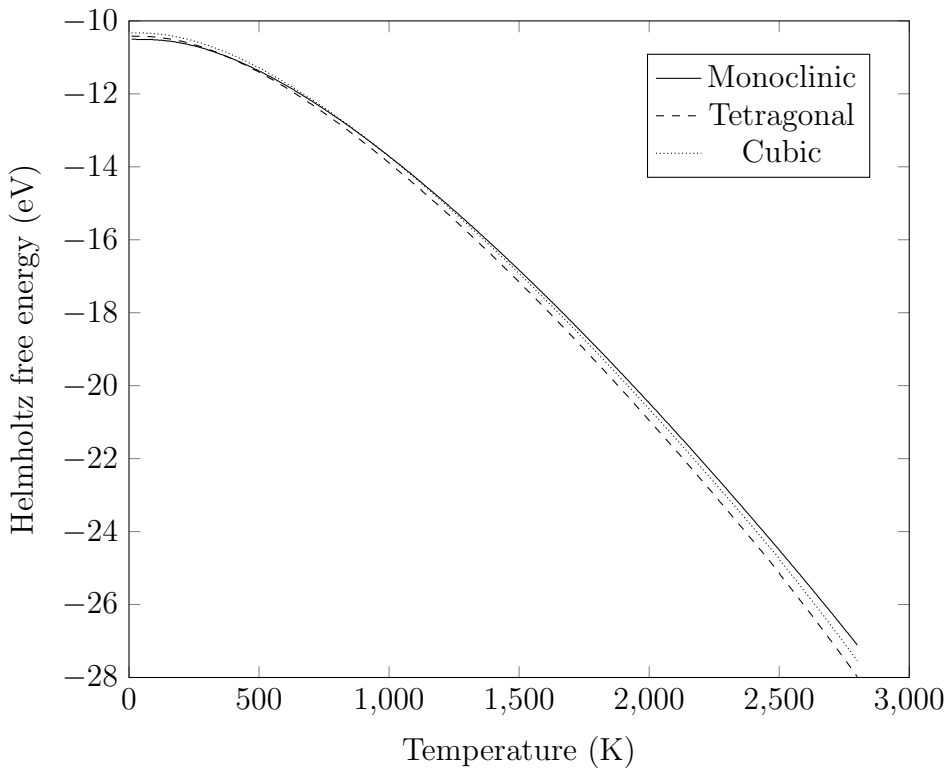


Figure 5.2: Helmholtz free energy as a function of temperature for the monoclinic, tetragonal, and cubic crystal structures of  $\text{ZrO}_2$ .

The lack of an observed transition to the cubic phase may further indicate an inability to accurately simulate the high-temperature phase using DFT techniques, possibly owing to finite-size effects which are known to affect  $\text{ZrO}_2$  in particular [225]. When proceeding to model certain

defects (see § 5.4.2), it was discovered that the cubic phase did indeed exhibit instabilities which yielded anomalous energy values. These results, in addition to the lack of experimental evidence showing pure cubic ZrO<sub>2</sub> in the internal oxide layer of Zr claddings, led to the decision to focus further studies only on the monoclinic and tetragonal phases.

## 5.4 Defective ZrO<sub>2</sub>

### 5.4.1 Formation energies

It is important to know the formation energies of different atomic defects because they can be used to predict which defects are likely to form in the lattice and their respective concentrations. Calculated point defect formation energies of lattice vacancies are provided and discussed below as a function of the Fermi level, defined as the electrochemical potential above the energy of the VBM. Formation energies are plotted up to a Fermi level of 6 eV in order to span the entire experimental band gap of ZrO<sub>2</sub>. Only the defects with the lowest formation energies at each Fermi level are shown.

#### Monoclinic

Oxygen vacancies in the monoclinic phase are shown in Figure 5.3 for both the III and IV coordinated oxygen atoms. At Fermi levels between 0 and 3 eV, formation of V<sub>O</sub><sup>••</sup> defects is expected, with III coordinated oxygen atoms having formation energies 0.6 eV smaller. This energy difference between the two types of oxygen vacancy is substantial, and since both are anion sites of the same charge, this suggests that the size of the site may be the reason for

the difference in energy. In this case, the III oxygen site is slightly smaller than the IV oxygen site and therefore causes a larger relaxation in the lattice when a III-coordinated oxygen ion is removed (see § 5.4.3 for defect volumes). Additionally, the negative energies reveal that the non-defective monoclinic structure is too large at low Fermi levels. At Fermi levels above 3 eV,  $V_O^\times$  defects become the most favourable at both oxygen sites, with almost the same formation energy (0.9 eV).

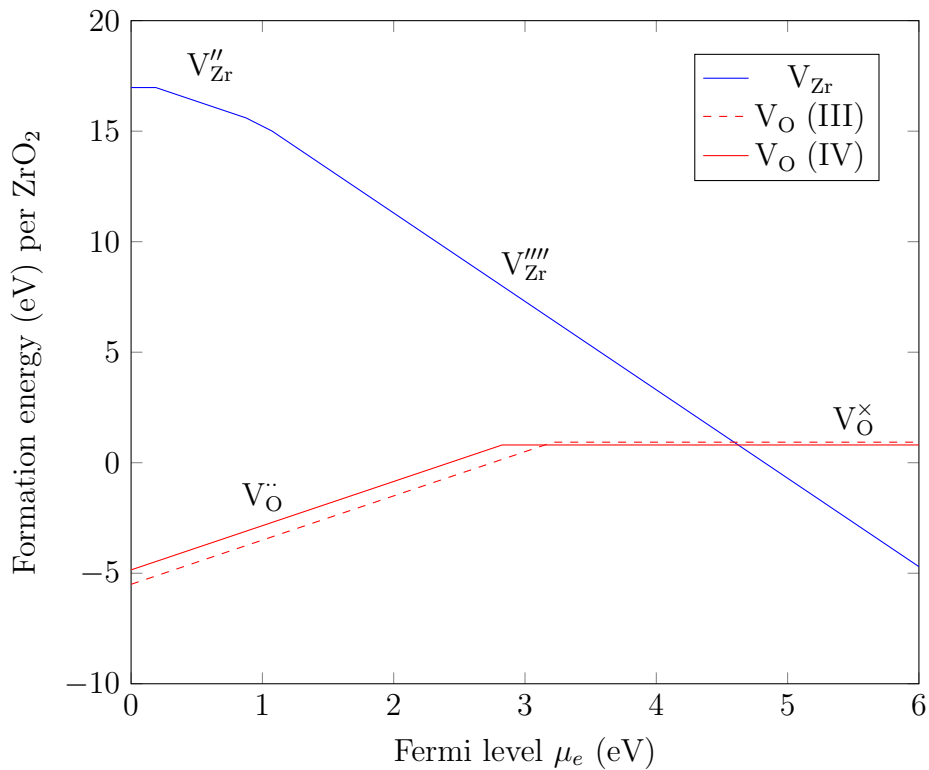


Figure 5.3: Monoclinic phase formation energies of intrinsic vacancy defects as a function of Fermi level. Gradient indicates defect charge. Oxygen coordination number shown in legend.

The O vacancy defect with the smallest formation energy switches from  $V_O^{\bullet\bullet}$  to  $V_O^\times$  as the Fermi level is increased. The absence of  $V_O^\bullet$  defects is due to their relatively higher formation energies at any Fermi level within the band gap. This could be because of the suboptimal orbital occupancy in the surrounding ions when a single electron is missing rather than two. A similar effect is seen for the Zr vacancies, with only the neutral and even charged defects ( $V_O^\times$ ,  $V_{Zr}''$ ,

$V_{Zr}''''$ ) having the smallest formation energies.

At high Fermi levels ( $>4.6$  eV),  $V_{Zr}''''$  defect energies become negative and are even more favourable than  $V_O^\times$ . It is possible that such high Fermi levels may occur at the metal-oxide interface (high availability of electrons from the metal). It is also expected that the concentration of O vacancy defects will be larger at the metal-oxide interface, but the formation energies predict that these will be uncharged and therefore not capable of compensating for the negative charge at the Zr vacancies. It is possible that hole defects may form instead, but at high Fermi levels the formation energy of hole defects will be almost as large as the band gap itself, providing a significant energy barrier.

### Tetragonal

The formation energies of vacancy defects in tetragonal  $ZrO_2$  shown in Figure 5.4 show similar behaviour to those in the monoclinic phase. A transition from  $V_O^{\bullet\bullet}$  to  $V_O^\times$  defects is seen at a Fermi level of 3 eV, and Zr vacancies will likely exist as  $V_{Zr}''''$  at Fermi levels above 0.7 eV. The calculated formation energies show excellent agreement with other tetragonal phase studies [196].

Formation energies of  $V_{Zr}''''$  defects in the tetragonal phase are smaller than in monoclinic by 1 eV and they become more favourable than  $V_O^\times$  defects at a Fermi level of 4.3 eV compared to 4.6 eV in the monoclinic phase. It is therefore expected that the tetragonal phase will contain a larger concentration of Zr vacancies, likely in the form of Schottky defects due to the small formation energy of O vacancies as well.

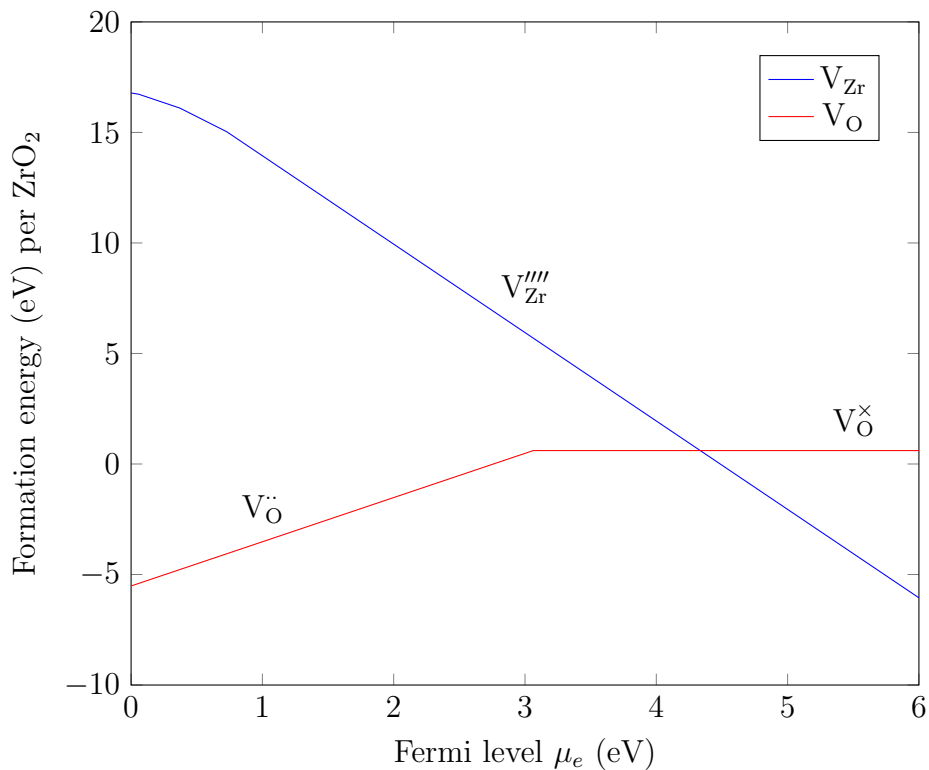


Figure 5.4: Tetragonal phase formation energies of intrinsic vacancy defects as a function of Fermi level. Gradient indicates defect charge.

## Cubic

The formation energies of vacancy defects in the cubic phase are shown in Figure 5.5. O vacancies in the cubic phase have smaller formation energies than in both the monoclinic and tetragonal phases by 2.5 eV, and  $V_{\text{O}}^{\bullet\bullet}$  defects are favourable across a larger range of Fermi levels. The transition from  $V_{\text{O}}^{\bullet\bullet}$  to  $V_{\text{O}}^{\times}$  as the most favourable oxygen defect occurs above a Fermi level of 3.8 eV.

The greater stability of fully-charged O vacancies in the cubic phase provides more evidence indicating that the monoclinic and tetragonal phases in  $\text{ZrO}_2$  are distortions of the cubic phase due to the small Zr ion. This is because  $V_{\text{O}}^{\bullet\bullet}$  defects reduce the size of the cell (see Table 5.7 for defect volumes), thereby allowing Zr ions to bond to their 8 O neighbours in a cubic

configuration.

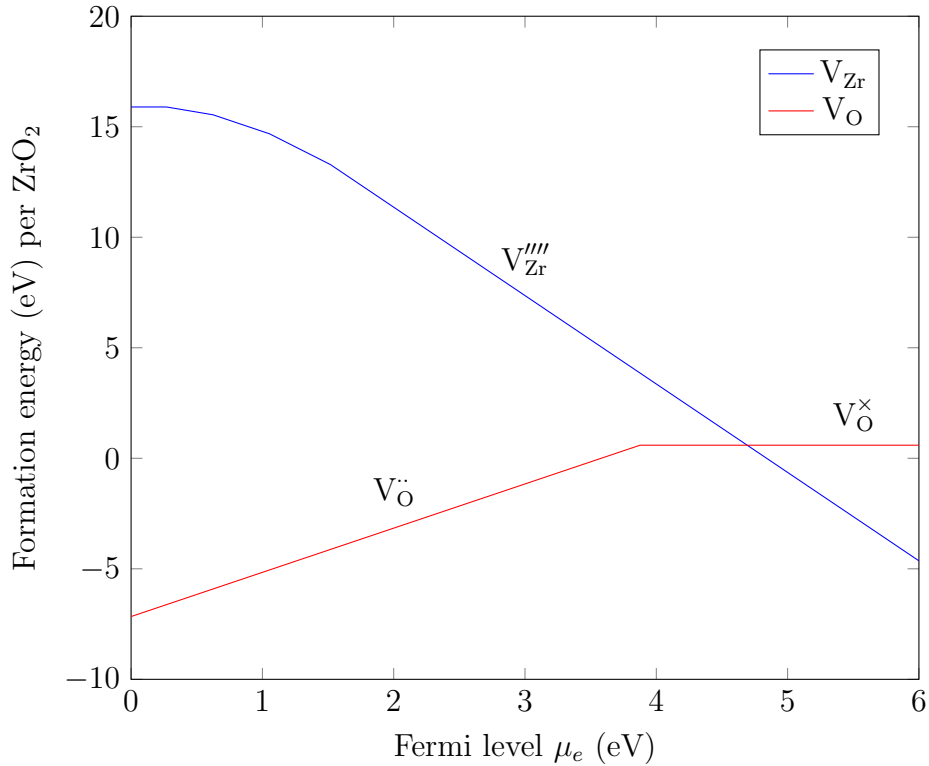


Figure 5.5: Cubic phase formation energies of intrinsic vacancy defects as a function of Fermi level. Gradient indicates defect charge.

### 5.4.2 Frenkel and Schottky defects

Formation energies for Frenkel and Schottky defects were calculated in either a *bound* or *isolated* configuration. A bound defect means that the entire defect (interstitial + vacancy for a Frenkel defect or three vacancies for a Schottky defect) is modelled inside a single supercell. An isolated defect means that the formation energy was calculated from the constituent point defects (individual vacancy or interstitial defects). Both of these methods were used for completeness and because the bound defects include binding energy contributions. Bound and isolated defects are described in more detail below.

## Isolated Frenkel defects

Zr and O Frenkel pair defect formation energies were determined via point defect DFT calculations for the three structures. The formation energies of the isolated Frenkel defect pairs were defined as:

$$E_{Frenkel} = E_{DFT}(V_X^q) + E_{DFT}(X_i^{-q}) - 2E_{DFT}(ZrO_2) \quad (5.5)$$

where  $X$  is either Zr or O,  $E_{DFT}(V_X^q)$  is the energy of a supercell of  $ZrO_2$  containing a single vacancy of charge  $q$ ,  $E_{DFT}(X_i^{-q})$  is the energy of a supercell of  $ZrO_2$  containing a single interstitial with opposing charge  $-q$ , and  $E_{DFT}(ZrO_2)$  is the energy of the non-defective supercell. Charges ranged from the fully charged case (+2 for oxygen vacancies, -4 for zirconium vacancies) to neutral. The interstitial sites, shown in Table 5.4, were chosen based on standard vacant Wyckoff positions in each crystal structure [226]. In the case of oxygen vacancies in monoclinic  $ZrO_2$ , a defect energy was obtained for both the (III) and (IV) co-ordinated oxygen sites, with the lowest energy value being used in the calculation of the Frenkel defect energy.

Table 5.4: Wyckoff positions of interstitial sites used for each crystal structure.

Crystal Structure	Interstitial Sites
Monoclinic	$2a, 2b, 2c, 2d$
Tetragonal	$2b, 8e$
Cubic	$24d, 4b$

The isolated defect formation energies reported in Table 5.5 indicate that fully-charged Schottky defects have the lowest formation energy per atom (most energetically favourable) in all phases, followed by oxygen Frenkel defects and then zirconium Frenkel defects. A trend is seen where the high-temperature phases result in lower formation energies for both Schottky and oxygen Frenkel defects, whereas zirconium Frenkel defects have similar formation energies in all

three phases. The formation energy of a neutral oxygen vacancy-oxygen atom Frenkel pair is calculated as 7.52 eV, which is in good agreement with another DFT study (using the LDA) in the literature which calculated the formation energy as 7.3 eV [218]. Theoretical calculations of the oxygen Frenkel formation energy in cubic  $ZrO_2$  gave an energy of 9.1 eV [128], compared to 8.48 eV in this study for the neutral oxygen Frenkel defect in the cubic phase. Ab initio calculations of zircon, which has a tetragonal crystal structure, also yielded a formation energy of 7.3 eV [227].

It has been suggested that the relatively small cation size leads to defect structures where oxygen vacancies are favoured over interstitial defects [228]. As the zirconium ion is too small to maintain a strong 8-fold bond coordination with its neighbouring oxygen ions, the introduction of oxygen vacancies (which have the added effect of reducing cell volume) will have a stabilising effect.

Table 5.5: Formation energies in eV of Frenkel and Schottky defects calculated from point defects in  $ZrO_2$ .

<b>Defect</b>	<b>Equation</b>	<b>Formation Energy (eV)</b>		
		Monoclinic	Tetragonal	Cubic
<b>Zr Frenkel</b>	$Zr_{Zr}^{\times} \rightarrow V_{Zr}^{''''} + Zr_i^{\bullet\bullet\bullet}$	5.43	5.64	5.61
	$Zr_{Zr}^{\times} \rightarrow V_{Zr}^{'''} + Zr_i^{\bullet\bullet}$	8.70	8.94	8.48
	$Zr_{Zr}^{\times} \rightarrow V_{Zr}^{''} + Zr_i^{\bullet\bullet}$	12.12	12.06	11.63
	$Zr_{Zr}^{\times} \rightarrow V_{Zr}' + Zr_i^{\bullet}$	16.02	15.70	13.32
	$Zr_{Zr}^{\times} \rightarrow V_{Zr}^{\times} + Zr_i^{\times}$	20.56	20.09	18.17
<b>O Frenkel</b>	$O_O^{\times} \rightarrow V_O^{\bullet\bullet} + O_i''$	4.46	4.00	3.73
	$O_O^{\times} \rightarrow V_O^{\bullet} + O_i'$	6.43	6.59	7.06
	$O_O^{\times} \rightarrow V_O^{\times} + O_i^{\times}$	7.52	7.45	8.48
<b>Schottky</b>	$\emptyset \rightarrow V_{Zr}^{''''} + 2V_O^{\bullet\bullet}$	5.12	3.78	1.75
	$\emptyset \rightarrow V_{Zr}^{''} + 2V_O^{\bullet}$	11.35	10.83	9.62
	$\emptyset \rightarrow V_{Zr}^{\times} + 2V_O^{\times}$	18.55	18.23	17.07

## Bound Frenkel Defects

Bound Zr and O Frenkel defect formation energies were calculated from DFT energies of supercells where a single ion was moved from its lattice site to an interstitial site. The formation energies of the bound Frenkel defect pairs were defined as:

$$E_{\text{BoundFrenkel}} = E_{\text{DFT}}(\text{BoundFrenkel}) - E_{\text{DFT}}(\text{ZrO}_2) \quad (5.6)$$

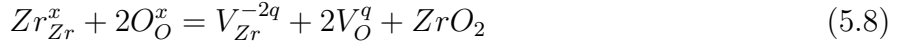
where  $E_{\text{DFT}}(\text{BoundFrenkel})$  is the energy of a supercell of  $\text{ZrO}_2$  containing both a vacancy and interstitial defect of the same ion. The two defects were placed as far apart in the supercell as possible (7-8 Å) to avoid recombination. The interstitial defect is assumed to fully compensate the charge of the vacancy defect, resulting in no overall charge on the supercell. The number and type of ions in the defective and non-defective supercell are the same, requiring no further steps to calculate the formation energy. The formation energies calculated for these defects in each crystal structure are presented in Table 5.6.

## Isolated Schottky Defects

Three Schottky energies were calculated for each structure, corresponding to fully charged, partially charged, and uncharged point defect energies. The Schottky formation energy was defined as:

$$E_{\text{Schottky}} = E_{\text{DFT}}(V_{\text{Zr}}^{-2q}) + 2E_{\text{DFT}}(V_O^q) - \frac{3(n-1)}{n} E_{\text{DFT}}(\text{ZrO}_2) \quad (5.7)$$

where  $n$  denotes the number of atoms in the supercell,  $V_O^q$  denotes an oxygen vacancy with charge  $q$ , where  $q$  varies from 2 to 0. This form maintains both the mass and charge balance of the Schottky defect description for ZrO<sub>2</sub>:



This implies a rearrangement rather than complete removal of ions from the system. As with the Frenkel defects, the lowest energy vacancy energies were used to calculate Schottky formation energies. While there are multiple configurations of Schottky defects, such nuance cannot be accurately represented through a sum of individual vacancy defect energies. The values presented for Schottky defect formation energies should therefore be considered the lower bound for defect formation.

### Bound Schottky Defects

Bound Schottky defects were modelled in a supercell of ZrO<sub>2</sub> by removing one Zr and two O atoms, in one of several possible nearest neighbour configurations as shown in Figures 3.3, 5.6 and 5.7. For the monoclinic phase, Schottky defects included one threefold and one fourfold coordinated oxygen to maintain equal amounts of each oxygen type in the supercell.

Charge neutrality is maintained by the removal of a stoichiometric unit, therefore these defects were defined as neutral tri-vacancies (NTVs). The NTV formation energy was defined as:

$$E_{NTV} = E_{DFT}(NTV) - \frac{n-3}{n} E_{DFT}(ZrO_2) \quad (5.9)$$

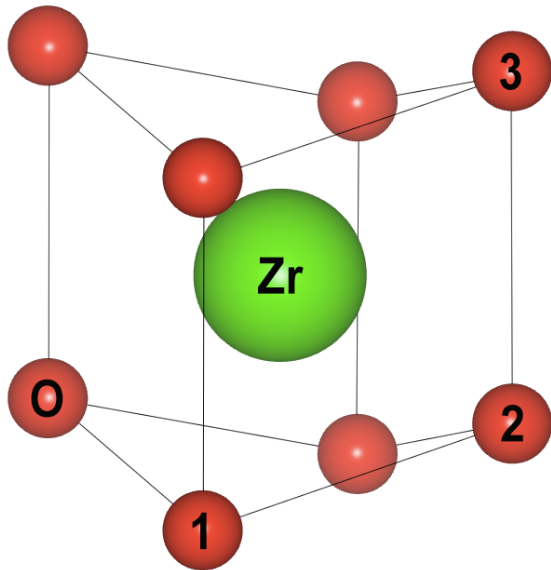


Figure 5.6: Zirconium centre cell showing nearest oxygen atoms in tetragonal  $\text{ZrO}_2$ . Schottky trios indicated by oxygen enumeration with Zr, O and a second oxygen in either the 1<sup>st</sup>, 2<sup>nd</sup> or 3<sup>rd</sup> nearest neighbour with respect to the initial oxygen. Zirconium atoms are shown in green and oxygen atoms in red.

Where  $E_{DFT}(NTV)$  is the energy of a supercell containing the NTV defect. As the defective supercell contains three fewer ions than the non-defective cell, the energy of the non-defective cell was adjusted by a proportional factor in our calculation. This form maintains both mass and charge balance of the Schottky defect description for  $\text{ZrO}_2$  described in Equation 5.8.

## Bound Defects

The bound defect formation energies shown in Table 5.6 show that NTV defects, on a per defect atom basis, are the most energetically favourable defects, followed by oxygen and zirconium Frenkel defects respectively. The NTV3 exhibited the smallest formation energy in all three crystal structures, with a single exception of the NTV2 in the cubic phase where a much smaller formation energy was observed due to collapse<sup>1</sup> of the supercell during geometry optimisation.

<sup>1</sup>Upon inspecting the output cell, it was found that all the oxygen atoms shifted positions along the [001] direction, becoming more like the tetragonal  $\text{ZrO}_2$  structure. The cell size was constrained so the lattice parameters could not be changed, therefore this was not a  $\text{P}4_2/\text{nmc}$  tetragonal cell.

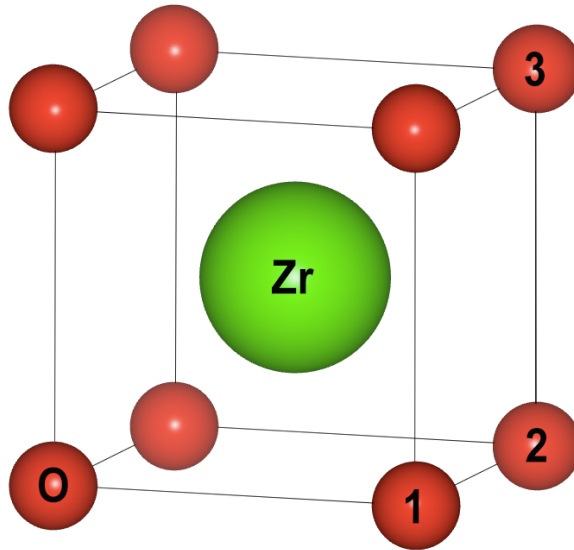


Figure 5.7: Zirconium centre cell showing nearest oxygen atoms in cubic  $ZrO_2$ . Schottky trios indicated by oxygen enumeration with Zr, O and a second oxygen in either the 1<sup>st</sup>, 2<sup>nd</sup> or 3<sup>rd</sup> nearest neighbour with respect to the initial oxygen. Zirconium atoms are shown in green and oxygen atoms in red.

Table 5.6: Formation energies of bound defects in  $ZrO_2$ .

Defect	Formation Energy (eV)		
	Monoclinic	Tetragonal	Cubic
O Frenkel	4.12	4.03	6.44
Zr Frenkel	8.42	7.86	6.33
NTV1	5.23	3.58	2.70
NTV2	5.14	4.23	0.18
NTV3	4.66	3.36	2.41

The symmetry of cubic  $ZrO_2$  has previously been reported to sometimes break when relaxing supercells with interstitial oxygen defects [229]. However, reports of Schottky defect clusters breaking cubic symmetry in  $ZrO_2$  have not been found in the literature. Later studies by Burr *et al.* [225] have shown that the energies of NTVs calculated in  $MO_2$  cubic fluorite structures are highly sensitive to the size of the supercell, with larger errors found when using smaller supercells. It was also found that the symmetry of cubic  $ZrO_2$  could not be retained during relaxation in large supercells (324 and 768 atoms) due to the stability of the monoclinic phase. Cubic supercells with 96 atoms are studied in this thesis, and while cubic symmetry of  $ZrO_2$

can be retained at this size, the instability of the phase when introducing defect clusters puts the bound defect energies into question.

### 5.4.3 Defect Volumes

Tables 5.7 and 5.8 show the calculated point defect and cluster defect volumes respectively. The Frenkel and Schottky defect volumes are calculated from the sum of the relevant point defects that would result in an overall neutral charge, with clusters of fully-charged point defects being the expected defect structures in a real material (e.g.  $V_O^{++} + O_i''$  for an O Frenkel defect).

Table 5.7: Individual point defect volumes in the three  $ZrO_2$  structures.

Defect	Defect volume relative to non-defective cell ( $\text{\AA}^3$ )		
	Monoclinic	Tetragonal	Cubic
$V_{Zr}^{''''}$	9.38	5.92	-2.63
$V_{Zr}'''$	6.17	5.58	-0.80
$V_{Zr}''$	-2.69	5.30	1.35
$V_{Zr}'$	1.46	3.64	3.11
$V_{Zr}^\times$	2.13	2.76	5.01
$Zr_i^{****}$	4.05	23.26	15.56
$Zr_i^{***}$	6.35	20.08	15.24
$Zr_i^{**}$	12.96	19.85	15.25
$Zr_i^*$	14.98	14.94	15.71
$Zr_i^\times$	15.88	11.66	16.41
$V_O^{++}$ [4coord]	-2.82	-7.22	-1.42
$V_O^{+}$ [4coord]	-0.65	-4.11	-1.31
$V_O^+$ [4coord]	-0.62	-2.65	-0.80
$V_O^{++}$ [3coord]	-3.60		
$V_O^+$ [3coord]	-2.12		
$V_O^\times$ [3coord]	-1.80		
$O_i''$	6.06	6.82	2.44
$O_i'$	3.64	9.18	3.56
$O_i^\times$	12.17	16.65	10.50

The fully-charged O Frenkel defect has the smallest defect volume in the tetragonal phase,

Table 5.8: Defect volumes of Frenkel and Schottky defects in the three  $ZrO_2$  structures calculated from individual point defects.

Defect	Defect volume relative to non-defective cell ( $\text{\AA}^3$ )		
	Monoclinic	Tetragonal	Cubic
$V_{Zr}^{''''} + Zr_i^{***}$	13.43	29.18	12.94
$V_{Zr}^{'''} + Zr_i^{***}$	12.52	25.66	14.44
$V_{Zr}^{''} + Zr_i^{**}$	10.27	25.15	16.61
$V_{Zr}' + Zr_i^*$	16.44	18.57	18.82
$V_{Zr}^x + Zr_i^x$	18.01	14.41	21.42
$V_O^{**} + O_i''$	2.45	-0.40	1.02
$V_O^* + O_i'$	1.52	5.07	2.24
$V_O^x + O_i^x$	10.37	14.00	9.71
$V_{Zr}^{''''} + 2V_O^{**}$	2.96	-8.53	-5.47
$V_{Zr}^{''} + 2V_O^*$	-6.94	-2.91	-1.27
$V_{Zr}^x + 2V_O^x$	-1.47	-2.55	3.42

followed by the cubic phase. The tetragonal phase also exhibits larger  $O_i''$  and  $V_O^{**}$  defects than the other phases. This can be explained partly by the relative elastic stiffness of the different phases. Most of the calculated elastic stiffness constants in the tetragonal phase are smaller than in the monoclinic phase (Table 5.2), and by significant amounts for the  $C_{23}$ ,  $C_{44}$  and  $C_{55}$  components. In the monoclinic phase, none of the calculated elastic components are below 71 GPa, whereas four of the elastic components in the tetragonal phase are below 50 GPa. The overall effect on stiffness can be seen when calculating the bulk modulus of each phase (see § 5.3.2). The monoclinic phase bulk modulus is 190.87 GPa compared to 169.94 GPa in tetragonal  $ZrO_2$ , making the tetragonal phase more compliant to volume changes.

The Zr Frenkel defect is significantly larger than the O Frenkel, mostly due to the large positive strain contribution from the Zr interstitial defects. The tetragonal phase in particular has a larger fully-charged Zr Frenkel defect than the other phases, again partly due to the low stiffness of the tetragonal phase. Compared to the O Frenkel defect, these defects are larger and will

therefore impose larger strains in the lattice, leading to larger formation energies.

#### 5.4.4 Defect equilibria

##### Monoclinic

The monoclinic Brouwer diagram (Figure 5.8) predicts that at 650 K, intrinsic defects will be present at very low ( $<10$  ppb  $\text{ZrO}_2$ ) concentrations. This is typical of defect behaviour in a ceramic at temperatures far below their melting points [230, 231]. As a result, stoichiometry occurs at a  $p_{\text{O}_2}$  of  $10^{-27}$  atm. At oxygen pressures below  $10^{-20}$  atm, the major defects are  $e'$  and  $h^\bullet$  which fully charge-compensate each other.

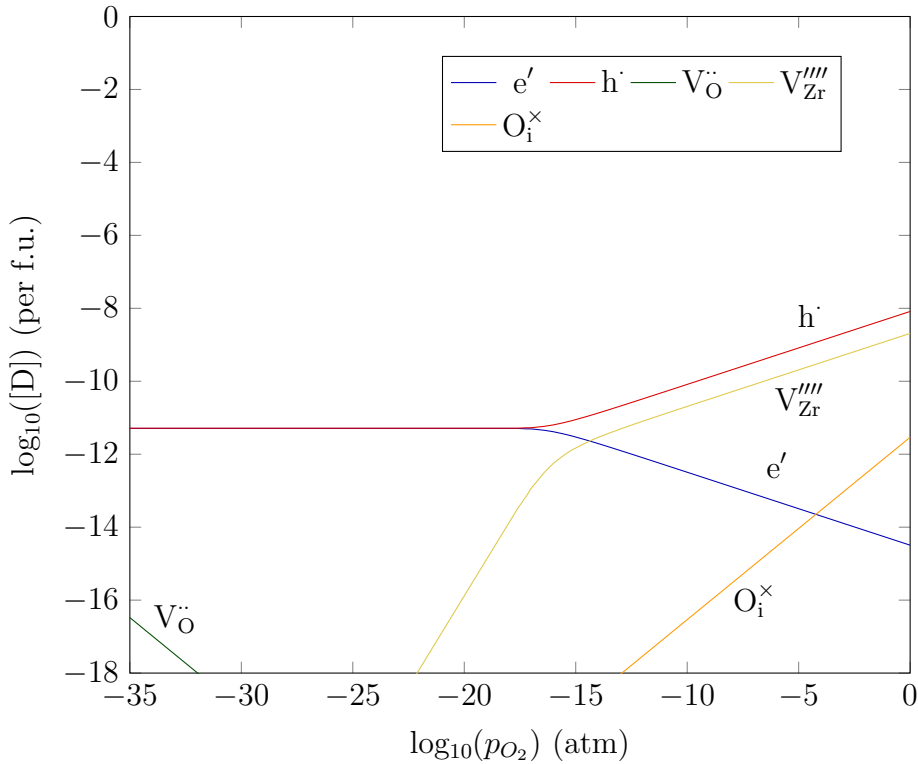


Figure 5.8: Monoclinic phase Brouwer diagram of intrinsic defects at 650 K.

As the oxygen pressure increases,  $V_{\text{Zr}}^{\bullet\bullet\bullet}$  defects become more numerous and overtake  $e'$  defects as

the dominant negatively charged defect. The greater charge magnitude of the  $\text{V}_{\text{Zr}}^{'''}$  defects force the formation of more  $\text{h}^{\bullet}$  defects as these are the easiest positively charged defects which can be produced to achieve charge neutrality (i.e.  $\text{V}_\text{O}^{\bullet\bullet}$  and  $\text{Zr}_\text{i}^{\bullet\bullet\bullet\bullet}$  defects require too much energy to produce at high oxygen pressures).  $\text{O}_\text{i}^{\times}$  defects are also present at high oxygen pressures, but these do not compensate for the charge of other defects.

### Tetragonal

Figure 5.9 shows a much greater concentration of defects across a wide range of  $p_{\text{O}_2}$ , mainly owing to an elevated temperature of 1500 K where the tetragonal crystal structure is fully stabilised. At low levels of  $p_{\text{O}_2}$ , electronic defects are again the dominant defect, but are now charge-compensated by the formation of fully-charged oxygen vacancies. Stoichiometry occurs at a  $p_{\text{O}_2}$  of  $10^{-11}$  atm where  $[\text{V}_\text{O}^{\bullet\bullet}] = 2[\text{V}_{\text{Zr}}^{'''}]$  and  $[\text{h}^{\bullet}] = [\text{e}']$ . As with the monoclinic phase, Schottky defects are expected to be the main defect structure instead of anion Frenkel defects. Higher levels of  $p_{\text{O}_2}$  are dominated by fully-charged zirconium vacancies charge-compensated by the formation of positive hole defects. Comparison of these results with other DFT studies show good agreement of defect equilibria in the tetragonal phase [196].

### Cubic

Figure 5.10 shows a Brouwer diagram constructed for intrinsic defects in cubic  $\text{ZrO}_2$  at 2000 K. As explained in § 5.2.3, a temperature of 2000 K was used because higher temperatures where the cubic phase is thermally stabilised yielded extremely high defect concentrations, leading to unusual defect behaviour. For example, the stoichiometric  $p_{\text{O}_2}$  from the Brouwer diagram

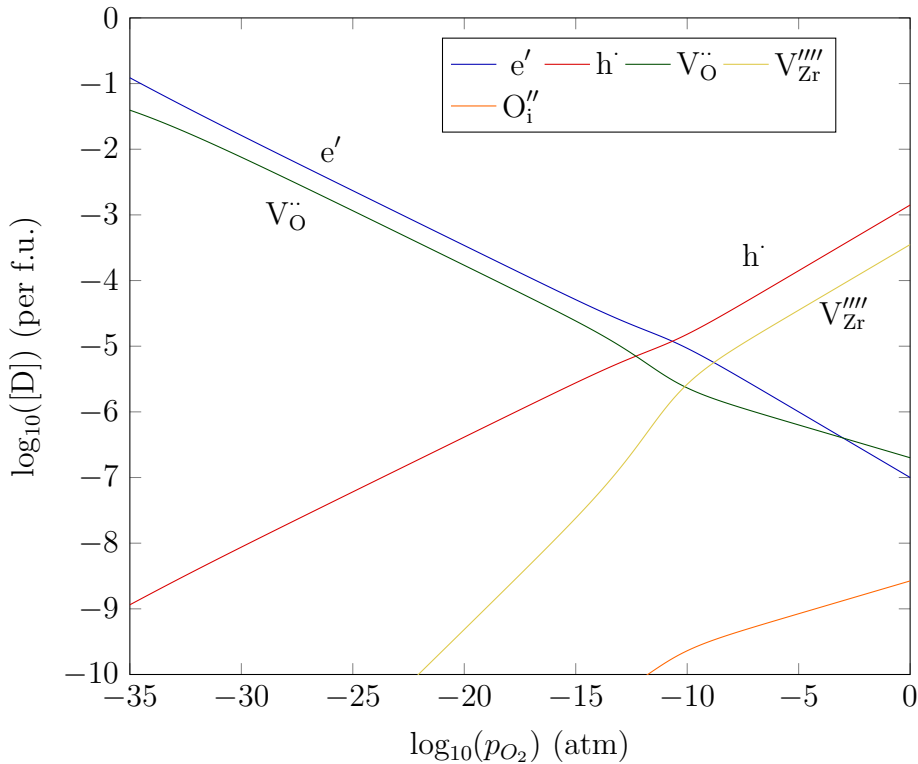


Figure 5.9: Tetragonal phase Brouwer diagrams of intrinsic defects at 1500 K.

is predicted to be greater than 1 atm. While zirconia does exhibit some non-stoichiometry (e.g. hypostoichiometric  $ZrO_{2-x}$ ), the  $p_{O_2}$  at stoichiometry is typically below 1 atm (e.g. stoichiometric  $p_{O_2}$  in  $ZrO_2$  thin films lies in the region of  $10^{-9}$  to  $10^{-7}$  atm [232]). The Brouwer diagram is still included here for the purpose of completeness and to show the limitations of modelling defect equilibria in high-temperature phases near a material's melting point.

One insight which can be obtained from the cubic Brouwer diagram is that the preference for Schottky rather than Frenkel defects is still predicted. Concentrations of Zr and O interstitials are still small relative to vacancies and electronic defects.

Relaxed supercells of cubic phase  $ZrO_2$  are more dense than monoclinic and tetragonal supercells (see § 3.1.3), therefore it is expected that interstitial defects would be even more unfavourable in the cubic phase due to the smaller sites they must occupy.

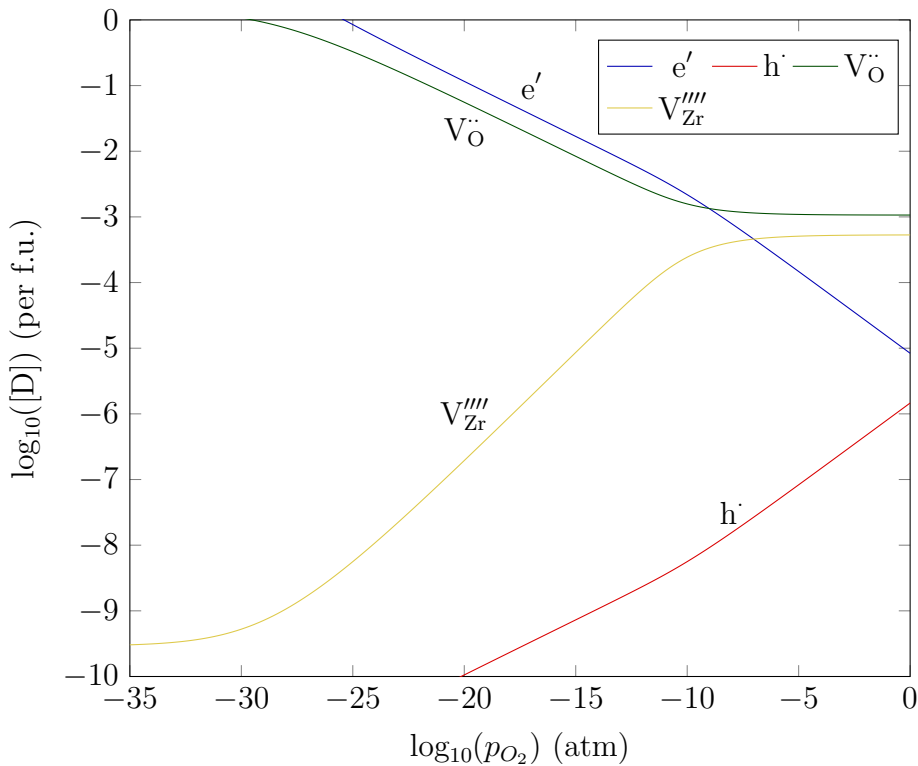


Figure 5.10: Cubic phase Brouwer diagrams of intrinsic defects at 2000 K.

## 5.5 Conclusions

- The correct order of phase stability is calculated for the monoclinic, tetragonal and cubic phases of  $\text{ZrO}_2$  from DFT energies and harmonic phonon calculations.
- Helmholtz free energy calculations show that, as temperature is increased, the lowest energy phase changes from monoclinic to tetragonal, but not from tetragonal to cubic.
- Elastic stiffness constants for each phase were calculated from DFT. Bulk moduli for the monoclinic and tetragonal phases agreed to within 5% of experimental values.
- Formation energy calculations for each phase show that Zr vacancies will be  $\text{V}_{\text{Zr}}''''$  over most Fermi levels, while O vacancies will be reduced from  $\text{V}_\text{O}^{\bullet\bullet}$  to  $\text{V}_\text{O}^\times$  as the Fermi level increases.

- Fully-charged Schottky defects are shown to have the smallest formation energy per defect in all three phases, followed by O Frenkel defects and then Zr Frenkel defects.
- Schottky defects are calculated to have the smallest defect volume in the tetragonal and cubic phase, while O Frenkel defects have the smallest volume in the monoclinic phase. Zr Frenkel defects have the largest defect volume in all three phases.
- Some defects were found to be unstable in cubic  $\text{ZrO}_2$  calculations, causing loss of supercell symmetry. This behaviour, in addition to results from the free energy calculations, leads to the conclusion that cubic phase  $\text{ZrO}_2$  cannot be modelled accurately with present DFT methods. Work by Burr *et al.* [225] supports this result.
- Brouwer diagrams show that defect equilibria in each phase are dominated by  $V_{\text{Zr}}''''$ ,  $V_{\text{O}}^{\bullet\bullet}$ ,  $h^\bullet$  and  $e'$  defects. At high  $p_{\text{O}_2}$ ,  $V_{\text{Zr}}''''$  will be charge-compensated by  $h^\bullet$  defects. At low  $p_{\text{O}_2}$ ,  $V_{\text{O}}^{\bullet\bullet}$  will be charge-compensated by  $e'$  defects.

# Chapter 6

## Iodine defect energies and equilibria in $\text{ZrO}_2$

*The work in this chapter has been published in:*

A. Kenich *et al.* J. Nucl. Mater. **511** (2018) 390-395. Ref [233].

### 6.1 Introduction

As discussed in Chapter 1, SCC in nuclear fuel pins is an issue related to early integrity of fuel assemblies in LWRs. SCC studies of the internal surface of zirconium-based fuel claddings have been conducted, which indicate that iodine is likely to be one of the main corrosive species involved in promoting crack growth [38, 81, 82, 234]. The exact mechanism for iodine SCC has not yet been determined due to difficulties observing the internal cladding surface in-situ, while experimental studies are not yet capable of reproducing the conditions under which such

failures occur. The quantum-mechanical simulation approach is therefore particularly useful to model the behaviour of iodine within the oxide layer of the cladding, the layer preceding the zirconium metal.

Iodine is produced in the fuel pellet directly from fission (see Chapter 1 for details) and also from the decay of tellurium precursors. As shown in Figure 1.2, both iodine and tellurium are relatively common fission products, with combined independent yields from thermal fission of  $U^{235}$  above 26% [235–240]. The majority of thermal fission events occur in the outer rim of the fuel pellet, and a fission product penetration depth of up to  $8\ \mu m$  in  $ZrO_2$  [241] suggests a large degree of implantation within the oxide and the Zr metal into which the oxide grows, raising the concentration of I well above the equilibrium value. Iodine and many of its relevant compounds (as  $ZrI_4$ ,  $CsI$ ) are volatile and fuel pellets contain many cracks and spaces through which iodine may be rapidly transported to the cladding. When reactor power is increased during start-up, iodine is released in substantial quantities from the  $UO_2$  pellet [242]. This is believed to cause crack propagation in the cladding when combined with tensile stresses imposed on the cladding by the fuel pellet, and this contributes to PCI, a phenomenon discussed in Chapter 1. Upper limits on power ramping and holding times have therefore been established by fuel suppliers to mitigate potential PCI failures [243]. While these restrictions have reduced or prevented the incidence of PCI failures, they also impose costs on the operator due to longer ramping periods. This also restricts the ability of the nuclear reactor to load-follow grid demand. Cladding/fuel materials resistant to PCI failure are therefore of great interest in the nuclear power industry, promoting research into solutions such as cladding liners and doped fuel pellets [244, 245].

Iodine is an oxidising agent, which, under standard conditions, will oxidise Zr metal to produce  $ZrI_4$ . However, oxygen is also present in the internal fuel pin environment, both from the native

$\text{ZrO}_2$  layer on the cladding, and the evolution of oxygen from the fuel pellet during burnup. Liberated oxygen will compete with iodine in the oxidation of the Zr metal, but whereas iodine promotes crack growth under stress, oxygen provides a more protective effect, self-limiting its diffusion into the metal [95, 246]. Furthermore, oxygen is a more powerful oxidising agent than iodine, reacting together to produce  $\text{I}_2\text{O}_5$ . For these reasons, the internal oxide layer of the cladding is often considered a barrier to the ingress of iodine into the Zr metal.

Unlike oxygen and hydrogen, which readily diffuse into Zr metal to occupy interstitial sites, iodine atoms have been predicted in atomistic studies to have very high energy barriers to bulk interstitial diffusion [100, 247, 248]. This is due to the relatively large radius of the iodine atom, which imposes large local strains when penetrating the Zr lattice. This suggests that iodine will instead be transported towards crack tips via grain boundaries. Indeed, intergranular cracking has been observed in PCI failures, but only for a few hundred nm before a more rapid transgranular crack propagation [234, 249–252]. Conversely, no atomic scale studies of iodine in  $\text{ZrO}_2$  were found in the literature.

As discussed in § 2.2.3, there is an oxide layer on the internal surface of the cladding consisting of monoclinic and tetragonal oxide grains. The effectiveness of the oxide layer as a barrier to iodine is debated, with one study presuming that the oxide is bypassed entirely by iodine due to fracturing, leaving the Zr metal underneath exposed [100]. The outermost part of the oxide, which is porous, exhibits networks of interconnected grain boundary diffusion pathways towards the oxide/metal interface which are certainly wide enough (1-3 nm) to allow iodine transport [253]. The oxygen-saturated Zr at the oxide/metal interface is not, however, taken into account, and it is expected that this will influence the corrosion mechanism due to iodine-oxygen competition: even the much smaller hydrogen atom has its rate of diffusion into the

metal reduced by the presence of oxygen, as shown in both computational [254] and experimental hydrogen pick-up studies [255]. This means that some barrier to iodine ingress must already exist near the oxide/metal interface. The varying levels of oxygen across the oxide layer itself also have an effect on defect behaviour, and will therefore influence the initiation mechanisms behind PCI failures. Thus here, we predict iodine incorporation energies and defect equilibria in  $ZrO_2$  as a function of oxygen pressure through Brouwer diagrams, in order to predict the resulting iodine defect response.

## 6.2 Methodology

### 6.2.1 Simulation parameters

The simulation parameters for CASTEP calculations in this chapter were the same as those described in § 5.2.1.

### 6.2.2 Defect Equilibrium Response to Oxygen Partial Pressure

Brouwer diagrams were generated using the method previously outlined in § 4.4.2. Defect concentrations for the monoclinic and tetragonal phases were calculated at 650 K and 1500 K respectively to reflect the temperatures at which these structures are stable. Brouwer diagrams at extrinsic defect concentrations of  $10^{-5}$  and  $10^{-3}$  parts/fu (i.e. parts per  $ZrO_2$  formula unit) were generated to examine low and high dopant concentrations, respectively. These two concentrations were examined because the amount of fission products present at a particular point in a fuel pellet depends on macroscopic parameters, including its position in the core and

the time since the last shutdown, but also microscopic parameters such as the radial position in the pellet. These two concentrations were selected because  $10^{-3}$  parts/fu is high enough to model an aggregation of iodine (such as at a crack tip), and  $10^{-5}$  parts/fu was found to be the concentration below which iodine did not have a significant effect on defect equilibria.

## 6.3 Results

### 6.3.1 Incorporation energies

#### Interstitial Sites

Iodine incorporation energies at interstitial sites for each phase are reported in Table 6.1. The  $2a$  and  $2c$  sites in monoclinic  $\text{ZrO}_2$  provide the least unfavourable iodine incorporation energy, followed by the  $2b$  and  $8e$  sites in tetragonal  $\text{ZrO}_2$ , although in all cases energies are positive and large, indicating a large energy penalty against interstitial incorporation. The difference in incorporation energies between monoclinic and tetragonal  $\text{ZrO}_2$  is approximately 1 eV, whereas the difference between tetragonal and cubic is 3.5 eV, indicating especially unfavourable conditions in cubic  $\text{ZrO}_2$ . These differences are likely due to the larger interstitial sites in the lower-temperature phases, as monoclinic  $\text{ZrO}_2$  exhibits the least and cubic  $\text{ZrO}_2$  the most dense cell, (see Chapter 3).

While the incorporation energies of iodine in the interstitial sites of  $\text{ZrO}_2$  are large for a fixed iodine concentration, they become relevant as the intrinsic defect populations become small, such as at low temperatures relative to the melting point. This is because interstitial sites

Table 6.1: Incorporation energies of iodine at different interstitial sites of  $ZrO_2$ .

Structure	Site	Incorporation Energy (eV)		
		$I_i^\times$	$I_i'$	$I_i^\bullet$
<b>Monoclinic</b>	2a	8.55	12.10	6.55
	2b	10.81	16.40	5.63
	2c	8.79	12.20	4.62
	2d	10.94	13.66	6.92
<b>Tetragonal</b>	2b	9.49	13.96	5.99
	8e	9.53	12.73	5.10
<b>Cubic</b>	24d	13.02	18.24	7.62
	4b	13.08	16.46	9.82

are always available, whereas at low intrinsic defect concentrations, substitutional sites become saturated and accommodation at a lattice site first requires the creation of a vacancy defect, which has a formation energy penalty associated with it.

When Brouwer diagrams are generated, iodine is also considered as a charged species at an interstitial site (see § 6.3.3). This includes  $I^+$  and  $I^-$ , where  $I^+$  is a smaller ion that is more easily accommodated at an interstitial site. Energy values for  $I^+$  and  $I^-$  are also reported in Table 6.1, however, values for different charge states cannot be compared because an electron has been added or removed from the I atom to form the specific charge state. An interstitial site will always be uncharged (resultant charge is distributed onto nearby ions instead), meaning that there is no pre-existing charged interstitial site to incorporate an atom onto. It is therefore only appropriate to consider the *formation* energy (i.e. including the addition or removal of an electron) of a charged interstitial defect.

## Oxygen Sites

Table 6.2 reports incorporation energies of iodine at various oxygen sites. In each phase, the lowest incorporation energy was that for accommodation at a vacant oxygen site such that iodine is in the 1- oxidation state, resulting in the overall defect  $I_O^\bullet$ . This anionic behaviour is expected from a halogen atom in a highly reducing site as it promotes the filling of the  $p$  shell. I is most readily accommodated in the monoclinic phase for all I charge states.

Table 6.2: Incorporation energies of iodine in oxygen sites of the monoclinic, tetragonal, and cubic  $ZrO_2$  phases.

Structure	Incorporation energy (eV)		
	$I_O^{\bullet\bullet}$	$I_O^\bullet$	$I_O^\times$
Monoclinic (3 co-ord)	4.54	2.90	3.67
Monoclinic (4 co-ord)	5.63	3.77	4.87
Tetragonal	6.19	4.02	4.44
Cubic	8.37	5.74	6.66

## Zirconium Sites

Incorporation energies of iodine on zirconium sites are reported in Table 6.3. The incorporation energy decreases as the charge of the defect decreases from -4 to 0 (i.e. nominally from  $I^0$  to  $I^{4+}$ ). This is due to the decrease in the size of the iodine species with increasing positive charge, fitting better into the small vacant  $Zr^{4+}$  cation site. This alone does not guarantee the emergence of uncharged iodine defects ( $I^{4+}$ ) on zirconium sites when all energy terms are considered. In particular, there is also an energy penalty incurred in the change in charge of iodine. A Mulliken population analysis revealed a charge localised on the iodine of +2.31 at the  $I_{Zr}^\times$  defect, and a +0.86 charge on the  $I_{Zr}'''$  defect, with the remaining charge accommodated

by other ions in the lattice<sup>1</sup>. Again, I is most readily accommodated in the monoclinic phase for all charge states.

Table 6.3: Incorporation energies of iodine in zirconium sites of  $ZrO_2$ .

<b>Structure</b>	<b>Incorporation energy (eV)</b>				
	$I_{Zr}^{''''}$	$I_{Zr}^{'''}$	$I_{Zr}^{''}$	$I_{Zr}'$	$I_{Zr}^{\times}$
<b>Monoclinic</b>	6.78	3.65	0.89	-2.84	-5.08
<b>Tetragonal</b>	7.58	3.64	1.69	-2.13	-4.57
<b>Cubic</b>	9.70	6.81	3.01	0.38	-3.14

### 6.3.2 Dopant interstitial defects

The formation energies of iodine interstitial defects are useful not only to determine whether interstitial defects will form, but also which interstitial sites in particular they will occupy. As shown in Table 5.4,  $ZrO_2$  has four interstitial sites in the monoclinic phase, and two interstitial sites in the tetragonal and cubic phase (based on crystallographic data of the three phases). For each phase, the formation energies of each iodine interstitial defect as a function of Fermi level are calculated and provided below.

#### Monoclinic interstitial defects

Figure 6.1 shows how the formation energy of an iodine interstitial defect in monoclinic  $ZrO_2$  varies based on site and Fermi level. In this phase, the  $2b$  Wyckoff position is the site of lowest formation energy across the entire range of Fermi levels that span the band gap, with a maximum of 8.1 eV at a Fermi level of 2.8 eV. The next most favourable site is at  $2a$ , with

<sup>1</sup>Defects in Kröger-Vink notation are labelled with integer charges, but real materials are typically not perfectly ionic. Formal charges are not assigned to individual ions in DFT calculations. Rather, a charge on the system is initially defined and then the energy minimisation process changes the distribution of electron density to obtain the ground state density.

formation energies at least 0.4 eV greater at similar Fermi levels. Iodine at the  $2c$  and  $2d$  sites exhibits formation energies between 1 and 4 eV larger than at the  $2b$  site, making these sites significantly unfavourable. This shows that there are indeed four unique sites which iodine atoms can occupy in the monoclinic phase (as evidenced by the different formation energy evolutions at each site), and that of these sites, the  $2b$  is the most energetically favourable for iodine.

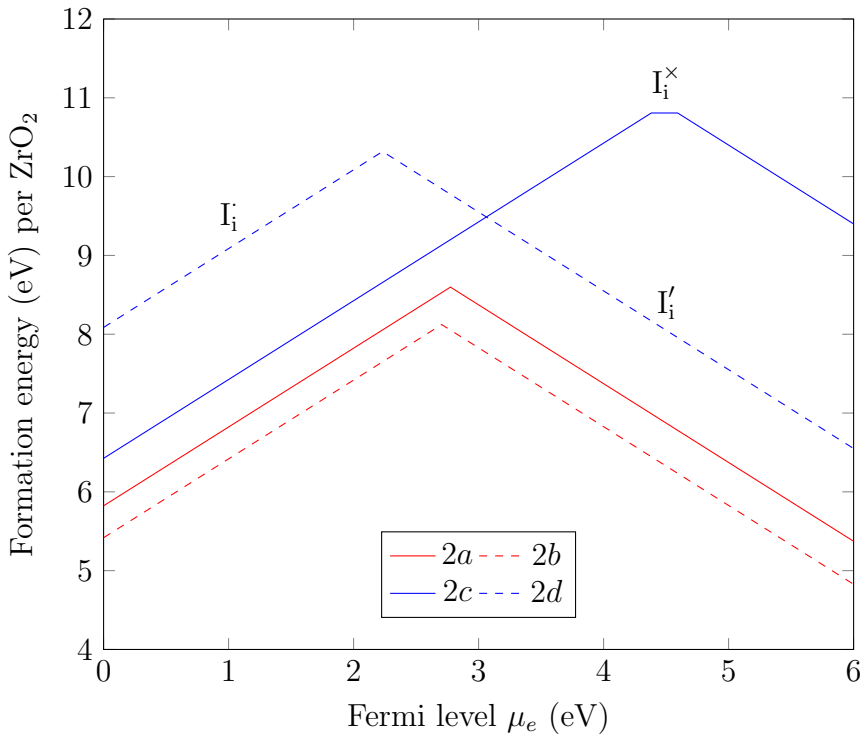


Figure 6.1: Iodine interstitial formation energies in monoclinic  $\text{ZrO}_2$  as a function of Fermi level. Gradient indicates defect charge.

It should also be noted that iodine will occupy these interstitial sites as either  $I_i^\bullet$  or  $I_i'$  (the slope of the curve indicates defect charge).  $I_i^X$  appears for a small range of Fermi levels in the  $2c$  site, but the formation energy is so large compared to the other sites that this will not be present in the crystal. The preference for a charged state of +1 or -1 may be due to a combination of electron availability and ionic radius.  $I_i^\bullet$ , being positively charged, has a smaller ionic radius than  $I_i^X$ . The smaller size of this defect comes with a smaller energy penalty when occupying

an interstitial site, and at low Fermi levels the iodine is more susceptible to oxidation. At high Fermi levels,  $I'_i$  forms because iodine has a large electron affinity and electrons are more readily available. This compensates energetically for the increased ionic radius.

### Tetragonal interstitial defects

Figure 6.2 shows the formation energies of iodine interstitial defects in the tetragonal phase as a function of Fermi level. In this phase, both the  $2b$  and  $8e$  sites are predicted to be occupied (i.e. the site of lowest formation energy changes) by iodine at different Fermi levels. The  $2b$  site, which is an octahedral site with 8 O nearest neighbour ions, is the lowest energy site for  $I'_i$  defects at Fermi levels above 3 eV. The  $8e$  site is a tetrahedral site with two Zr and two O nearest neighbour ions, and is the lowest energy site for  $I_i^\bullet$  defects below Fermi levels of 3 eV. Of the two sites, the  $2b$  site is larger (the shortest I-O distance before relaxation is 2.07 Å, compared to 1.29 Å for the  $8e$  site). It is therefore reasonable that the larger  $I^-$  ion will preferentially accommodate the  $2b$  site. The eight  $O^{2-}$  ions enclosing the  $2b$  site also make it more reducing, promoting the negative charge state ( $I^{-1}$ ) when occupied.

### Cubic interstitial defects

Much like in the tetragonal phase, the formation energies of iodine interstitials in cubic  $ZrO_2$  (Figure 6.3) show that the preferred interstitial site will change based on Fermi level and the defect charge. Once again,  $I_i^\bullet$  will occupy the octahedral site ( $4b$ ) and  $I'_i$  will occupy the tetrahedral site ( $24d$ ). The transition from  $I_i^\bullet$  to  $I'_i$  is predicted to occur above a Fermi level of 3.8 eV, higher than in the tetragonal phase (3 eV). The tetragonal and cubic structures are very

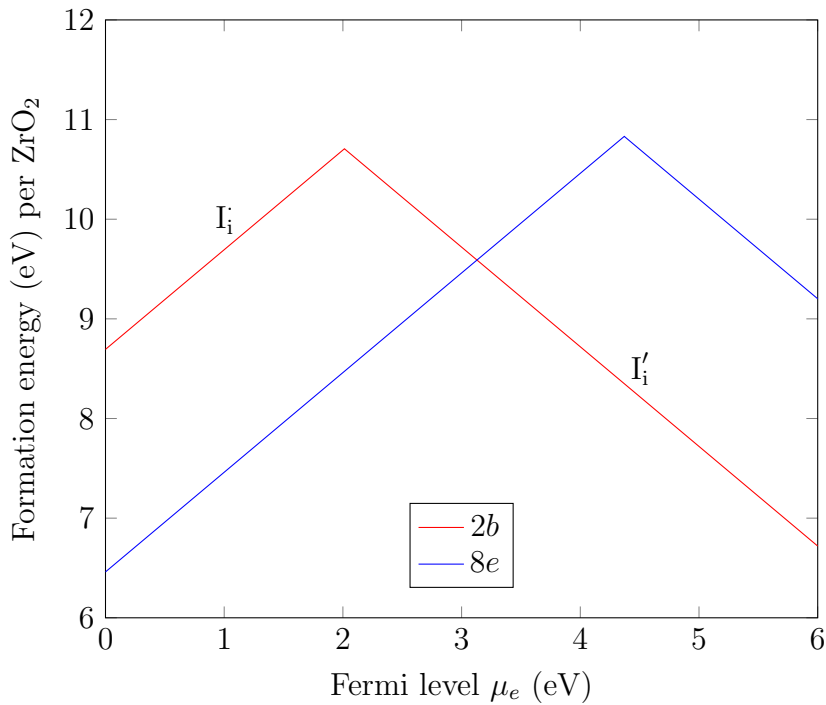


Figure 6.2: Iodine interstitial formation energies in tetragonal  $\text{ZrO}_2$  as a function of Fermi level. Gradient indicates defect charge.

similar, and so the same reasoning of relative site sizes can be used to explain this behaviour.

### 6.3.3 Brouwer Diagrams

#### Monoclinic Phase

Brouwer diagrams associated with the monoclinic phase, at 650 K, at which temperature this  $\text{ZrO}_2$  phase is stable, are shown in Figure 6.4. At 650 K, this phase exhibits a relatively low concentration of intrinsic defects; concentrations of  $\text{V}_\text{O}^{\bullet\bullet}$  and  $\text{V}_{\text{Zr}}^{''''}$  remained below  $10^{-10}$  parts/fu across the majority of oxygen pressures and do not appear in the diagrams. At lower iodine concentrations, the intrinsic electronic defects,  $e'$  and  $h^\bullet$ , were more significant, with  $h^\bullet$  defects being a major fraction of the total defect population near stoichiometry (i.e. at an oxygen pressure of approximately  $10^{-7.5}$  atm).

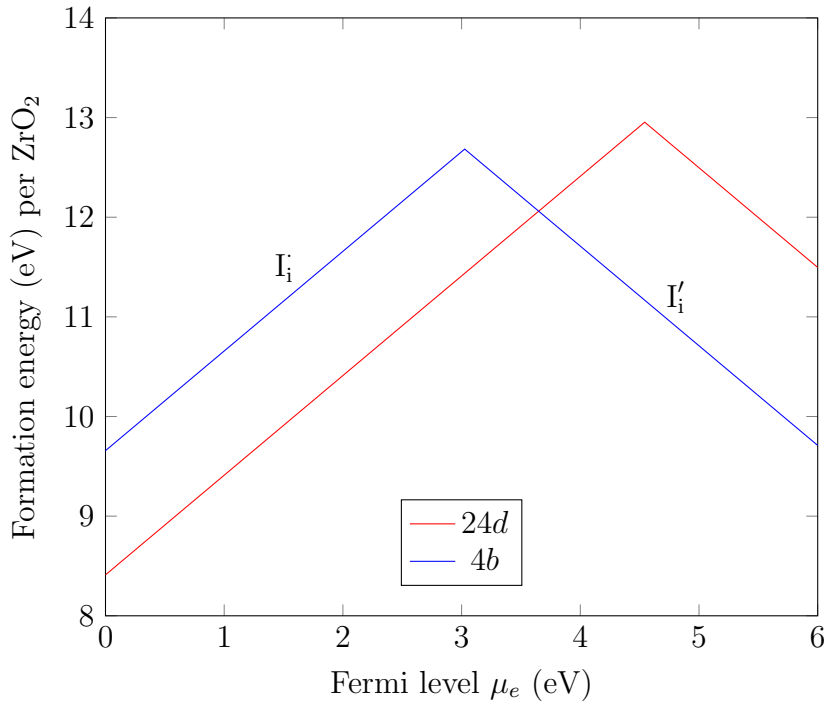


Figure 6.3: Iodine interstitial formation energies in cubic  $ZrO_2$  as a function of Fermi level. Gradient indicates defect charge.

Between oxygen pressures of  $10^{-35}$  and  $10^{-10}$  atm, the dominant defects were  $I_O^\bullet$  charge-compensated by  $I_{Zr}'''$ . Above an oxygen pressure of  $10^{-10}$  atm, a combination of  $I_i^\bullet$ ,  $I_{Zr}'''$  and  $I_O^{+\bullet}$  defects were dominant. This demonstrates that iodine will adopt a +1 oxidation state in order to facilitate iodine incorporation into the lattice. The effective ionic radius of  $I^-$  is 2.20 Å in VI-fold coordination, compared to 1.38 Å for  $O^{2-}$  in IV-fold coordination, as is the case in  $ZrO_2$  [167]. Iodine with a higher positive charge state will have a smaller ionic radius, and thus impose less strain on the lattice (and therefore a smaller energy penalty) in each defect configuration, including substitution on a Zr site. At the highest oxygen pressures, the Brouwer diagrams show that oxidation of iodine, substituted at an oxygen site, to the +1 oxidation state (i.e.  $I_O^{+\bullet}$ ) becomes a necessary charge compensating defect. This is because the energy penalty to form additional hole defects is too large, as is the formation of other positive charge defects such as  $Zr_i^{+\bullet\bullet\bullet}$ . This may translate to iodine out-competing oxygen for oxygen sites in

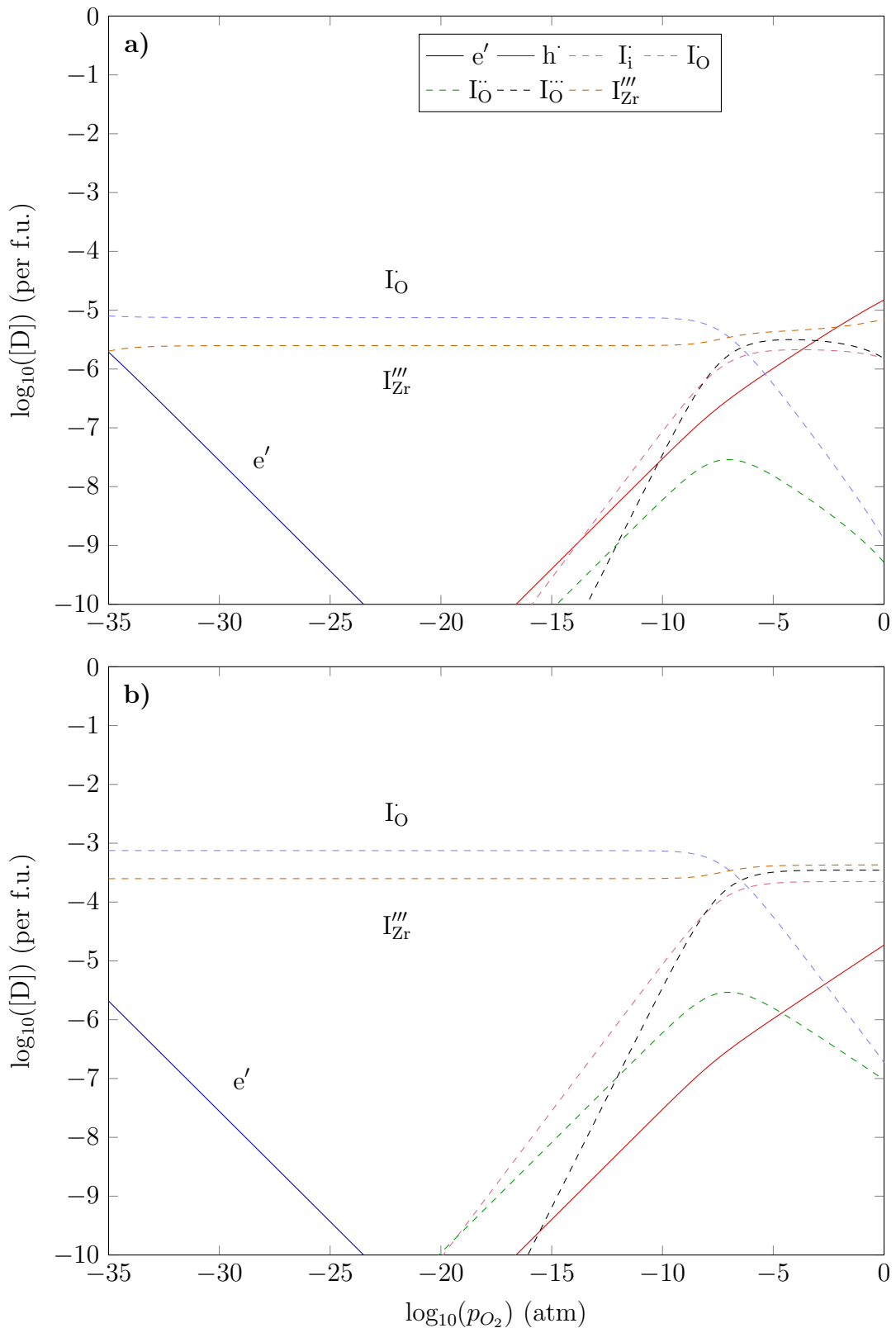


Figure 6.4: Monoclinic phase Brouwer diagrams of point defects at iodine concentrations of a)  $10^{-5}$  and b)  $10^{-3}$ , at a temperature of 650 K.

monoclinic  $ZrO_2$ , with higher oxygen pressures providing very little in terms of a barrier effect.

## Tetragonal Phase

Brouwer diagrams for the tetragonal phase are shown in Figure 6.5. As these diagrams were generated at a temperature of 1500 K (at which the tetragonal phase becomes stable), intrinsic defect concentrations were significantly higher than in the monoclinic diagrams for all oxygen pressures (though trends remained the same). Intrinsic defects  $e'$ ,  $h^\bullet$ ,  $V_O^{\bullet\bullet}$  and  $V_{Zr}^{\prime\prime\prime\prime}$  were dominant across most oxygen pressures at an iodine concentration of  $10^{-5}$  parts/fu. Only near stoichiometry do extrinsic defect concentrations approach intrinsic values (which as mentioned earlier is why this concentration of iodine was chosen). Across all oxygen pressures,  $I_O^\bullet$  and  $I_{Zr}^{\prime\prime\prime}$  are the major iodine defects. Between  $10^{-15}$  and  $10^{-5}$  atm, Figure 6.5 illustrates that the major iodine defect swaps from being  $I_O^\bullet$  to  $I_{Zr}^{\prime\prime\prime}$ .

When the iodine concentration was increased to  $10^{-3}$  parts/fu, a significant change in defect equilibria was predicted. The oxygen pressure at stoichiometry increased from  $10^{-10}$  to  $10^{-6.5}$  atm (for monoclinic  $ZrO_2$ , it remained at  $10^{-7.5}$  atm regardless of iodine concentration). Nevertheless,  $I_O^\bullet$  and  $I_{Zr}^{\prime\prime\prime}$  remain the dominant defect pair between oxygen pressures of  $10^{-15}$  and  $10^{-5}$  atm (as they are at the lower iodine concentration). However,  $I_O^\bullet$  and  $I_{Zr}^{\prime\prime\prime}$  became higher concentration defects than both intrinsic  $V_O^{\bullet\bullet}$  and  $V_{Zr}^{\prime\prime\prime\prime}$  defects. We also observe that Zr vacancies no longer serve as the main negative charge-compensation defect near stoichiometry, leaving  $I_{Zr}^{\prime\prime\prime}$  as the most energetically favourable negatively-charged defect.

Unlike in the Brouwer diagrams for the monoclinic phase, for the tetragonal phase, the concentration of iodine substitutional defects on oxygen sites decreases more steeply at high oxygen

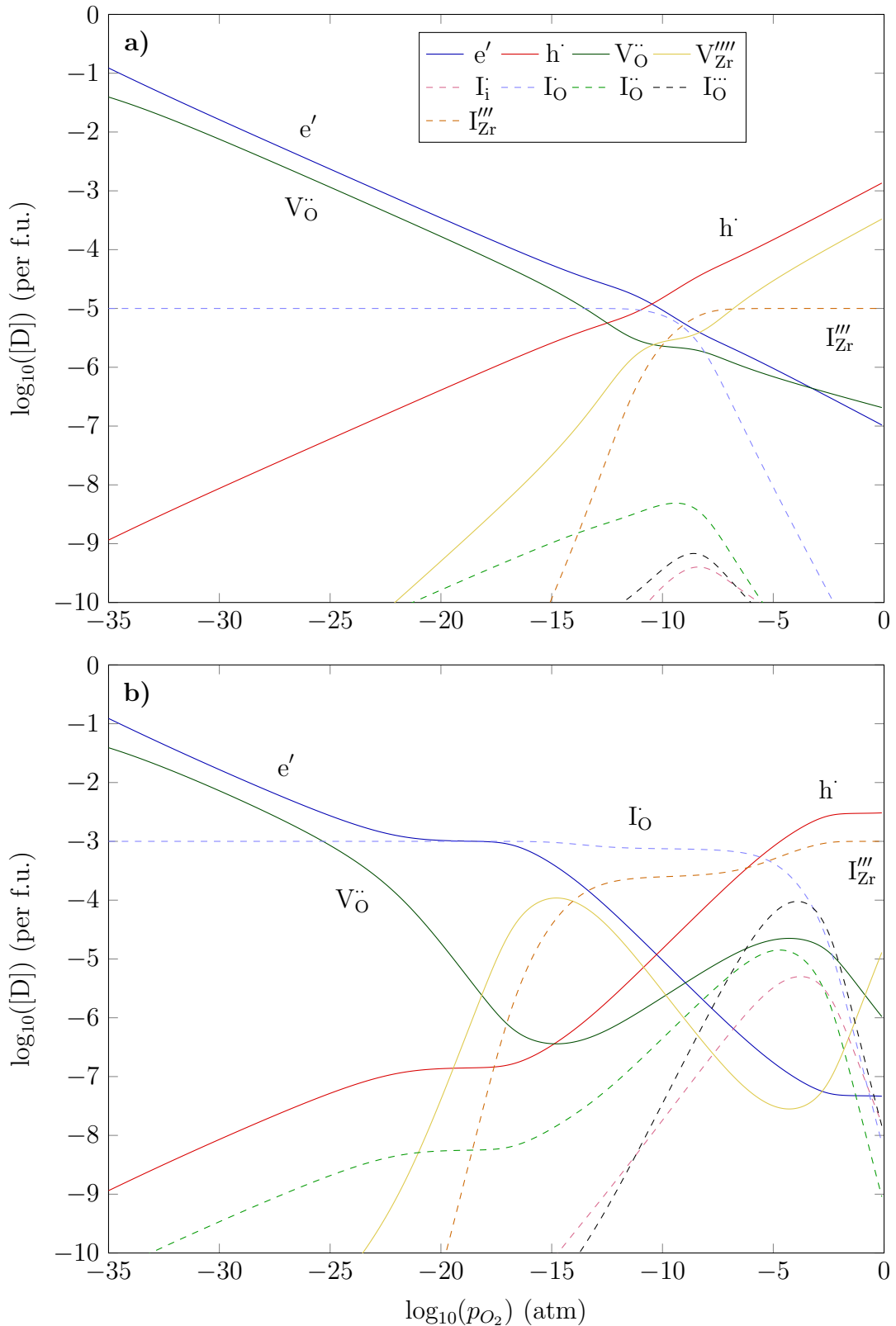


Figure 6.5: Tetragonal phase Brouwer diagrams of point defects at iodine concentrations of a)  $10^{-5}$  and b)  $10^{-3}$ , at a temperature of 1500 K.

pressures, peaking near stoichiometry.  $\text{I}_\text{O}^{\bullet\bullet}$  in particular, which was the dominant defect at high oxygen pressures in monoclinic  $\text{ZrO}_2$ , becomes insignificant under the same conditions in the tetragonal phase, with iodine confined to Zr sites. This behaviour is indicative of a ‘barrier’ effect against iodine at high oxygen partial pressures, with oxygen out-competing iodine for oxygen sites. Given that the inner oxide is likely to have a higher tetragonal phase fraction than the external oxide, due to the incorporation of fission products, this result could help to explain why there appears to be an oxygen effect on PCI-related SCC of zirconium alloys [256].

Another effect considered was the space charge of the system. Electrons have a higher rate of diffusion than oxygen vacancies in  $\text{ZrO}_2$ , leading to a build-up of oxygen vacancies near the metal-oxide interface as corrosion progresses [199]. This results in an overall positive charge (since the dominant oxygen vacancy is  $\text{V}_\text{O}^{\bullet\bullet}$ ) referred to as a space charge. When included in our Brouwer diagrams, this space charge had a negligible effect on the concentration or charge state of iodine up to a charge of  $10^{-1}$  holes/fu. This corresponds to a high concentration of oxygen vacancies relative to the equilibrium concentration, predicting that a significant deviation from equilibrium is not expected near the metal oxide interface as a result of a positive space charge.

## 6.4 Conclusions

- Iodine exhibits lower incorporation energies when occupying defects in monoclinic  $\text{ZrO}_2$  than in the tetragonal phase. However, as monoclinic is the low-temperature phase, intrinsic defect concentrations as calculated in the Brouwer diagrams will also be low, thereby requiring additional energy input to produce vacancies when the concentration of iodine is much larger than that of the intrinsic defects. This leads to relatively large

concentrations of iodine interstitial defects predicted in the monoclinic Brouwer diagrams, as interstitial sites are always available in the lattice.

- Defects involving iodine in the +1 oxidation state are present in significant concentrations, especially in monoclinic  $\text{ZrO}_2$ , indicating that filling of the  $p$  electronic sub-shell is not always energetically favourable compared to forming iodine with a smaller ionic radius developed through oxidation.
- The competition between iodine and oxygen for anion sites in  $\text{ZrO}_2$  is phase and oxygen pressure dependent. Higher oxygen pressures will reduce the equilibrium concentration of iodine substitutional defects on oxygen sites and iodine interstitial defects.
- At high oxygen pressures in monoclinic  $\text{ZrO}_2$ , iodine in the +1 oxidation state is predicted to occupy oxygen and interstitial sites. The reduction in  $\text{I}_\text{O}^{\bullet\bullet\bullet}$  and  $\text{I}_\text{i}^\bullet$  defects is small at higher oxygen pressures, indicating that iodine defects are still favourable even at high  $p_{\text{O}_2}$ .
- In tetragonal  $\text{ZrO}_2$  at high oxygen pressures, the concentration of iodine defects on anion sites decreases steeply. This is indicative of a barrier effect in the tetragonal phase with oxygen out-competing iodine for anion sites.

# Chapter 7

## Radioparagenesis of fission products in tetragonal $\text{ZrO}_2$

### 7.1 Introduction

As described in previous chapters, corrosive species in the pin such as iodine, produced directly as a result of uranium fission, are known to play a role in SCC [80, 81, 83]. However, iodine nuclei produced from fission are unstable. Furthermore, fission produces iodine precursors, mainly unstable isotopes of tellurium. As discussed in § 1.1.5, both iodine and tellurium are relatively common fission products, with combined independent yields from thermal fission of  $\text{U}^{235}$  above 25% [235–237, 239, 240]. In addition, xenon and caesium are also common fission products, as shown in Figure 7.1, with fission product masses firmly within the heavy nuclide peak of uranium and plutonium fission product distribution curves.

In Chapter 6, defect equilibria in  $\text{ZrO}_2$  were studied to examine the internal oxide layer's

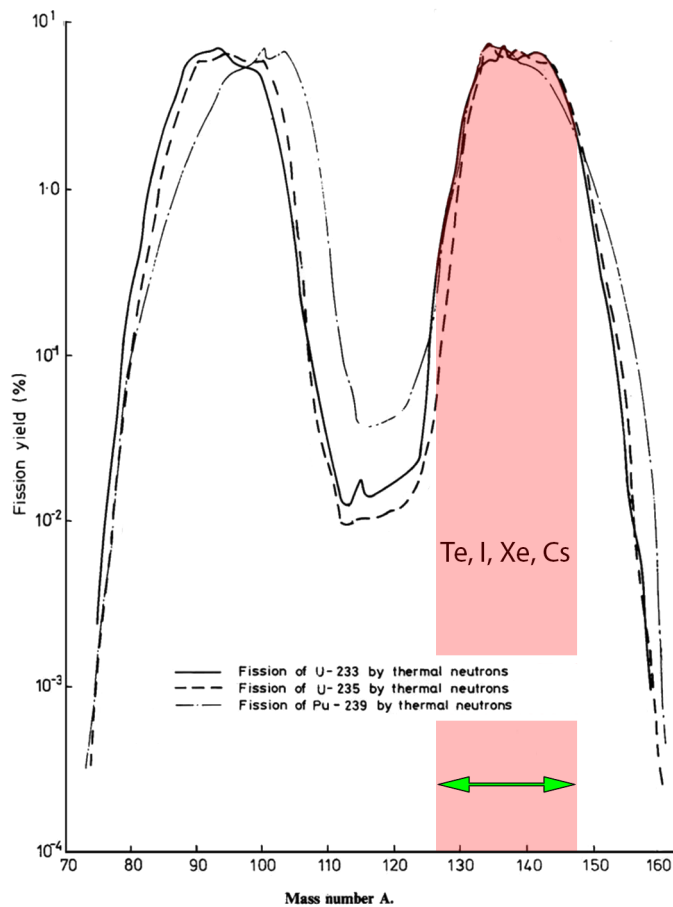


Figure 7.1: Plot of the percentage yield of nuclei with a given mass following a fission event. Range of masses corresponding to isotopes of Te, I, Xe and Cs are highlighted. Adapted from [25].

effectiveness as a barrier to iodine [233]. It was found that the tetragonal phase of  $\text{ZrO}_2$  is a better barrier to iodine ingress than monoclinic  $\text{ZrO}_2$ , especially at higher oxygen partial pressures. The iodine defect study, however, only informs us about one part of the SCC process. For a more holistic understanding, the life cycle of the iodine must also be taken into account.

Nuclei produced during fission are typically neutron-rich, resulting in decay modes such as  $\beta-$  or neutron emission. These will typically decay into other unstable nuclei, creating a decay chain. An example of a decay chain starting from  $\text{Te}^{135}$  is shown in Figure 7.2. In the case of tellurium nuclei, most decay into iodine, which then decays into xenon with different half-lives depending on the isotope. Several of these isotopes' fission yield and decay data were shown in

Table 1.2. The decay chain continues with xenon nuclei decaying into caesium, many isotopes of which have half lives measured in years. At this point, conventional power reactor fuel is retired long before a significant proportion of the caesium decays into barium. For this reason, only the elements tellurium through caesium are considered in this study.

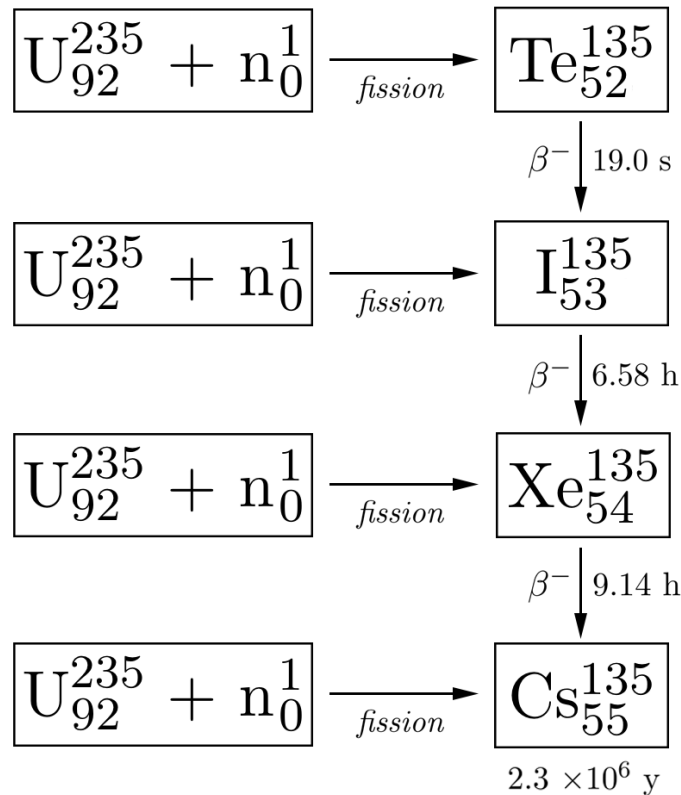


Figure 7.2: Diagram of the production of Te<sup>135</sup> decay chain elements with decay modes and half-lives shown.

The majority of thermal fission events occur in the outer rim of a fuel pellet. Given a fission product penetration depth of up to 8  $\mu\text{m}$  in ZrO<sub>2</sub> [241], a large proportion of fission products implant within the oxide. Implantation was discussed in detail in § 2.1.6. It has also been observed in PCI failures that there is a highly variable time delay (depending on burnup, fuel power history and ramping rate) of up to several hours between the power ramping of the reactor and the subsequent detection of failure of the cladding [250, 257, 258].

Figure 2.6 shows cladding failures occurring within 77 minutes following a ramp, whereas figure

2.8 shows how a cladding failure was detected within 4 hours of a power ramp<sup>1</sup>. Detection of a cladding failure gives an upper bound for the time delay because it relies on sensors in the core registering the presence of fission products in the coolant. This time delay is in line with the half-lives of many Te and I isotopes (Table 1.2) such that significant proportions of these isotopes will decay during this time delay, hinting that these phenomena could be related.

With each nuclear decay comes a change in the chemical interaction of the atom with its immediate environment. For example, an iodine dopant in  $\text{ZrO}_2$  may decay into xenon, which may then have a significantly different thermodynamic site preference from the one it inherited. This phenomenon, termed *radioparagenesis* by Stanek *et al.* [259–261], is known of and studied mainly in the context of nuclear wastes. By considering the implantation of fission products and the short half-lives of tellurium decay chain isotopes, this phenomenon is now examined in the context of in-pile operation. Determining the behaviour of each of these elements in the oxide layer may provide information about the initiation of SCC in fuel cladding. A quantum-mechanical calculation approach has therefore been adopted to model the behaviour of the decay chain elements tellurium through caesium within tetragonal  $\text{ZrO}_2$ .

## 7.2 Methodology

### 7.2.1 Defect volumes and stress states

As described in § 4.3.8, defect volumes were calculated by relaxing an unconstrained, defective supercell using the geometry optimisation task in CASTEP. Corrected defect volumes are

---

<sup>1</sup>These fuel pins had been irradiated before, but were stored outside a reactor 10 months prior to this test, resulting in a lower fission product inventory than what would normally be present in a real scenario.

reported for charged defects, where the reference volume is a supercell of equivalent charge. Similarly, in order to calculate the stress state on the supercell imposed by a defect, an isochoric calculation is performed as described in § 4.3.3. This type of calculation will generate the resultant stress tensor of the supercell after an energy minimisation. The magnitude of this stress tensor is then computed to give the overall pressure on the supercell.

### 7.2.2 Brouwer diagrams

Brouwer diagrams were constructed as outlined in § 4.4.2 in order to examine the defect equilibria of Te, I, Xe and Cs as a function of the oxygen partial pressure in tetragonal ZrO<sub>2</sub>. These diagrams were generated at 1500 K, corresponding to the temperature at which tetragonal ZrO<sub>2</sub> is thermally stabilised. A pair of Brouwer diagrams with extrinsic defect concentrations of 10<sup>-5</sup> and 10<sup>-3</sup> parts/fu were generated to examine low and high dopant concentrations, respectively. These values were chosen following from the iodine defect study in Chapter 6, as the concentrations of Te, Xe and Cs will be related to the concentration of I due to being part of the same decay series (e.g. all unstable isotopes of Te decay into I).

## 7.3 Results

### 7.3.1 Brouwer diagrams

#### Tellurium

Brouwer diagrams for tellurium defects are shown in Figure 7.3. At a tellurium defect concentration of  $10^{-5}$  parts/fu, the dominant defect was  $\text{Te}_\text{O}^{\bullet\bullet}$  over the oxygen pressure range of  $10^{-28}$  to  $10^{-7}$  atm.  $\text{Te}_\text{O}^{\bullet\bullet}$  is mainly charge compensated by intrinsic electronic defects at lower oxygen pressures, and zirconium vacancies at higher oxygen pressures. At higher oxygen pressures, tellurium preferentially occupies zirconium sites, producing the defect  $\text{Te}_{\text{Zr}}^{''''}$ , this time charge compensated by positive hole defects.

Tellurium on an oxygen site adopts a 0 charge state, which while not obvious (it may be expected to act like oxygen, also a group 6 element), can be understood when considering chemical behaviour and defect volume. Oxygen on its native site will readily adopt a charge state of -2. Tellurium on the other hand, exhibits an electronegativity of 2.1, significantly lower than the 3.5 value exhibited by oxygen. Nonetheless, the  $\text{V}_\text{O}^{\bullet\bullet}$  site is highly reducing, and will counter the tellurium ion's proclivity to oxidise. However, this is based on the usual ion positions in  $\text{ZrO}_2$ , especially for the  $\text{Zr}^{4+}$  ions, which lead to the high Madelung potential which stabilises the  $\text{O}^{2-}$  charge. Tellurium is a large atom which leads to a relaxation of the surrounding  $\text{Zr}^{4+}$  ions outwards by 0.58 Å (nearest neighbour Zr distances increase from 2.07 Å to 2.65 Å). This reduces the Madelung field at the site [262]. The overall effect results in a preference for tellurium to maintain a 0 oxidation state. Finally, when the tellurium concentration is increased to  $10^{-3}$  parts/fu, greater occupancy of the zirconium site is predicted above oxygen pressures of

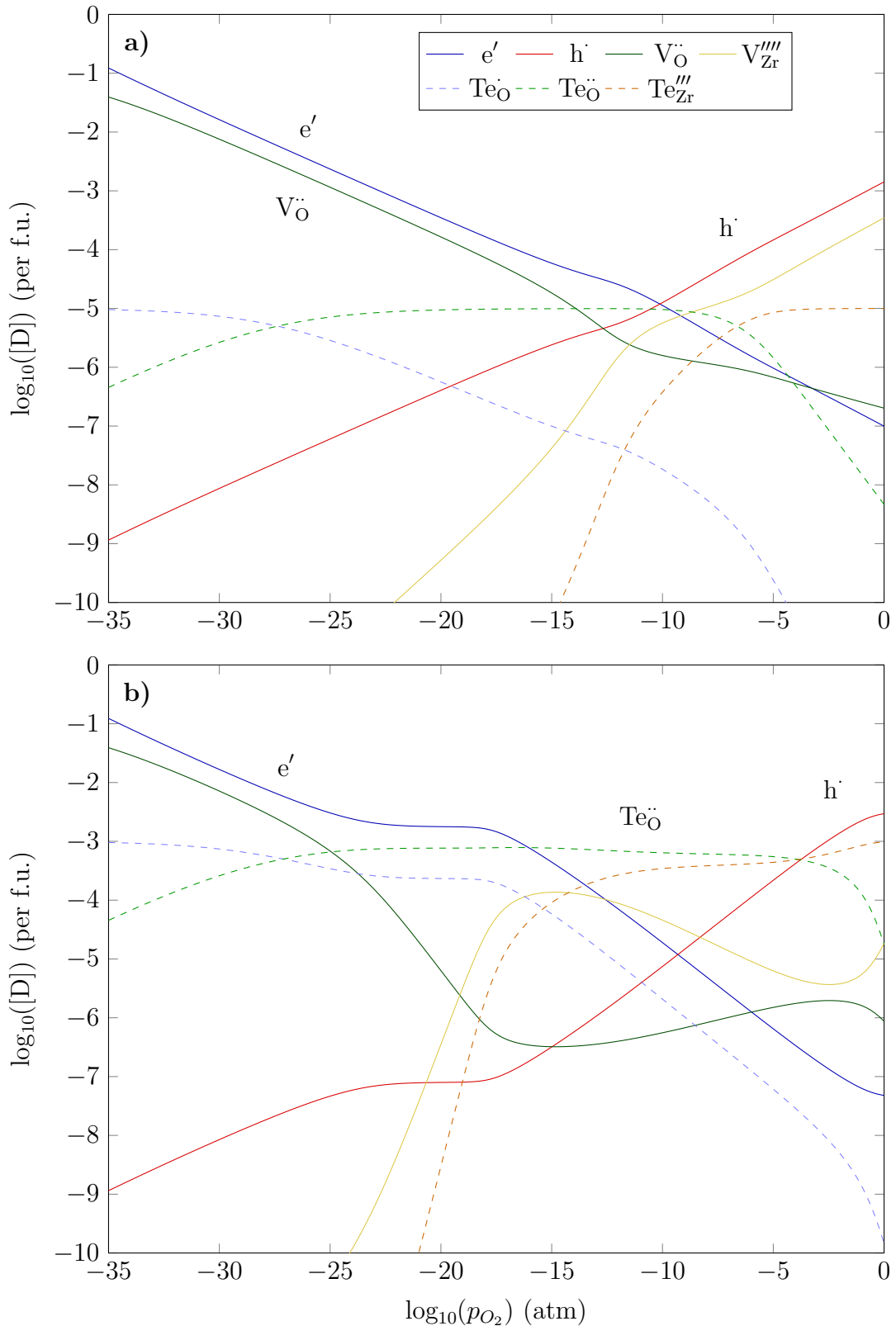


Figure 7.3: Brouwer diagrams for tetragonal phase  $ZrO_2$  point defects at tellurium concentrations of a)  $10^{-5}$  and b)  $10^{-3}$ , at a temperature of 1500 K.

$10^{-17}$  atm, forming the defect  $\text{Te}_{\text{Zr}}'''$ . This corresponds to a tellurium charge state of +1. While a drive to form an even more positive charge state for tellurium would normally be expected, in this case it is the dominant negative defect by an order of magnitude and provides charge compensation for positive hole and  $\text{Te}_\text{O}^{\bullet\bullet}$  defects. This time, the surrounding  $\text{O}^{2-}$  ions relax outwards from the Zr site, which lowers the Madelung field so that electrons are not forced away from the site to as great an extent [262].

As mentioned above, the presence of these defects and their sizes leads to lattice relaxation. This will impose an overall strain on the lattice and therefore a stress. Relative to the perfect crystal,  $\text{Te}_\text{O}^{\bullet\bullet}$  has a volume of  $35.98 \text{ \AA}^3$  (shown in Table 7.1). This is quite large for a positively charged defect due to the large size of the Te atom itself. When Te occupies the Zr site, the resulting  $\text{Te}_{\text{Zr}}'''$  has a defect volume of  $21.12 \text{ \AA}^3$ . This smaller defect volume than on the O site is due to Te adopting a +1 oxidation state while on the Zr site (as opposed to 0 on the O site), reducing its ionic radius. The defect volumes of Zr substitutional defects do however tend to increase as the decay chain progresses, as will be reported below.

## Iodine

Iodine was previously predicted in Brouwer diagrams (Figure 6.5) to produce the defects  $\text{I}_\text{O}^\bullet$  and  $\text{I}_{\text{Zr}}'''$  at low and high oxygen pressures respectively. Since the extrinsic defect site is similar for tellurium defects over most oxygen pressures,  $\beta$ - decay of tellurium could have directly produced iodine defects without requiring a change of site. Thus,  $\text{Te}_\text{O}^{\bullet\bullet}$  would decay and produce  $\text{I}_\text{O}^\bullet$  with a defect volume of  $46.94 \text{ \AA}^3$ , and  $\text{Te}_{\text{Zr}}'''$  would decay and produce  $\text{I}_{\text{Zr}}'''$  with a defect volume of  $27.15 \text{ \AA}^3$ . At the oxygen site, this means a defect volume change from  $35.98 \text{ (\text{Te}_\text{O}^{\bullet\bullet})}$  to  $46.94 \text{ \AA}^3$

( $I_O^\bullet$ ). This increase is in large part due to the change in charge state of the occupying ion from 0 to -1, as the ions are of similar size otherwise.

Similarly at the Zr site, the defect volume changes from 21.12 to 27.15 Å<sup>3</sup>. Both of these are relatively large increases in defect volume and will come with an increase in lattice stress in the immediate vicinity of the defect, especially if highly constrained. Of course, this process will take place continuously over time as tellurium atoms decay, with half-lives ranging from seconds to hours depending on the isotope. It is of note however, that PCI failures tend to occur after power ramps with a time delay, ranging from several minutes to hours after the transient. While not conclusive, this may hint at a mechanism involving decay processes.

## Xenon

Brouwer diagrams for xenon defects are shown in Figure 7.4. At a xenon concentration of  $10^{-5}$  parts/fu  $ZrO_2$ , the dominant xenon defect is  $Xe_O^{\bullet\bullet}$  at low oxygen pressures, and a combination of  $Xe_O^{\bullet\bullet}$ ,  $Xe_{Zr}^{''''}$  and  $Xe_{Zr}^{'''}$  at stoichiometry ( $10^{-9}$  atm) and higher. At a higher xenon concentration of  $10^{-3}$  parts/fu  $ZrO_2$ ,  $Xe_O^{\bullet\bullet}$  becomes the dominant defect over a greater oxygen pressure range, from  $10^{-30}$  to  $10^{-5}$  atm, with  $Xe_{Zr}^{''''}$  also present in high concentrations at oxygen pressures above  $10^{-20}$  atm. As a noble gas, it is expected that xenon in a 0 charge state ( $Xe_O^{\bullet\bullet}$  and  $Xe_{Zr}^{''''}$ ) will be prevalent since the full electronic shell provides a stable configuration.

$Xe_O^{\bullet\bullet}$  and  $Xe_{Zr}^{''''}$  have defect volumes of 42.26 and 32.48 Å<sup>3</sup> respectively. Following from the decay of iodine (which will likely be  $I_O^\bullet$ ), the defect volume on the oxygen site will fall marginally from 46.94 Å<sup>3</sup>, while the defect volume on the zirconium site increases from 27.15 Å<sup>3</sup>. The defect volume reduction on the oxygen site can be attributed to the charge state changing from -1 to

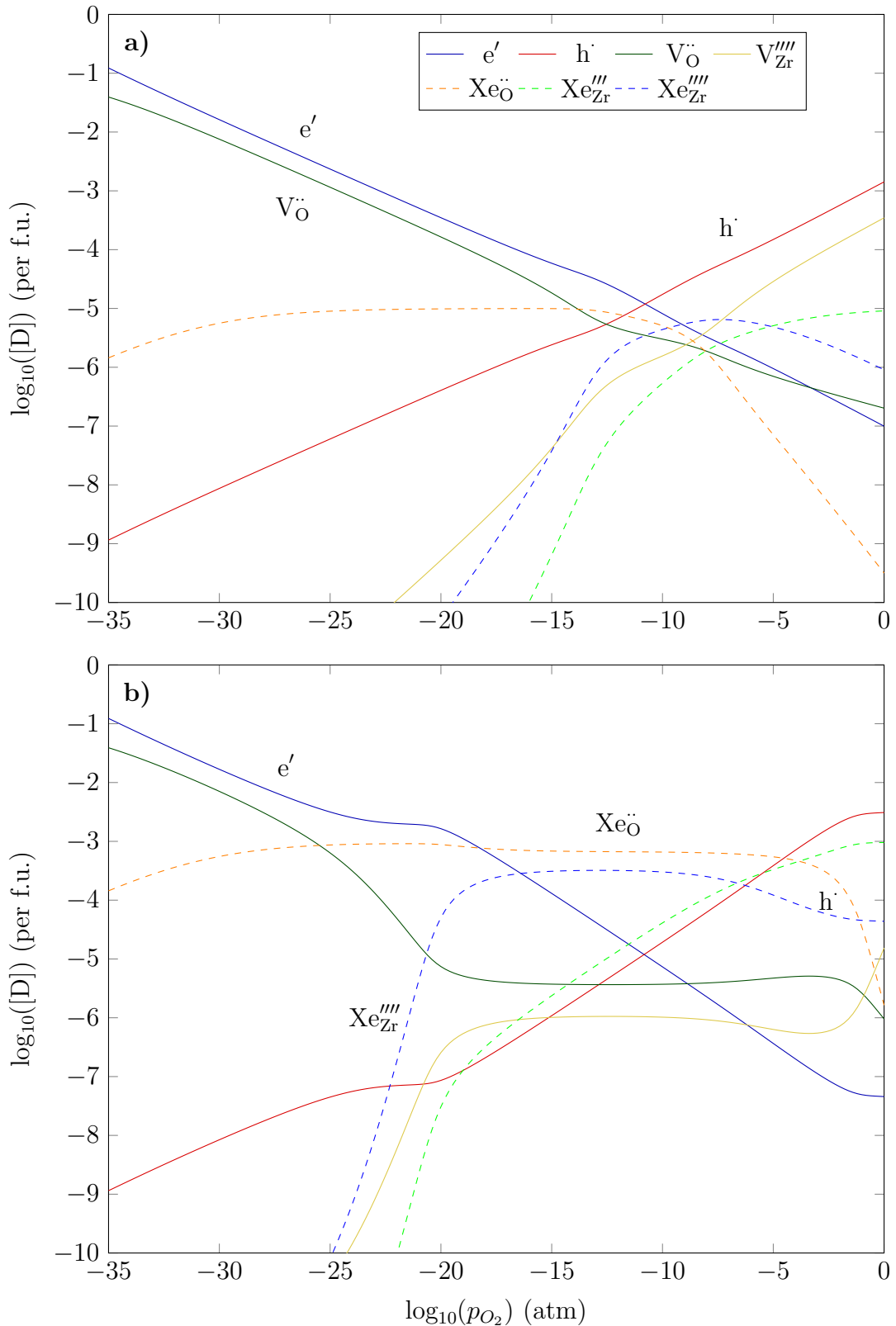


Figure 7.4: Brouwer diagrams for tetragonal phase  $ZrO_2$  point defects at xenon concentrations of a)  $10^{-5}$  and b)  $10^{-3}$ , at a temperature of 1500 K.

$0$  (i.e.  $I_O^\bullet$  to  $Xe_O^{\bullet\bullet}$ ), resulting in a smaller defect. The opposite is true for the zirconium site, where the charge state changes from  $+1$  to  $0$  (i.e.  $I_{Zr}'''$  to  $Xe_{Zr}''''$ ).

## Caesium

Brouwer diagrams for caesium defects are shown in Figure 7.5. Caesium defects were mostly unaffected by a change in oxygen pressure, with dominant defects only changing from  $Cs_O^{\bullet\bullet}$  to  $Cs_{Zr}'''$  at an oxygen pressure of  $10^{-30.5}$  atm, regardless of the caesium concentration. However, because additional charge compensation for caesium defects is necessary at higher caesium concentrations, an increase is seen in the concentration of  $V_O^{\bullet\bullet}$  to compensate for the negative  $Cs_{Zr}'''$  defects. The tendency for Cs to form cation substitutional defects is supported by implantation studies in cubic  $ZrO_2$  [89].

The defect volumes of  $Cs_O^{\bullet\bullet}$  and  $Cs_{Zr}'''$  were  $37.61$  and  $30.44 \text{ \AA}^3$  respectively, less than the Xe defects on the same site. This is consistent with the fact that Cs has a much smaller first ionisation energy than Xe, therefore presenting a smaller energy barrier to reducing its size on either site to improve lattice fit. Because of this, no further stresses are imposed on the lattice after Xe decays to Cs. It is therefore expected that only Te, I and Xe will be significant in this mechanism, as the only contribution to lattice stresses due to Cs would have occurred through direct implantation after fission.

### 7.3.2 Stress magnitudes and defect volumes

Table 7.1 shows the calculated defect volumes and stresses (based on the magnitude of the DFT calculated stress tensor) generated by the dominant defect types in tetragonal  $ZrO_2$ . In

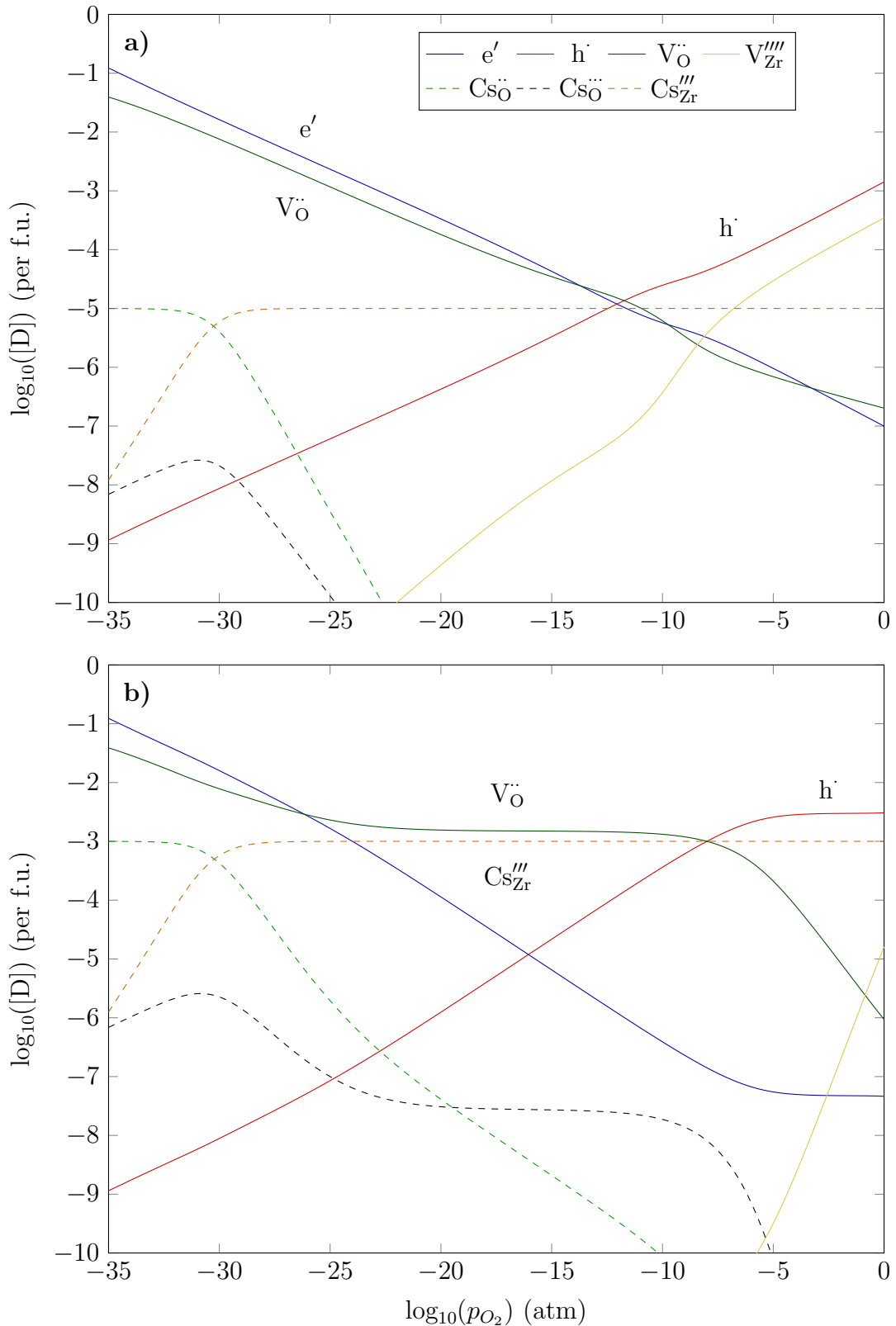


Figure 7.5: Tetragonal phase Brouwer diagrams of point defects at caesium concentrations of a)  $10^{-5}$  and b)  $10^{-3}$ , at a temperature of 1500 K.

this table, a negative stress value implies that the defective supercell is in a compressive stress state.

Table 7.1: Calculated defect volumes and stress tensor magnitudes of the dominant defect types in tetragonal ZrO<sub>2</sub>. Stress tensors are calculated for defective supercells.

Defect type	Defect volume relative to perfect crystal (Å <sup>3</sup> )	Defect volume relative to vacant site (Å <sup>3</sup> )	Stress tensor magnitude (GPa)
V <sub>O</sub> <sup>••</sup>	-7.22	0	-5.13
V <sub>Zr</sub> <sup>'''</sup>	5.92	0	9.21
Te <sub>O</sub> <sup>••</sup>	35.98	43.20	0.84
Te <sub>O</sub> <sup>•</sup>	41.65	48.88	3.29
Te <sub>Zr</sub> <sup>'''</sup>	29.01	23.09	13.04
Te <sub>Zr</sub> <sup>''</sup>	21.12	15.20	10.08
I <sub>O</sub> <sup>•••</sup>	30.57	37.79	-1.61
I <sub>O</sub> <sup>•</sup>	46.94	54.16	3.25
I <sub>Zr</sub> <sup>''</sup>	27.15	21.23	11.76
Xe <sub>O</sub> <sup>••</sup>	42.26	49.48	0.88
Xe <sub>Zr</sub> <sup>'''</sup>	32.48	26.57	13.53
Xe <sub>Zr</sub> <sup>''</sup>	31.72	25.81	10.65
Cs <sub>O</sub> <sup>••</sup>	37.61	44.84	1.50
Cs <sub>Zr</sub> <sup>''</sup>	30.44	24.53	10.60

The calculated stresses range from 1 to 13 GPa, with notable exceptions V<sub>O</sub><sup>••</sup> and I<sub>O</sub><sup>•••</sup> which are negative. These stresses are large because the supercell dimensions are constrained (to the dimensions of the non-defective tetragonal supercell), whereas in a real material some relaxation would occur. The more useful information contained here is the difference in stresses between defects (e.g. change in stress from Te<sub>O</sub><sup>••</sup> to I<sub>O</sub><sup>•</sup> is +2.41 GPa). It must also be noted that due to the size of the supercell, these reflect values at an effective defect concentration of 1 at.% each, and without the presence of other defects such as V<sub>O</sub><sup>••</sup> which will reduce overall stress.

As with the calculated stresses, it is useful to look at the change in defect volume between different defects to better understand the effect upon transmutation. In Table 7.1, the defect

volumes relative to those of the vacant site are provided as a first comparison, but other defects can also be compared (e.g. change in defect volume from  $\text{Te}_\text{O}^\bullet$  to  $\text{I}_\text{O}^\bullet$  is  $+5.29 \text{ \AA}^3$ ). Looking at the defect volumes relative to the vacant site, it was found that defects on O sites will have larger volumes than on Zr sites, regardless of the dopant ion.

Curiously, the calculated defect volumes do not follow the same proportional relationship with stress when looking at different atoms. For example,  $\text{Xe}_\text{O}^{\bullet\bullet}$  has a defect volume of  $42.26 \text{ \AA}^3$  (relative to the perfect crystal) while  $\text{Cs}_\text{O}^{\bullet\bullet}$  has a lower defect volume of  $37.61 \text{ \AA}^3$ . However, a greater stress is generated in the lattice by  $\text{Cs}_\text{O}^{\bullet\bullet}$  defects. Upon closer inspection of the calculated stress tensors,  $\text{Cs}_\text{O}^{\bullet\bullet}$  was found to produce a much more anisotropic stress state than  $\text{Xe}_\text{O}^{\bullet\bullet}$  (i.e. Xe exerts similar forces in all directions, whereas Cs exerts most force in the *a* and *b* directions). This is most likely due to the shape of the electronic orbitals. The Cs ion in this case mostly pushes in the high stiffness *a* and *b* directions (see Table 5.2 for the calculated elastic constants in tetragonal  $\text{ZrO}_2$ ), resulting in smaller strains and therefore a smaller overall defect volume.

## 7.4 Conclusions

- As fission products proceed down the decay chain from Te to Xe, the defects they produce in  $\text{ZrO}_2$  have progressively larger volumes.
- Substitutional defects on the Zr and O sites have volumes ranging from  $+20$  to  $+50 \text{ \AA}^3$  relative to the non-defective crystal.
- The defect evolution on the O site is predicted to be  $\text{Te}_\text{O}^{\bullet\bullet} \rightarrow \text{I}_\text{O}^\bullet \rightarrow \text{Xe}_\text{O}^{\bullet\bullet} \rightarrow \text{Cs}_\text{O}^{\bullet\bullet}$ . On the Zr site, the Brouwer diagrams predict  $\text{Te}_{\text{Zr}}'''' \rightarrow \text{I}_{\text{Zr}}''' \rightarrow \text{Xe}_{\text{Zr}}'''' \rightarrow \text{Cs}_{\text{Zr}}'''$ .

- The change in defect volume when Te<sub>Zr</sub><sup>'''</sup> decays and produces I<sub>Zr</sub><sup>'''</sup> is +6.03 Å<sup>3</sup>. This then decays and produces the defect Xe<sub>Zr</sub><sup>''''</sup>, which leads to another change in defect volume of +5.33 Å<sup>3</sup>. Similarly, at the oxygen site, Te<sub>O</sub><sup>••</sup> decays to produce I<sub>O</sub><sup>•</sup>, with a resulting defect volume change of +10.96 Å<sup>3</sup>.
- Cs substitutional defects have volumes smaller than Xe defects (though still positive), indicating that defect volumes will peak and then fall as the decay chain proceeds.
- The lattice mismatch of these defects in ZrO<sub>2</sub> will generate stresses. This may promote the formation of new surfaces (i.e. cracking).
- If enough fission products are implanted simultaneously, the rate of crack formation may become faster than the rate at which new passivating oxide can be produced, and typical I-SCC mechanisms will take over to failure.
- This process could be a contributing factor to fuel cladding failures observed after a power ramp, with reported time delays between ramp and failure commensurate with the decay rate of Te and I isotopes.

# Chapter 8

## Summary and further work

### 8.1 Structure properties and intrinsic defects in ZrO<sub>2</sub>

DFT calculations of non-defective ZrO<sub>2</sub> predicted the correct order of phase stability for the monoclinic, tetragonal and cubic phases. Calculated lattice parameters of each phase also agreed to within 2% of experimental values. Calculated band gaps of each phase were underestimated by approximately 2 eV, which is typical when modelling using GGA-DFT. A Hubbard +U study revealed that the calculated band gaps could be increased by up to 1 eV, but that the symmetry of the supercells would be distorted in the process.

Helmholtz free energy calculations at temperatures ranging from 0 to 2500 K showed that the lowest energy phase changes from monoclinic to tetragonal, but not from tetragonal to cubic. Furthermore, the predicted transition temperature of the monoclinic-tetragonal phase change is underestimated by almost 1100 K. This is attributed to lack of thermal expansion in the constant-volume harmonic model but could also be a consequence of the kinetic barrier of the

phase transformation.

Elastic constants were calculated and reported for each phase. The cubic phase was predicted to have the highest stiffness, followed by monoclinic and then tetragonal. The elastic constants were used to calculate the bulk modulus of each phase, and it was shown that the monoclinic and tetragonal bulk moduli agreed with experimental values to within 5%. The calculated bulk modulus in the cubic phase could not be compared to an experimental value in pure  $\text{ZrO}_2$ , but was 15% larger than that of YSZ.

Formation energy calculations showed that Zr vacancies in all three phases are fully-charged ( $V_{\text{Zr}}^{'''}$ ) over most Fermi levels, while O vacancies change from  $V_O^{\bullet\bullet}$  at low Fermi levels to  $V_O^\times$  when the Fermi level is larger than 3 eV. The defect cluster with the lowest formation energy per defect was the fully-charged Schottky, followed by O Frenkel defects and then Zr Frenkel defects. This can be partly attributed to defect sizes, with Schottky defects predicted to have the smallest defect volumes in all phases, again followed by O Frenkel defects and then Zr Frenkel defects.

Brouwer diagrams were constructed for each phase, and showed that the defect equilibria are dominated by  $V_{\text{Zr}}^{'''}$ ,  $V_O^{\bullet\bullet}$ ,  $h^\bullet$  and  $e'$  defects. Interstitial defects appear only at very low concentrations relative to these defects. This suggests that Schottky defects will be the main cluster defect near stoichiometry. At high  $p_{\text{O}_2}$ ,  $V_{\text{Zr}}^{'''}$  is charge-compensated by  $h^\bullet$  defects, while at low  $p_{\text{O}_2}$ ,  $V_O^{\bullet\bullet}$  is charge-compensated by  $e'$  defects.

Cubic  $\text{ZrO}_2$  supercells sometimes exhibited a loss of symmetry when performing defect energy minimisations. This behaviour and anomalous results from other calculations led to the conclusion that the cubic phase might not be modelled accurately with present DFT methods. Work

by Burr *et al.* [225] supports this result. In addition, the high temperatures required to stabilise the cubic phase limit the ability to examine defect equilibria due to the high intrinsic defect concentrations. Cubic phase Brouwer diagrams were therefore not constructed in subsequent extrinsic defect studies.

## 8.2 Iodine doping and oxygen competition

Iodine point defects were studied in the three phases to investigate defect energies and these were used to construct Brouwer diagrams in the monoclinic and tetragonal phases. It was found that in monoclinic  $\text{ZrO}_2$ , iodine has lower incorporation energies onto both Zr and O sites than in the tetragonal phase. In all phases,  $\text{I}_\text{O}$  defects exhibit the smallest incorporation energies, followed by  $\text{I}_\text{Zr}$  and then  $\text{I}_\text{i}$ .

Four unique interstitial sites for iodine were found in the monoclinic phase, and two in the tetragonal and cubic phases. It was found that the lowest energy interstitial sites changed in the tetragonal and cubic phases depending on the Fermi level, whereas only one site was favourable in the monoclinic phase. Iodine interstitial defects will only exist as  $\text{I}_\text{i}^\bullet$  at low Fermi levels or  $\text{I}_\text{i}'$  at high Fermi levels, whereas  $\text{I}_\text{i}^\times$  defects will have a higher formation energy regardless of the Fermi level. At the O site, iodine will form  $\text{I}_\text{O}^\bullet$  and to a lesser extent,  $\text{I}_\text{O}^{\bullet\bullet}$  defects. At the Zr site, iodine will form  $\text{I}_\text{Zr}'''$  defects.

Brouwer diagrams showed that there is competition between iodine and oxygen for anion sites in  $\text{ZrO}_2$ , and that this competition is dependent on both phase and oxygen pressure. It was found that higher oxygen pressures will reduce the equilibrium concentration of  $\text{I}_\text{O}$  and  $\text{I}_\text{i}$  defects

in both phases, but with a more significant effect in the tetragonal phase. A combination of high oxygen pressure and tetragonal phase led to oxygen out-competing iodine for anion sites. This will reduce diffusion rates of iodine in the oxide layer.

### 8.3 Decay chain elements in $\text{ZrO}_2$

I nuclei produced during nuclear fission are unstable and will therefore be part of a decay chain. Decay of Te precursors are the major source of I. Furthermore, Xe and Cs are predicted to be present in significant concentrations based on decay rates and fission yields. Decay rates of Te and I isotopes were also found to be commensurate with the time taken for PCI failures to occur following a power ramp, hinting that these phenomena may be related. From the iodine study, tetragonal phase  $\text{ZrO}_2$  was predicted to provide a greater barrier effect against iodine. Thus, defect equilibria and defect volumes of decay chain elements Te to Cs were investigated in tetragonal  $\text{ZrO}_2$ .

Brouwer diagrams predicted low concentrations of interstitial defects relative to O and Zr substitutional defects. At the O site, the defect evolution is predicted to be  $\text{Te}_{\text{O}}^{\bullet\bullet} \rightarrow \text{I}_{\text{O}}^{\bullet} \rightarrow \text{Xe}_{\text{O}}^{\bullet\bullet} \rightarrow \text{Cs}_{\text{O}}^{\bullet\bullet}$  while at the Zr site, the Brouwer diagrams predict  $\text{Te}_{\text{Zr}}^{\prime\prime\prime} \rightarrow \text{I}_{\text{Zr}}^{\prime\prime\prime} \rightarrow \text{Xe}_{\text{Zr}}^{\prime\prime\prime} \rightarrow \text{Cs}_{\text{Zr}}^{\prime\prime\prime}$ .

As Te decays towards Xe, the defects produced have progressively larger volumes. All substitutional defects have positive volumes ranging from +21 to +46  $\text{\AA}^3$  relative to the non-defective crystal, with the largest major defect being  $\text{I}_{\text{O}}^{\bullet}$  ( $46.94 \text{\AA}^3$ ). All O substitutional defects were found to be larger than those on the Zr site. The stresses generated by defects on a constrained supercell were also calculated and shown to follow the same trends as the defect volumes.

Stresses imposed by implanted fission products and their decay chain elements will promote the formation of new surfaces. During a power ramp, the rate of fission product implantation within the oxide will increase. The largest stresses will occur in the hours following the ramp when I concentrations reach a maximum level. Stresses will begin to fall as more I nuclei decay into Xe and Cs, which have smaller defect volumes. This mechanism is proposed as a contributing factor to PCI failures, as larger ramps are more likely to lead to failure and the rate of new crack formation may exceed the rate at which a passivating oxide is developed.

## 8.4 Further work

### 8.4.1 Temperature effects in intrinsic defect simulations

$\text{ZrO}_2$  crystal structures are sensitive to changes in interatomic spacing, sometimes causing a loss of supercell symmetry when defects are modelled. There is a need to accurately represent anisotropic effects such as thermal expansion in the different phases over a broad temperature range. This can be achieved by developing potentials and conducting classical or quantum MD simulations to test their performance through comparison to experimental data. Quantum MD simulations, however, are very computationally expensive. A good starting point is to perform phonon calculations of the different  $\text{ZrO}_2$  phases in conjunction with the quasi-harmonic method. This is an extension to the method outlined in § 4.3.5 which can be used to find the ground state lattice positions (and therefore interatomic spacings) at different temperatures. These values are used to determine thermal expansion coefficients of  $\text{ZrO}_2$  along each lattice vector. Potentials can then be developed with these thermal expansion coefficients, which will

be able to reproduce the anisotropic effects in different phases.

### 8.4.2 Fission product empirical potential

In order to study the interaction of fission products with larger features in the cladding microstructure, such as dislocations and grain boundaries, it is necessary to develop empirical potentials for use in molecular dynamics simulations. Grain boundary transport is of particular interest, but this would require something on the order of  $10^4$  atoms to represent a system large enough to develop a reasonable degree of accuracy. This cannot currently be achieved using DFT due to the significant amount of computing resources required to run such a simulation.

The development of an iodine and xenon potential with  $\text{ZrO}_2$  should be prioritised in order to run simulations to determine the migration of iodine within  $\text{ZrO}_2$ , followed by the behaviour of xenon at sites occupied by iodine.

### 8.4.3 $\text{Zr}/\text{ZrO}/\text{ZrO}_2$ interface study

The inner oxide is not a homogeneous structure, as described in Chapter 3. Figure 8.1 shows the existence of a  $\text{ZrO}$  phase up to 200 nm thick at the interface between  $\text{ZrO}_2$  and Zr metal. The presence of  $\text{ZrO}$  and even oxygen-saturated Zr metal will have an effect on the thermodynamic equilibria of different fission products. An interface study can be conducted using DFT, to determine stresses at the interfaces of Zr and  $\text{ZrO}$ , and  $\text{ZrO}$  and  $\text{ZrO}_2$ . Studying the aggregate effect of these interfaces on fission product behaviour may require larger molecular dynamics simulations.

The crystal structure of the ZrO phase has been studied using both simulation and high-resolution electron microscopy, with two likely crystal structures being proposed [263]. Further atomistic studies must be conducted to determine the stability of each crystal structure of ZrO when constrained by ZrO<sub>2</sub> and oxygen-saturated Zr metal interfaces (i.e. can we determine if stress stabilises the ZrO layer?).

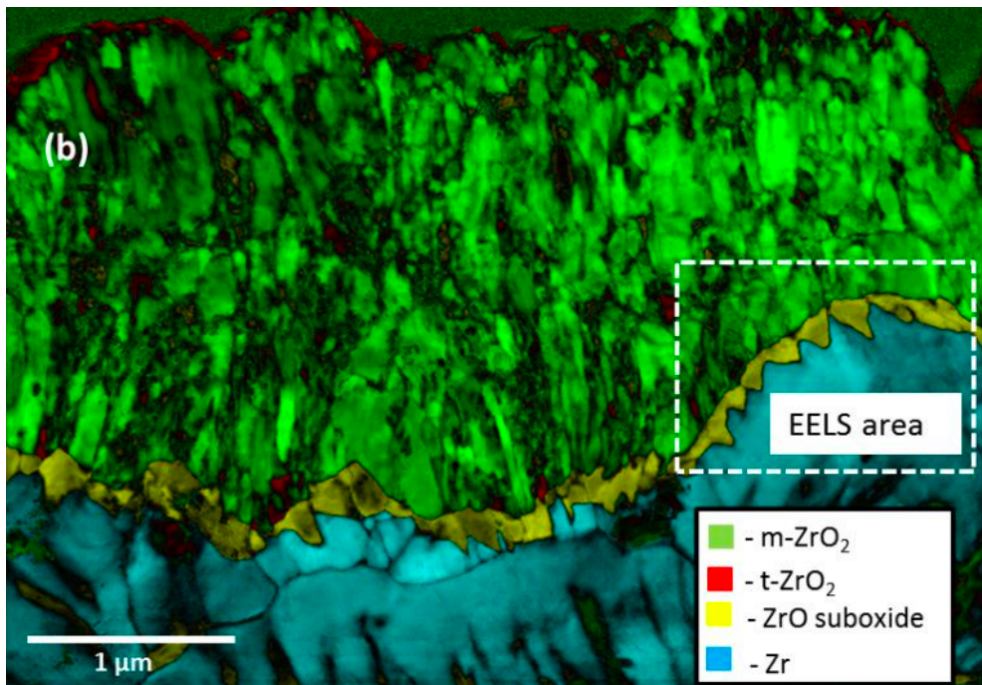


Figure 8.1: STEM image of a Zr-1.0%Nb sample oxidised in simulated PWR water at 360 °C for 120 days. Taken from [264].

## Bromine

Bromine is another halogen atom produced from fission, although in smaller quantities than iodine. Since bromine has similar chemical behaviour to iodine, though it is somewhat smaller ( $I^-$  radius = 2.20 Å,  $Br^-$  radius = 1.96 Å [167]), it would be of interest to conduct a defect study with bromine in ZrO<sub>2</sub> similar to that in Chapter 6. Iodine produced defects which were in either the +1 or -1 oxidation states (e.g.  $I''_{Zr}$  and  $I_O^\bullet$ ). This would help determine if Br defects also exhibit this behaviour, or if the 0 oxidation state demonstrates greater stability at certain

sites. Furthermore, the pathway to Br isotopes will be different to I in terms of decay rates and this must also be considered.

#### 8.4.4 Defect volumes

Defect volumes are useful quantities for comparing different defects and explaining their behaviour, however, the calculation of defect volumes for charged defects in DFT models is a contentious topic. While defect volumes of charged point defects are often reported in the literature, reported values are often unphysically large [265]. For this reason, the charged defect volumes reported in this thesis used the volume of an equivalently charged non-defective supercell as the reference volume. This method has been shown to yield more reasonable defect volumes for charged defects [187], but this is still only a rudimentary correction.

One method for obtaining more accurate defect volumes is to use larger supercells (to reduce finite size effects and self-interaction errors across the periodic boundary). Another possibility is using hybrid-AE functionals which reproduce a more accurate electronic band structure, thereby reducing energy errors and improving the accuracy of interatomic forces when adding or removing electrons in a defective system with non-zero charge [266].

#### 8.4.5 Experimental work

##### Tetragonal phase stabilisation

A key finding in this thesis is that tetragonal phase ZrO<sub>2</sub> (as opposed to monoclinic) provides the barrier effect against corrosive fission products. It would therefore be useful to conduct

experiments on claddings designed to maximise the content of tetragonal phase  $ZrO_2$  in the internal oxide layer. While this can be achieved with a tetragonal stabilising dopant (e.g. scandium or yttrium), this will increase the concentration of oxygen vacancies which may lead to reduced corrosion performance.

Another method to increase the proportion of tetragonal phase in the oxide layer is to reduce the Zr grain size. This is an attractive option because the chemical composition of the cladding will be unchanged, and the increased strength does not come at the cost of ductility. The very small grain sizes required (nanoscale) will, however, negatively impact the creep resistance of the cladding, so if this is not a realistic modification for the entire clad, it may be better to refine only the Zr liner grain size.

### Oxygen environment control

A key result in Chapter 6 was that at a high enough  $p_{O_2}$  above stoichiometry, the concentration of  $I_O$  and  $I_i$  defects began to fall significantly, indicating competition between oxygen and iodine for anion sites in tetragonal  $ZrO_2$ . Increasing the  $p_{O_2}$  in fuel pins may therefore impede the bulk diffusion of iodine through the oxide layer, slowing the corrosion process. In-pile irradiation tests (e.g. power ramps, high burn-up behaviour) to examine the effect of increasing the oxygen content in fuel pins would provide useful data on PCI performance. Presently, fuel pins are filled with helium because it is an inert gas, it does not affect the neutronics within the core and has a high thermal conductivity (compared to other gases). One option for varying oxygen content in a fuel pin is to use a fill gas which is a mixture of helium and oxygen. Although oxygen (most of which is  $O_8^{16}$ ) is not inert and has a lower thermal conductivity than helium,

it is highly resistant to neutron activation due to a combination of very low thermal neutron absorption cross-section and three stable isotopes (i.e. three consecutive neutron captures are required to produce an unstable  $O_8^{19}$  nucleus). Adding oxygen to the fill gas is also a much simpler (and therefore cheaper) method of increasing oxygen content compared to changing the stoichiometry of the fuel.

# References

- [1] A. Gando, Y. Gando, K. Ichimura, H. Ikeda, K. Inoue, Y. Kibe, Y. Kishimoto, M. Koga, Y. Minekawa, T. Mitsui, and Others. Partial radiogenic heat model for Earth revealed by geoneutrino measurements. *Nature Geoscience*, 4(9):647, 2011. (Cited on page 1)
- [2] W. M. Thornton. XV. The relation of oxygen to the heat of combustion of organic compounds. *The London, Edinburgh, and Dublin Philosophical Magazine and Journal of Science*, 33(194):196–203, 1917. (Cited on page 1)
- [3] A. Lokhov. Technical and economic aspects of load following with nuclear power plants. *NEA, OECD, Paris, France*, 2011. (Cited on page 2, 6)
- [4] N. K. Aras, M. P. Menon, and G. E. Gordon. Ranges of fragments from fission of U<sup>235</sup> with thermal neutrons and the kinetic energy deficit. *Nuclear Physics*, 69(2):337–361, 1965. (Cited on page 3)
- [5] Fastfission. Binding energy curve. Available at <https://tinyurl.com/binding192>. Accessed 03-08-2019, 2012. (Cited on page 5)
- [6] K. D. Kok. *Nuclear engineering handbook*. CRC Press, 2016. (Cited on page 5)
- [7] W. L. Server and R. K. Nanstad. International Atomic Energy Agency Coordinated Research Projects on Structural Integrity of Reactor Pressure Vessels. In *Effects of Radiation on Nuclear Materials and the Nuclear Fuel Cycle: 24th Volume*. ASTM International, 2010. (Cited on page 5)
- [8] A. Durmaz and H. Yavuz. Exergy analysis of a pressurized-water reactor nuclear-power plant. *Applied Energy*, 69:39–57, 2001. (Cited on page 5)

- [9] C. E. Beyer and D. D. Lanning. Review of fuel thermal conductivity data and models. *Seminar on Thermal Performance of High Burn-Up LWR Fuel*, page 57, 1998. (Cited on page 6)
- [10] World Nuclear Association. World Nuclear Performance Report 2018. 2018. (Cited on page 7)
- [11] C. J. Christensen, A. Nielsen, A. Bahnsen, W. K. Brown, and B. M. Rustad. Free-neutron beta-decay half-life. *Physical Review D*, 5(7):1628, 1972. (Cited on page 7)
- [12] A. C. Marino. Crack and dishing evolution models and PCI-SCC considerations for fuel pellets in a quasi-bi-dimensional environment. In *Pellet-clad Interaction in Water Reactor Fuels: Seminar Proceedings, Aix-en-Provence, France, 9-11 March 2004*, page 379. OECD Publishing, 2005. (Cited on page 8)
- [13] W. Doerr, A. Hoff, W. Jentzen, D. Curran, A. Chotard, and P. Deydier. Nuclear reactor green and sintered fuel pellets, corresponding fuel rod and fuel assembly, 2015. (Cited on page 8)
- [14] A. G. Croff. *Nuclear Fuels and Isotopes*. Wiley Online Library, 2003. (Cited on page 8)
- [15] P. P. King. Pressurization Of Nuclear Fuel Rods Using Laser Welding. *Advances in Laser Engineering and Applications*, 247:24–29, 1980. (Cited on page 9)
- [16] D. Pramanik, M. Ravindran, R. Hemantha, and R. N. Jayaraj. Innovative Process Techniques to Optimize Quality and Microstructure of UO<sub>2</sub> Fuel for PHWRs in India. Technical report, 2010. (Cited on page 9)
- [17] J. Tulenko and G. Subhash. Development of an enhanced accident-tolerant composite UO<sub>2</sub> fuel pellet with a dopant of SiC whiskers. Technical report, 2013. (Cited on page 10)
- [18] S. Wisner and R. B. Adamson. Combined effects of radiation damage and hydrides on the ductility of Zircaloy-2. *Nuclear Engineering and Design*, 185(1):33–49, 1998. (Cited on page 11)

- [19] K. Nogita and K. Une. Formation of pellet-cladding bonding layer in high burnup BWR fuels. *Journal of Nuclear Science and Technology*, 34(7):679–689, 1997. (Cited on page 11, 22, 41)
- [20] T. Einfal, O. Planinšek, and K. Hrovat. Methods of amorphization and investigation of the amorphous state. *Acta Pharmaceutica*, 63(3):305–334, 2013. (Cited on page 11)
- [21] L. M. Wang, S. X. Wang, and R. C. Ewing. Amorphization of cubic zirconia by caesium-ion implantation. *Philosophical Magazine Letters*, 80(5):341–347, 2000. (Cited on page 11, 37)
- [22] K. E. Sickafus, H. Matzke, T. Hartmann, K. Yasuda, J. A. Valdez, P. Chodak III, M. Nas-tasi, and R. A. Verrall. Radiation damage effects in zirconia. *Journal of Nuclear Materials*, 274(1):66–77, 1999. (Cited on page 12, 37)
- [23] K. Konashi, T. Yato, and H. Kaneko. Radiation effect on partial pressure of fission product iodine. *Journal of Nuclear Materials*, 116(1):86–93, 1983. (Cited on page 12, 35)
- [24] BenRG. Plot of atomic isotopes. Available at <https://tinyurl.com/isotopes192>. Accessed 03-08-2019. (Cited on page 13)
- [25] T. R. England and B. F. Rider. ENDF/B Yield Evaluation for 1992: Methods and Content. Technical report, Los Alamos National Lab., 1992. (Cited on page 15, 149)
- [26] R. L. Auble, H. R. Hiddleston, and C. P. Browne. Nuclear data sheets for  $A = 131$ . *Nuclear Data Sheets*, 17(4):573–615, 1976. (Cited on page 16)
- [27] M. M. Bé, V. Chisté, C. Dulieu, E. Browne, V. Chechev, N. Kuzmenko, R. Helmer, A. Nichols, E. Schönfeld, and R. Dersch. Table of radionuclides (Vol. 1,  $A = 1$  to 150). *Bureau International des Poids et Mesures, France: Sèvres*, 2004. (Cited on page 16)
- [28] M. M. Bé, V. Chisté, C. Dulieu, X. Mougeot, V. P. Chechev, N. K. Kuzmenko, F. G. Kondev, A. Luca, M. Galán, and A. L. Nichols. Table of Radionuclides (Vol. 6,  $A = 22$  to 242). *Monographie BIPM-5*, 2011. (Cited on page 16)
- [29] Y. Khazov, A. Rodionov, and F. G. Kondev. Nuclear data sheets for  $A = 133$ . *Nuclear Data Sheets*, 112(4):855–1113, 2011. (Cited on page 16)

- [30] M. M. Bé, V. Chisté, C. Dulieu, E. Browne, V. Chechev, N. Kuzmenko, F. G. Kondev, A. Luca, M. Galán, and A. Pearce. Table of radionuclides (Vol. 4-A= 133 to 252). *BIPM, Sevres*, 2008. (Cited on page 16)
- [31] A. A. Sonzogni. Nuclear Data Sheets for A = 134. *Nuclear Data Sheets*, 103(1):1–182, sep 2004. (Cited on page 16)
- [32] B. Singh, A. Rodionov, and Y. Khazov. Nuclear Data Sheets for A = 135. *Nuclear Data Sheets*, 109(3):517–698, mar 2008. (Cited on page 16)
- [33] E. A. Mccutchan. Nuclear Data Sheets for A = 136. *Nuclear Data Sheets*, 152:331–667, 2018. (Cited on page 16)
- [34] E. Browne and J. K. Tuli. Nuclear data sheets for A = 137. *Nuclear Data Sheets*, 108(10):2173–2318, 2007. (Cited on page 16)
- [35] J. Chen. Nuclear Data Sheets for A = 138. *Nuclear Data Sheets*, 146:1–386, 2017. (Cited on page 16)
- [36] OECD. *Plutonium Fuel: An Assessment*. NEA, Paris, 1989. (Cited on page 17)
- [37] R. C. Ewing, W. J. Weber, and J. Lian. Nuclear waste disposal-pyrochlore ( $A_2B_2O_7$ ): Nuclear waste form for the immobilization of plutonium and minor actinides. *Journal of Applied Physics*, 95(11):5949–5971, 2004. (Cited on page 17)
- [38] B. Cox. Pellet-clad interaction (PCI) failures of zirconium alloy fuel cladding — A review. *Journal of Nuclear Materials*, 172(3):249–292, 1990. (Cited on page 19, 20, 25, 29, 131)
- [39] T. Alam, M. K. Khan, M. Pathak, K. Ravi, R. Singh, and S. K. Gupta. A review on the clad failure studies. *Nuclear Engineering and Design*, 241(9):3658–3677, 2011. (Cited on page 19, 20)
- [40] M. F. Lyons, D. H. Coplin, and G. G. Jones. High performance UO<sub>2</sub> Fuel program. *General Electric Co., Quarterly Progress Reports*, (GEAP-3771-10), 1963. (Cited on page 19)

- [41] D. O. Sheppard. Data Report IFA-507 From BOL to 15.4 MWd/kgUO<sub>2</sub>, 1982. (Cited on page 20)
- [42] M. Oguma. Cracking and relocation behavior of nuclear fuel pellets during rise to power. *Nuclear Engineering and Design*, 76(1):35–45, 1983. (Cited on page 21)
- [43] L. A. Walton and D. L. Husser. Fuel pellet fracture and relocation. *International Working Group on Water Reactor Fuel Performance and Technology*, 17(2):147–161, 1983. (Cited on page 21)
- [44] C. Bagger, M. Mogensen, and C. T. Walker. Temperature measurements in high burnup UO<sub>2</sub> nuclear fuel: Implications for thermal conductivity, grain growth and gas release. *Journal of Nuclear Materials*, 211(1):11–29, 1994. (Cited on page 22)
- [45] M. Suzuki, H. Saitou, and T. Fuketa. RANNS code analysis on the local mechanical conditions of cladding of high burnup fuel rods under PCMI in RIA-simulated experiments in NSRR. *Journal of Nuclear Science and Technology*, 43(9):1097–1104, 2006. (Cited on page 22)
- [46] P. Rudling, R. Adamson, B. Cox, F. Garzarolli, and A. Strasser. High burnup fuel issues. *Nuclear Engineering and Technology*, 40(1):1–8, 2008. (Cited on page 22)
- [47] W. J. Penn, R. K. Lo, and J. C. Wood. CANDU fuel—power ramp performance criteria. *Nuclear Technology*, 34(2):249–268, 1977. (Cited on page 23)
- [48] R. D. MacDonald, D. G. Hardy, C. E.L. Hunt, and J. A. Scoberg. Unirradiated UO<sub>2</sub> in irradiated zirconium alloy sheathing. *Atomic Energy of Canada Limited (Report)*, (AECL-6579), 1979. (Cited on page 23, 29, 31)
- [49] D. Hardy, A. Bain, and R. Meadowcroft. in:. *Proc. ANS Topical Meeting on Water Reactor Fuel Performance*, page 198, 1977. (Cited on page 23)
- [50] H. Knaab, M. Gartner, and F. Sontheimer. KWU’s experimental basis for power ramping and cycling performance of LWR fuel. In *Technical committee meeting on power ramping, cycling and load following behaviour of water reactor fuel*, pages 84–93, 1987. (Cited on page 23)

- [51] M. Billaux and H. Moon. Pellet-cladding mechanical interaction in boiling water reactors. In *Pellet-clad Interaction in Water Reactor Fuels: Seminar Proceedings, Aix-en-Provence, France, 9-11 March 2004*, page 43. OECD Publishing, 2005. (Cited on page 23)
- [52] S. K. Yagnik, D. J. Sunderland, and B. C. Cheng. Effect of PWR Re-start Ramp Rate on Pellet-Cladding Interactions. *Nuclear Science - Seminar Proceedings*, pages 31–50, 2004. (Cited on page 23, 24)
- [53] J. Brochard, F. Bentejac, N. Hourdequin, S. Seror, C. Verdeau, O. Fandeur, S. Lansiart, and P. Verpeaux. Modelling of pellet cladding interaction in PWR fuel. *Proceedings of the SMIRT 16 conference*, 1314, 2001. (Cited on page 25)
- [54] M. Peehs, H. Stehle, and E. Steinberg. Out-of-Pile Testing of Iodine Stress Corrosion Cracking in Zircaloy Tubing in Relation to the Pellet-Cladding Interaction Phenomenon. *American Society for Testing and Materials, Special Technical Publication*, (681):244–260, 1978. (Cited on page 26)
- [55] R. Haddad and B. Cox. Investigations of crack initiation during environmentally induced cracking of the Zircaloys. *Atomic Energy of Canada Limited, (Report)*, (AECL-8104), 1983. (Cited on page 26)
- [56] T. A. Haynes, J. A. Ball, J. H. Shea, and M. R. Wenman. Modelling pellet-clad mechanical interaction during extended reduced power operation in bonded nuclear fuel. *Journal of Nuclear Materials*, 465:280–292, 2015. (Cited on page 26)
- [57] J. C. Wood, B. A. Surette, I. M. London, and J. Baird. Environmentally induced fracture of zircaloy by iodine and cesium: the effects of strain rate, localized stresses and temperature. *Journal of Nuclear Materials*, 57(2):155–179, 1975. (Cited on page 26)
- [58] B. N. Nobrega, J. S. King, G. S. Was, and R. B. Adamson. The influence of localized stresses and strains on the iodine scc behavior of Zircaloy-2 tubing. *Journal of Nuclear Materials*, 131(3):126–135, 1985. (Cited on page 26)
- [59] B. C. Syrett, R. L. Jones, and D. Cubicciotti. The effect of axial stress to hoop stress ratio on the susceptibility of unirradiated Zircaloy-4 to iodine stress corrosion cracking. *Journal of Nuclear Materials*, 1981. (Cited on page 26)

- [60] S. Shimada and M. Nagai. A fractographic study of iodine-induced stress corrosion cracking in irradiated Zircaloy-2 cladding. *Journal of Nuclear Materials*, 114(2-3):222–230, 1983. (Cited on page 26)
- [61] K. Kitano, C. Losin, J. Arborelius, and M. Limbäck. Study on incipient cracks at inner surface of cladding liner after high power irradiation test. *Journal of Nuclear Science and Technology*, 43(9):1015–1020, 2006. (Cited on page 26, 27)
- [62] I. Takagi, T. Hattori, M. Hashizumi, and K. Higashi. Deuterium radial redistribution in Zr-liner cladding tubes. *Nuclear Instruments and Methods in Physics Research, Section B: Beam Interactions with Materials and Atoms*, 118(1-4):238–241, 1996. (Cited on page 26)
- [63] T. Andersson. Fuel failure mitigation at the Ringhals plant. *Fuel failure in water reactors: Causes and mitigation*, page 123, 2003. (Cited on page 26)
- [64] W. Klinger, C. Petit, and J. Willse. Experience and Reliability of Framatome ANP's PWR and BWR Fuel. *Fuel failure in water reactors: Causes and mitigation*, page 21, 2003. (Cited on page 26)
- [65] F. Groeschel, G. Bart, R. Montgomery, and S. K. Yagnik. Failure root cause of a PCI suspect liner fuel rod. Technical report, 2003. (Cited on page 26)
- [66] G. R. Thomas. The Studsvik Inter Ramp Project: An international power ramp experimental program. *Journal of Nuclear Materials*, 87(2-3):215–226, 1979. (Cited on page 27)
- [67] H. Mogard, U. Bergenlid, S. Djurle, E. Larsson, G. Lysell, G. Roennberg, K. Saltvedt, and H. Tomani. The Studsvik inter-ramp project. An international power ramp experimental study. Technical report, 1979. (Cited on page 27)
- [68] D. G. Franklin, S. Djurle, and D. Howl. Performance of niobia-doped fuel in power-ramp tests. In *Nuclear fuel performance. 2 v*, pages 1–141. 1985. (Cited on page 27)
- [69] H. Mogard and H. Heckermann. The international SUPER-RAMP project at Studsvik. In *Proc. ANS Topical Meeting on Light Water Reactor Fuel Performance, Orlando, Fla, USA*, pages 21–24, 1985. (Cited on page 27)

- [70] S. Djurle. The Super-Ramp Project. *Studsvik STSR-32*, 1984. (Cited on page 27)
- [71] T. Howe, S. Djurle, and G. Lysell. Ramp Testing of 9x9 BWR Fuel. Fuel for the 90 s. In *International Topical Meeting on LWR Fuel Performance. Avignon, France*, volume 1, pages 828–837, 1991. (Cited on page 27)
- [72] T. Baba, T. Takahashi, H. Kubo, Y. Fujiwara, and Y. Kondo. Power cycling and ramp test in R-2 and Mihama Unit 2 for MHI PWR fuels. Technical report, 1983. (Cited on page 27)
- [73] S. Suzuki, K. Murakami, and T. Takahashi. Burnup Extension and Improved Reliability. In *Proc. 1994 International Topical Meeting On Light Water Reactor Fuel Performance. West Palm Beach, FL, USA*, pages 17–21, 1994. (Cited on page 27)
- [74] D. A. Wesley, K. Mori, and S. Inoue. Mark-BEB Ramp Testing Program. In *Proc. 1994 International Topical Meeting On Light Water Reactor Fuel Performance. West Palm Beach, FL, USA*, pages 17–21, 1994. (Cited on page 27)
- [75] S. Djurle. Studsvik Over-Ramp Project. Final report. Technical Report EPRI-NP-3007, Studsvik Energiteknik AB, 1983. (Cited on page 27)
- [76] T. E. Hollowell, P. Knudsen, and H. Mogard. The International Overramp Project at Studsvik. In *American Nuclear Society Topical Meeting on LWR Extended Burnup*, pages 5–17. American Nuclear Society, 1982. (Cited on page 27)
- [77] H. Mogard, D. Howe, and M. Grounes. Topical Meeting on LWR Fuel Performance, Williamsburg, VA. *Proc. ANS*, page 232, 1988. (Cited on page 28)
- [78] J. C. Wood. Interactions between Stressed Zirconium Alloys and Iodine at 300°C. *Nuclear Technology*, 23(1):63–79, 1974. (Cited on page 28)
- [79] A. L. Bement, J. C. Tobin, and R. G. Hoagland. Effects of Neutron Irradiation on the Flow and Fracture Behavior of Zircaloy-2. In *Flow and Fracture of Metals and Alloys in Nuclear Environments*. 1965. (Cited on page 29)
- [80] D. Le Boulch, L. Fournier, and C. Sainte-Catherine. Testing and Modelling Iodine-Induced Stress Corrosion Cracking in Stress-Relieved Zircaloy-4. In *Pellet-clad Interaction*

- in *Water Reactor Fuels: Seminar Proceedings*, page 253. OECD Publishing, 2004. (Cited on page 32, 148)
- [81] P. S. Sidky. Iodine stress corrosion cracking of Zircaloy reactor cladding: iodine chemistry (a review). *Journal of Nuclear Materials*, 256(1):1–17, 1998. (Cited on page 32, 131, 148)
- [82] H. S. Rosenbaum. The interaction of iodine with Zircaloy-2. *Electrochemical Technology (US) Absorbed by J. Electrochem. Soc.*, 4, 1966. (Cited on page 32, 131)
- [83] M. Fregonese, G. Delette, G. Ducros, and F. Lefebvre. Amount of iodine responsible for I-SCC of Zircaloy-4 in PCI-conditions: recoil-implanted and thermally released iodine. *Nuclear Engineering and Design*, 186(3):307–322, 1998. (Cited on page 32, 148)
- [84] B. J. Lewis, W. T. Thompson, M. R. Kleczek, K. Shaheen, M. Juhas, and F. C. Iglesias. Modelling of iodine-induced stress corrosion cracking in CANDU fuel. *Journal of Nuclear Materials*, 408(3):209–223, 2011. (Cited on page 32, 33)
- [85] C. Anghel, A. A. Holston, G. Lysell, S. Karlsson, R. Jakobsson, J. Flygare, S. Mahmood, D. Le Boulch, and I. Arimescu. Experimental and finite element modeling parametric study for iodine-induced stress corrosion cracking of irradiated cladding. *Proceedings of Top Fuel*, 2010:218–228, 2010. (Cited on page 32, 35)
- [86] R. W. Grimes, R. G. J. Ball, and C. R. A. Catlow. Site preference and binding of iodine and caesium in uranium dioxide. *Journal of Physics and Chemistry of Solids*, 53(4):475–484, 1992. (Cited on page 32)
- [87] B. J. Lewis, R. D. MacDonald, and H. W. Bonin. Release of Iodine and Noble Gas Fission Products from Defected Fuel Elements during Reactor Shutdown and Start-Up. *Nuclear Technology*, 92(3):315–324, 1990. (Cited on page 33)
- [88] F. Brossard, G. Carlot, A. Chevarier, N. Chevarier, D. Crusset, J. C. Duclot, H. Faust, C. Gaillard, N. Millard-Pinard, and N. Moncoffre. Use of fission product implantation in nuclear waste management. In *AIP Conference Proceedings*, volume 447, pages 83–91. AIP, 1998. (Cited on page 36)

- [89] L. Thomé, J. Jagielski, and F. Garrido. Location of fission products in zirconia single crystals. *Europhysics Letters*, 47(2):203, 1999. (Cited on page 36, 158)
- [90] K. C. Radford and R. J. Bratton. Zirconia electrolyte cells - Part 2 Electrical properties. *Journal of Materials Science*, 14(1):66, 1979. (Cited on page 37)
- [91] O. J. Whittemore and D. W. Marshall. Fused stabilized zirconia and refractories. *Journal of the American Ceramic Society*, 35(4):85–89, 1952. (Cited on page 37)
- [92] L. Wang and T. Liang. Ceramics for high level radioactive waste solidification. *Journal of Advanced Ceramics*, 1(3):194–203, 2012. (Cited on page 37)
- [93] C. J. Howard, R. J. Hill, and B. E. Reichert. Structures of  $\text{ZrO}_2$  polymorphs at room temperature by high-resolution neutron powder diffraction. *Acta Crystallographica Section B*, 44(2):116–120, 1988. (Cited on page 37, 52, 107)
- [94] G. Teufer. The crystal structure of tetragonal  $\text{ZrO}_2$ . *Acta Crystallographica*, 15(11):1187, 1962. (Cited on page 37, 55)
- [95] R. A. Causey, D. F. Cowgill, and R. H. Nilson. Review of the oxidation rate of zirconium alloys. Technical report, Sandia National Laboratories, 2005. (Cited on page 38, 133)
- [96] F. Garzarolli, H. Seidel, R. Tricot, and J.P. Gros. Oxide growth mechanism on zirconium alloys. In *Zirconium in the Nuclear Industry: Ninth International Symposium*. ASTM International, 1991. (Cited on page 38, 56)
- [97] J. K. Dawson, G. Long, W. E. Seddon, and J. F. White. The kinetics and mechanism of the oxidation of zircaloy-2 at 350–500°C. *Journal of Nuclear Materials*, 25(2):179–200, 1968. (Cited on page 38)
- [98] H. A. Porte, J. G. Schnizlein, R. C. Vogel, and D. F. Fischer. Oxidation of zirconium and zirconium alloys. *Journal of the Electrochemical Society*, 107(6):506–515, 1960. (Cited on page 38)
- [99] B. Cox. Some factors which affect the rate of oxidation and hydrogen absorption of Zircaloy-2 in steam. Technical report, United Kingdom Atomic Energy Authority. Research Group., 1963. (Cited on page 38)

- [100] M. L. Rossi and C. D. Taylor. First-principles insights into the nature of zirconium–iodine interactions and the initiation of iodine-induced stress–corrosion cracking. *Journal of Nuclear Materials*, 458:1–10, 2015. (Cited on page 39, 133)
- [101] J. P. Abriata, J. Garcés, and R. Versaci. The O-Zr (Oxygen-Zirconium) system. *Bulletin of Alloy Phase Diagrams*, 7(2):116–124, 1986. (Cited on page 40)
- [102] J. Hu, B. Setiadinata, T. Aarholt, A. Garner, A. Vilalta-Clemente, M. J. Partezana, P. Frankel, P. Bagot, S. Lozano-Perez, A. Wilkinson, M. Preuss, M. Moody, and C. R. M. Grovenor. *High-resolution characterization of Zr nuclear fuel cladding alloys*. 2016. (Cited on page 41)
- [103] C. Ciszak. *Etude de l'accrochage pastille/gaine des crayons combustibles des réacteurs à eau pressurisée*. PhD thesis, Université Bourgogne Franche-Comté, 2017. (Cited on page 41)
- [104] C. Gibert. *Influence de l'irradiation et de la présence de lithium sur la nature cristallographique de la zircone dans le cadre de l'étude de la corrosion du zircaloy 4 en milieu réacteur à eau pressurisée*. PhD thesis, Châtenay-Malabry, Ecole centrale de Paris, 1998. (Cited on page 41)
- [105] N. Lozano, L. Desgranges, D. Aymes, and J. C. Niepce. High magnification SEM observations for two types of granularity in a high burnup PWR fuel rim. *Journal of Nuclear Materials*, 257(1):78–87, 1998. (Cited on page 42, 43)
- [106] S. G. Prussin, D. R. Olander, P. Goubeault, and D. Bayen. Release of volatile fission products from UO<sub>2</sub>. In *Proceedings of the American Nuclear Society of Topical Meeting on Fission Product Behaviour and Source Term Research*, Snowbird, UT, 1984. (Cited on page 41)
- [107] S. G. Prussin, D. R. Olander, W. K. Lau, and L. Hansson. Release of fission products (Xe, I, Te, Cs, Mo and Tc) from polycrystalline UO<sub>2</sub>. *Journal of Nuclear Materials*, 154(1):25–37, 1988. (Cited on page 41)
- [108] J. J. Katz. *The Chemistry of the Actinide and Transactinide Elements (Volumes 1-5)*, volume 1. Springer Science and Business Media, 2007. (Cited on page 44)

- [109] M. H. Rand, R. J. Ackermann, F. Gronvold, F. L. Oetting, and A. Pattoret. The thermodynamic properties of the urania phase. *Revue Internationale des Hautes Temperatures et des Refractaires*, 15(4):355–365, 1978. (Cited on page 44)
- [110] P. Chevalier, E. Fischer, and B. Cheynet. Progress in the thermodynamic modelling of the O–U binary system. *Journal of nuclear materials*, 303(1):1–28, 2002. (Cited on page 44)
- [111] C. Guéneau, M. Baichi, D. Labroche, C. Chatillon, and B. Sundman. Thermodynamic assessment of the uranium–oxygen system. *Journal of Nuclear Materials*, 304(2-3):161–175, 2002. (Cited on page 44)
- [112] I. Efthymiopoulos, D. Grenier, M. Meddahi, P. Trilhe, S. Evrard, H. Vincke, C. Theis, N. Charitonidis, C. Hessler, and A. Pardons. HiRadMat: a new irradiation facility for material testing at CERN. Technical report, 2011. (Cited on page 45)
- [113] H. C. Andersen. Molecular dynamics simulations at constant pressure and/or temperature. *The Journal of Chemical Physics*, 72(4):2384–2393, 1980. (Cited on page 45)
- [114] P. K. Schelling, S. R. Phillipot, and D. Wolf. Mechanism of the Cubic-to-Tetragonal Phase Transition in Zirconia and Yttria-Stabilized Zirconia by Molecular-Dynamics Simulation. *Journal of the American Ceramic Society*, 84(7):1609–1619, 2001. (Cited on page 45)
- [115] M. S. Khan, M. S. Islam, and D. R. Bates. Cation doping and oxygen diffusion in zirconia: A combined atomistic simulation and molecular dynamics study. *Journal of Materials Chemistry*, 8(10):2299–2307, 1998. (Cited on page 45)
- [116] H. B. Lee, F. B. Prinz, and W. Cai. Atomistic simulations of grain boundary segregation in nanocrystalline yttria-stabilized zirconia and gadolinia-doped ceria solid oxide electrolytes. *Acta Materialia*, 61(10):3872–3887, 2013. (Cited on page 45)
- [117] C. A. J. Fisher and H. Matsubara. Oxide ion diffusion along grain boundaries in zirconia: A molecular dynamics study. *Solid State Ionics*, 113:311–318, 1998. (Cited on page 45)
- [118] F. Pietrucci, M. Bernasconi, A. Laio, and M. Parrinello. Vacancy-vacancy interaction and oxygen diffusion in stabilized cubic  $ZrO_2$  from first principles. *Physical Review B*, 78(9):094301, 2008. (Cited on page 45)

- [119] X. Li and B. Hafskjold. Molecular dynamics simulations of yttrium-stabilized zirconia. *Journal of Physics: Condensed Matter*, 7(7):1255, 1995. (Cited on page 45)
- [120] S. P. Miller, B. I. Dunlap, and A. S. Fleischer. Effects of dopant clustering in cubic zirconia stabilized by yttria and scandia from molecular dynamics. *Solid State Ionics*, 253(1):130–136, 2013. (Cited on page 45)
- [121] D. S. Aidhy, Y. Zhang, and W. J. Weber. Radiation damage in cubic  $\text{ZrO}_2$  and yttria-stabilized zirconia from molecular dynamics simulations. *Scripta Materialia*, 98(1):16–19, 2015. (Cited on page 45)
- [122] S. Davis, A. B. Belonoshko, A. Rosengren, A. C. T. van Duin, and B. Johansson. Molecular dynamics simulation of zirconia melting. *Central European Journal of Physics*, 8(5):789–797, 2010. (Cited on page 46)
- [123] S. J. Clark, M. D. Segall, C. J. Pickard, P. J. Hasnip, M. J. Probert, K. Refson, and M. C. Payne. First principles methods using CASTEP. *Zeitschrift für Kristallographie*, 220(5/6):567–570, 2005. (Cited on page 46, 105)
- [124] M. Challacombe and E. Schwegler. Linear scaling computation of the Fock matrix. *The Journal of Chemical Physics*, 106(13):5526–5536, 1997. (Cited on page 46)
- [125] E. Schwegler and M. Challacombe. Linear scaling computation of the Hartree-Fock exchange matrix. *Journal of Chemical Physics*, 105(7):2726–2734, 1996. (Cited on page 46)
- [126] V. M. Orera, R. I. Merino, Y. Chen, R. Cases, and P. J. Alonso. Intrinsic electron and hole defects in stabilized zirconia single crystals. *Physical Review B*, 42(16):9782, 1990. (Cited on page 47, 105)
- [127] C. Jiang, X-Y. Liu, and K. E. Sickafus. First-principles prediction of the thermodynamic stability of xenon in monoclinic, tetragonal, and yttrium-stabilized cubic  $\text{ZrO}_2$ . *Physical Review B*, 83(5):52103, 2011. (Cited on page 47, 105)
- [128] W. C. Mackrodt and P. M. Woodrow. Theoretical estimates of point defect energies in cubic zirconia. *Journal of the American Ceramic Society*, 69(3):277–280, 1986. (Cited on page 47, 105, 119)

- [129] C. Århammar, C. M. Araújo, and R. Ahuja. Energetics of Al doping and intrinsic defects in monoclinic and cubic zirconia: First-principles calculations. *Physical Review B*, 80(11):115208, 2009. (Cited on page 47, 105)
- [130] J. X. Zheng, G. Ceder, T. Maxisch, W. K. Chim, and W. K. Choi. First-principles study of native point defects in hafnia and zirconia. *Physical review B*, 75(10):104112, 2007. (Cited on page 47, 104)
- [131] A. S. Foster, V. B. Sulimov, F. L. Gejo, A. L. Shluger, and R. M. Nieminen. Modelling of point defects in monoclinic zirconia. *Journal of non-crystalline solids*, 303(1):101–107, 2002. (Cited on page 47, 104)
- [132] A. S. Foster, V. B. Sulimov, F. L. Gejo, A. L. Shluger, and R. M. Nieminen. Structure and electrical levels of point defects in monoclinic zirconia. *Physical Review B*, 64(22):224108, 2001. (Cited on page 47, 104)
- [133] C. Gionco, M. C. Paganini, E. Giamello, R. Burgess, C. Di Valentin, and G. Pacchioni. Paramagnetic defects in polycrystalline zirconia: An EPR and DFT study. *Chemistry of Materials*, 25(11):2243–2253, 2013. (Cited on page 47)
- [134] J. Eichler, U. Eisele, and J. Rödel. Mechanical properties of monoclinic zirconia. *Journal of the American Ceramic Society*, 87(7):1401–1403, jul 2004. (Cited on page 47)
- [135] Y. Zhang and J. Zhang. First principles study of structural and thermodynamic properties of zirconia. *Materials Today: Proceedings*, 1(1):44–54, 2014. (Cited on page 47)
- [136] R. French, S. Glass, F. Ohuchi, Y. Xu, and W. Ching. Experimental and theoretical determination of the electronic structure and optical properties of three phases of ZrO<sub>2</sub>, 1994. (Cited on page 47, 111)
- [137] B. Králik, E. K. Chang, and S. G. Louie. Structural properties and quasiparticle band structure of zirconia. *Physical Review B - Condensed Matter and Materials Physics*, 57(12):7027, 1998. (Cited on page 47)

- [138] X. Zhao and D. Vanderbilt. Phonons and lattice dielectric properties of zirconia. *Physical Review B - Condensed Matter and Materials Physics*, 65(7):075105, 2002. (Cited on page 47, 79)
- [139] Chetvorno. Solid State Electronic Band Structure Diagram. Made available at <https://tinyurl.com/bandstr192>. Accessed 03-08-2019, 2017. (Cited on page 48)
- [140] E. H. Kisi and C. J. Howard. Crystal structures of zirconia phases and their inter-relation. In *Key Engineering Materials*, volume 153, pages 1–36. Trans Tech Publ, 1998. (Cited on page 51, 52, 59)
- [141] S. P. Terblanche. Thermal-expansion coefficients of yttria-stabilized cubic zirconias. *Journal of Applied Crystallography*, 22(3):283–284, 1989. (Cited on page 52)
- [142] S. M. Lang. Axial Thermal Expansion of Tetragonal ZrO<sub>2</sub> Between 1150° and 1700°C. *Journal of the American Ceramic Society*, 47(12):641–644, 1964. (Cited on page 52)
- [143] O. Ohtaka, T. Yamanaka, S. Kume, N. Hara, H. Asano, and F. Izumi. Structural analysis of orthorhombic ZrO<sub>2</sub> by high resolution neutron powder diffraction. *Proceedings of the Japan Academy, Series B*, 66(10):193–196, 1990. (Cited on page 52)
- [144] J. Haines, J. M. Léger, and A. Atouf. Crystal Structure and Equation of State of Cotunnite-Type Zirconia. *Journal of the American Ceramic Society*, 78(2):445–448, 1995. (Cited on page 52)
- [145] E. H. Kisi, C. J. Howard, and R. J. Hill. Crystal structure of orthorhombic zirconia in partially stabilized zirconia. *Journal of the American Ceramic Society*, 72(9):1757–1760, 1989. (Cited on page 52, 60)
- [146] X. Xia. *Computational Modelling Study of Yttria-stabilized Zirconia*. PhD thesis, University College London, 2010. (Cited on page 53)
- [147] E. C. Subbarao, H. S. Maiti, and K. K. Srivastava. Martensitic transformation in zirconia. *Physica status solidi (a)*, 21(1):9–40, 1974. (Cited on page 54)
- [148] J. D. McCullough and K. N. Trueblood. The crystal structure of baddeleyite (monoclinic ZrO<sub>2</sub>). *Acta Crystallographica*, 12(7):507–511, 1959. (Cited on page 54)

- [149] T. K. Gupta, J. H. Bechtold, R. C. Kuznicki, L. H. Cadoff, and B. R. Rossing. Stabilization of tetragonal phase in polycrystalline zirconia. *Journal of Materials Science*, 12(12):2421–2426, 1977. (Cited on page 54)
- [150] G. M. Wolten. Diffusionless Phase Transformations in Zirconia and Hafnia. *Journal of the American Ceramic Society*, 46(9):418–422, 1963. (Cited on page 55)
- [151] O. Ruff and F. Ebert. Refractory ceramics: I. The forms of zirconium dioxide. *Z Anorg Allg Chem*, 180(1):19–41, 1929. (Cited on page 55)
- [152] S. Block, J. A. H. D. Jornada, and G. J. Piermarini. Pressure-Temperature Phase Diagram of Zirconia. *Journal of the American Ceramic Society*, 68(9):497–499, 1985. (Cited on page 57)
- [153] S. D. Cramer and B. S. Covino. *Corrosion: fundamentals, testing and protection*, volume 13. ASM international, 2003. (Cited on page 56)
- [154] N. B. Pilling and R. E. Bedworth. The oxidation of metals at high temperatures. *Journal of the Institute of Metals*, 29(3):529–582, 1923. (Cited on page 56)
- [155] N. Pétigny, P. Barberis, C. Lemaignan, C. Valot, and M. Lallement. In situ XRD analysis of the oxide layers formed by oxidation at 743 K on Zircaloy 4 and Zr-1NbO. *Journal of Nuclear Materials*, 280(3):318–330, 2000. (Cited on page 56)
- [156] M. Preuss, P. Frankel, S. Lozano-Perez, D. Hudson, E. Polatidis, N. Ni, J. Wei, C. English, S. Storer, and K. B. Chong. Studies Regarding Corrosion Mechanisms in Zirconium Alloys. *Journal of ASTM International*, 8(9):649–681, 2012. (Cited on page 56)
- [157] P. Barberis. Zirconia powders and Zircaloy oxide films: tetragonal phase evolution during 400°C autoclave tests. *Journal of Nuclear Materials*, 226(1-2):34–43, 1995. (Cited on page 57)
- [158] E. O. Hall. The deformation and ageing of mild steel: III discussion of results. *Proceedings of the Physical Society. Section B*, 64(9):747, 1951. (Cited on page 57)
- [159] N. J. Petch. The Cleavage Strength of Polycrystals. *J. of the Iron and Steel Inst.*, 174:25–28, 1953. (Cited on page 57)

- [160] C. J. Howard, E. H. Kisi, and O. Ohtaka. Crystal structures of two orthorhombic zirconias. *Journal of the American Ceramic Society*, 74(9):2321–2323, 1991. (Cited on page 58)
- [161] J. Haines, J. M. Léger, S. Hull, J. P. Petitet, A. S. Pereira, C. Perottoni, and J. H. Jornada. Characterization of the Cotunnite-Type Phases of Zirconia and Hafnia. *Journal of the American Ceramic Society*, 80(7):1910–1914, 1997. (Cited on page 61)
- [162] O. Ohtaka, T. Yamanaka, and T. Yagi. New high-pressure and-temperature phase of  $\text{ZrO}_2$  above 1000 °C at 20 GPa. *Physical Review B*, 49(14):9295, 1994. (Cited on page 61)
- [163] A. P. Mirgorodsky, M. B. Smirnov, and P. E. Quintard. Phonon spectra evolution and soft-mode instabilities of zirconia during the c-t-m transformation. *Journal of Physics and Chemistry of Solids*, 60(7):985–992, 1999. (Cited on page 62)
- [164] C. H. Perry, F. Lu, D. W. Liu, and B. Alzyab. Phonons and phase transitions in zirconia. *Journal of Raman Spectroscopy*, 21(9):577–584, 1990. (Cited on page 62)
- [165] D. Simeone, G. Baldinozzi, D. Gosset, M. Dutheil, A. Bulou, and T. Hansen. Monoclinic to tetragonal semireconstructive phase transition of zirconia. *Physical Review B - Condensed Matter and Materials Physics*, 67(6):064111, 2003. (Cited on page 62)
- [166] W. Harlow, A. C. Lang, B. J. Demaske, S. R. Phillpot, and M. L. Taheri. Thickness-dependent stabilization of tetragonal  $\text{ZrO}_2$  in oxidized zirconium. *Scripta Materialia*, 145(1):95–98, 2018. (Cited on page 62)
- [167] R. D. Shannon. Revised effective ionic radii and systematic studies of interatomic distances in halides and chalcogenides. *Acta Crystallographica Section A*, 32(5):751–767, 1976. (Cited on page 63, 142, 169)
- [168] F. A. Kröger and H. J. Vink. Relations between the concentrations of imperfections in crystalline solids. In *Solid state physics*, volume 3, pages 307–435. Elsevier, 1956. (Cited on page 63)
- [169] W. Kohn and L. J. Sham. Self-consistent equations including exchange and correlation effects. *Physical Review*, 140(4A):A1133, 1965. (Cited on page 67)

- [170] D. C. Langreth and J. P. Perdew. Theory of nonuniform electronic systems. I. Analysis of the gradient approximation and a generalization that works. *Physical Review B*, 21(12):5469, 1980. (Cited on page 68)
- [171] D. C. Langreth and M. J. Mehl. Beyond the local-density approximation in calculations of ground-state electronic properties. *Physical Review B*, 28(4):1809, 1983. (Cited on page 68)
- [172] A. D. Becke. Density-functional exchange-energy approximation with correct asymptotic behavior. *Physical Review A*, 38(6):3098, 1988. (Cited on page 68)
- [173] J. P. Perdew, A. Ruzsinszky, G. I. Csonka, O. A. Vydrov, G. E. Scuseria, L. A. Constantin, X. Zhou, and K. Burke. Restoring the density-gradient expansion for exchange in solids and surfaces. *Physical review letters*, 100(13):136406, 2008. (Cited on page 68)
- [174] J. Perdew, K. Burke, and M. Ernzerhof. Generalized Gradient Approximation Made Simple. *Physical review letters*, 77(18):3865, 1996. (Cited on page 68, 105)
- [175] M. C. Payne, M. P. Teter, D. C. Allan, T. A. Arias, and J. D. Joannopoulos. Iterative minimization techniques for ab initio total-energy calculations: Molecular dynamics and conjugate gradients. *Reviews of Modern Physics*, 64(4):1045, 1992. (Cited on page 70)
- [176] P. J. Hasnip. Introduction to First-Principles Modelling and CASTEP, 2010. (Cited on page 74)
- [177] H. Monkhorst and J. Pack. Special points for Brillouin zone integrations. *Physical Review B*, 13(12):5188, jun 1976. (Cited on page 74, 105)
- [178] S. T. Murphy and N. D. M. Hine. Point Defects and Non-stoichiometry in Li<sub>2</sub>TiO<sub>3</sub>. *Chemistry of Materials*, 26(4):1629–1638, 2014. (Cited on page 78, 85)
- [179] B. D. C. Bell, S. T. Murphy, P. A. Burr, R. W. Grimes, and M. R. Wenman. Accommodation of tin in tetragonal ZrO<sub>2</sub>. *Chemistry of Materials*, 117(8):084901, 2015. (Cited on page 78)
- [180] P. Pulay. Convergence acceleration of iterative sequences. the case of scf iteration. *Chemical Physics Letters*, 73(2):393–398, jul 1980. (Cited on page 78, 105)

- [181] G. Makov and M. C. Payne. Periodic boundary conditions in ab initio calculations. *Physical Review B*, 51(7):4014, 1995. (Cited on page 79)
- [182] G. Makov, R. Shah, and M. Payne. Periodic boundary conditions in ab initio calculations. II. Brillouin-zone sampling for aperiodic systems. *Physical Review B - Condensed Matter and Materials Physics*, 53(23):15513, 1996. (Cited on page 79)
- [183] S. T. Murphy and N. D. M. Hine. Anisotropic charge screening and supercell size convergence of defect formation energies. *Physical Review B - Condensed Matter and Materials Physics*, 87(9):094111, 2013. (Cited on page 79)
- [184] X. Zhao and D. Vanderbilt. First-principles study of structural, vibrational, and lattice dielectric properties of hafnium oxide. *Physical Review B - Condensed Matter and Materials Physics*, 65(23):233106, 2002. (Cited on page 79)
- [185] P. A. Burr, S. C. Middleburgh, and R. W. Grimes. Crystal structure, thermodynamics, magnetics and disorder properties of Be–Fe–Al intermetallics. *Journal of Alloys and Compounds*, 639:111–122, 2015. (Cited on page 79)
- [186] M. L. Jackson, P. A. Burr, and R. W. Grimes. Resolving the structure of TiBe<sub>12</sub>. *Acta Crystallographica*, 72:277–280, 2016. (Cited on page 79)
- [187] A. Goyal, K. Mathew, R. G. Hennig, A. Chernatynskiy, C. R. Stank, S. T. Murphy, D. A. Andersson, S. R. Phillpot, and B. P. Uberuaga. The conundrum of relaxation volumes in first-principles calculations of charge defects. *Applied Sciences*, 9(24):5276, 2019. (Cited on page 83, 170)
- [188] S. T. Murphy, M. W. D. Cooper, and R. W. Grimes. Point defects and non-stoichiometry in thoria. *Solid State Ionics*, 267(1):80–87, dec 2014. (Cited on page 85)
- [189] I. Batyrev, A. Alavi, and M. Finnis. Equilibrium and adhesion of Nb/sapphire: The effect of oxygen partial pressure. *Physical Review B*, 62(7):4698–4706, 2000. (Cited on page 85)
- [190] A. Y. Lozovoi, A. Alavi, and M. W. Finnis. Surface energy and the early stages of oxidation of NiAl(110). *Computer Physics Communications*, 137(1):174–194, 2001. (Cited on page 85)

- [191] M. W. Finnis, A. Y. Lozovoi, and A. Alavi. The oxidation of NiAl: What can we learn from ab initio calculations? *Annual Review of Materials Research*, 35(1):167–207, 2005. (Cited on page 85)
- [192] P. Brown, E. Curti, B. Grambow, C. Ekberg, F. Mompean, J. Perrone, and M. Ille-massene. Chemical thermodynamics of zirconium (Chemical Thermodynamics Series vol. 8), 2005. (Cited on page 85)
- [193] R. C. Weast, M. J. Astle, and W. H. Beyer. CRC handbook of chemistry and physics CRC Press. Inc. Florida (USA), 1984. (Cited on page 86)
- [194] B. D. C. Bell. *The influence of alloying elements on the corrosion of Zr-based nuclear fuel cladding using density functional theory*. PhD thesis, Imperial College London, Department of Materials, 2016. (Cited on page 86, 87)
- [195] S. Kasamatsu, T. Tada, and S. Watanabe. Parallel-sheets model analysis of space charge layer formation at metal/ionic conductor interfaces. *Solid State Ionics*, 226(1):62–70, 2012. (Cited on page 86)
- [196] M. Youssef and B. Yildiz. Intrinsic point-defect equilibria in tetragonal ZrO<sub>2</sub>: Density functional theory analysis with finite-temperature effects. *Physical Review B*, 86(14):144109, 2012. (Cited on page 88, 105, 115, 127)
- [197] M. Youssef and B. Yildiz. Hydrogen defects in tetragonal ZrO<sub>2</sub> studied using density functional theory. *Physical Chemistry Chemical Physics*, 16(4):1354–1365, 2014. (Cited on page 88)
- [198] U. Otgonbaatar, W. Ma, M. Youssef, and B. Yildiz. Effect of niobium on the defect chemistry and oxidation kinetics of tetragonal ZrO<sub>2</sub>. *Journal of Physical Chemistry C*, 118(35):20122–20131, 2014. (Cited on page 88)
- [199] M. Bojinov, V. Karastoyanov, P. Kinnunen, and T. Saario. Influence of water chemistry on the corrosion mechanism of a zirconium–niobium alloy in simulated light water reactor coolant conditions. *Corrosion Science*, 52(1):54–67, 2010. (Cited on page 88, 146)

- [200] D. R. Hartree. The wave mechanics of an atom with a non-Coulomb central field. Part I. Theory and methods. In *Mathematical Proceedings of the Cambridge Philosophical Society*, volume 24, pages 89–110. Cambridge University Press, 1928. (Cited on page 93)
- [201] J. P. Perdew. Unified theory of exchange and correlation beyond the local density approximation. *Electronic structure of solids' 91*, page 11, 1991. (Cited on page 94)
- [202] J. P. Perdew, J. A. Chevary, S. H. Vosko, K. A. Jackson, M. R. Pederson, D. J. Singh, and C. Fiolhais. Atoms, molecules, solids, and surfaces: Applications of the generalized gradient approximation for exchange and correlation. *Physical Review B*, 46(11):6671, 1992. (Cited on page 94)
- [203] D. R. Lide. CRC Handbook of Chemistry and Physics, 97th Edition, 2016-2017. *Handbook of Chemistry and Physics*, 2016. (Cited on page 96)
- [204] P. Atkins and J. De Paula. *Atkins Physical Chemistry 8th edition.* 2006. (Cited on page 97)
- [205] T. Ukaji and K. Kuchitsu. Effect of temperature on the molecular structure of iodine observed by gas electron diffraction. *Bulletin of the Chemical Society of Japan*, 39(10):2153–2156, 1966. (Cited on page 97)
- [206] D. Sangalli, A. Lamperti, E. Cianci, R. Ciprian, M. Perego, and A. Debernardi. Role of oxygen vacancies on the structure and density of states of iron-doped zirconia. *Physical Review B - Condensed Matter and Materials Physics*, 87(8):085206, 2013. (Cited on page 98)
- [207] A. R. Puigdollers, S. Tosoni, and G. Pacchioni. Turning a Nonreducible into a Reducible Oxide via Nanostructuring: Opposite Behavior of Bulk ZrO<sub>2</sub> and ZrO<sub>2</sub> Nanoparticles Toward H<sub>2</sub> Adsorption. *Journal of Physical Chemistry C*, 120(28):15329–15337, 2016. (Cited on page 98, 99)
- [208] H. Y. T. Chen, S. Tosoni, and G. Pacchioni. Adsorption of ruthenium atoms and clusters on anatase TiO<sub>2</sub> and tetragonal ZrO<sub>2</sub>(101) surfaces: A comparative DFT study. *Journal of Physical Chemistry C*, 119(20):10856–10868, 2014. (Cited on page 98)

- [209] A. R. Puigdollers, P. Schlexer, and G. Pacchioni. Gold and Silver Custers on TiO<sub>2</sub> and ZrO<sub>2</sub> (101) Surfaces: Role of Dispersion Forces. *Journal of Physical Chemistry C*, 119(27):15381–15389, 2015. (Cited on page 98)
- [210] J. P. Watt. Hashin-Shtrikman bounds on the effective elastic moduli of polycrystals with monoclinic symmetry. *Journal of Applied Physics*, 51(3):1520–1524, 1980. (Cited on page 109)
- [211] S. Wu, S. S. Naghavi, G. H. Fecher, and C. Felser. A Critical Study of the Elastic Properties and Stability of Heusler Compounds: Phase Change and Tetragonal X<sub>2</sub>YZ Compounds. *Journal of Modern Physics*, 9:775–805, 2018. (Cited on page 109)
- [212] S. Wu, S. S. Naghavi, G. H. Fecher, and C. Felser. A critical study of the elastic properties and stability of Heusler compounds: Cubic Co<sub>2</sub>YZ compounds with L2<sub>1</sub> structure. *Journal of Applied Physics*, 125(8):82523, 2019. (Cited on page 109)
- [213] S. Chan, Y. Fang, M. Grimsditch, Z. Li, M. V. Nevitt, W. M. Robertson, and E. S. Zouboulis. Temperature Dependence of the Elastic Moduli of Monoclinic Zirconia. *Journal of the American Ceramic Society*, 74(7):1742–1744, 1991. (Cited on page 109)
- [214] P. Bouvier, E. Djurado, G. Lucazeau, and T. Le Bihan. High-pressure structural evolution of undoped tetragonal nanocrystalline zirconia. *Physical Review B - Condensed Matter and Materials Physics*, 62(13):8731, 2000. (Cited on page 109)
- [215] J. Cai, C. Raptis, Y. S. Raptis, and E. Anastassakis. Temperature dependence of Raman scattering in stabilized cubic zirconia. *Physical Review B*, 51(1):201, 1995. (Cited on page 109)
- [216] R. J. Nicholls, A. J. Morris, C. J. Pickard, and J. R. Yates. OptaDOS - A new tool for EELS calculations. *Journal of Physics: Conference Series*, 371(1):12062, 2012. (Cited on page 109)
- [217] A. J. Morris, R. J. Nicholls, C. J. Pickard, and J. R. Yates. OptaDOS: A tool for obtaining density of states, core-level and optical spectra from electronic structure codes. *Computer Physics Communications*, 185(5):1477–1485, 2014. (Cited on page 109)

- [218] A. S. Foster, V. B. Sulimov, F. Lopez Gejo, A. L. Shluger, and R. M. Nieminen. Modelling of point defects in monoclinic zirconia. *Journal of Non-Crystalline Solids*, 303(1):101–107, 2002. (Cited on page 111, 119)
- [219] J. E. Jaffe, R. A. Bachorz, and M. Gutowski. Low-temperature polymorphs of  $\text{ZrO}_2$  and  $\text{HfO}_2$ : A density-functional theory study. *Physical Review B - Condensed Matter and Materials Physics*, 72(14):144107, 2005. (Cited on page 111)
- [220] A. Eichler. Tetragonal Y-doped zirconia: Structure and ion conductivity. *Physical Review B - Condensed Matter and Materials Physics*, 64(17):174103, 2001. (Cited on page 111)
- [221] M. Morinaga, H. Adachi, and M. Tsukada. Electronic structure and phase stability of  $\text{ZrO}_2$ . *Journal of Physics and Chemistry of Solids*, 44(4):301–306, 1983. (Cited on page 111)
- [222] F. Zandiehnadem, R. A. Murray, and W. Y. Ching. Electronic structures of three phases of zirconium oxide. *Physica B+C*, 150(1-2):19–24, 1988. (Cited on page 111)
- [223] G. K. Bansal and A. H. Heuer. On a martensitic phase transformation in zirconia ( $\text{ZrO}_2$ )—I. Metallographic evidence. *Acta Metallurgica*, 20(11):1281–1289, 1972. (Cited on page 112)
- [224] G. K. Bansal and A. H. Heuer. On a martensitic phase transformation in zirconia ( $\text{ZrO}_2$ )—II. Crystallographic aspects. *Acta Metallurgica*, 22(4):409–417, 1974. (Cited on page 112)
- [225] P. A. Burr and M. W. D. Cooper. Importance of elastic finite-size effects: Neutral defects in ionic compounds. *Physical Review B*, 96(9):94107, 2017. (Cited on page 112, 123, 130, 165)
- [226] T. Hahn. International tables for crystallography: Brief teaching edition of volume A, Space-group symmetry. In *Crystal Research and Technology*, volume 21, page 486, 1996. (Cited on page 118)
- [227] J. P. Crocombe. Theoretical study of point defects in crystalline zircon. *Physics and Chemistry of Minerals*, 27(2):138–143, 1999. (Cited on page 119)

- [228] A. Dwivedi and A. Cormack. A computer simulation study of the defect structure of calcia-stabilized zirconia. *Philosophical Magazine A*, 61(1):1–22, 1990. (Cited on page 119)
- [229] A. Samanta, T. Lenosky, and J. Li. Thermodynamic stability of oxygen point defects in cubic zirconia. *arXiv*, 1009.5567, 2010. (Cited on page 123)
- [230] W. D. Kingery, Y. M. Chiang, and D. P. Birnie. Physical Ceramics: Principles for Ceramic Science and Engineering. pages 136–146, 1997. (Cited on page 126)
- [231] J. Ball. *Computer Simulation of Disorder in Ceramic Materials*. PhD thesis, Ph. D. Thesis, University of London, Department of Materials, 2006. (Cited on page 126)
- [232] M. Bellotto, A. Caridi, E. Cereda, G. Gabetta, M. Scagliotti, and G. M. Braga-Marcazzan. Influence of the oxygen stoichiometry on the structural and optical properties of reactively evaporated ZrO<sub>x</sub> films. *Applied Physics Letters*, 63(15):2056–2058, 1993. (Cited on page 128)
- [233] A. Kenich, M. R. Wenman, and R. W. Grimes. Iodine defect energies and equilibria in ZrO<sub>2</sub>. *Journal of Nuclear Materials*, 511:390–395, 2018. (Cited on page 131, 149)
- [234] M. Fregonese, C. Régnard, L. Rouillon, T. Magnin, F. Lefebvre, and C. Lemaignan. Failure Mechanisms of irradiated Zr alloys related to PCI: Activated slip systems, localized strains, and iodine-induced stress corrosion cracking. In *Zirconium in the Nuclear Industry: Twelfth International Symposium*, pages 377–398. ASTM International, 2000. (Cited on page 131, 133)
- [235] T. J. Kennett and H. G. Thode. Mass Spectrometrically Determined Independent Yields of I<sup>128</sup>, I<sup>130</sup>, Br<sup>80</sup>, and Br<sup>82</sup> for U<sup>233</sup>, U<sup>235</sup>, and Pu<sup>239</sup> Fission. *Physical Review*, 103(2):323, 1956. (Cited on page 132, 148)
- [236] B. C. Purkayastha and G. R. Martin. The Yields of <sup>129</sup>I in Natural and in Neutron-Induced Fission of Uranium. *Canadian Journal of Chemistry*, 34(3):293–300, 1956. (Cited on page 132, 148)

- [237] N. Imanishi, I. Fujiwara, and T. Nishi. Independent isomer yields of Sb and Te isotopes in thermal-neutron fission of  $^{233}\text{U}$ ,  $^{235}\text{U}$  and  $^{239}\text{Pu}$ . *Nuclear Physics A*, 263(1):141–149, 1976. (Cited on page 132, 148)
- [238] A. L. Nichols, D. L. Aldama, M. Verpelli, and M Verpelli A. L. Nichols D. L. Aldama. *Handbook of Nuclear Data for Safeguards: Database Extensions*. International Atomic Energy Agency, 2008. (Cited on page 132)
- [239] A. A. Delucchi and A. E. Greendale. Fission Yields of Several Iodine Isotopes and Half-Life and Fission Yield of Te 135. *Physical Review C*, 1(4):1491, 1970. (Cited on page 132, 148)
- [240] S. Amiel and H. Feldstein. Odd-even systematics in neutron fission yields of  $\text{U}^{233}$  and  $\text{U}^{235}$ . *Physical Review C*, 11(3):845, 1975. (Cited on page 132, 148)
- [241] C. Degueldre, M. Pouchon, M. Döbeli, K. Sickafus, K. Hojou, G. Ledergerber, and S. Abolhassani-Dadras. Behaviour of implanted xenon in yttria-stabilised zirconia as inert matrix of a nuclear fuel. *Journal of nuclear materials*, 289(1-2):115–121, 2001. (Cited on page 132, 150)
- [242] M. Peehs and G. Kaspar. Experimental investigations of caesium and iodine release from irradiated  $\text{UO}_2$ . *High Temperatures-High Pressures*, 14(5):517–522, 1982. (Cited on page 132)
- [243] S. K. Yagnik, B. C. Chang, and D. J. Sunderland. Effect of PWR Re-start Ramp Rate on Pellet-cladding Interactions. In *Pellet-clad Interaction in Water Reactor Fuels: Seminar Proceedings, Aix-en-Provence, France*, page 31. International Nuclear Information System, 2004. (Cited on page 132)
- [244] C. Nonon, J. C. Menard, S. Lansiart, J. Noirot, S. Martin, G. M. Decroix, O. Rabouille, C. Delafoy, and B. Petitprez. PCI behaviour of chromium oxide-doped fuel. In *Proceedings of the Pellet-Clad Interaction in Water Reactor Fuels, Aix-en-Provence, France*, pages 305–319. International Nuclear Information System, 2004. (Cited on page 132)
- [245] J. H. Yang, K. S. Kim, I. H. Nam, J. S. Oh, D. Kim, Y. W. Rhee, and J. H. Kim. Effect of step wise variation of oxygen potential during the isothermal sintering on the grain growth

- behavior in Cr<sub>2</sub>O<sub>3</sub> doped UO<sub>2</sub> pellets. *Journal of Nuclear Materials*, 429(1-3):25–33, 2012. (Cited on page 132)
- [246] S. B. Farina, G. S. Duffo, and J. R. Galvele. Stress Corrosion Cracking of Zircaloy-4 in Halide Solutions: Effect of Temperature. *Materials Research*, 5(2):107–112, 2002. (Cited on page 133)
- [247] A. Legris and C. Domain. Ab initio atomic-scale modelling of iodine effects on hcp zirconium. *Philosophical Magazine*, 85(4-7):589–595, 2005. (Cited on page 133)
- [248] G. Carlot and D. Davesne. Energetically favourable sites of iodine atoms in zirconium: an ab initio approach. *Philosophical Magazine B*, 82(1):73–83, 2002. (Cited on page 133)
- [249] K. Une. Threshold values characterizing iodine-induced SCC of Zircaloys. *Res Mechanica*, 12(3):161–188, 1984. (Cited on page 133)
- [250] J. C. Wood and J. R. Kelm. Effects of irradiation on the iodine-induced stress corrosion cracking of Candu zircaloy fuel cladding. *Res Mechanica*, 8(3):127–161, 1983. (Cited on page 133, 150)
- [251] L. Lunde, K. Videm, and S. Aas. Stress corrosion testing of irradiated zircaloy cladding and its relevance to PCI failure. Technical report, 1981. (Cited on page 133)
- [252] K. O. Vilpponen, N. Foerdestroemmen, K. Svanholm, and Y. Minagawa. Fuel performance under power ramp conditions in the HBWR. Technical report, 1981. (Cited on page 133)
- [253] N. Ni, S. Lozano-Perez, M. L. Jenkins, C. English, G. D. W. Smith, J. M. Sykes, and C. R. M. Grovenor. Porosity in oxides on zirconium fuel cladding alloys, and its importance in controlling oxidation rates. *Scripta Materialia*, 62(8):564–567, 2010. (Cited on page 133)
- [254] M. V. Glazoff, A. Tokuhiro, S. N. Rashkeev, and P. Sabharwall. Oxidation and hydrogen uptake in zirconium, Zircaloy-2 and Zircaloy-4: Computational thermodynamics and ab initio calculations. *Journal of Nuclear Materials*, 444(1-3):65–75, 2014. (Cited on page 134)

- [255] A. Couet, A. T. Motta, and R. J. Comstock. Hydrogen pickup measurements in zirconium alloys: Relation to oxidation kinetics. *Journal of Nuclear Materials*, 451(1-3):1–13, 2014. (Cited on page 134)
- [256] P. Hofmann and J. Spino. Stress corrosion cracking of Zircaloy-4 cladding at elevated temperatures and its relevance to transient LWR fuel rod behaviour. *Journal of Nuclear Materials*, 125(1):85–95, 1984. (Cited on page 146)
- [257] U. Bergenlid and H. Mogard. Experimental observations of the PCI failure occurrence on power ramping. *Res Mechanica Letters*, 1(5):229–234, 1981. (Cited on page 150)
- [258] P. J. Pankaskie. Mechanistic considerations pertinent to the PCI fuel failure phenomenon. *Pellet-Cladding Interaction in Water Reactors*, 12(17):255–287, 1981. (Cited on page 150)
- [259] C. R. Stanek, C. Jiang, K. E. Sickafus, B. P. Uberuaga, and N. A. Marks. Radioparagenesis: the Effects of Transmutation on Crystalline Stability. In *10th International Conference on Computer Simulation of Radiation Effects in Solids - COSIRES*, page 74, 2010. (Cited on page 151)
- [260] C. Jiang, B. P. Uberuaga, K. E. Sickafus, F. M. Nortier, J. J. Kitten, N. A. Marks, and C. R. Stanek. Using ‘radioparagenesis’ to design robust nuclear waste forms. *Energy and Environmental Science*, 3(1):130–135, 2010. (Cited on page 151)
- [261] C. Jiang, C. R. Stanek, N. A. Marks, K. E. Sickafus, and B. P. Uberuaga. Radioparagenesis: The formation of novel compounds and crystalline structures via radioactive decay. *Philosophical Magazine Letters*, 90(6):435–446, 2010. (Cited on page 151)
- [262] R. W. Grimes. The Effect of a Crystalline Environment on Calculated Electron Densities. *Molecular Simulation*, 5(1-2):9–22, 1990. (Cited on page 153, 155)
- [263] R. J. Nicholls, N. Ni, S. Lozano-Perez, A. London, D. W. McComb, P. D. Nellist, C. M. Grovenor, C. J. Pickard, and J. R. Yates. Crystal structure of the ZrO phase at zirconium/zirconium oxide interfaces. *Advanced Engineering Materials*, 17(2):211–215, 2015. (Cited on page 169)

- [264] J. Hu, B. Setiadinata, T. Aarholt, P. Bagot, M. Moody, S. Lozano-Perez, C. R. M. Grovenor, A. Garner, A. Harte, K. Moore, P. Frankel, M. Preuss, and N. Ni. High-resolution characterization of corrosion and hydrogen pickup of Zr cladding alloys. In *Proceedings of the TopFuel conference*, 2015. (Cited on page 169)
- [265] F. Bruneval, C. Varvenne, J. P. Crocombette, and E. Clouet. Pressure, relaxation volume, and elastic interactions in charged simulation cells. *Physical Review B - Condensed Matter and Materials Physics*, 91(2):024107, 2015. (Cited on page 170)
- [266] E. N. Brothers, A. F. Izmaylov, J. O. Normand, V. Barone, and G. E. Scuseria. Accurate solid-state band gaps via screened hybrid electronic structure calculations. *Journal of Chemical Physics*, 129(011102), 2008. (Cited on page 170)
- [267] G. L. Stefani, J. R. Maiorino, T. A. Santos, and P. R. Rossi. Neutronic and thermal-hydraulic calculations for the AP-1000 NPP with the MCNP6 and SERPENT codes. *INAC 2015: International Nuclear Atlantic Conference*, 46(48), 2015. (Cited on page 208)

# Appendix A

## ParaSweep

ParaSweep is a generalised sensitivity analysis visualisation tool which was developed during this project. Initially, it was built to help visualise the effects of changing single parameters in Brouwer diagrams, such as temperature or concentration of defects. Generalisation of the sweeping parameters was a natural extension of this tool, allowing sensitivity analyses to be performed in conjunction with any program that has variable inputs. The program has since been open-sourced and is available at <https://github.com/v1thesource/ParaSweep> along with supporting documentation.

## Appendix B

### CASTEP Scripts and Other Files

Throughout the course of this project, many useful scripts were created to help with preparing CASTEP jobs and analysing their outputs. These scripts have been made available online and for free at <https://github.com/v1thesource/CASTEP>. The purpose of open-sourcing these scripts is to simplify the experience for new users of CASTEP and help them save a considerable amount of time. Additionally, the `.tex` and data files necessary to compile this thesis have been made available at <https://github.com/v1thesource/PhD-Thesis>.

# **Appendix C**

## **Defect volumes without charge correction**

Defect relaxation volumes for charged defects were initially calculated only with respect to the uncharged non-defective cell, a method which has been shown to yield inaccurate values. These values are provided in Tables C.1, C.2 and C.3 below for comparison.

Table C.1: Individual point defect volumes in the three  $\text{ZrO}_2$  structures.

Defect	Defect volume relative to non-defective cell ( $\text{\AA}^3$ )		
	Monoclinic	Tetragonal	Cubic
$V_{\text{Zr}}''''$	55.95	88.93	48.47
$V_{\text{Zr}}'''$	42.48	51.08	36.94
$V_{\text{Zr}}''$	29.90	34.28	25.93
$V_{\text{Zr}}'$	17.10	18.43	15.08
$V_{\text{Zr}}^\times$	4.06	4.70	4.32
$\text{Zr}_i^{****}$	-34.62	-41.94	-27.34
$\text{Zr}_i^{***}$	-22.76	-27.74	-16.95
$\text{Zr}_i^{**}$	-11.79	-12.02	-6.24
$\text{Zr}_i^*$	2.68	-0.02	4.69
$\text{Zr}_i^\times$	15.94	13.40	15.97
$V_O^{**}$ [4coord]	-22.52	-40.45	-22.76
$V_O^*$ [4coord]	-12.41	-19.53	-12.19
$V_O^\times$ [4coord]	-0.69	-2.80	-1.11
$V_O^{**}$ [3coord]	-26.13		
$V_O^*$ [3coord]	-14.42		
$V_O^\times$ [3coord]	-1.71		
$O_i''$	27.01	40.00	28.58
$O_i'$	15.36	24.56	16.30
$O_i^\times$	2.66	11.06	8.95

Table C.2: Defect volumes of Frenkel and Schottky defects in the three  $\text{ZrO}_2$  structures calculated from individual point defects.

Defect	Defect volume relative to non-defective cell ( $\text{\AA}^3$ )		
	Monoclinic	Tetragonal	Cubic
$V_{\text{Zr}}'''' + \text{Zr}_i^{***}$	21.33	46.99	21.13
$V_{\text{Zr}}''' + \text{Zr}_i^{**}$	19.72	23.35	20.00
$V_{\text{Zr}}'' + \text{Zr}_i^{**}$	18.11	22.25	19.69
$V_{\text{Zr}}' + \text{Zr}_i^*$	19.78	18.41	19.76
$V_{\text{Zr}}^\times + \text{Zr}_i^\times$	19.99	18.11	20.29
$V_O^{**} + O_i''$	0.88	-0.45	5.82
$V_O^* + O_i'$	0.95	5.03	4.11
$V_O^\times + O_i^\times$	0.96	8.26	7.84
$V_{\text{Zr}}'''' + 2V_O^{**}$	3.70	8.03	2.94
$V_{\text{Zr}}'' + 2V_O^*$	1.07	-4.79	1.56
$V_{\text{Zr}}^\times + 2V_O^\times$	0.65	-0.90	2.09

Table C.3: Calculated defect volumes and stress tensor magnitudes of the dominant defect types in tetragonal  $\text{ZrO}_2$ . Stress tensors are calculated for defective supercells.

Defect type	Defect volume relative to perfect crystal ( $\text{\AA}^3$ )	Defect volume relative to vacant site ( $\text{\AA}^3$ )	Stress tensor magnitude (GPa)
$\text{V}_{\text{O}}^{\bullet\bullet}$	-37.53	0	-5.13
$\text{V}_{\text{Zr}}^{\prime\prime\prime\prime}$	67.41	0	9.21
$\text{Te}_{\text{O}}^{\bullet\bullet}$	2.74	40.26	0.84
$\text{Te}_{\text{O}}^{\bullet}$	24.61	62.14	3.29
$\text{Te}_{\text{Zr}}^{\prime\prime\prime\prime}$	83.01	15.60	13.04
$\text{Te}_{\text{Zr}}^{\prime\prime\prime}$	59.93	-7.48	10.08
$\text{I}_{\text{O}}^{\bullet\bullet\bullet}$	-18.59	18.94	-1.61
$\text{I}_{\text{O}}^{\bullet}$	29.90	67.43	3.25
$\text{I}_{\text{Zr}}^{\prime\prime\prime}$	87.07	19.66	11.76
$\text{Xe}_{\text{O}}^{\bullet\bullet}$	9.02	46.55	0.88
$\text{Xe}_{\text{Zr}}^{\prime\prime\prime\prime}$	115.50	48.09	13.53
$\text{Xe}_{\text{Zr}}^{\prime\prime\prime}$	91.65	24.24	10.65
$\text{Cs}_{\text{O}}^{\bullet\bullet}$	4.38	41.91	1.50
$\text{Cs}_{\text{Zr}}^{\prime\prime\prime}$	90.37	22.96	10.60

## Appendix D

### Steady state calculation of iodine inventory

Consider a reactor such as the AP1000 with thermal efficiency  $\eta_t = 1/3$  and electrical power output  $P_e = 1000$  MWe. Thermal power output ( $P_t$ ) is therefore:

$$P_t = \frac{P_e}{\eta_t} = \frac{1000}{1/3} = 3000 \text{ MWt} \quad (\text{D.1})$$

Assuming all thermal energy comes from fission events with each fission of U<sup>235</sup> releasing 170 MeV, the mean rate of fission ( $\dot{f}$ ) is given by:

$$\dot{f} = \frac{P_t}{E_{fission}} = \frac{3 \times 10^9}{(170 \times 10^6)(1.60 \times 10^{-19})} = 1.10 \times 10^{20} \text{ s}^{-1} \quad (\text{D.2})$$

Each fission of U<sup>235</sup> is an independent event, therefore the production rate of a particular isotope from fission ( $\dot{f}_X$ ) is related to its independent fission yield ( $y_X$ ) as follows:

$$\dot{f}_X = \dot{f}y_X \quad (\text{D.3})$$

The total inventory of iodine at steady state operation is dependent on four factors:

- Production directly from fission
- Production from decay of tellurium precursors
- Loss of iodine through radioactive decay
- Loss (of a particular iodine isotope) through neutron capture

The rate of change of tellurium and iodine populations ( $N_{\text{Te}}$  and  $N_I$ ) can therefore be expressed by:

$$\frac{dN_{\text{Te}}}{dt} = \dot{f}_{Te} - \lambda_{Te}N_{\text{Te}} \quad (\text{D.4})$$

$$\frac{dN_I}{dt} = \dot{f}_I + \lambda_{Te}N_{\text{Te}} - \lambda_I N_I - \phi\sigma_{a_I}N_I \quad (\text{D.5})$$

where  $\lambda$  is the decay constant,  $\phi$  is the thermal neutron flux and  $\sigma_{a_I}$  is the microscopic thermal neutron absorption cross-section of iodine. Assuming a clean reactor core at start-up and using the boundary condition of  $N_{\text{Te}}(t = 0) = 0$ , a general solution for  $N_{\text{Te}}$  at time  $t$  can be found:

$$N_{\text{Te}}(t) = \frac{\dot{f}_{Te}}{\lambda_{Te}}(1 - e^{-\lambda_{Te}t}) \quad (\text{D.6})$$

Using this form of  $N_{Te}(t)$  in Equation D.5, a solution for  $N_I$  at time  $t$  can also be found:

$$N_I(t) = \frac{\dot{f}_{Te} + \dot{f}_I}{\lambda_I + \phi\sigma_{a_I}}(1 - e^{-(\lambda_I + \phi\sigma_{a_I})t}) + \frac{\dot{f}_{Te}}{\phi\sigma_{a_I} - \lambda_{Te} + \lambda_I}(e^{-(\lambda_I + \phi\sigma_{a_I})t} - e^{-\lambda_{Te}t}) \quad (\text{D.7})$$

A steady state quantity of iodine is reached after a few days due to the short half-lives of many isotopes. This steady state quantity is given by:

$$N_I(t = \infty) = \frac{\dot{f}_{Te} + \dot{f}_I}{\lambda_I + \phi\sigma_{a_I}} \quad (\text{D.8})$$

The quantity  $\phi\sigma_{a_I}$  varies non-linearly in the reactor core and is therefore difficult to evaluate. Instead, an order of magnitude analysis of the denominator terms in Equation D.8 is conducted to determine their relative significance. The thermal neutron flux  $\phi$  at the core center in an AP1000 reported by Westinghouse is  $5.47 \times 10^{13}$  n/cm<sup>2</sup>s [267]. The largest thermal neutron capture cross section for an iodine isotope ( $I^{131}$ ) is approximately 100 barns ( $1 \times 10^{-22}$  cm<sup>2</sup>). The smallest decay constant  $\lambda$  for a major iodine isotope ( $I^{131}$ ) is  $1 \times 10^{-6}$  s<sup>-1</sup>. Using these values, the quantity  $\phi\sigma_{a_I}$  is  $5.47 \times 10^{-9}$  s<sup>-1</sup>, more than two orders of magnitude smaller than the decay constant of  $I^{131}$ . Thus, the decay constant of an iodine isotope will always be the dominant term in the denominator of Equation D.8, therefore:

$$\lambda_I \gg \phi\sigma_{a_I} \quad (\text{D.9})$$

therefore Equation D.8 can be written as:

$$N_I(t = \infty) = \frac{\dot{f}_{Te} + \dot{f}_I}{\lambda_I} \quad (\text{D.10})$$

---

With all values in Equation D.10 now known, the steady state number of atoms for each iodine isotope from mass 130 to 138 was computed. These values were converted to moles, and then to mass. A total mass of 203.84 grams of iodine was calculated at steady state operation in the core of a 1000 MWe reactor with this method. In an AP1000 reactor, which holds 157 fuel assemblies, this amounts to an average of approximately 1.3 grams of iodine per fuel assembly. This does not include contributions to the iodine inventory from radioactive decay of Sb, and therefore must be considered a lower-bound estimate of the total inventory at steady-state operation.